

**INVESTIGATION OF NEW PHASE CHANGE MATERIAL BASED THERMAL
MANAGEMENT SYSTEMS FOR LI-ION BATTERIES**

By
Monu Malik

A Thesis Submitted in Partial Fulfilment
of the Requirements for the Degree of Doctor of Philosophy
in
Mechanical Engineering

Faculty of Engineering and Applied Science
University of Ontario Institute of Technology

Oshawa, Ontario, Canada

© **Monu Malik, 2017**

Abstract

In this thesis, a battery pack consisting of three A123 20Ah cells connected in series is tested with various cooling methods at different discharge rates. Four different coolant inlet temperatures are selected for the investigation. The results from the battery pack tests at no cooling show that the surface temperature of the battery increases with an increase in discharge rate. The highest average temperature of the battery pack is 56.5°C, corresponding to no cooling case at a high discharge rate. With cold plates, the battery temperature remains in the specified temperature range at all discharge rates, when the coolant temperature is 30°C. The results show that the thermal management system developed in the present study using 6 mm thick phase change composite plates can manage the battery temperature in the required range. *n-Octadecane* and polyurethane foam are used to make 3 mm and 6 mm thick plates. The battery pack is tested with the developed phase change material based plates. Carbon nanotubes are used to improve the thermal conductivity of the phase change material, along with polyurethane foam. The results show that 3 mm thick plates made from pure phase change material, 3% (wt.) Carbon nanotubes and polyurethane foam can maintain the battery temperature within the required range at all discharge rates.

The internal resistance of the cylindrical and prismatic Li-ion batteries is measured at different states of charge and operating temperatures. The obtained results are used to develop a model for the battery pack in MATLAB Simulink. The good agreement attained between the simulation results and the experimental data shows that the developed model can be used to predict the behaviour of Li-ion batteries with reasonable accuracy. An economic analysis shows that the material cost of the developed PCM-based passive thermal management system for a complete battery pack on a lab scale will be approximately \$4500. The material cost of the developed thermal management system is reduced by approximately 44% when carbon nanotubes are used with the pure PCM and can be further reduced with production on an industrial scale. A preliminary optimisation of the developed system is performed using a genetic algorithm to maximise the driving range of the vehicle.

Acknowledgements

I would like to express my deep and sincere gratitude to my supervisor, Dr. Ibrahim Dincer, and my co-supervisor, Dr. Marc Rosen, for their support in my research and for supporting me throughout my studies. This PhD would not be possible without their guidance, understanding, patience, motivation, and continuous support. I hope to keep working with Dr. Dincer and Dr. Rosen in the future, and to keep improving my skills and knowledge.

I also sincerely thank Dr. Michael Fowler for allowing me to work in his labs at the University of Waterloo, and for providing me with the access to his lab facilities and equipment.

I would like to offer my deepest thanks to Vishavdeep Singh and Farrukh Khalid for all their help during my PhD study. I should also express my gratitude to Manoj Matthew and co-op students, John, Jackson and Melody, at the University of Waterloo for their help and support.

Of course, I would like to thank my family: my father Randhir Singh, my brother Sonu Malik, my sister Babita, and my sister-in-law Renu Malik for their understanding and encouragement throughout my education. Lastly, I take this opportunity to thank my dear wife, Manjeet Kaur, for her constant support, understanding and motivation.

Table of Contents

Abstract	ii
Acknowledgements	iii
Table of Contents	iv
List of Tables	x
List of Figures	xiv
Nomenclature	xxi
Chapter 1. Introduction	1
1.1 Importance and Context	1
1.2 Motivation and Problem Statement	2
1.3 Objectives	4
1.4 Methodology	7
1.5 Thesis Outline	9
Chapter 2. Background	10
2.1 Development of Electric Vehicles	10
2.2 Fundamentals of Electric and Hybrid Electric Vehicles	12
2.3 Batteries for Electric and Hybrid Electric Vehicles	15
2.3.1 Lithium-ion Batteries	16
2.3.2 Types of Li-ion Batteries	17
2.4 Degradation in Li-ion Batteries	19
2.4.1 Effect of Low Temperature on Degradation Process	21
2.4.2 Effect of High Temperature on Degradation Process	22
2.5 Thermal Management Systems for Li-ion Batteries	23
	iv

2.5.1 Design of Battery Thermal Management Systems	24
2.5.2 Existing Battery Thermal Management Systems	25
2.6 Phase Change Materials and their Applications	27
2.6.1 Types of Phase Change Materials	28
2.6.2 Drawback of Phase Change Materials and their Solutions	31
2.7 Carbon Nanotube Materials and their Applications	32
2.7.1 Dispersion Methods of Carbon Nanotubes	33
2.8 Optimization Methods	35
2.8.1 Genetic Algorithm	36
2.9 Closing Remarks	37
Chapter 3. Literature Review	39
3.1 Heat Generation and Thermal Management of Li-ion Batteries	39
3.1.1 Heat Generation in Li-ion Batteries	40
3.1.2 Battery Thermal Management Systems	41
3.2 Phase Change Materials and their Applications in Li-ion Batteries	44
3.2.1 Phase Change Materials	44
3.2.2 Phase Change Material Applications with Cylindrical Cells	46
3.2.3 Phase Change Material Applications with Prismatic Cells	47
3.3 Improvement in Thermal conductivity of Phase Change Materials	48
3.3.1 Conductive Materials	48
3.3.2 Carbon Based Filler	49
3.4 Exergy Analyses of Battery Thermal Management Systems	52
3.5 Optimisation of Battery Thermal Management Systems	54
3.6 Main Gaps in the Literature	55
Chapter 4. Experimental Setup	57

4.1 Experimental Setups for Battery Pack Testing	57
4.1.1 Prismatic Cell	60
4.1.2 Data Acquisition System	60
4.1.3 Thermocouple Locations	62
4.2 Battery Pack with No Cooling	63
4.3 Battery Pack with Conventional Liquid Cooling	65
4.3.1 Cold Plate	65
4.3.2 Battery Cooling System	67
4.4 Battery Pack with Phase Change Composite Material	68
4.4.1 Phase Change Composite Material	69
4.5 Battery Pack with Phase Change Materials	70
4.5.1 Selection of Phase Change Material	70
4.5.2 Selection of Foam	72
4.5.3 Phase Change Material Plates	73
4.5.4 Trays to Prepare Plates	74
4.5.5 Procedure to Make Phase Change Material Plates	75
4.6 Battery Pack with Phase Change Materials and Carbon Nanotubes	76
4.6.1 Carbon Nanotubes	76
4.6.2 Plates of Phase Change Materials and Carbon Nanotubes	78
4.7 Experimental Procedure for Prismatic Battery Pack Testing	79
4.8 Microscopic Test for Carbon Nanotube Distribution	82
4.9 Resistance Measurement of Prismatic Li-ion Cell	82
4.10 Resistance Measurement of Cylindrical Cell	83
4.10.1 Experimental Setup for Cylindrical Cell	84
4.11 Experimental Plan for Resistance Measurement of Prismatic and Cylindrical Cells	86

4.12 Uncertainty Analysis	86
4.12.1 Uncertainty in Temperature and Heat Generation	87
Chapter 5. Modelling, Analysis and Optimisation Methods	92
5.1 Battery Pack Modelling using MATLAB Simulink	92
5.2 Battery Simulation in ANSYS	96
5.2.1 Model for Numerical Study	96
5.2.2 Solver and Discretization Scheme	97
5.2.3 Mesh Generation	100
5.2.4 Initial and Boundary Conditions	101
5.2.5 Convergence Criteria	102
5.2.6 Model Input Parameters	102
5.2.7 Governing Equations for Cell Testing	103
5.2.8 Heat Generation Rate in Cell	106
5.3 Energy Efficiency of the Battery Pack	106
5.4 Thermal Conductivity of PCM and CNT Mixture	109
5.5 Exergy Analyses of Battery Thermal Management Systems	110
5.6 Economic Analyses of Battery Thermal Management Systems	112
5.7 Optimisation of Battery Thermal Management Systems	114
5.7.1 Objective Function	115
5.7.2 Decision Variables and Constraints	118
Chapter 6. Results and Discussion	119
6.1 Experimental Results for No Cooling Case	119
6.1.1 Temperature Profile	119
6.1.2 Voltage Profile	121
6.1.3 Heat Generation Rate	122

6.2 Experimental Results with Liquid Cooling at Various Coolant Temperatures	123
6.2.1 Coolant at 10°C	123
6.2.2 Coolant at 20°C	126
6.2.3 Coolant at 30°C	128
6.2.4 Coolant at 40°C	130
6.2.5 Comparison of No Cooling and Liquid Cooling Results	132
6.3 Experimental Results with Phase Change Composite Material	133
6.3.1 6 mm Thick Plates of Phase Change Composite Material	133
6.3.2 9 mm Thick Plates of Phase Change Composite Material	135
6.3.3 12 mm Thick Plates of Phase Change Composite Material	137
6.3.4 Comparison of No Cooling and with Phase Change Composite Plates Results	138
6.4 Experimental Results with Phase Change Composite Material and Liquid Cooling	144
6.4.1 Coolant at 10°C with Phase Change Composite Material Plates	144
6.4.2 Coolant at 20°C with Phase Change Composite Material Plates	147
6.4.3 Coolant at 30°C with Phase Change Composite Material Plates	150
6.4.4 Coolant at 40°C with Phase Change Composite Material Plates	153
6.5 Experimental Results with Phase Change Materials and Carbon Nanotubes	157
6.5.1 3 mm Thick Plates of Technical Grade Phase Change Material	157
6.5.2 3 mm Thick Plates of Pure Phase Change Material	163
6.5.3 6 mm Thick Plates of Technical Grade Phase Change Material	168
6.5.4 6 mm Thick Plates of Pure Phase Change Material	173
6.5.5 Comparison of No Cooling and with Phase Change Material Results	177
6.6 Comparison of Results Obtained from No cooling and Different Cooling Methods	179
6.6.1 Applications and Limitations of PCM-based BTMS	188
6.7 Microscopic Study for Agglomerations	189
	viii

6.8 Thermal Conductivity of PCMs and CNTs Mixture	193
6.9 Resistance Measurement of Li-ion Cell	195
6.9.1 Internal Resistance of Prismatic Cell	195
6.9.2 Internal Resistance of Cylindrical Cell	196
6.10 Results from Modelling in Simulink	197
6.11 Results from ANSYS Simulation	201
6.12 Energy and Exergy Analyses Result	204
6.13 Economic Analysis Results	206
6.14 Optimisation Results	210
Chapter 7. Conclusions and Recommendations	213
7.1 Conclusions	214
7.2 Recommendations	216
References	218

List of Tables

Table 2.1: Characteristics of battery types used in EVs and HEVs.....	16
Table 3.1: Trade-off analysis of the battery thermal management.	44
Table 3.2: Properties of some organic paraffin waxes and inorganic PCMs.....	45
Table 3.3: Various methods used to enhance PCMs thermal conductivity.	52
Table 4.1: LiFePO ₄ 20Ah lithium-ion pouch cell specifications.....	61
Table 4.2: Cold plate parameters.	66
Table 4.3: Properties of different type of PCC materials.....	69
Table 4.4: Properties of the selected PCMs.....	72
Table 4.5: Properties of open cell polyurethane foam.	72
Table 4.6: Polyurethane foam dimensions and their weight with and without PCM.	76
Table 4.7: Selected discharge and charge rates along with respective currents and minimum/maximum voltages.....	80
Table 4.8: NCR18650B, 3400mAh cylindrical cell specification.	85
Table 4.9: Relative and absolute uncertainty in battery surface temperature at four operating temperatures.....	88
Table 4.10: Summary of uncertainties for various parameters.	91
Table 5.1: Grid independence results for the cell temperature.	101
Table 5.2: Heat generation rate and volumetric heat generation rate considered for the study..	106
Table 5.3: Summary of experimental conditions analysed.....	108
Table 5.4: Fixed parameters in the objective function.....	118
Table 6.1: Maximum temperature, average temperature, and rise in temperature of the battery pack for various discharge rates with no cooling case.....	121
Table 6.2: Maximum temperature, average temperature, and rise in temperature of the battery pack with 10°C coolant temperature at various discharge rates.	125
Table 6.3: Maximum temperature, average temperature, and rise in temperature of the battery pack with 20°C coolant temperature at various discharge rates.	127
Table 6.4: Maximum temperature, average temperature, and rise in temperature of the battery pack with 30°C coolant temperature at various discharge rates.	130

Table 6.5: Maximum temperature, average temperature, and rise in temperature of the battery pack with 40°C cooling bath temperature at various discharge rates.	131
Table 6.6: Battery pack capacity at various cooling conditions.	132
Table 6.7: Temperature range with colour shade.....	133
Table 6.8: Maximum and average temperatures of the battery pack at no cooling and liquid cooling.	133
Table 6.9: Maximum temperature, average temperature, and rise in temperature of the battery pack with 6 mm thick PCC plates at various discharge rates.	135
Table 6.10: Maximum temperature, average temperature, and rise in temperature of the battery pack with 9 mm thick PCC plates at various discharge rates.....	137
Table 6.11: Maximum temperature, average temperature, and rise in temperature of the battery pack with 12 mm thick PCC plates at various discharge rates.....	138
Table 6.12: Battery pack capacity with and without PCC plates.....	139
Table 6.13: Temperature drop in maximum and average temperatures of the battery pack by using PCC plates compared to no cooling case.....	140
Table 6.14: Maximum and average temperatures of the battery pack with and without PCC plates at various discharge rates.....	142
Table 6.15: Maximum and average temperatures of the battery pack with PCC plates at various discharge rates.	157
Table 6.16: Maximum temperature, average temperature, and rise in temperature of the battery pack with 3 mm thick technical grade PCM plates at various discharge rates.....	159
Table 6.17: Maximum temperature, average temperature and rise in temperature of the battery pack with 3 mm thick technical grade PCM and 1.5 % CNT plates at various discharge rates.	160
Table 6.18: Maximum temperature, average temperature, and rise in temperature of the battery pack with 3 mm thick technical grade PCM and 3% CNT plates at various discharge rates.	162
Table 6.19: Maximum temperature, average temperature, and rise in temperature of the battery pack with 3 mm thick pure PCM plates at various discharge rates.....	164

Table 6.20: Maximum temperature, average temperature, and rise in temperature of the battery pack with 3 mm thick pure PCM and 1.5% CNT plates at various discharge rates.....	165
Table 6.21: Maximum temperature, average temperature, and rise in temperature of the battery pack with 3 mm thick pure PCM and 3% CNT plates at various discharge rates.....	167
Table 6.22: Maximum temperature, average temperature, and rise in temperature of the battery pack with 6 mm thick technical grade PCM plates at various discharge rates.....	169
Table 6.23: Maximum temperature, average temperature, and rise in temperature of the battery pack with 6 mm thick technical grade PCM and 1.5% CNT plates at various discharge rates.	171
Table 6.24: Maximum temperature, average temperature, and rise in temperature of the battery pack with 6 mm thick technical grade PCM and 3% CNT plates at various discharge rates.	172
Table 6.25: Maximum temperature, average temperature, and rise in temperature of the battery pack with 6 mm thick pure PCM plates at various discharge rates.	174
Table 6.26: Maximum temperature, average temperature, and rise in temperature of the battery pack with 6 mm thick pure PCM and 1.5% CNT plates at various discharge rates.....	175
Table 6.27: Maximum temperature, average temperature and rise in temperature of the battery pack with 6 mm thick pure PCM and 3 % CNT plates at various discharge rates.....	177
Table 6.28: Maximum and average temperatures of the battery pack with and without PCM based plates at various discharge rates.	179
Table 6.29: Comparison of maximum and average temperatures of the battery pack with various cooling conditions at various discharge rates.	187
Table 6.30: Maximum temperature obtained, and total heat generation during experiment and modelling at various discharge rates.	198
Table 6.31: Electrical efficiencies at various cooling conditions and discharge rates.....	205
Table 6.32: Exergy destructions at various cooling conditions and discharge rates.	206
Table 6.33: Parameters of Chevy Volt and electricity prices in Ontario.	207
Table 6.34: Parameters used to calculate the cost of developed passive BTMS.	208
Table 6.35: The material cost of the developed systems.	208
Table 6.36: PCC material cost provided by the manufacturer.	209

Table 6.37: Design parameters and their range.	210
Table 6.38: Optimised parameter and objective function.	212

List of Figures

Figure 1.1 Vehicle emissions of carbon dioxide (equivalent) and total fuel costs for selected types of vehicles, per 161 km (100 miles) trip in the US.....	2
Figure 2.1: Annual sales of HEVs, PHEVs, and EVs in the US from 2011 to May 2015.	11
Figure 2.2: Line diagrams of typical; (a) EV, (b) PHEV.....	12
Figure 2.3: Line diagrams of (a) series, (b) parallel, (c) series-parallel, HEV arrangements.....	14
Figure 2.4: Processes in Li-ion battery; (a) charging, (b) discharging.	17
Figure 2.5: Comparison of suitable Li-ion batteries for EVs (The more the dark green coloured shape for each cell extends along a given axis, the better the performance in that direction).	18
Figure 2.6: A general capacity fading trend of the Li-ion cell with cycle number.....	19
Figure 2.7: Schematic representation of SEI layer in a Li-ion cell.....	20
Figure 2.8: Changes at the interface of anode and electrolyte.....	22
Figure 2.9: Classification of thermal management systems for Li-ion batteries.	24
Figure 2.10: (a) Cold plate used in TMS of Chevy Volt; (b) design and arrangement of different components in TMS of Chevy Volt.....	26
Figure 2.11: (a) Line diagram of TMS of Tesla model S battery (1 module); (b) line diagram of cooling plate used in Tesla Model S-TMS for cylindrical cells.	26
Figure 2.12: Classification of PCMs.....	29
Figure 2.13: Structure of single and multi-walled carbon nanotubes.	33
Figure 2.14: Calendering process using three roll mill.....	34
Figure 2.15: Flowchart of a genetic algorithm.	37
Figure 4.1: Experimental setup 1; (a) line diagram, (b) actual setup.....	58
Figure 4.2: Experimental setup 2; (a) line diagram, (b) actual setup.....	59
Figure 4.3: Thermal data acquisition system; (a) 8-channel thermocouple input module (FP-TC-120), (b) analogue input circuitry on one channel, (c) actual system with 3 modules and 18 thermocouples.....	62
Figure 4.4: User interface developed in LabVIEW for thermal data acquisition.	62
Figure 4.5: Thermocouple locations; (a) drawing with dimensions, (b) actual cell with the thermocouple.	63

Figure 4.6: Arrangement of cells in the battery pack; (a) expanded view, (b) actual battery pack, (c) top view, (d) rear view.	64
Figure 4.7: Battery pack arrangement with liquid cooling; (a) expanded view, (b) front view of the actual battery pack, (c) side view and (d) rear view.	66
Figure 4.8: Aluminium cold plate used in experiments.	67
Figure 4.9: Battery liquid cooling system; (a) line diagram of cooling system along with cold plates and valves, (b) actual cooling system.	67
Figure 4.10: Battery pack with PCC plates; (a) expanded view, (b) actual setup, (c) actual setup with all side insulation, (d) PCC plate.	68
Figure 4.11: Step by step process of assembling the prismatic battery pack with the PCM cooling jacket.	71
Figure 4.12: Open cell polyurethane foam; (a) roll for 3 mm thick foam, (b) sheet of 6 mm thick foam, (c) 3 mm thick plates, (d) 6 mm thick plates.	73
Figure 4.13: Custom made tray for making samples; (a) tray, (b) tray with foam samples, (c) tray cover, (d) tray with foam and cover.	74
Figure 4.14: Foams after soaking in the PCM; (a) 200×152×6 mm, (b) 75×152×3 mm, (c) 55×152×3 mm.	75
Figure 4.15: Battery pack with the PCM and CNT plates; (a) expended view, (b-c) actual battery pack while assembling, (d) complete battery pack.	77
Figure 4.16: Preparation of the PCM and CNT mixture; (a) ultrasonic water bath, (b) 6 mm thick plate of PCM and CNTs in the tray.	78
Figure 4.17: Experimental plan for prismatic battery testing.	80
Figure 4.18: Optical microscope used for tests.	82
Figure 4.19: Experimental setup for internal resistance measurement of the prismatic cell.	83
Figure 4.20: Experimental setup for internal resistance measurement of the cylindrical cell.	84
Figure 4.21: Step by step process of assembling the cylindrical cell to form a battery pack.	85
Figure 4.22: Experimental plan for internal resistance measurement of cylindrical and prismatic cells.	86
Figure 5.1: Thevenin equivalent circuit model for battery along with RC-pair.	93
Figure 5.2: Block diagram of the Simulink battery pack model.	95

Figure 5.3: Actual view of the voltage estimation subsystem.	95
Figure 5.4: Actual view of the heat generation subsystem.	96
Figure 5.5: Single cell configuration along with the PCM plates considered for the study.	97
Figure 5.6: Overview of solvers available in ANSYS Fluent 14.0. (a) pressure-based segregated algorithm, (b) pressure-based coupled algorithm, (c) density-based algorithm.	98
Figure 6.1: The temperature profiles of cell 1, 2, and 3 obtained from the experiments at various charge and discharge rates.	120
Figure 6.2: Variation in the surface temperature of the battery pack with time at various discharge rates.	120
Figure 6.3: Rise in the battery pack temperature at various discharge rates.	121
Figure 6.4: Experimental voltages and currents at various charging and discharging rates.	122
Figure 6.5: Variation in the battery pack voltage observed during experiments at various discharge rates.	122
Figure 6.6: Heat generation rate in the battery pack with respect to time at various discharge rates.	123
Figure 6.7: Variation in voltage at 10°C coolant temperature for various discharge rates.	124
Figure 6.8: Battery pack temperature; (a) variation, (b) rise, at various discharge rates.	124
Figure 6.9: Variation in voltage and temperature with respect to time for the selected drive cycle.	125
Figure 6.10: Variation in voltage at 20°C coolant temperature for various discharge rates.	126
Figure 6.11: At 20°C coolant temperature; (a) variation in temperature at various discharge rates, (b) rise in temperature at various discharge rates, (c) variation in voltage and temperature during the drive cycle.	127
Figure 6.12: Variation in voltage at 30°C coolant temperature for various discharge rates.	128
Figure 6.13: Battery pack temperature; (a) variation, (b) rise, at various discharge rates.	128
Figure 6.14: Variation in the battery pack and coolant outlet temperatures at various discharge rates.	129
Figure 6.15: Variation in voltage at 40°C coolant temperature for various discharge rates.	130
Figure 6.16: Battery pack temperature; (a) variation, (b) rise, at various discharge rates.	131

Figure 6.17: With 6 mm thick PCC plate; (a) variation in temperature, (b) rise in temperature, (c) variation in voltage, at various discharge rates.....	134
Figure 6.18: With 9 mm thick PCC plates; (a) variation in temperature, (b) rise in temperature, (c) variation in voltage, at various discharge rates.....	136
Figure 6.19: With 12 mm thick PCC plates; (a) variation in temperature, (b) rise in temperature, (c) variation in voltage, at various discharge rates.	137
Figure 6.20: Temperature profile of the battery pack with and without PCC plates.	139
Figure 6.21: Variation in the battery pack temperature with and without PCC plates at; (a) 1C, (b) 2C, (c) 3C, (d) 4C, discharge rates.	141
Figure 6.22: Rise in the battery pack temperature with and without PCC plates at; (a) 1C, (b) 2C, (c) 3C, (d) 4C, discharge rates.	142
Figure 6.23: Comparison of the rise in the battery pack temperature with 6 mm thick PCC plates, and with liquid cooling at; (a) 1C, (b) 2C, (c) 3C, (d) 4C, discharge rates.	144
Figure 6.24: Variation in voltage with 10°C coolant temperature at various discharge rates with; (a) 6 mm, (b) 9 mm, (c) 12 mm, thick PCC plates.	145
Figure 6.25: Variation in temperature of the battery pack with 10°C coolant temperature at various discharge rates with; (a) 6 mm, (b) 9 mm, (c) 12 mm, thick PCC plates.	146
Figure 6.26: Temperature rise in the battery pack with 10°C coolant temperature at various discharge rates with; (a) 6 mm, (b) 9 mm, (c) 12 mm, thick PCC plates.	147
Figure 6.27: Variation in voltage with 20°C coolant temperature at various discharge rates with; (a) 6 mm, (b) 9 mm, (c) 12 mm, thick PCC plates.	148
Figure 6.28: Variation in temperature of the battery pack with 20°C coolant temperature at various discharge rates with; (a) 6 mm, (b) 9 mm, (c) 12 mm, thick PCC plates.	149
Figure 6.29: Temperature rise in the battery pack with 20°C coolant temperature at various discharge rates with; (a) 6 mm, (b) 9 mm, (c) 12 mm, thick PCC plates.	150
Figure 6.30: Variation in voltage with 30°C coolant temperature at various discharge rates with; (a) 6 mm, (b) 9 mm, (c) 12 mm, thick PCC plates.	151
Figure 6.31: Variation in temperature of the battery pack with 30°C coolant temperature at various discharge rates with; (a) 6 mm, (b) 9 mm, (c) 12 mm, thick PCC plates.	152

Figure 6.32: Temperature rise in the battery pack voltage with 30°C coolant temperature at various discharge rates with; (a) 6 mm, (b) 9 mm, (c) 12 mm, thick PCC plates.....	153
Figure 6.33: Variation in the battery pack voltage with 40°C coolant temperature at various discharge rates with; (a) 6 mm, (b) 9 mm, (c) 12 mm, thick PCC plates.....	154
Figure 6.34: Variation in temperature of the battery pack with 40°C coolant temperature at various discharge rates with; (a) 6 mm, (b) 9 mm, (c) 12 mm, thick PCC plates.....	155
Figure 6.35: Temperature rise in the battery pack with 40°C coolant temperature at various discharge rates with; (a) 6 mm, (b) 9 mm, (c) 12 mm, thick PCC plates.....	156
Figure 6.36: With 3 mm thick technical grade PCM plates; (a) variation in temperature, (b) rise in temperature, (c) variation in voltage, at various discharge rates.	158
Figure 6.37: With 3 mm thick technical grade PCM and 1.5% CNT plates; (a) variation in temperature, (b) rise in temperature, (c) variation in voltage, at various discharge rates. ..	160
Figure 6.38: With 3 mm thick technical grade PCM and 3% CNT plates; (a) variation in temperature, (b) rise in temperature, (c) variation in voltage, at various discharge rates. ..	161
Figure 6.39: Temperature profile of the battery pack with 3 mm thick technical grade PCM based plates at various charge and discharge rates.....	162
Figure 6.40: With 3 mm thick pure PCM plates; (a) variation in temperature, (b) rise in temperature, (c) variation in voltage, at various discharge rates.	163
Figure 6.41: With 3 mm thick pure PCM and 1.5% CNT plates; (a) variation in temperature, (b) rise in temperature, (c) variation in voltage, at various discharge rates.	165
Figure 6.42: With 3 mm thick pure PCM and 3% CNT plates; (a) variation in temperature, (b) rise in temperature, (c) variation in voltage, at various discharge rates.	166
Figure 6.43: Temperature profile of the battery pack with 3 mm thick pure PCM based plates at various charge and discharge rates.	167
Figure 6.44: With 6 mm thick technical grade PCM plates; (a) variation in temperature, (b) rise in temperature, (c) variation in voltage, at various discharge rates.	168
Figure 6.45: With 6 mm thick technical grade PCM and 1.5% CNT plates; (a) variation in temperature, (b) rise in temperature, (c) variation in voltage, at various discharge rates. ..	170
Figure 6.46: With 6 mm thick technical grade PCM and 3% CNT plates; (a) variation in temperature, (b) rise in temperature, (c) variation in voltage, at various discharge rates. ..	171

Figure 6.47: Temperature profile of the battery pack with 6 mm thick technical grade PCM based plates at various charge and discharge rates.	172
Figure 6.48: With 6 mm thick pure PCM plates; (a) variation in temperature, (b) rise in temperature, (c) variation in voltage, at various discharge rates.	173
Figure 6.49: With 6 mm thick pure PCM and 1.5% CNT plates; (a) variation in temperature, (b) rise in temperature, (c) variation in voltage, at various discharge rates.	175
Figure 6.50: With 6 mm thick pure PCM and 3% CNT plates; (a) variation in temperature, (b) rise in temperature, (c) variation in voltage, at various discharge rates.	176
Figure 6.51: Comparison of the battery pack temperature with no cooling and 6 mm thick plates made with different combinations of pure PCM and CNTs at various discharge rates.	177
Figure 6.52: Temperature profiles of the battery pack with no cooling and with PCM and CNT-based plates.	178
Figure 6.53: Discharge capacity of the battery pack with various cooling conditions and discharge rates.	180
Figure 6.54: Temperature profile of the battery pack with no cooling, with PCC, and with PCM based plates.	181
Figure 6.55: Variation in the battery pack temperature at no cooling, and with PCC, PCM plates at; (a) 1C, (b) 2C, (c) 3C, and (d) 4C, discharge rates.	181
Figure 6.56: Variation in the battery pack temperature at no cooling, and PCC, PCM with 1.5% CNT plates at; (a) 1C, (b) 2C, (c) 3C, and (d) 4C, discharge rates.	182
Figure 6.57: Variation in the battery pack surface temperature at no cooling, and with PCC, PCM with 3% CNT plates at; (a) 1C, (b) 2C, (c) 3C, and (d) 4C, discharge rates.	183
Figure 6.58: Rise in the battery pack temperature at no cooling, with PCC, and PCM plates at; (a) 1C, (b) 2C, (c) 3C, and (d) 4C, discharge rates.	184
Figure 6.59: Rise in the battery pack temperature at no cooling, and with PCC, PCM with 1.5% CNT plates at; (a) 1C, (b) 2C, (c) 3C, and (d) 4C, discharge rates.	185
Figure 6.60: Rise in the battery pack temperature with no cooling, and PCC, PCM with 3% CNT plates at; (a) 1C, (b) 2C, (c) 3C, and (d) 4C, discharge rates.	186
Figure 6.61: Micrographs of (a) pure PCM (n-Octadecane), (b) pure CNTs.	189

Figure 6.62: Micrographs of pure PCM with; (a) 1.5% CNT before melting, (b) 1.5% CNT after melting, (c) 3% CNT before melting, (d) 3% CNT after melting.	190
Figure 6.63: Micrographs of pure PCM after melting with; (a) 1.5% CNT without foam, (b) 1.5% CNT with foam, (c) 3% CNT without foam, (d) 3% CNT with foam.	192
Figure 6.64: Variation in the effective thermal conductivity of PCM and CNT mixture with a change in CNTs concentration, assuming CNTs in parallel and series arrangement.	193
Figure 6.65: Variation in the thermal conductivity of PCM and CNT mixture with a change in the probability of series arrangement of the nanotubes.	194
Figure 6.66: Variation in the thermal conductivity of PCM and CNT mixture with a change in the probability of series arrangement of CNTs and CNT concentration.	195
Figure 6.67: Variation in total internal resistance of the cylindrical cell with respect to change in the temperature and SOC.	196
Figure 6.68: Variation in total internal resistance of prismatic cell with respect to change in the temperature and SOC.	196
Figure 6.69: Average temperatures of the battery pack from modelling and experiments at; (a) 1C, (b) 2C, (c) 3C, (d) 4C, discharge rates.	198
Figure 6.70: Experimental and modeling voltages of the battery pack at; (a) 1C, (b) 2C, (c) 3C, (d) 4C, discharge rates.	199
Figure 6.71: Heat generation rates in the battery pack obtained from modelling and experimental at; (a) 1C, (b) 2C, (c) 3C, (d) 4C, discharge rates.	200
Figure 6.72: Average temperatures of the battery pack from simulation and experiments at; (a) 1C, (b) 2C, (c) 3C, (d) 4C, discharge rates.	202
Figure 6.73: Temperature contours at the end of 1C discharge cycle; (a) cell surface, (b) PCM plate surface.	203
Figure 6.74: Convergences of the objective function with number of generations.	211

Nomenclature

A	area, m ²
b	constant
C	constant
C_D	drag coefficient
C_p	specific heat, J/kgK
ex	specific exergy, J/kg
$\dot{E}x$	exergy rate, W
g	Gibbs free energy, J/mol
h	specific enthalpy, J/kg
h_s	convective heat transfer coefficient, W/m ² K
I	current, A
k	thermal conductivity, W/mK
L	length, m
m	mass, kg
\dot{m}	mass flow rate, kg/s
n	number of electrons per mole
p	pressure, kPa
P	probability, %
\dot{q}	volumetric heat generation rate, W/m ³
\dot{Q}	heat transfer rate, W
R	resistance, Ω
s	specific entropy, J/kgK
S	entropy, J/K
t	time, s
T	temperature, K
U	open circuit potential, V
v	velocity, m/s
V	cell potential, V
z	elevation, m

Greek letters

β	coefficient of thermal expansion, 1/K
ρ	density, kg/m ³
μ	dynamic viscosity, kg/m-s
\emptyset	arbitrary variable
η	energy efficiency, %
Ψ	exergy efficiency, %
φ	energy dissipation rate, m ² /s ³
δ	delta function (units vary)
τ	shear stress, N/m ²
Γ	coefficient of diffusion

Subscripts

0	ambient
a	actual
ae	aerodynamic
<i>A</i>	area
amb	ambient
avg	average
batt	battery
cool	coolant
cond	conduction
conv	convection
d	design
D	destruction
disch	discharge
e	exit
eff	effective
ele	electrical
env	environmental
exp	experimental

f	frontal
gen	generation
i	inlet
k	any number
L	length
Li	lithium
m	material
mix	mixture
mn	manufacturing
N	number
o	operational
ocv	open circuit voltage
p	parallel
PCM	phase change material
r	refrigerant
rec	recurring
<i>rev</i>	reversible
rr	rolling resistance
s	source
sen	sensible
sim	simulated
surf	surface
surr	surrounding
theo	theoretical
thick	thickness
trans	transmission
w	water
x,y,z	cartesian coordinate directions

A123	A lithium-ion pouch cell manufactured by A123
ARC	Accelerating Rate Calorimeter
BAS	Belt-Alternator-Starter
BMS	Battery Management System
BMU	Battery Management Unit
BTMS	Battery Thermal Management System
CC	Constant Current
CD	Charge-Depleting
CNT	Carbon Nanotube
COP	Coefficient of Performance
DOD	Depth of Discharge
DME	Dimethyl Ether
DR	Driving Range
DSC	Differential Scanning Calorimeter
EOL	End of Life
EV	Electric Vehicle
G	Gauss function
GA	Genetic Algorithm
GHG	Green House Gas
GM	General Motors
GNP	Graphene Nanoplatelets
HEV	Hybrid Electric Vehicle
HPPC	Hybrid Pulse Power Characterization
HTF	Heat Transfer Fluid
ICE	Internal Combustion Engine
IMA	Integrated Motor Assist
LCO	Lithium Cobalt Oxide
LFP	Lithium Iron Phosphate
LMO	Lithium Manganese Oxide
LTO	Lithium Titanate Oxide

MEPCM	Microencapsulated Phase Change Material
MWCNT	Multiwall Carbon Nanotube
NCA	Lithium Nickel Cobalt Aluminium Oxide
NI	National Instrument
NiMH	Nickel Metal Hydrate
NMC	Lithium Nickel Manganese Cobalt Oxide
OCV	Open-Circuit Voltage
OTR	Onset-of-Thermal Runaway
PCM	Phase Change Material
PCC	Phase Change Composite
PHEV	Plug-in Hybrid Electric Vehicle
PVP	Polyvinylpyrrolidone
SEI	Solid Electrolyte Interphase
SPI	Solid Permeable Interphase
SOC	State of Charge
SOH	State of Health
SWCNT	Single Wall Carbon Nanotube
TC	Thermocouple
TESS	Thermal Energy Storage System
TIM	Thermal Interface Material
TMS	Thermal Management System
UDF	User-Defined Functions
VRLA	Valve-Regulated Lead-Acid

Chapter 1. Introduction

1.1 Importance and Context

The significant increase in the average global temperature over the last five decades indicates that global warming is not a natural phenomenon [1]. According to reports [2], 2015 was the hottest year on record and scientists predict that future years will break similar records. Although it is debatable, many scientists believe that global warming is man-made and mainly caused by greenhouse gases (such as CO₂, CH₄, N₂O, O₃, and chlorofluorocarbons) emissions [3, 4]. Various other environmental and human health impacts are associated with greenhouse gas (GHG) emissions, including rising sea levels, the risk of floods, and higher risk of cardiovascular and respiratory problems, as well as certain types of cancers [5]. The transportation sector is a major contributor to GHG emissions and air pollution [6]. In the year 2014, approximately 23% of GHG emissions in Canada and 30% in the US came from the transportation sector [5, 7], which includes aviation, road transport (such as cars and buses), rail and ships. In Canada, road transport contributes 69% of GHG emissions for the transportation sector [8]. Conventional vehicles use fossil fuel as a source of energy and emit various air pollutants. Over the decades, significant improvements have been made in the efficiency of conventional vehicles but there are still limitations to the reduction of GHG emissions from these vehicles.

Therefore, there is a need to find an alternative source of energy for vehicles. One of the best alternatives for the overall reduction of pollution and attaining a sustainable transport policy is a shift towards electric vehicles (EVs). Studies show that the use of electric or hybrid electric vehicles significantly reduces the CO₂ emissions from vehicles [9]. Figure 1.1 shows the emissions in terms of CO₂ equivalent and total fuel costs for various vehicle types, for a 161 km (100 miles) trip in the US [9]. From Figure 1.1, it can be seen that the emissions and total fuel costs are much higher for a conventional vehicle (45 kg CO₂ and \$9.96) than for hybrid electric vehicles (HEVs), plug-in hybrid electric vehicles (PHEVs), and EVs. CO₂ emissions are found to be lowest for the HEVs (23 kg of CO₂), while the total fuel cost is low for the EVs (\$3.56) [9]. Complementary systems, such as regenerative braking, which recover energy during braking, make EVs and HEVs more efficient.

It is also important to consider the source of electricity that is stored in EV and HEV batteries. As in the case of EVs and HEVs, there is an option to use electricity produced from any source. The environmental impact from EVs and HEVs can be further reduced by using electricity from renewable energy sources. However, there exist some challenges in the development of EVs and HEVs, such as range anxiety, thermal management of batteries, battery pack performance, safety, and infrastructure. Upgrading existing EVs will change the landscape of the transportation sector.

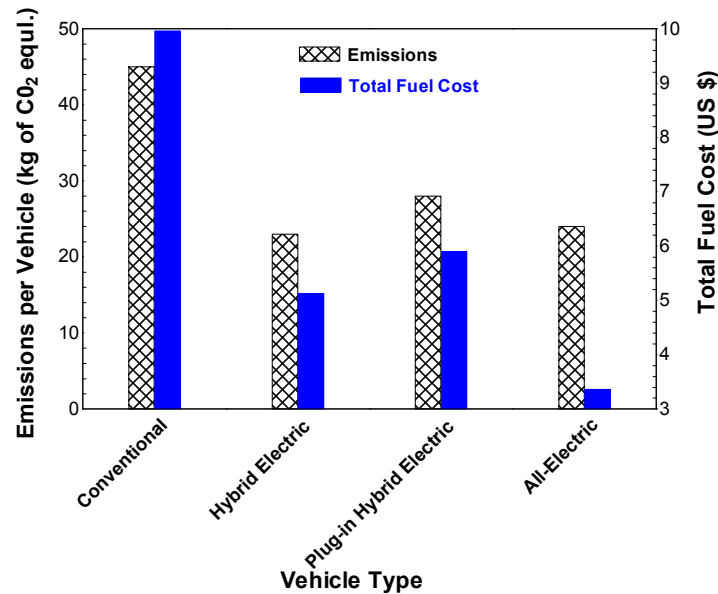


Figure 1.1 Vehicle emissions of carbon dioxide (equivalent) and total fuel costs for selected types of vehicles, per 161 km (100 miles) trip in the US (Data from [9]).

1.2 Motivation and Problem Statement

The electric energy storage system (the battery) is the heart of an EV or HEV. Li-ion batteries are the most commonly used batteries in EVs or HEVs due to performance qualities such as high power, high energy density, and longer life. However, heat is generated in Li-ion batteries during charging and discharging. The accumulation of heat in Li-ion batteries increases the degradation rate of the battery, hence reduces its capacity and life.

Therefore, a battery thermal management system (BTMS) is used to extract the heat generated from the Li-ion battery. A BTMS is also used to provide heat to the battery in cold weather. BTMSs are of two types: active and passive. Generally, an active system uses air or liquid as heat transfer fluid, while a passive system uses air as heat transfer fluid. An active system is complex and more

effective compared to a passive system. In stressful conditions, such as overcharging, over discharging, high charge and discharge rate, and short circuit, neither active nor passive air cooling systems are sufficient to keep the battery temperature within the required range [10]. An active liquid cooling system takes energy from the battery pack to run the cooling cycle. The energy extraction from the battery pack to run the cooling cycle reduces the driving range of the vehicle. Furthermore, in some cases, an active liquid cooling system fails to maintain the battery temperature and the temperature gradient across the battery pack within the specified limits. The accumulation of heat in the battery pack can further lead to fire, which is also known as thermal runaway. Therefore, this is a serious issue regarding the safety and life of the battery.

Phase change materials (PCMs) have high latent heat and can absorb the heat generated by Li-ion batteries, keeping the battery temperature almost constant. The use of PCMs also reduces the temperature gradient between the Li-ion cells [10]. In larger EVs and HEVs, a PCM is always combined with active air or liquid cooling, especially when there is continuous charging and discharging. In small EVs and HEVs, a PCM can be used as a stand-alone BTMS, along with natural air cooling. The use of PCMs as a passive BTMS reduces the cooling load from the battery pack, which helps to improve the driving range of the vehicle and life of the battery pack. However, the low thermal conductivity of PCMs reduce their effectiveness to absorb heat from the battery pack.

Various studies have been made by different researchers regarding the use of PCMs as a thermal management system for Li-ion batteries [10-12]. Most of these studies considered a PCM around the cells, where the cells are placed in a container filled with a PCM. However, it is not clear what happens when a PCM melts and the vehicle is in motion. It is unclear if the PCMs will be separated from the cell terminals and other components, and possibly exit from the container. It is also not clear if the cells will be intact in their respective locations, when a PCM between them melts, especially in prismatic cells. Therefore, the practical application of these studies in an actual battery pack is questionable.

Most of the studies related to use of PCMs with Li-ion batteries are either experimental studies with cylindrical cells or a simulation of prismatic cells. Some studies are available regarding the use of PCMs in the sides of thick prismatic cells. Also, the objective of most of the available studies

in literature is not to maintain the temperature within a required range at various discharge rates, but to observe the reduction in temperature of the battery by using PCM. A detailed experimental study of PCM application in-between the commonly used prismatic Li-ion cells (LiFePO_4) in EVs and HEVs is not available in the literature.

Several studies have been conducted by various researchers to improve the thermal conductivity of PCMs. However, practical applications of these methods are not considered with Li-ion batteries. Some studies show that the thermal conductivity of PCMs can be improved using carbon nanotubes (CNTs), which have very high thermal conductivity ($2000\sim 6000 \text{ W/m K}$) [13]. However, CNTs starts combining with each other and form clusters as soon as the phase change process of PCMs starts, which is also referred to as the agglomeration effect [14]. Moreover, it is observed that, with the passage of time, CNTs settle down on the bottom surface, leaving no or few CNTs on the top section. None of the existing dispersion methods addresses the issue of re-agglomeration of CNTs upon PCM melting [15-17]. This reduces the effectiveness of CNTs in improving the overall thermal conductivity of PCMs.

There is a lack of knowledge related to the use of commercially developed phase change composite (PCC) material having phase change material and graphene with the prismatic Li-ion batteries. It is unclear if the PCC material is capable of managing the prismatic Li-ion battery temperature within the required range and the amount of material required.

1.3 Objectives

In order to resolve the issues mentioned above, the main objective of this thesis is to develop, test, analyse, and improve a novel PCM-based passive thermal management system for Li-ion batteries used in EVs and HEVs. The developed system should be capable of managing the Li-ion battery temperature within the required range. The present study aims to achieve the following objectives:

- To develop a PCM-based passive thermal management system for Li-ion batteries used in EVs and HEVs.
- To test and analyse the developed system under different operating conditions.
- To improve the effectiveness of the developed system by increasing the thermal conductivity of the PCMs.

- To analyse and compare the developed BTMSs with and without a conventional liquid cooling system to validate their application.
- To model and simulate the developed system in order to understand its behaviour, effectiveness and temperature variation across the cells.
- To perform energy, exergy, and economic analyses of the developed system to determine its feasibility.

The tasks and subtasks required to complete the objectives of this thesis are as follows:

- I. To develop and test the battery pack with no BTMS and with conventional liquid- based BTMS, as required to compare with further studies.
 - To develop an experimental setup to test the developed battery pack at different discharge rates.
 - To develop the battery pack with and without liquid-based BTMS.
 - To test the battery pack with no cooling system at different discharge rates.
 - To examine the effect of change in liquid coolant temperature and discharge rate on voltage, temperature, and heat generation rate of the battery pack.
- II. To develop a passive BTMS capable of managing the Li-ion battery pack temperature within the required range by using commercially developed phase change composite (PCC) material.
 - To prepare phase change composite material plates of required dimensions.
 - To develop, test and analyse the battery pack with plates made from PCC material.
 - To investigate the integration of conventional liquid-based BTMS with PCC plates.
 - To compare the results with no cooling and conventional liquid cooling options.
- III. To develop a new PCM-based passive BTMS, capable of managing the Li-ion battery pack temperature within the required range.
 - To develop a process for preparing plates from the PCM and polyurethane foam.
 - To develop and test the battery pack with developed PCM plates.
 - To analyse whether the developed system is capable of managing the required temperature of the Li-ion battery pack.
- IV. To improve the developed BTMS by using CNTs and polyurethane foam.

- To develop a process for preparing plates made from different combinations of the PCM, CNTs, and polyurethane foam.
 - To develop and test the battery pack with plates made from different combinations of the PCM, CNTs and polyurethane foam.
 - To analyse the effect of using CNTs with PCM on the effectiveness of the developed system.
 - To examine the effect of using polyurethane foam on the distribution of CNTs in the PCM.
- V. To develop and analyse a model in MATLAB in order to investigate the behaviour of the Li-ion battery pack at different operating conditions.
- To develop an experimental setup for measuring the internal resistance of the cylindrical and prismatic Li-ion cells.
 - To examine the effect of temperature and state of charge on the internal resistance of the Li-ion cells for the input data in the model.
 - To consider the layout of the battery pack consisting of three Li-ion cells.
 - To develop the temperature, voltage, and heat generation models in MATLAB Simulink.
 - To calculate the temperature, voltage, and heat generation rate from the developed model.
 - To validate modelling results with experimental results to determine if the developed model can provide results with the required accuracy.
- VI. To develop and analyse a model in ANSYS for temperature distribution in the cell with PCM plates.
- To consider the layout of the module comprising one cell and two PCM plates.
 - To develop a model in ANSYS Fluent by considering the required assumptions and input parameters.
 - To analyse the temperature distribution in the cell, and validate the obtained results with experimental results.
- VII. To carry out energy, exergy, and economic analyses and optimise the developed system.
- To analyse the developed systems energetically and exergetically.

- To analyse the technical and economic feasibility of the developed systems.
- To maximise the performance of the battery pack through optimisation techniques for various operational conditions.

1.4 Methodology

The following methodological steps are taken to achieve the thesis objectives:

1. A comprehensive literature survey of the existing methods to manage the battery temperature will be performed, and gaps in literature will be identified. Based on these literature gaps, different tasks will be identified, such as the type of experiments, modelling, and necessary simulations.
2. An experimental facility will be developed to perform the required experiments, where the Li-ion battery pack can be tested. Based on the availability and capacity of the testing equipment, the necessary components will be identified and arranged. According to the capacity of the testing equipment, a battery pack will be developed and tested at different discharge rates with and without a conventional liquid cooling system to form a base case. The results obtained from these experiments will be used to compare the results from further studies.
3. PCC-based BTMS: the cold plates in the existing battery pack, with a conventional liquid cooling system, will be replaced with commercially developed custom made phase change composite (PCC) material plates. The developed battery pack will be tested at the same discharge rates as in the case of no cooling and liquid cooling. Observations will be made if there is any PCM leakage from the PCC material plates.
4. PCM-based BTMS: the selection of the PCM will be based on its melting temperature, latent heat, and the required temperature range of the Li-ion batteries. The existing battery pack will be modified to place the PCM between the cells. The battery pack will be designed in such a way that the PCM remains between the cells, even when it melts. The battery pack will be tested at the different discharge rates considered in previous cases. The battery pack will be placed in horizontal and vertical positions, and tests will be conducted to determine whether there is any PCM leakage from the battery pack.

5. To improve the developed BTMS: based on previous studies, a method will be selected to improve the thermal conductivity of the PCM. The PCM in the previous battery pack will be replaced with the PCM having improved thermal conductivity. Similar to the previous case, the new battery pack will be tested at different discharge rates.
6. The results obtained from all the experiments performed with different BTMSs will be compared in order to establish the most efficient thermal management system for Li-ion batteries.
7. Experiments are costly and time-consuming, while modelling and simulation can provide reasonably accurate results with a few assumptions and inputs. To develop a temperature, voltage, and heat generation model in the MATLAB Simulink, the change in internal resistance of the Li-ion cell will be experimentally measured at different temperatures and state of charges (SOCs). An experiment facility will be developed to identify the internal resistance of the cylindrical and prismatic Li-ion battery at different ambient temperature. The results from the developed model will be validated with experimental results.
8. ANSYS simulations will be performed at various discharge rates to better understand the temperature gradient across the cell and PCM plates. A model will be developed in ANSYS DesignModeler, and boundary conditions will be defined in ANSYS Fluent. A constant rate of heat generation obtained from the experimental results will be considered over the cell as the only heat source. The results from ANSYS simulation will be analysed to find the effectiveness of PCM application with cell and validated with experimental results.
9. To better understand the performance of the battery pack, energy and exergy analyses will be conducted corresponding to different operating conditions. A feasibility analysis of the developed system will be made by considering the cost and effectiveness of the developed system. The material cost of the developed systems will be calculated and compared with the conventional liquid cooling system.
10. An objective function will be defined for optimisation. The selection of optimisation techniques will be based on availability, literature survey, and the type of objective function. Various parameters, assumptions and constraints will be defined. These results will be analysed and discussed.

1.5 Thesis Outline

Several steps have been taken to develop and examine PCM-based thermal management systems in the present study. This thesis is organised into seven chapters including the current chapter, which highlight the problem definition, motivations, and objectives of the present study. Chapter 2 provides background information about EVs and HEVs, Li-ion batteries, battery degradation mechanisms, BTMSs, passive thermal management using PCMs and different methods to increase the thermal conductivity of PCMs.

Chapter 3 provides a literature review of heat generation in Li-ion batteries and applications of BTMSs. Various studies that focus on the use of PCMs for the passive thermal management of batteries, including the main gaps in those studies, are presented in detail. Exergy analysis of BTMSs performed by various researchers are also discussed in detail.

Chapter 4 provides detailed information about the experimental setups for various cooling conditions and internal resistance measurements. A brief description of the tools and equipment used in experiments is provided along with experimental plans and procedures.

Chapter 5 provides specific details of the modelling and simulation of the Li-ion battery. Assumptions and procedures for the developed model are discussed in detail. The governing equations for ANSYS simulation, geometry, and solving methods are presented, as are the equations used for energy and exergy analysis of the battery packs. Details about optimisation and the objective function are covered in the last section of this chapter.

The results from the experiments, modelling, and simulations are presented in Chapter 6, the first section of which provides the experimental results of various cooling options for the Li-ion battery along with internal resistance of the prismatic and cylindrical cell. The results from an optical microscope are then presented. The second part of Chapter 6 provides the validation of modelling and simulation results with experimental results, while the last section provides energy, exergy, and optimisation results.

The thesis concludes with chapter 7, where conclusions from the present work and recommendations for future studies are provided.

Chapter 2. Background

This chapter includes the basic concept of EVs and HEVs, Li-ion batteries, and the process of heat generation in Li-ion batteries. The process of degradation of the battery pack with the accumulation of heat is briefly discussed. Details about an active as well as a passive thermal management system of the battery are provided. Different types of PCMs available for a passive thermal management system are introduced. The basic concept of CNTs and its application with PCMs is explained.

2.1 Development of Electric Vehicles

The first electric vehicle, a tricycle, was launched in 1880. This was followed by a golden period for EVs, from 1890 to 1905 [18], as six EVs were launched in 1893 at the Chicago world exhibition. By 1903, more than 4000 EVs were registered in New York, accounting for approximately 20% of total cars on the road [18]. By 1912, there were around 30000 EVs in the United States. Due to advancements in the internal combustion engine (ICE) and various other reasons, there followed an inactive period for EVs, mainly from 1920 to 1950.

The early 1960s are considered as the re-birth of EVs; this was when, in 1962, Rachel Carson published her book *“Silent Spring”*, raising concerns about environmental impact. At that time, ICE cars were considered as major contributors to an environmental problem and EVs were regarded as the main solution. In the mid-1960s, General Motors (GM) build an electric car with a driving range of 200 km using a zinc-air battery. However, this car was never commercialised due to several issues. An energy problem in the western world in the 1970s and an oil crisis in 1973 provided a very active period for the development of electric cars. City air pollution and zero-emission regulations in California in 1990 sparked further research into the development of EVs [18].

In 1997, Toyota launched its model Toyota Prius, a HEV in the Japanese market and in 1999 in the North American market. In 2001, Honda launched the Honda Civic Hybrid in Japan and later in the US. With the enrollment of Li-ion batteries, the driving range of EVs and HEVs significantly improved. In 2010, GM introduced the Volt, a PHEV with an all-electric range of 38 miles. In the latest developments, to overcome range anxiety and to increase the acceptance of the EV in society,

in 2013 Tesla Motors launched the Model S, an electric car. According to Tesla company reports, the latest Model S (P100D) has approximately 400 miles driving range at an average speed of 90 km/h [19].

It has been concluded from several studies that the developments of EVs and electrical infrastructure holds the key to present issues of commuting and the environment [20, 21]. EVs and HEVs are expected to further improve vehicle efficiency as well as reduce overall energy consumption. The boost in demand will positively impact the usage of renewable energy technologies to supply electricity to the transport sector. The wider use of EVs will eventually reduce noise pollution and improve local air quality by reducing pollutants in the air [21].

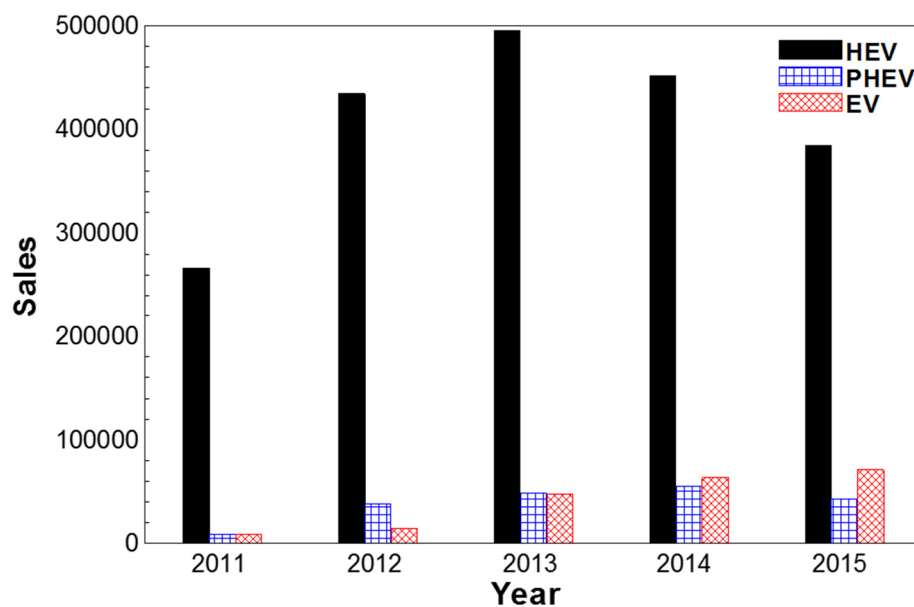


Figure 2.1: Annual sales of HEVs, PHEVs, and EVs in the US from 2011 to May 2015 (data from [22]).

From Figure 2.1, a continuous growth can be seen in the sales of EVs in the US from 2011 to 2015. However, since 2013, the sales of HEVs and PHEVs have been rapidly declining. This observation is mainly attributed to the improvement in the driving range of EVs and government incentives [22]. Less local environmental impact and lower fuel costs for operating HEVs, PHEVs, and EVs compared to ICE-based vehicles are the main reasons for their development and improved government initiatives for their use [23].

2.2 Fundamentals of Electric and Hybrid Electric Vehicles

An EV does not have an internal combustion engine and uses one or more electric motors to supply power to the wheels [23]. Generally, a battery is used to power the electric motor, therefore it does not have any immediate GHG emissions. However, GHG emissions from an EV depend upon the type of power source used to produce electricity for charging the EV battery. An EV can be any motored vehicle such as a scooter, boat, car, bus, train or any other vehicle powered by an electric motor. Figure 2.2 shows the line diagram of a typical EV and PHEV.

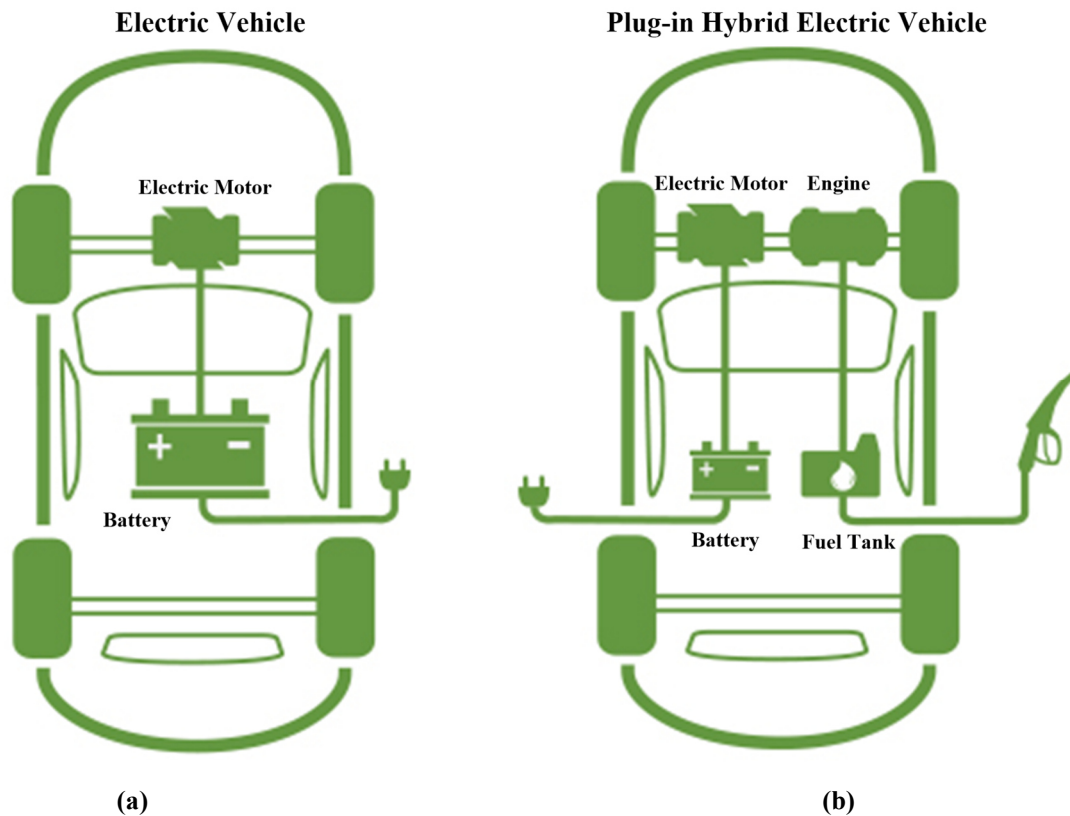


Figure 2.2: Line diagrams of typical; (a) EV, (b) PHEV (modified from [24]).

A PHEV uses both an electric motor and an internal combustion engine to power the wheels. However, in the case of a PHEV, the battery is charged through an external circuit; it can run in all-electric mode until the charge is completely depleted and then work as a normal HEV. On the other hand, an HEV uses a combination of an electric motor and ICE to power the wheels and does not have the option to charge the battery through the external circuit. The primary source of energy in an HEV is diesel, gasoline or any other fuel such as ethanol. The size of the engine in an HEV

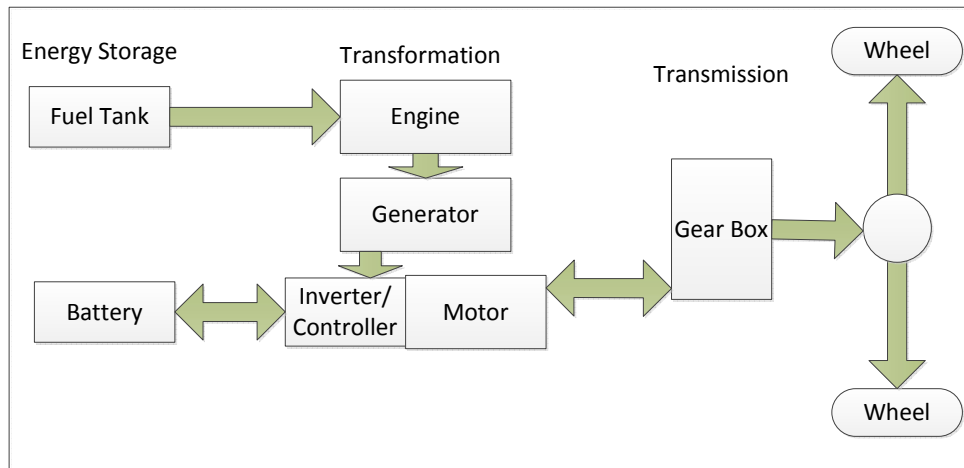
is comparatively smaller than a conventional ICE vehicle, therefore it provides better fuel economy [25]. As previously discussed, advanced EVs, HEVs, and PHEVs use regenerative braking to prolong the charge on their batteries by converting kinetic energy from the wheels to electricity during braking. An HEV uses extra thrust from the ICE (during idling or cruising) to spin an electric generator and produce electricity. This electricity can be used to recharge the battery or to power the electric motor.

The three main types of hybrid configurations available in the market are listed below [26]:

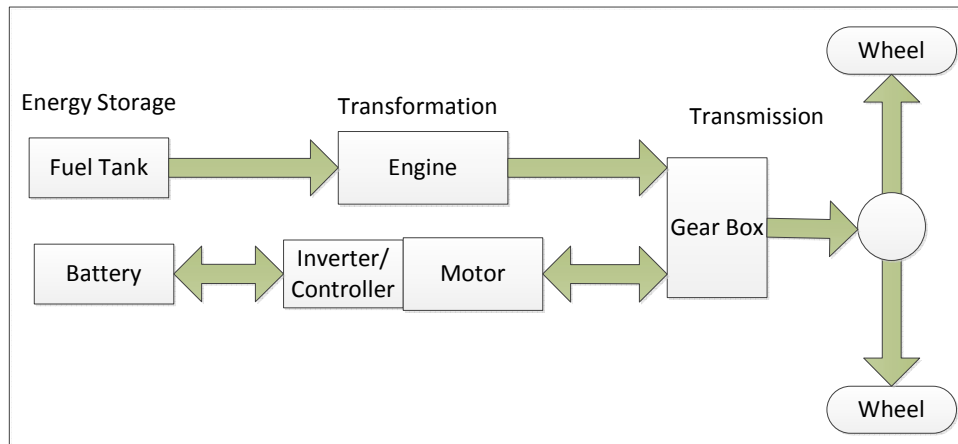
- i. Series hybrid vehicle configuration
- ii. Parallel hybrid vehicle configuration
- iii. Series-parallel hybrid vehicle configuration

Figure 2.3 shows a line diagram of all three arrangements of HEVs. In the series hybrid vehicle configuration, the wheels are powered only by the electric motor. The internal combustion engine is used to drive a generator to produce electricity. This electricity is used to either power the electric motor or to recharge the battery. Series HEVs are generally higher power systems and sometimes even uses a gas turbine with a capacity of 150 kW and 1000 kW [27]. Series HEVs are more efficient in city driving due to a smaller engine and larger battery pack compared to parallel HEVs. An example of this type of vehicle is the Chevrolet Volt developed by GM.

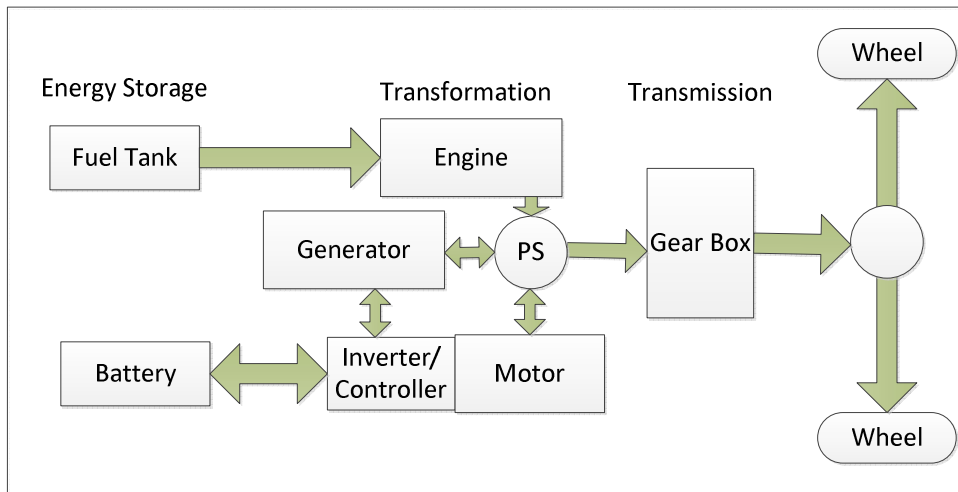
In a parallel HEV configuration, both the electric motor and ICE can simultaneously power the wheels. Both the motor and engine are coupled to the drive shafts. The battery is charged through regenerative braking, where the motor runs in a reverse direction to produce electricity through the generator. A parallel HEV can run in an all-electric mode for shorter distances, mainly in city driving. Parallel hybrids are usually lower power vehicles, such as passenger cars, where the hybrid system is used to enhance performance [28]. Examples of this type of vehicles include the Honda Civic Hybrid and the BMW Hybrid 7. In a series-parallel configuration, the engine can deliver direct power to the wheels, and can also power a generator, which supplies electricity to the battery. The battery supplies electricity to the motor and then delivers power to the wheels. The electric motor can charge the battery through regenerative braking energy. This is also called a “power-split” hybrid system, in which the hybrid makes use of a power splitting device, typically a planetary gear mechanism [26].



(a)



(b)



(c)

Figure 2.3: Line diagrams of (a) series, (b) parallel, (c) series-parallel, HEV arrangements (data from [26]).

It has become a popular design due to its unique modes of operation and its implementation in the commercially successful Toyota Prius. Toyota's hybrid system can function as a continuously variable transmission, where a single and variable gear is used instead of standard six-speed automatic gears. This provides smooth power delivery and very efficient operation. One of the greatest benefits of this type of hybrid system is the high potential reduction in vehicle emissions. Examples of these types of vehicles include the Toyota Prius and Ford Escape Hybrid [26].

EVs and HEVs have their own advantages and disadvantages. However, their benefits mainly depend upon the battery technology used in these vehicles. Therefore, further analysis of the battery technologies used in EVs and HEVs is required.

2.3 Batteries for Electric and Hybrid Electric Vehicles

Batteries, which are considered the major component of EVs and HEVs, can be categorised into different types. The batteries can either be high energy density type or high power density type. Energy density is the amount of energy with regards to the mass or volume of the battery. Power density provides a good measure of how much energy can be released during discharge at a given time with per unit mass or volume of the battery. A high energy density battery is suitable for automobile applications, e.g. in an EV, which is intended to be driven on pure electricity for longer distances. A high power density battery is useful in an application where a short but intensive power pulse is required, e.g. in an ordinary HEV, as the electric motor often only assists the combustion engine for short periods [29].

In the 1990s, lead-acid batteries were used for EVs, the driving range of which was then around 100 kilometres. However, due to the low energy density of lead-acid batteries and high weight, other chemistries were used in the following years [30]. Due to the higher power, high energy density, and improved cycle life, EVs started to use nickel metal hydrate (NiMH) batteries, which are still used in HEVs and PHEVs for their low cost per watt. However, due to limited SOC operational range, high self-discharge, and low specific energy, NiMH batteries are not suitable for advanced EVs and HEVs. Sodium Nickel Chloride batteries, commonly known as ZEBRA (Zero Emissions Batteries Research Activity) batteries were also used in EVs and HEVs due to their low cost and high safety. However, due to low power density and high operating temperature (270-350°C), these batteries are no longer popular [31]. Currently, Li-ion batteries are the most

widely used in EVs and HEVs due to performance qualities such as high energy density, high power, and longer life. However, the cost of Li-ion batteries is higher than other available batteries. Table 2.1 presents the characteristics of different types of batteries used in EVs and HEVs. Although the cost of Li-ion is higher, it can be observed from Table 2.1 that they have better characteristic from all other batteries. Therefore, Li-ion batteries are most suitable for EVs and HEVs.

Table 2.1: Characteristics of battery types used in EVs and HEVs (Data from[31]).

Characteristic	Lead Acid	NiMH	Zebra	Li-ion
Nominal Cell Voltage (V)	2	1.2	2.58	2.5/ 3.3/ 3.6/3.7
Specific Energy (Wh/kg)	30-45	30-80	90-100	90-220
Energy Density (Wh/L)	60-75	140-300	160	280-400
Specific Power (Wh/kg)	180	250-1000	150	600-3400
Cycle Life (Number of Cycle)	500-800	500-1000	1000	1000-8000
Self-Discharge (%/Month)	2-4	20-30	0	2-5
Temperature Range (°C)	-20 - 60	-20 - 60	270 - 350	-20 - 60
Relative Cost	Low	Moderate	Low	High

2.3.1 Lithium-ion Batteries

In Li-ion cells, lithium ions are used to store and provide energy. A li-ion cell consists of an anode and cathode as two electrodes. A separator is used between the anode and cathode and a current collector is used on each side of the electrodes. The separator is a porous material, which enables transport of Li-ions between the anode and cathode and prevents short-circuiting in the cell. It also helps to protect the cell from thermal runaway [32]. Both the electrodes and separator are soaked in an electrolyte. The Li-ion cell is connected to the external circuit through the aluminium current collector on the cathode side and copper current collector on the anode side. The anode is generally made from graphite, while the cathode is made from a composite material [33]. The name of the Li-ion batteries is defined by the material used in the cathode. The process of charging and discharging in the Li-ion cell is described below.

During the discharge cycle, Li-ions travel from the anode to the cathode through the electrolyte. The intercalation of Li-ions into the cathode makes the cathode more positive and the current flows through an external circuit due to the potential difference in the anode and the cathode. During the

charge cycle, a reverse effect occurs. Intercalation and deintercalation refers to insertion and extraction of Li-ions, respectively. The supply of current from an external circuit deintercalates the Li-ions from the cathode and the Li-ion travels from the cathode to the anode. The intercalation of i-ions to the anode recharges the battery. Theoretically, the process of intercalation and deintercalation at the anode and cathode can continue infinitely. However, in practice, the capacity and life of the cell reduce with time due to degradation of the cell material and various other chemical reactions in the cell. The process of intercalation and deintercalation in Li-ion batteries during charging and discharging is shown in Figure 2.4.

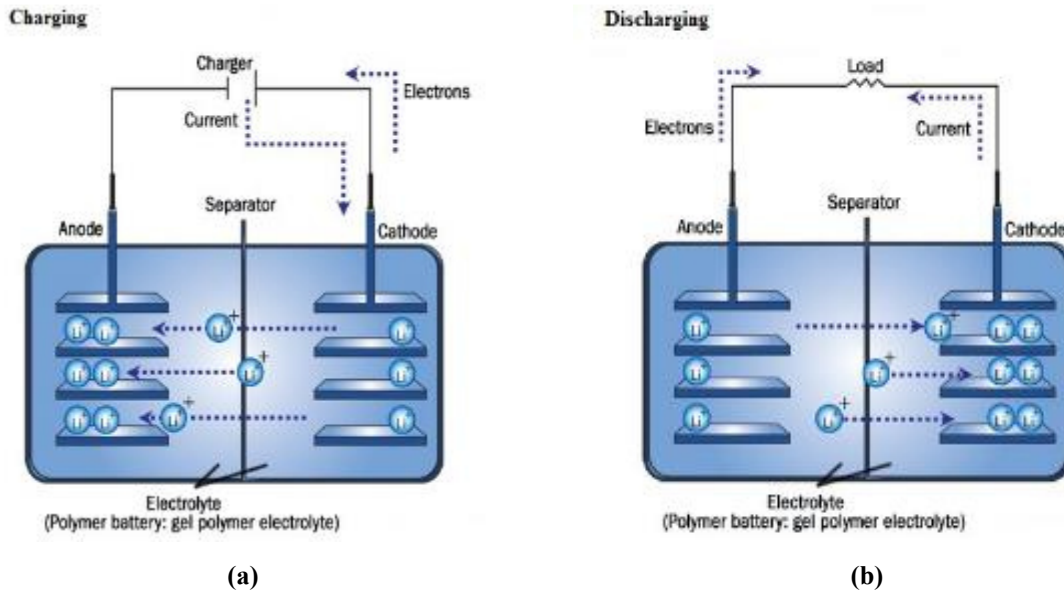


Figure 2.4: Processes in Li-ion battery; (a) charging, (b) discharging [34].

2.3.2 Types of Li-ion Batteries

The term ‘Lithium-ion’ includes a number of different chemistries. There are various types of Li-ion batteries available for EV and HEV applications, each having their own advantages and disadvantages. These batteries are sold in the market for EVs and HEVs, while new Li-ion batteries are continuously developed. The selection of the type of Li-ion battery depends on the type of EV and HEV application. Li-ion batteries can be compared according to various parameters. Figure 2.5 shows the comparison of different Li-ion batteries suitable for EVs and HEVs based on their performance, life span, safety, specific energy, specific power, and cost. The names of all the Li-ion batteries in Figure 2.5 refer to different cathode material. The anode material is the same in all the Li-ion batteries except lithium-titanate-oxide (LTO), which has a different anode material.

Lithium-cobalt-oxide ($\text{LiCoO}_2/\text{LCO}$) batteries are most commonly used in small electronics such as cell phones and laptops, mainly due to its high specific energy. However, due to a short life span, safety issues and low specific power, LCO batteries are not preferred for EVs and HEVs [35]. The specific energy of lithium-nickel-manganese-cobalt-oxide ($\text{LiNiMnCoO}_2/\text{NMC}$) and lithium-nickel-cobalt-aluminium-oxide ($\text{LiNiCoAlO}_2/\text{NCA}$) batteries are close to the specific energy of LCO. The life span and specific power of NCA batteries are better compared to NMC and LCO. However, NCA batteries is more prone to thermal runaway compared to all other Li-ion batteries due to an exothermic reaction at high temperature. On the other hand, lithium-iron-phosphate ($\text{LiFePO}_4/\text{LFP}$) batteries are least prone to thermal runaway due to an endothermic reaction at the cathode and no release of oxygen at high temperatures [36]. As no nickel or cobalt is used in LFP and lithium-manganese-oxide ($\text{LiMnO}_4/\text{LMO}$) batteries, these are most beneficial in terms of cost. LFP batteries are highly safe with long life, better power capabilities, and lowest cost per kW and Ampere-hour [36, 37]. However, they have poor performance at low temperatures and low specific energy.

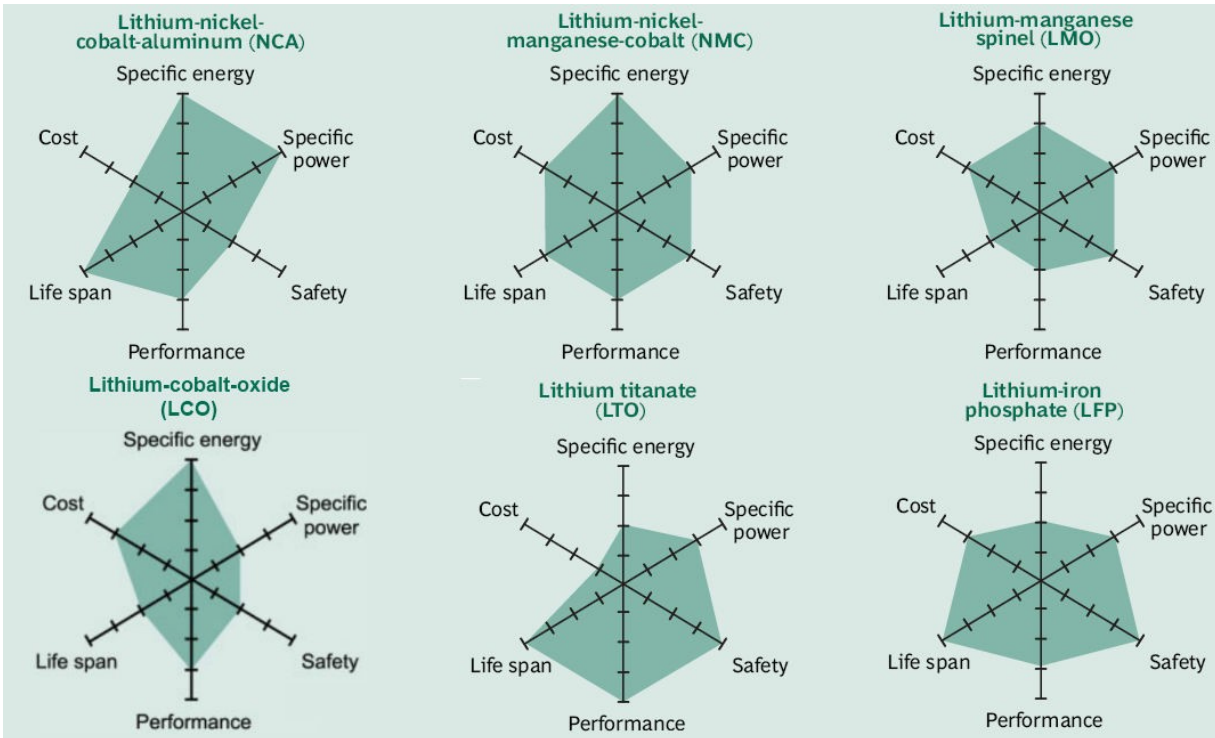


Figure 2.5: Comparison of suitable Li-ion batteries for EVs [38] (The more the dark green coloured shape for each cell extends along a given axis, the better the performance in that direction).

Despite various advantages, heat generation during charging and discharging is one of the major problems in Li-ion cells. Heat is generated in the Li-ion cells due to Joule heating and electrochemical reaction (change in entropy). The increase in cell temperature due to heat generation leads to faster degradation of the Li-ion cell, which reduces the life and capacity of the cell. As several cells connected in series or parallel are used to form a complete battery pack, heat is accumulated within the battery pack. The accumulation of heat may lead to thermal runaway in the battery pack.

2.4 Degradation in Li-ion Batteries

It is important to understand the concept of degradation of the battery before discussing the effect of temperature on degradation. The degradation process of the Li-ion battery can be divided into four stages, as shown in Figure 2.6. The loss of active material and Li-ions are the main reasons for a decrease in cell capacity during normal operation. The capacity loss of a Li-ion cell is high in region A, but occurs for a short initial period, as seen from the manufacturing data. The capacity fading of the Li-ion cell is slow in region B and then in region C. The end of life (EOL) of a Li-ion cell is reached when the capacity of the cell reduces below 80% of its nominal capacity and occurs in region D.

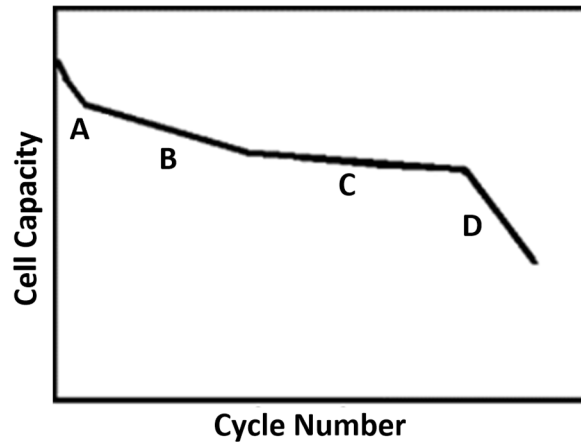


Figure 2.6: A general capacity fading trend of the Li-ion cell with cycle number (modified from [39]).

Stage A: A fast decrease in cell capacity can be seen in the first stage, mainly due to loss of Li-ion to a solid electrolyte interphase (SEI) layer. A SEI layer forms as a side reaction on the interface between the anode and electrolyte near the separator. A schematic of a SEI layer in the Li-ion cell

is shown in Figure 2.7. It is observed that capacity fading in the first stage is more severe at lower C-rates compared to higher C-rates [40]. This happens due to the availability of more Li-ions for SEI layer formation at the lower C-rate. The C-rate is a measure of the cell current and is scaled to the nominal capacity of the cell provided by the manufacturer. If a cell is charged or discharged ideally within one hour, it means that the C-rate is 1C, while half an hour means 2C and two hours means C/2.

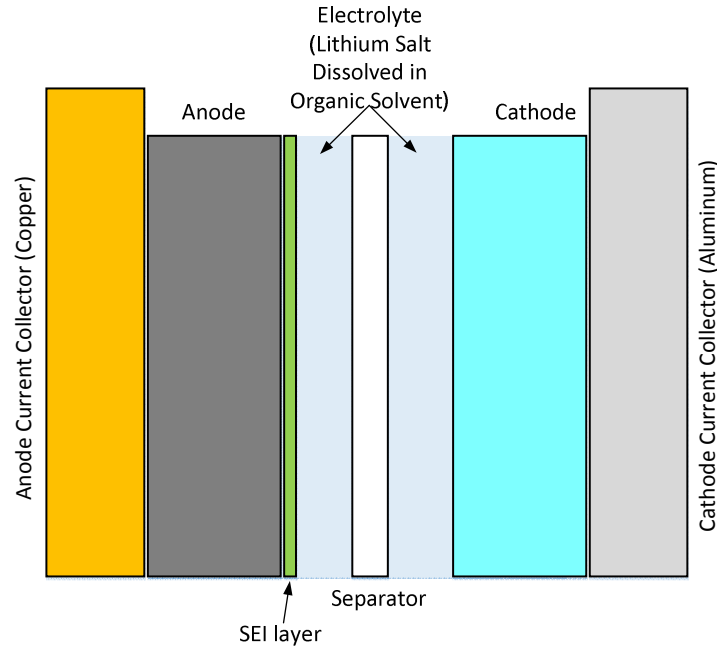


Figure 2.7: Schematic representation of SEI layer in a Li-ion cell (modified from [41]).

Stage B: The anode is the limiting electrode in the second stage [42]. The availability of active material reduces due to the formation of the SEI layer on the anode. Therefore, the intercalation of Li-ion into the anode during charging reduces. The formation of cracks in the SEI layer as a result of continuous intercalation and deintercalation exposes more active material, causing more side reaction. This leads to the growth of a less porous SEI layer, which ultimately increases the loss of Li-ions.

Stage C: The rate of degradation of active cathode material is higher compared to the loss of Li-ions in the third stage. In this stage, a solid permeable interphase (SPI) layer is formed at the interface of the cathode and electrolyte, similar to the SEI layer at the anode [43]. Due to cycling,

the cathode deforms at a faster rate compared to the loss of Li-ions. However, the loss of Li-ions at the anode still dominates the degradation in this stage.

Stage D: The cathode is the limiting electrode in the fourth stage. In this stage, the amount of available active cathode material is less compared to the amount of cyclable Li-ions. Therefore, the amount of Li-ion that intercalates to the anode during charging does not intercalate in the cathode during discharging. The complete intercalation of the cathode during charging increases the rate of active cathode material loss, which accelerates the cell capacity fading [42].

The rate of degradation during all four stages is different for different Li-ion cells. In the case of LiFePO_4 , the capacity of the cell mainly reduces due to the loss of Li-ion to the SEI layer and the loss of active anode material [40]. As the formation of an SPI layer in LiFePO_4 cells is not enhanced by temperature changes and cycling, the loss of active cathode material is very slow. This leads to a higher cycling life of a LiFePO_4 cell compared to other types of Li-ion cells.

Under ideal conditions, Li-ion cells only degrade through these four stages. However, these ideal conditions never exist in practice, and non-ideal conditions can accelerate capacity fading and reduce the cell life. For example, the capacity and life of the Li-ion cells are strongly affected by variation in temperature [44]. Li-ion cells have an optimal operating temperature range and experience a significant capacity loss outside this range. Each manufacturer provides an operating temperature range for the Li-ion cell. However, the optimal operating temperature range is much narrower compared to the temperature range given by the manufacturer.

2.4.1 Effect of Low Temperature on Degradation Process

Higher activation energy is required for the chemical reaction to occur at low temperatures, meaning that more energy is needed for the intercalation and deintercalation process at the anode and cathode. Therefore, fewer Li-ions participate in the active cell process, which leads to a temporary capacity loss. However, the nominal capacity of the cell is restored once the temperature increases to the nominal level. The main effect of low temperature on the degradation mechanism is due to lithium plating [44, 45]. At a low temperature, Li-ion does not intercalate to the anode as fast as electric energy transferred to the cell because it polarises the anode and causes a reaction between Li-ion and li-metal. The li-metal is deposited on the anode, which is known as lithium

plating, and blocks the SEI layer pores [45]. Therefore, fewer Li-ions can intercalate to the anode, leading to capacity fading of the cell.

2.4.2 Effect of High Temperature on Degradation Process

Initially, the discharge capacity and power of the Li-ion cell increases at high temperature as low activation energy is required for the chemical reaction. At higher temperatures, more Li-ions take part in intercalation and deintercalation, which leads to higher current and higher cell voltage. Although the increase in temperature increases the cell capacity, in the long term this leads to severe damage to the cell [44].

The SEI layer at the anode deteriorates at high temperatures and starts to break down or dissolve within the electrolyte [46], which increases the side reaction due to partial exposure of the active anode material to the electrolyte. The SEI layer is restored again due to the side reaction. Figure 2.8 shows the changes that occur with the SEI layer and anode at the interface of the anode and electrolyte. Due to the high temperature, some metastable organic components of the new SEI layer convert to more stable and less porous inorganic molecules [46]. This makes intercalation at the anode more challenging and lowers the ionic conductivity. A similar degradation process occurs with the SPI layer at the cathode.

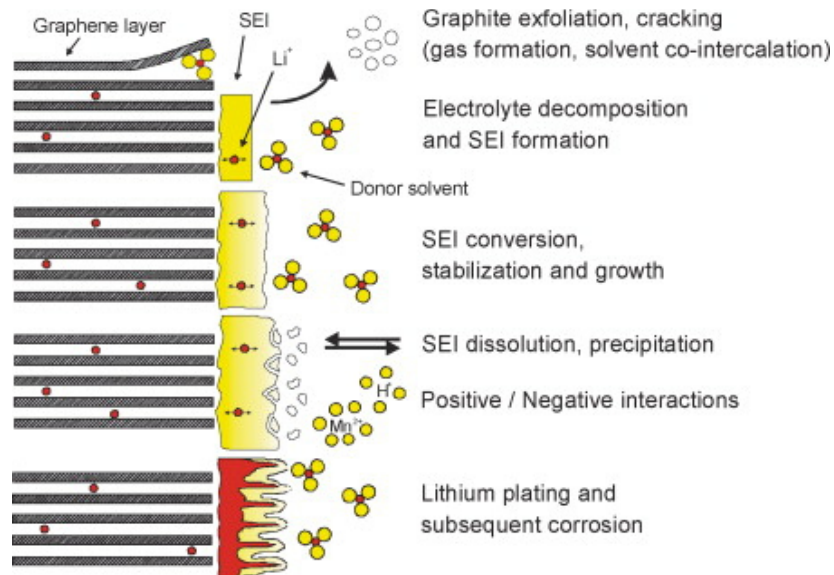


Figure 2.8: Changes at the interface of anode and electrolyte [46].

The anode also deforms at high temperature. At higher temperatures, the solvent of Li-ion and electrolyte have higher energy, which sometimes leads to intercalation of the entire solvent; it can crack and deform the anode. The similar process can occur at the cathode.

Depending on the cathode material of the Li-ion cell, gas formation can also occur at high temperatures due to decomposition of the electrolyte. This reduces the amount of Li-ion that can be transported between the anode and cathode, leading to a decrease in cell conductivity and ultimately the capacity of the cell.

The separator between the anode and cathode also decomposes at high temperature, making the cell more prone to short circuit. The binder used to connect the electrodes as well as the current collectors also decompose at high temperature, resulting in a poor contact between the current collectors and electrodes [46]. This bad contact reduces cell conductivity and leads to power fading. The rise in temperature of the cell temporarily increases the cell capacity, but leads to severe damage to the cell. It is estimated that in the range of 30°C - 40°C, each degree rise in temperature reduces the life of Li-ion batteries up to two months [47]. The operating temperature should not exceed 40°C to achieve full life span while the acceptable temperature gradient should be less than 5°C. Therefore, an effective and efficient BTMS is required to reduce the temperature difference and degradation in Li-ion cells.

2.5 Thermal Management Systems for Li-ion Batteries

Traditionally, an active or a passive thermal management system is used in EVs and HEVs to control the temperature of the battery pack within a specified range. A general classification of thermal management systems for Li-ion batteries is given in Figure 2.9. An active BTMS uses air or liquid as heat transfer fluid (HTF). A liquid HTF is more effective in absorbing the heat from the battery pack compared to air. Due to its low heat transfer coefficient, air needs a larger area for heat exchange. The temperature increase is also higher and air needs to be distributed parallel across all manifolds [48]. In a passive system, ambient air is used to carry the heat rejected by cells. Effective passive design avoids the use of components such as fans, and manifolds. However, studies show that passive air systems are not capable of managing battery temperature within the required range at a high discharge rate [10, 49].

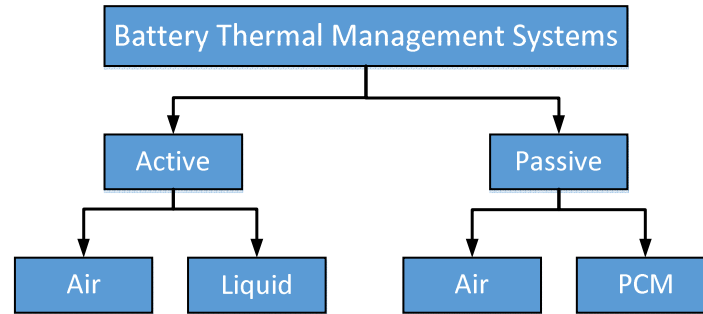


Figure 2.9: Classification of thermal management systems for Li-ion batteries.

2.5.1 Design of Battery Thermal Management Systems

An efficiently designed BTMS optimises available and waste heat to reduce losses and improve efficiency. The next generation EVs/HEVs need to be equipped with efficient heat sources and sinks to improve the overall energy utilisation. This will result in improved battery life and longer driving range. Any attempts to improve energy efficiency need to address both safety and long-term durability, because of potential overheating and thermal runaway [50]. Therefore, an efficient and effective cooling system is very critical for the smooth operations of EVs/HEVs. The cooling system can be passive and active, depending on applicability. A step-by-step procedure to design a thermal management system is explained as follows (modified from [51]):

1. To define the objectives and constraints of a BTMS, which set the specifications for the desired system (e.g., temperature range for safe operation, space, and ventilation to release hazardous gases).
2. To measure or estimate the battery pack heat dissipation rate and heat capacity: The heat generated over a period is measured experimentally, e.g. by a calorimetry method.
3. To carry out a first-order BTMS evaluation: In order to select the HTF, the battery pack and modules are tested for their steady state and transient response. This step also tests flow models, e.g. parallel, series or combination.
4. To characterise the module and battery pack heat transfer behaviour: Define the overall thermal conductivity of the system and employ a software to predict the heat transfer rate between the battery pack and the environment.
5. To design a basic BTMS.
6. To construct, install, and test the BTMS: Build a BTMS prototype based on the basic design and test it under predefined operational conditions.

7. To optimise the BTMS.

2.5.2 Existing Battery Thermal Management Systems

Existing EVs/HEVs, such as the Chevrolet Volt and Tesla Model S, use the active liquid cooling system for the battery [52]. In the case of BMW i3, no liquid coolant is used between the cells, as the bottom of the battery case is cooled by the refrigerant. The Chevy Volt HEV has a T-shaped battery pack that contains 288 prismatic cells. Therefore, a well-designed BTMS is required in order to remove generated heat and to maintain the required temperature of the battery pack. The Chevy Volt TMS has a number of heat sources and cooling loops [53]. These loops may have a slight variation in the components and structure for different vehicles, but the objective in all cases is to maintain proper operating conditions. The performance and energy consumed by the vehicle are significantly affected by the cooling loop. The four cooling loops in the Chevy Volt are listed as follows [54]:

- High voltage battery cooling system
- Power electronics cooling system
- Cooling system and heater loop for the engine
- Electric drive unit and lubricating system

The above four loops operate independently of each other. A premixed solution of Dexcool coolant and deionised water is used as the HTF. Cold plates are used between cells to circulate the HTF (coolant) and to absorb heat from the cells [54]. These cold plates are generally made of aluminium and have five inlets and five outlets. Figure 2.10 (a) shows a typical cold plate as used in the Chevy Volt, and the design and arrangement of different components used in the thermal management system [Figure 2.10 (b)].

On the other hand, Tesla uses around 7000 cylindrical cells connected in series and parallel [52]. In this case, a snake-shaped flat cooling tube, as shown in Figure 2.11, is used for the battery cooling. The use of a single tube makes a very simple cooling scheme with very few points for leakage [52].

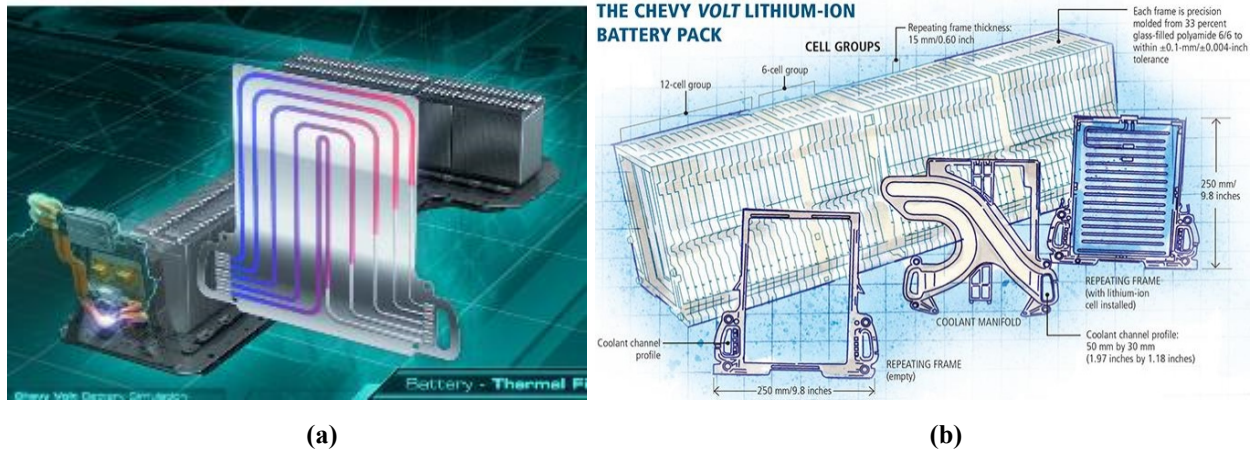


Figure 2.10: (a) Cold plate used in TMS of Chevy Volt; (b) design and arrangement of different components in TMS of Chevy Volt [12, 55]

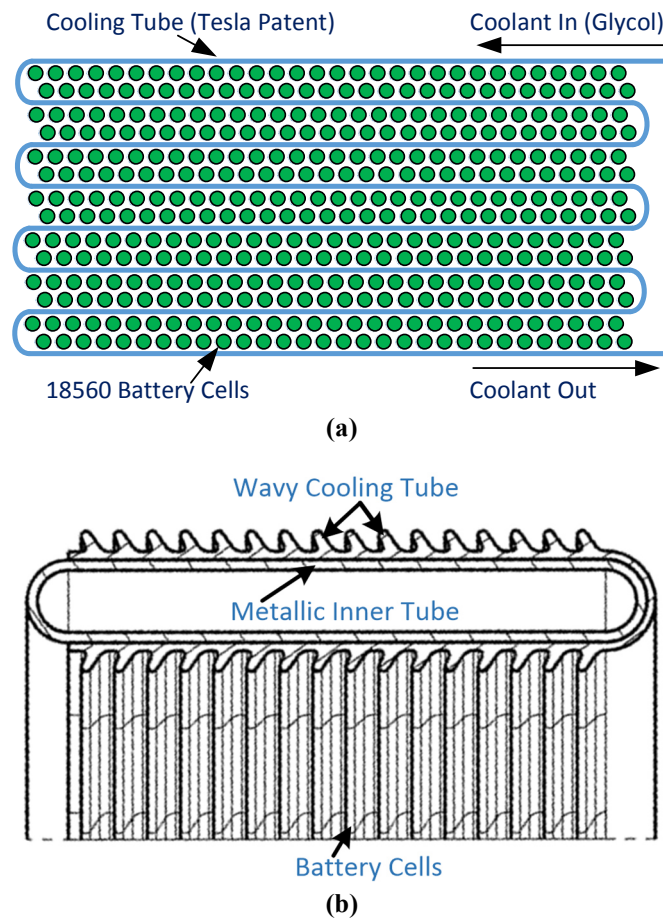


Figure 2.11: (a) Line diagram of TMS of Tesla model S battery (1 module); (b) line diagram of cooling plate used in Tesla Model S-TMS for cylindrical cells (modified from ([56])).

By comparing the BTMSs used by different automakers, it can be concluded that Volt's cooling scheme provides very effective cooling, but its design is complicated and increases the probability of leakage [52]. On the other hand, the very simple design in Tesla cars reduces the possibility of leakage to a great extent. At the same time, the effectiveness of the Tesla cooling design is questionable as the same fluid flows through the cooling tube [52]. The temperature of the fluid keeps on increasing as it passes through the tube, and cells near the exit are exposed to high temperature fluid. In cold weather, GM, Tesla and most other electric car manufacturers use electric resistance heating to maintain the required temperature of the battery [53].

Although an active BTMS is effective in controlling battery pack temperature, it is very complicated, bulky and expensive due to various components such as fans, blowers, pumps, compressors, and pipes. This type of system also incurs a running cost, as energy is required to flow the HTF through the circuit and to manage its temperature [10]. The advent of PCMs is regarded as an alternative to these active systems, and their application as a BTMS requires investigation.

2.6 Phase Change Materials and their Applications

Thermal energy is mainly stored by means of latent heat, sensible heat, and chemical energy. Of first two ways, latent heat can store large quantities without considerable losses [57]. Therefore, PCMs are being used to store heat in various applications, including heat pumps, solar engineering, and spacecraft thermal controls [58-60]. In EVs and HEVs, PCMs can be used to keep the temperature of the Li-ion battery pack within the required range and to maintain a uniform temperature across the cell and battery pack [23]. In the case of small EVs and HEVs, PCMs can also be used as a stand-alone BTMS, which reduces the cooling load from the battery pack as well as reduces complexity [61]. PCM layers can also halt thermal runaway propagation after a cell temperature crosses the critical range. The most important property for PCMs application is its melting point. Due to the phase change process, isothermal conditions are maintained. PCMs can be integrated between the cells of a battery pack and absorb the heat generated by the cell. Once the temperature of a cell increases up to the melting point of a PCM, the phase change process that occurs as further heat from the cell is absorbed by a PCM without any increase in temperature [61].

The application of PCMs offers several unique advantages over conventional cooling methods, such as uniformity in the temperature inside the battery, low system maintenance, and no need of parasitic power [23]. The limitation of using PCMs as an energy storage material is application specific. Their suitability varies with applications; e.g. additional weight is not favourable for vehicles, but does no harm in stationary applications. Higher initial cost and volume expansion during melting are included in the issues that need to be considered while designing a PCM-based BTMS [23].

The selection of a PCM depends on the battery operating temperature, as the melting point of a PCM should be nearly equal to the required battery temperature. The selection of a PCM also depends on various parameters, including the latent heat of fusion and density of a PCM. The selection of PCMs is expected to satisfy the following basic requirements [47]:

- High latent heat of fusion
- Easy availability and low cost
- No corrosion effect on the cells
- Higher density for compactness
- High thermal conductivity to decrease the melting and solidification time
- Melting point close to the operating temperature of the cell (marginally higher)
- Lower changes in volume during melting to reduce stresses over the cell
- Higher specific heat to store a larger amount of energy in the form of temperature
- Non-toxic material
- Environmentally benign
- Chemically stable
- Minor or no supercooling effect
- No chemical decomposition

2.6.1 Types of Phase Change Materials

As previously discussed in section 2.6, PCMs are suitable for various thermal storage applications. This study investigates the suitability of PCMs for EVs and HEVs; selection is based on standards such as weight, on-board storage, latent heat of fusion, and safety. These materials have varied

morphologies. The classification of PCMs is shown in Figure 2.12. Solid-liquid PCMs are the most widely used for thermal application [62, 63].

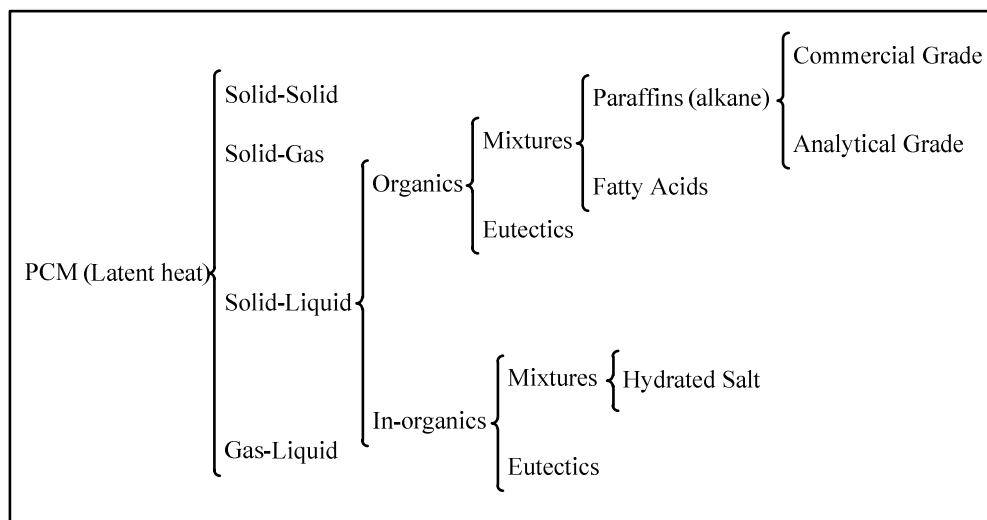


Figure 2.12: Classification of PCMs (modified from [62, 64]).

For scaled-up battery packs, the candidate PCM for Li-ion batteries should normally have a melting point of less than 40°C with a small mushy phase and small temperature interval for melting [47]. Furthermore, the material should have high latent heat of fusion and a thermally high cycle life, as well as be light, chemically stable, non-toxic and inert to other battery components. As shown in Figure 2.12, these materials can be further classified into organic and inorganic PCMs.

2.6.1.1 Organic PCMs

Organic PCMs are carbon compounds, which are chemically inert and non-corrosive in nature. The two broad classifications are paraffin and non-paraffin organic PCMs.

Paraffins

Paraffins are a mixture of long chain carbon compounds with the number of carbon atoms from 20 to 40. The solid form of paraffin is called paraffin wax. Organic paraffin waxes are grouped into two categories: commercial waxes and pure alkanes. These are carbon compounds and differentiated based on the number of carbon atoms in their structure. The compounds with between 8-15 carbon atoms are called commercial waxes, whereas pure alkanes have carbon atoms in the range of 14 to 40. The melting point of pure alkanes varies from 6 to 80°C [62]. The melting

point, which directly depends on the number of carbon atoms, increases with an increase in the number of carbon atoms. For example, paraffin with carbon atoms greater than 17 is generally found in solid form at room temperature. The n-paraffin exhibits greater increase in latent heat of fusion with an increase in carbon atoms, compared to iso-paraffin [65].

Generally, pure alkanes are more expensive than commercial paraffin. The higher costs of pure alkanes can be reduced by mixing these with other similar paraffin waxes [65]. The mixture can be optimised for cost and desired properties.

Non-Paraffin organics

The other organic PCMs are compounds based on fatty acids. These are featured with a relatively high latent heat of fusion and lower change in volume upon melting.

2.6.1.2 Inorganic PCMs

Inorganic PCMs are classified as mixtures and eutectics. Mixture PCMs are salty hydrates with high heat of fusion. Their higher density attributes to their compact size and ease of storage. Another significant advantage is their thermal conductivity, which is almost three times the thermal conductivity of organic PCMs [66]. Their higher conductivity is suitable in applications where the corrosive nature of inorganic PCMs does not significantly affect performance. These are inflammable in nature [66, 67]. Salty hydrates need to be handled with care, as their direct contact can irritate the skin.

Their use as a PCM is limited by the occurrence of segregation. When salts melt, the solid phase separates from an aqueous medium and does not recombine to form the original material. Due to this irreversible process, PCMs lose their structure and pose a practical difficulty in their use. The limitation of incongruent melting is addressed by employing suspension media or extra water principle. One more limitation of inorganic PCMs is their super-cooling nature. Nucleating materials, such as Borax (Glauber's salt), are added to these salts to reduce the super-cooling effect [62].

Eutectics

Eutectics are a mixture of compounds that exhibit congruent melting. Their melting point is lower than the constituting compounds and they can adjust to a range of melting temperatures by varying

the composition. Eutectics are largely inorganics and they exhibit the same limitations as discussed in section 2.6.1.2 for mixtures. Further investigation is needed for properties of this class of PCMs in comparison with their organic counterparts [62]. It is important to note that eutectic materials exhibit congruent melting, and that these materials have a high latent heat of fusion as compared to organic materials [68]. Eutectics show high volumetric changes and can cause damage or stress in the cells. The eutectics can be tailor-made to specific requirements, which also makes them more expensive in comparison to other organic alternatives [69].

2.6.2 Drawback of Phase Change Materials and their Solutions

The disadvantage of incorporating PCMs in a BTMS is the long charging time of the storage system attributed to their low thermal conductivity. Therefore, it is very important to determine how to increase the thermal conductivity of these materials in order to resolve the issue. Thermal conductivities of PCMs vary from 0.1 to 0.6 W/mK [70]. Various researchers have suggested different methods by which to increase the rate of heat transfer; these methods can be categorised mainly into four groups [71]:

- Utilisation of extended surfaces
- Employment of multiple PCMs
- Microencapsulation of the PCM
- Thermal conductivity enhancement

Each method has its own advantages and disadvantages. In the case of extended surfaces, heat transfer rate can be increased due to increase in surface area. At the same time, this may have an adverse effect due to increased wall resistances [71]. Some researchers have found it beneficial to use multiple PCMs, but the change in thermal conductivity is not significant, and this also degrades the other favourable properties of PCMs. The thermal conductivity of PCMs can also be enhanced by adding a high thermally conductive material. Examples of this include: by adding particles of highly conductive material in the PCM; by placing a metal structure in the PCM; or by impregnating a porous material with PCMs having high thermal conductivity. In all these methods, a specific amount of high conductive material can be added to increase the thermal conductivity of the PCM. However, the addition of another material with a PCM may create some negative impact such as increase in weight or decrease in latent heat of fusion [71]. Carbon nanotube

materials are highly conductive and can be used as an additive in a PCM to enhance its thermal conductivity, as explained in the next section.

2.7 Carbon Nanotube Materials and their Applications

Carbon nanotubes, which are miniature tubes formed by carbon atoms, were first introduced in 1991 [72]. The diameter of CNT is in the order of nanometers and length ranges in micrometres. Therefore, their aspect ratio (length to diameter ratio) is greater than 1000. CNTs can be considered as a one-dimensional structure. CNTs are highly preferred in nanofluids due to their high thermal and electrical conductivity. CNTs are mainly produced by three methods: laser ablation, chemical vapour deposition, and ARC discharge [73].

CNTs can be differentiated based on the orientation of layers. The cutting line on the planner surface defines different shapes of CNTs. CNTs can be broadly defined as single wall CNTs (SWCNTs) and multiwall CNTs (MWCNTs). SWCNTs have a smaller diameter in comparison to multi-walled tubes, typically in 1–2 nm range, and tend to be curved rather than straight. MWCNTs have a number of layers and the outer diameter ranges from about 2 nm to 100 nm [73]. In MWCNTs, the distance between two adjacent layers is similar to that of graphene layers, which is nearly 3.3 Å. Figure 2.13 shows the structure of SWCNTs and MWCNTs.

CNTs have considerable high axial thermal conductivity, and their values are reported in a wide range. The axial thermal conductivity of CNTs is estimated as high as 3000 W/mK and 6600 W/mK for individual multiwall CNTs and single-wall CNTs [74], respectively. Double-walled CNTs have a very similar morphology as single wall CNTs. Reduction in the cost of CNTs over time makes them affordable option for conventional purposes. The cost of MWCNTs varies from \$0.60-\$25 per gram, depending on diameter size and quantity of MWCNTs required [75].

CNTs are considered as ideal additives to PCMs due to their high thermal conductivity, but there is one practical difficulty in introducing CNTs due to their bonding nature. The weak molecular attractive forces negatively impact the prospects of their thermal application. CNTs do not form a stable bonding with surrounding molecules and tend to form large lumps with neighbouring nanotubes due to their hydrophobic nature, small size, high aspect ratio, and van der Waals forces

[76, 77]. To maintain the homogeneity of CNTs, a number of dispersion methods are used. Some of these methods are discussed in the next section.

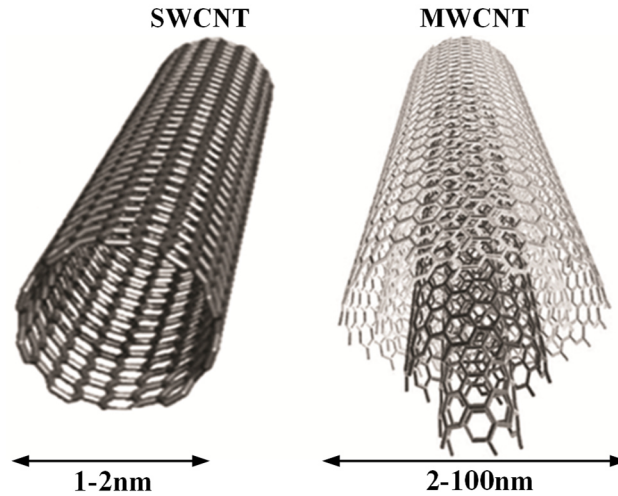


Figure 2.13: Structure of single and multi-walled carbon nanotubes (modified from [78]).

2.7.1 Dispersion Methods of Carbon Nanotubes

Dispersion of CNTs can be performed through either an external force such as sonication or mechanical stirring, or by using a solvent (both ionic and non-ionic) [79]. Although these methods can be used to disperse a variety of materials, the focus of the present study is limited to CNTs. Various mechanical dispersion methods are as follows:

Sonication: Sonication is the most commonly used dispersion method, where high-frequency sound waves are used to disperse CNTs into a solution [17]. Attenuated waves (shock waves) develop in the medium due to the passage of high-frequency sound waves. A medium can be any liquid with low viscosity. A medium with high viscosity need to be dissolved in the solvent to be used for sonication or can be heated to reduce viscosity in some cases. The shock waves peel off CNTs layer by layer and create a uniform distribution of CNTs in the medium. Sonication devices can be of two types: ultrasonic probe/horn (tip sonication) and ultrasonic bath (bath sonication). Both these sonication devices have their own advantages and selection is application specific. A combination of manual stirring and sonication is also used to disperse CNTs. In some cases, sonication used for CNT dispersion may lead to surface defects in the CNTs [15].

Calendering: In this process, a calender is used to reduce agglomeration. In a calender, three rolls are used to disperse or mix CNTs by using shear forces produced by rolls. The two side rollers, known as the apron and feeding rollers, rotate in the same direction while the central roller rotates in the opposite direction as shown in Figure 2.14. A blade is used to remove the final product from the apron roller. This process can be continued until the required level of mixing is achieved [17]. This process is limited to converting a large agglomeration to a small one, as the gap between the rollers is considerably larger than the diameter of a CNT.

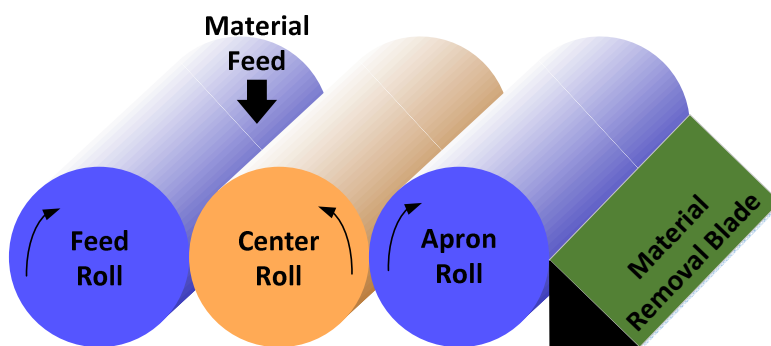


Figure 2.14: Calendering process using three roll mill.

Ball milling: High-quality ball mills can be used to reduce the size and disperse CNTs. Improvements in the performance of the process can be made by using some chemicals. Several studies show that the process of ball milling reduces the aspect ratio of CNTs [16].

High-shear mixing and extrusion: Studies show that large quantity of CNTs can be uniformly dispersed by using high-shear mixing [17]. Extrusion is also a common technique to disperse CNTs mainly in solid polymers. In the extrusion process, shear flow is developed by twin screws rotating at high speed to disperse CNTs in solids and liquids [80].

Other than mechanical methods, some chemical methods such as functionalization are also used to disperse or reduce agglomeration. In functionalization, the surface of CNTs is modified to improve their wetting/adhesive characteristics and reduce the tendency of agglomeration. Functionalization can be physical (covalent) or chemical (non-covalent). However, some chemical functionalization can digest CNTs at high temperature [14].

Most of these methods are used to uniformly disperse CNTs in solids and liquids. However, such methods are mainly effective to permanently disperse CNTs in solids since, in the case of liquids, CNTs re-agglomerate. Also, as discussed in Chapter 1, CNTs settle down on the bottom surface. According to the best of the author's knowledge and from the available literature, no successful method or process to tackle re-agglomeration and settlement of CNTs at the bottom in liquids has been developed.

In the present thesis, the author proposes a new method to tackle both the issues of re-agglomeration and settlement of CNTs on the bottom surface. In the proposed method, initially, a fixed amount of CNTs will be uniformly dispersed in a PCM through the ultrasonication water bath method. An open cell polyurethane foam will then be used to absorb the mixture of the PCM and CNTs through a specially designed process. Each cell (cavity) in polyurethane foam can hold the CNTs in their place, even when the PCM melts. This will provide a permanent dispersion of CNTs in the PCM and will not allow CNTs to settle down on the bottom surface. Further details about the complete process of using polyurethane foam with the PCM and CNTs will be given in Chapter 4.

2.8 Optimization Methods

In engineering design, optimisation is a necessary tool to identify the best possible solution. An optimal design can be obtained by using optimisation techniques without testing all possible cases. In the literature, there are several optimisation techniques/methods available; these can be mainly classified as continuous and combinatorial optimisation methods. These optimisation methods can be further classified into classical methods, heuristic, and metaheuristic [81]. Each optimisation method has its own advantages and possible limitations. Classical methods are analytical methods with limited scope of application. Heuristic optimisations are problem dependent and usually trapped in local optima, while metaheuristic optimisations can be applied to almost any problem. In the case of metaheuristic, it is possible to determine a global solution, but not guaranteed. The popular metaheuristic algorithms for optimisation include genetic algorithm, bee algorithm, particle swarm optimisation, and ant optimisation [81].

2.8.1 Genetic Algorithm

A genetic algorithm (GA) is an evolutionary algorithm. As the name suggests, it is based on natural genetics, which mimics biological evolution [82]. The GA was first developed by John Holland in the early 1970s to understand the adaptive processes of natural systems [83] and has since become recognized as a robust optimisation technique. This means that a GA can find the near optimal or global optimal point for any optimisation problem. Even with a small change in input parameter, it is able to provide a good solution [82].

Figure 2.15 shows the basic steps of a GA. In this method, a set of solutions are randomly created at the initial stage for the objective function to be optimised. The objective function can be minimised or maximised, depending upon the requirement. In a few cases, such as energy and exergy efficiencies, it is maximised while in other cases, such as heat losses, and capital and operational cost, it is minimised. A multi-objective function can also be defined, where some parameters can be minimised, while others can be maximised. Each solution has a set of properties that can be mutated. Each candidate solution is then converted into a coded string, which is known as the initial population. The size of the initial population depends upon the optimisation problem but can be between tens to several hundred. However, increasing the initial population does not mean an improvement in results [82]. Several trials (runs) are needed before obtaining a good number of populations. Once the initial population size is obtained, each solution obtained from the test is checked and evaluated with the required objective function to determine the fitness value (how good the solution is). The best solution from the current population is selected and modified through crossover and mutation to form a new population. In the crossover, two individuals are selected from the population. A site for crossover is randomly selected from two individual strings. The values of two strings are exchanged, and two new offspring are created for the next generation population. The purpose of mutation is to maintain diversity in the population and to avoid early convergence through flipping a portion of new individual bits [83]. The old population is replaced by a new population, and this new population is used for the next generation, hence the process continues [84]. Therefore, a stopping criterion is required to stop or continue the iterations. Generally, the number of generations is considered as the stopping criteria for the algorithm.

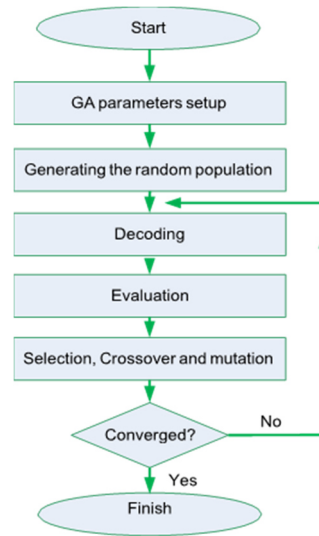


Figure 2.15: Flowchart of a genetic algorithm.

2.9 Closing Remarks

In this chapter, various aspects of topics related to the present thesis are discussed in detail. Development of EVs and HEVs over time and their recent growth are discussed. Types of battery-operated vehicles are discussed in brief to provide awareness of the arrangements of major components (mainly battery) in these vehicles. Different types of batteries along with their advantages and disadvantages are discussed to enable understanding of their application in EVs and HEVs. From the various studies available in the literature, it has been observed that Li-ion batteries are most suitable for EVs and HEVs. Therefore, details of Li-ion batteries and related issues, such as heat generation, are discussed. The ultimate target of this thesis is to maintain battery temperature within an optimum operating temperature range through a passive BTMS. Therefore, it is important to understand the effect of heat generation or increase in battery temperature on the capacity and life of the battery. The life and capacity of the battery decrease due to degradation, therefore the process of degradation and effect of temperature on degradation are discussed.

How a conventional BTMS is used to control battery temperature and ultimately reduce the degradation rate is discussed in detail. The advantages and disadvantages of various BTMSs used in EVs and HEVs are considered along with the need of a PCM-based BTMS. The types of PCMs that can be used for a passive BTMS are examined along with properties, advantages, and

limitations (mainly low thermal conductivity). Different methods to improve the thermal conductivity of PCMs are explained together with the application of CNTs. Different types of CNTs and their agglomeration issues are discussed. Various types of methods are available in the literature to uniformly disperse CNTs into solids and liquids. These dispersion methods are described with their limitations (re-agglomeration). In addition, methods to tackle the issue of CNT re-agglomeration and settlement on bottom surfaces are considered. Optimisation is required to find the best possible solution within a given constraint. In the present thesis, optimisation techniques will be used to improve the developed system. Therefore, at the end of this chapter, optimisation techniques are discussed. In the next chapter, research work by different researchers on various thesis-related topics will be discussed, and gaps in the literature will be highlighted.

Chapter 3. Literature Review

Current concerns about the environment and increasing cost of oil have propelled research into clean fuel technologies. The potential of EVs and HEVs as alternatives to conventional ICE-based vehicles leads to a significant increase in the volume of research conducted in this area in various scientific disciplines. The source of electricity is very important from an environmental impact point of view since fossil fuel-based electricity has substantial ecological footprints and lower overall efficiency. Although the source of electricity is important, the future of EVs depends on energy and power density, efficiency, safety and life of the battery. Therefore, significant efficiency improvement, lower cost, and high battery life are the main focus of research. One of the major concerns about the battery is its operation within a defined temperature range. PCMs can be one of the options available to control the temperature variation in the battery pack.

In the present chapter, a review of major studies into the types of electric energy storage systems (batteries) and their thermal management system (types, issue, and available solutions) will be conducted. A review of PCMs, their related applications, and related issues will also be made. Some of the available methods that were used by different researchers to improve the thermal conductivity of PCMs are also discussed in this chapter. Exergy analyses provide a better understanding of BTMSs as studied by various researchers. Therefore, various findings and limitations of these exergy analyses are included in this chapter. Optimisation techniques help to use the available resources in the best possible ways. Different optimisation methods used by various researchers to optimise the BTMSs are discussed. The chapter concludes with gaps in the literature regarding the application of PCMs in BTMSs.

3.1 Heat Generation and Thermal Management of Li-ion Batteries

Batteries, as the major power source of EVs and HEVs, undergo thousands of cycles of operation during the lifetime of a vehicle. There are various constraints in selecting the correct battery for vehicle applications. One of the major constraints is energy density. Although high energy density of Li-ion batteries makes them more prominent for EVs and HEVs application, heat generation during charging and discharging is a major drawback. The issue of heat generation in Li-ion batteries and thermal management systems, as studied by various researchers, is presented in this section.

3.1.1 Heat Generation in Li-ion Batteries

Three main sources for heat generation in cells as considered by Selman et al. [85] are given below:

- I. Irreversible heat, generated mainly due to ohmic factors and polarisation, and which increases with an increase in current load.
- II. Side reactions, including corrosion reactions, parasitic, and chemical shorts.
- III. Reversible heat, absorbed or released due to chemical reactions in the cell.

The second and third sources are the main sources of heat generation during abusive or excessive load conditions, while there is negligible effect during normal operation. During abusive or excessive load conditions, a non-uniform temperature distribution occurs in the cell, including a hot spot. Due to this hot spot, the second source of heat generation can lead to thermal runaway in the cell and the battery pack.

Saito et al. [86] have experimentally investigated heat generation for lithium-ion cells in overcharge conditions. The results show that heat generated in the lithium-ion cells during overcharging is directly proportional to the charging current. Thermal runaway can be avoided during this period by using a cooling system that is capable of removing the heat generated. An electrochemical calorimetric method has been used by Al-Hallaj et al. [87] in order to evaluate thermal behaviour and performance of cylindrical-type commercial Li-ion cells. The results show that heat dissipation rate is directly related to the rate of discharge (C-Rates). Moreover, the structural transformation or phase change in the cathode material leads to a noticeable temperature drop in some commercial cells.

Eddahech et al. [88] performed an analysis of the thermal behaviour of high-power lithium-ion cells. The authors use an ARC calorimeter to measure the heat produced by the lithium cell during charging and discharging at several current rates, and conclude that the overall heat generation in the battery is related to both joule heating and entropy change. Electrochemical reactions, which happen during charging and discharging, change the battery entropy and lead to heat generation. Joule heating takes place due to internal resistance to current flow. From this study, it was observed that the effect of a change in entropy on heat generation is negligible at high current rate.

Rao and Newman [89] developed a new technique to calculate heat generation rate using enthalpy potentials and compared the result with that obtained by Bernardi et al. [90] using the energy balance method. To calculate the heat generation rate of the entire cell, all components and species in the cell were taken into consideration. The study shows that the ohmic drop in the pores of electrodes is responsible for a large portion of heat generation.

The thermal behaviour of Li-ion batteries has been studied by Chen and Evan [91] through a mathematical model to identify the transient heat generation rate, temperature rise and temperature profile regarding module dimension and operating variables. An assumption was made that the electrochemical changes in the cell will not be significantly affected by a temperature change from 25°C to 50°C. They establish that the heat generation in a cell for medium-rate discharge (C/2) is about 10 kW/m³ and increases with an increase in discharge rate. The study concluded that for high discharge rates, even forced convection is not an effective means to control the temperature, and that it can lead to thermal runaway if the temperature reaches above 50°C. These studies show that the heat generation rate increases with an increase in discharge rate. Also, there is a lack of reliable and detailed experimental data for heat generation rate in the Li-ion battery. These studies show that for safety and longer life of the battery, an effective thermal management system is required.

3.1.2 Battery Thermal Management Systems

A thermal system is required to manage the battery temperature within a narrow optimum temperature range. Various active and passive BTMSs are studied by the researchers [51, 92, 93], where different liquids and the air is used as heat transfer fluid. Keller and Whitehead [94] studied the effect of battery operation in extreme temperature conditions without a BTMS and with an air or liquid BTMS. It was found that the vehicle driving range is lower in the absence of a BTMS, as heat spreads across the battery pack due to high ambient temperatures. This can lead to a premature cell failure and seasonal driving variability. From the study, it was also found that the mileage of the vehicle can be increased up to 20% by using a BTMS. Furthermore, the temperature distribution can be reduced to 2.3°C and 4.0°C compared to 11.6°C for a non-managed pack, by circulating air and liquid, respectively. However, the authors do not comment on the effect of a change in coolant temperature on battery capacity. The effect of discharge rate on cooling requirements and battery capacity were also missing from the study.

Kuper et al. [95] examined the different active cooling systems using air, water and refrigerant and also studied heat generation in batteries. The increase in battery temperature over time, based on internal heating and cooling rates, have been formulated. The study shows that the maximum and minimum cell temperatures should be maintained within a 3-5 K range to prevent 25% acceleration of the ageing kinetics and up to 50% variance in power capability. It is also recommended to keep the coolant inlet and outlet temperature difference to be less than 3 K to maintain uniform cell temperature. The study does not include the energy needs for different cooling options and their effect on battery capacity.

A comparison among various TMSs has been conducted by Pesaran [96], based on their functionality and capability, including active vs. passive, series vs. parallel, heating vs. cooling and air vs. liquid for NiMH, VRLA and Li-ion batteries. A comparison has also been made regarding heat generation and its impact on different temperatures and cycles. It is concluded that a passive BTMS can be used for a relatively small battery pack. It is simple, but less effective. However, the temperature of the air should be between 10°C to 35°C for the BTMS to work in passive mode, otherwise, it exposes the battery to extreme temperatures. On the other hand, a more sophisticated liquid-based BTMS is required in the case of EVs and HEVs, for their optimum thermal performance. The study does not provide a detailed analysis of a passive BTMS and circumstances where this type of application is limited. Also, the effect of a passive BTMS on battery performance needs to be included.

Liu et al. [97] developed and simulated a two-dimensional and transient model for the thermal management of a 20 flat-plate Li-ion battery stack. The purpose of the study was to investigate the effect of Reynolds number, discharge rate, and ambient temperature over the temperature distribution in the battery stack by using different cooling methods. The results show that, in the case of mild ambient temperature, liquid cooling is most effective in decreasing the temperature inside a battery compared to a PCM. The authors also advised to avoid fast and deep discharge in order to maintain the temperature in an acceptable range. The study shows that air-cooling is preferred at zero or sub-zero ambient conditions because, at these temperatures, heat needs to be retained rather than removed. The air circulation helps to reduce the temperature gradient in a battery at zero or sub-zero ambient conditions. There is a minor difference between the effect of

using air and liquid as a cooling medium when SOC is high, and the ambient temperature is mild. Selections of a suitable cooling material have a significant effect in the case of fast discharge and low ambient temperature. The study does not reveal why liquid cooling is better than a PCM with mild temperatures. Moreover, a similar study is required for high and low discharge rates as only 2C discharge rate has been considered by the author.

Zhang et al. [98] have presented three different methods for a 27.7 kWh Li-ion battery cooling/heating: phase change slurry (PCS) cycle; refrigerant circulation; and direct cabin air blow. From the results, it was observed that additional thermal load is added to an air-conditioner in the direct cabin air blow method. However, the refrigerant circulation method and the PCS cycle battery cooling/heating method have almost same amount of load on the air-conditioning system of the vehicle. In the case of the mild electrical load of the battery, the direct cabin air blow method requires a negligible amount of extra cooling/heating supply compared to the PCS and refrigerant circulation methods. At the same time, the increase in Li-ion battery cooling/heating load causes a much faster increase of the extra thermal load in the direct cabin air blow method compared to the PCS cycle and refrigerant circulation methods. It is also found that the exergy efficiency of the battery with the PCS cycle method is higher compared to the refrigerant circulation method.

Saw et al. [99] analysed the effect of temperature on the Li-ion battery and uses computational fluid dynamics to investigate liquid cooling system performance with the battery pack. The results show that, with natural convection cooling, the maximum temperature difference in the cells is 9°C at 5C discharge rate, while 6.5°C with forced convection cooling. The authors conclude that both natural and forced convection cooling is not sufficient to manage the battery pack temperature within the required range at high discharge rate. On the other hand, liquid cooling is capable of managing the temperature, but is more complex and draws significant power from the battery pack to run the cooling cycle.

From the literature, it is found that various studies of conventional BTMS are generally conducted for cylindrical cells, and very limited studies are performed on the thermal management of prismatic batteries. These studies generally consider a normal discharge rate at a particular coolant temperature. Therefore, a detailed study of a liquid based-BTMS is required by considering low as well as high discharge rates with different coolant temperature. Table 3.1 provides a trade-off

analysis of various thermal management systems by such factors as the level of integration, efficiency, maintenance, and capital cost. From this comparative analysis, it is evident that a PCM can be an advantageous option for thermal management compared to the other available options. Compared to the conventional cooling system using cold plates, a PCM is superior in almost every category. Although the capital cost of active air cooling is lowest among all options, PCMs are comparatively much more effective regarding temperature distribution and temperature drop in the cell.

Table 3.1: Trade-off analysis of the battery thermal management.

Parameter	Forced Air	Liquid	Heat Pipe	PCM	Thermoelectric	Cold Plate
Life	≥ 20 years	3–5 years	≥ 20 years	≥ 20 years	1–3 years	≥ 20 years
Ease of Use	Easy	Difficult	Moderate	Easy	Moderate	Moderate
Integration	Easy	Difficult	Moderate	Easy	Moderate	Moderate
Maintenance	Easy	Difficult	Moderate	Easy	Difficult	Moderate
Temperature Distribution	Uneven	Even	Moderate	Even	Moderate	Moderate
Efficiency	Low	High	High	High	Low	Medium
Temperature Drop in Cell	Small	Large	Large	Large	Medium	Medium
Annual Cost	Low	High	Moderate	Low	High	Moderate
Capital Cost	Low	High	High	Moderate	High	High

Source: modified from [13].

3.2 Phase Change Materials and their Applications in Li-ion Batteries

In this section, various types of PCMs, along with their application in the thermal management of Li-ion batteries as studied by various researchers, are discussed.

3.2.1 Phase Change Materials

PCMs with a low melting temperature are receiving more attention due to their extensive use in solar energy storage systems [62, 66, 67] and possible use in the thermal management of Li-ion batteries. A comprehensive study of PCMs was conducted by Sharma et al. [68], who include various characteristics of more than 200 PCMs and present their benefits in decreasing energy use in solar water heating. Organic and inorganic PCMs are studied by Abhat [62], who specified that organic fatty acids have superior thermal characteristics compared to organic paraffin wax materials and concluded that n-paraffin waxes have a fine or constant phase change temperature.

The author also reported the major drawbacks of inorganic PCMs, i.e. their corrosive property and relatively higher cost. The basic properties of organic and inorganic PCMs are given in Table 3.2.

Table 3.2: Properties of some organic paraffin waxes and inorganic PCMs (Adapted from [65]).

Materials/Organic Commercial Paraffins	Melting Point (°C)	Heat of Fusion (kJ/kg)	Thermal Conductivity (W/m K)	Density (Solid) (kg/m³)	Density (Liquid) (kg/m³)	Specific Heat (Solid) (kJ/kg K)
5913 (n-paraffin)	23	189	0.21	900	760	2.1
6106 (n-paraffin)	43	189	0.21	910	765	2.1
P116 (n-paraffin)	41	210	0.21	817	786	2.1
5838 (n-paraffin)	49	189	0.21	912	760	2.1
6035 (iso-paraffin)	59	189	0.21	920	795	2.1
6403 (iso-paraffin)	63	189	0.21	915	790	2.1
6499 (iso-paraffin)	67	189	0.21	930	830	2.1
n-Alkane						
Hexadecane	18	236	0.21		770	2.2
Heptadecane	22	213	0.21		778	2.2
Octadecane	28	244	0.21	814	774	1.90
Nonadecane	32	222	0.21	782		1.91
Eicosane	37	246	0.21	778		1.92
Docosane	44	249	0.21	791		1.93
Tricosane	48	232	0.21	764		1.93
Tetracosane	51	255	0.21	796		1.93
Parrafin wax	55	146	0.21	880		1.93
Hexacosane	57	256	0.21	770		1.85
Heptacosane	59	235	0.21	802		1.91
Dotriacontane	70	266	0.21	809		1.92
Octatriacontane	100	271	0.21	815		1.93
Inorganic PCMs (Salty Hydrates)						
LiClO ₃	8.1	253		1720	1530	2.11
KF.4H ₂ O	18.5	231		1455	1447	1.84
CaCl ₂ .6 H ₂ O	29.7	171	0.454	1710	1496	1.45
Na ₂ SO ₄ .10 H ₂ O	32.4	254	0.544	1485		1.93
Na ₂ HPo ₄ .12 H ₂ O	35	281	0.476	1520	1442	1.7
Na ₂ CO ₃ .10 H ₂ O	36	247		1438		
Zn(NO ₃) ₂ .6 H ₂ O	36.4	147		2065		1.34
KF.2H ₂ O	42	117		1670		1.51
Na ₂ S ₂ O ₃ .5 H ₂ O	48	201		1730	1670	1.46
NaCH ₃ COO.3H ₂ O	58	270	0.5	1150		1.90
NaOH.H ₂ O	61	260		1720		
Ba(OH) ₂ .8H ₂ O	78	267		2180		1.17
Mg(NO ₃) ₂ .6 H ₂ O	89	159		1640	1532	1.99
MgCl ₂ .6 H ₂ O	116	165		1570		

From Table 3.2, it can be seen that latent heat is highest in the case of Sodium Dihydrogen Phosphate Dodecahydrate ($\text{Na}_2\text{HPO}_4 \cdot 12 \text{H}_2\text{O}$). However, its application is limited due to its high cost and corrosive nature. Organic PCM Octatriacontane has the highest latent heat, but it cannot be used with a li-battery due to the very high melting point. Organic PCM Octadecane and Nonadecane are best suited for Li-ion batteries, as their melting point is closer to the optimum operating temperature of Li-ion batteries.

3.2.2 Phase Change Material Applications with Cylindrical Cells

Duan and Nature [100] examined the effects of PCMs on the thermal management of cylindrical cells by considering two different approaches. A line heat source (heater) is used to represent a cylindrical cell. In the first approach, the cell (line heat source) is wrapped with a PCM jacket, and in the second approach, the cell is surrounded by a PCM. The result shows that, in both cases, PCM is capable of keeping the cell temperature within narrow limits. The authors conclude that the same approach can be applied for TMS of HEVs, but do not comment on whether the thermal conductivity of the heater was the same as a cell or different. How the rate of heat transfer from the heater links to the heat generation rate in a cylindrical cell was also not clear.

Al-Hallaj and Selman [101] investigated a scaled-up battery pack with cylindrical cells and PCMs between the cells in the module. The research was among some of the pioneer studies which show that PCM is effective and capable of controlling the temperature, and can be used as a passive thermal management for batteries without any external power requirement. Another study of a battery module with cylindrical Li-ion cells and PCM as a TMS, by Al-Hallaj et al. [11], shows that PCM usage improves battery life and about 90% of the nominal capacity of the battery is accessible while using PCM with the battery pack.

Kizilel et al. [102] created a simulation of a scaled-up Li-ion battery pack, consisting of 67 modules, each module with 20 cylindrical Li-ion cells for normal and stressful or abusive conditions, by using active air cooling and a PCM-based TMS. The results show that air-cooling is almost enough to manage the temperature of the cell in normal discharge condition, but fails in stressful or abusive conditions to effectively remove the heat. Similar results were obtained in another study by Kizilel et al. [103], where a PCM has been used as a passive TMS in Li-ion. The

results were obtained by using different higher rates of discharge and an increased ambient temperature under stressful operating conditions.

A comparative study of active air cooling and passive cooling through PCMs was performed by Sabbah et al. [49] for a compact battery of a PHEV, where cell array was surrounded by a micro-composite graphite-PCM matrix. Again the results show that an active air-cooling system is not able to maintain the battery pack temperature within the safety range during abusive conditions, whereas a PCM cooling systems are able to handle such situations and meet TMS requirements.

3.2.3 Phase Change Material Applications with Prismatic Cells

Examples of a PCM application with prismatic cells are very limited in the literature. Javani et al. [104] examined a passive TMS for an EV battery pack, where n-Octadecane (PCM) is infused between the Li-ion cells, and finite volume-based simulations have been used to analyse the thermal characteristics of a four cell sub-module. Analysis has been performed by using different discharge rates, with and without the presence of n-Octadecane. The result shows that there is a decrease of 7.3 K in the battery surface temperature by replacing dry foam with the PCM-soaked wet foam, which also makes a uniform temperature in the cells. The study also shows that the combination of an active cooling system with the PCM-based passive thermal management can decrease the peak power requirements and cut down half of the power required from the cooling system. However, validation of simulation results from this study needs to be completed with experimental results. Also, when the ambient temperature in summer exceeds 40°C, PCMs start melting fast and do not solidify during the second charging/rest cycle, leading to a mushy phase formation by the end of the cycle. Even though a PCM does not act as a heat sink during the second and third cycles, the operating temperature of the battery remains within safe limits and is still better than air cooling [41].

These studies show the capability of a PCM for use in the passive thermal management of EV and HEV batteries. However, most of these studies are only conducted with cylindrical cells. Studies on PCM applications with prismatic cells are very limited, and are also simulation-based [54]. Most of these studies consider a PCM around the cells and do not discuss the practical application in an actual EV and HEV. It is not clear how the PCM will be managed within the container when it melts and the vehicle is in motion. In the open literature, no experimental studies with prismatic

cells and a PCM were performed at high discharge rates by placing PCM plates between the cells. Studies also reveal that the application of PCMs with EV and HEV batteries are limited due to the low thermal conductivity of PCMs. The thermal conductivity of PCMs must be enhanced for effective heat removal from the battery [10].

3.3 Improvement in Thermal conductivity of Phase Change Materials

The thermal conductivity of PCMs can be improved through various methods suggested by researcher [105-111], such as employment of multiple PCMs, utilisation of extended surfaces, and adding highly conductive material. Some such methods are discussed in this section.

3.3.1 Conductive Materials

Various studies suggest using other conductive materials as an additive in PCM to increase the overall thermal conductivity. Copper, aluminium, and nickel are the common materials used with a PCM to enhance thermal conductivity [109]. Martinelli et al. [105] experimentally studied the effect of using copper foam on the melting time of a PCM. Copper foams with 91% porosity are used to make rings around a copper pipe. The copper pipe, along with copper foams and a PCM, are placed inside a transparent tube, and hot water passes through the copper pipe. The result shows that the melting time of PCM reduces from 5400 s to 500 s by using copper foam compared to the case when no copper foam is used. This is a result of the increase in thermal conductivity of PCM with copper foam. In a similar study, Chen et al. [106] investigated the improvement in thermal conductivity of the PCM (paraffin) with the use of copper foam. A hot disk thermal analyser is used to measure the thermal conductivity. The results show that the thermal conductivity of the PCM increases from 0.272 W/m K to 2.142 W/m K with 98% porous copper foam.

Bauer and Wirtz [112] used aluminium foams and plates to improve the thermal conductivity of PCM (paraffin). Three samples of the PCM with a different metal fraction of aluminium were prepared. These samples were sandwiched between two 1 mm thick aluminium plates. A flat plate was used as a heat source on one side of the samples and a cold plate on the other side. The result shows that thermal conductivity of the PCM increases from 0.17 W/m K to 4.3 W/m K with an aluminium fraction of 0.077. Further, the thermal conductivity of the PCM increases from 4.3 W/m K to 5.0 W/m K with an increase in an aluminium fraction from 0.077 to 0.09. Nickel is also used

by various researchers [107, 108, 113] to improve the thermal conductivity of various types of PCMs.

From these studies, it can be seen that thermal conductivity of PCMs can be significantly improved by using different metals. However, the application of metal is limited to a PCM-based BTMS due to design limitation and extra weight. These are mostly used in large thermal energy storage systems (TESS). Further studies are required on different methods of enhancing the thermal conductivity of PCMs for a Li-ion battery application.

3.3.2 Carbon Based Filler

Babapoor et al. [111] studied thermal management of batteries by using the PCM and carbon fibre. Carbon fibre is used to enhance the thermal conductivity the PCM. The result shows 45% reduction in temperature with the use of carbon fibre. However, the study considers 60°C as the allowable temperature for Li-ion batteries, which is significantly higher than the optimum operating temperature. Also, instead of an actual battery, a battery simulator is used to simulate the temperature. It is not clear how the heat generation rate in the simulator is calculated, and on what basis the timeframe of the experiment is selected.

Shaikh et al. [110] investigated the change in the latent heat of fusion of the PCM by adding carbon nano-particles, i.e. single-walled CNTs, and multi-walled CNTs in pure wax, respectively. The result shows that there is an improvement in the latent heat for all samples compared to pure wax. It was found that a novel class of nano-fluid PCMs with enhanced thermal conductivity can be obtained by adding a small amount of MWCNTs in the liquid paraffin. Although the author uses ultrasonication to equally distribute CNTs into the PCM, it is not clear what happen to CNTs once the phase change process starts. The application of these composites with Li-ion cells has not been studied.

Kumaresan et al. [114] prepared stable nano-fluid PCMs by adding a small volume fraction of MWCNTs (0.15, 0.3, 0.45 and 0.6%). From differential scanning calorimetry results, a small change in the latent heat values of nano-fluid PCMs was observed, but no significant changes were observed in freezing/melting temperatures. The results show that thermal conductivity of various nano-fluid PCMs increase with an increase in volume fraction of MWCNTs. An approximate

33.64% decrease in solidification time was obtained due to an increase in heat transfer for the nano-fluid PCMs with a volume fraction of 0.6% MWCNTs. Again, the issues of agglomeration of CNTs and the application of composite with Li-ion batteries were not studied.

Zhang et al. [115] investigated a novel heat transfer fluid (HTF) which have water with microencapsulated PCM (MEPCM) and MWCNTs. The result shows that there was an effective improvement in the thermal conductivity of the suspension by adding MWCNTs into MEPCM. The optimal thermal performance and stability are found with a blend of 10% (wt.) MEPCMs and 1% (wt.) MWCNT. The study does not include an application of the developed system in the thermal management of Li-ion batteries.

Choi et al. [116] investigated the effect of carbon additive over thermal conductivity, dispersion stability, and heat transfer rate of PCMs through the transient hot-wire method. The study shows that the PCM thermal conductivity increases with an increase in the concentrations of Graphite, Graphene, and MWCNTs. More increase in the PCM thermal conductivity is obtained by Polyvinylpyrrolidone (PVP) as a dispersion stabiliser with graphite. An approximate 21.5% increase in thermal conductivity of the PCM is obtained by adding 0.1 % (vol.) Graphene. The rate of heat transfer increased by 3.35 times with 5% (vol.) Graphite. The authors studied the effect of the phase change process on the distribution of carbon nanoparticles in the PCM. The result shows that, in the case of Graphite and Graphene, the dispersion stability of the PCM lasts for three and eight days, respectively, and ten days in the case of MWCNT. However, no possible solution to maintain the dispersion of the carbon additive was studied or suggested.

In another study [117], treated MWCNTs are used to enhance the thermal conductivity of PCM (Palmitic acid). The result shows that there was an increase of 46.0% at 25°C and 38.0% at 65°C in the thermal conductivity of composite PCMs by adding treated 0.01 (mass fraction) CNT. The study also interestingly reveals that the thermal conductivity of the composite PCMs suddenly increase near the melting point in the solid state and suddenly decrease when PCMs turn into a liquid state. Although the authors do not explain the possible reason, it may be due to an agglomeration of CNTs when the PCM melts. Again the study was limited to observing the change in thermal conductivity of the PCM with MWCNTs and does not cover the agglomeration issue.

Fan et al. [118] have experimentally investigated the change in energy storage properties and thermal conductivity of paraffin-based nanocomposite PCMs by adding various carbon nanofillers. Samples of PCM and graphene nanoplatelets (GNPs), long MWCNTs, and carbon nanofibers are prepared with concentrations varying from 1-5% (wt.). The transient hot-wire method is used to identify the thermal conductivity of the samples, and a differential scanning calorimeter is used to determine energy storage properties such as enthalpies and melting/solidification temperatures. Negligible changes in the melting point of the PCM are observed due to the presence of the nanofillers, while phase change enthalpies slightly decrease. Up to 164% enhancement in thermal conductivity of the nanocomposite PCMs was obtained with the addition of 5% (wt.) GNPs, which is the maximum among all four types of the carbon nanofillers examined. The study does not include the effect of agglomeration in MWCNTs on the thermal conductivity of the composite when the PCM melts. Furthermore, it does not examine the application of developed composite with the Li-ion batteries.

Javani et al. [119] developed a new passive thermal management system for EVs, where a TESS containing the PCM and nanoparticles has been designed and optimised. The result shows that, without using nanoparticles, even the optimum length of TESS is so large that it cannot be employed in a vehicle due to the very low thermal conductivity of the PCM filled inside the TESS. Therefore, a mixture of the PCM (n-octadecane) and CNTs was used, and heat transfer rates varying from 300 W to 600 W were applied to optimise the TESS. The results from the optimisation show that the heat exchanger (TESS) length can be minimised by using smaller tube diameters and by increasing the CNT concentration. The study includes only a theoretical analysis of TESS for varying concentrations of nanoparticles and does not comment on either the agglomeration effect or possible integration of composite PCM with Li-ion batteries.

Lin et al. [12] conducted an experimental study of a rectangular Li-ion battery pack (LiFePO_4) with composite PCM and a graphite sheet. Six 40Ah cells connected in series were surrounded from the side by composite PCM and graphite plates were placed between the cells. The battery pack was discharged at 1C and 2C discharge rates. The results show that the temperature of the battery pack reduced by 32% and 37% by using the PCM-based BTMS at 1C and 2C discharge rates, respectively. The simulation result shows underutilisation of the PCM on the sides of the

cells. Therefore, further studies are required, by considering high discharge rates and placing composite PCM between the cells.

Table 3.3 summarises the various methods to enhance the thermal conductivity of PCMs. A comparison of methods indicates that graphite or expanded graphite are good options as additive materials. Although there are several methods for enhancing the thermal conductivity of PCMs, analysis of additive effects on the latent heat of PCMs is necessary. As an example, by using a silver nanowire as an additive, the thermal conductivity of the PCM increases from 0.32 to 1.46 W/m K, while the latent heat is reduced by more than 63%, based on our present calculations [47].

Table 3.3: Various methods used to enhance PCMs thermal conductivity (compiled from [47, 48]).

PCM/Thermal Conductivity (W/m K)	Additives/Thermal Conductivity (W/m K)	Composites Thermal Conductivity (W/m K)	Ratio of Composite (%wt)	Latent Heat of PCM Without/With Additives (kJ/kg)
Paraffin/0.2	Graphite	70	35	179/136
RT-42 Paraffin/0.2	Expanded Graphite/4-100	16.6	26.6	250/185
Paraffin/0.2697	Expanded Graphite/4-100	4.676	6.25	n/a
Eicosane/0.423	Copper Porous Foam	3.06	95	n/a
Inorganic Eutectic/0.47	Carbon Fiber/175–200	1.8	8	195/180
1-Tetradecanol/0.32	Ag Nanowire/10-191.5	1.46	62.73	210/76.5
Polyethylene Glycol/0.299	Expanded Graphite/4-100	1.324	10	187.3/161.2
Hexadecane/0.15	Aluminum Particles	1.25	n/a	236/167
n-Octadecane/0.27	Expanded Graphite/4-100	1.07	16.7	232/189
n-Docosane/0.22	Graphite Powder/2–90	0.82	10	94.6/178.3
Stearic acid/0.3	Expanded Graphite/4-100	0.8	10	198.8/183.1
n-Octadecane/0.1505	Inorganic Silica Shell/1.3	0.6213	50	214.6/123
Stearic Acid/0.3	Carbon Fiber/190	0.62	10	198.8/184.6
Paraffin/0.31	Graphite Powder/2–90	0.46	12	133.1/90

Most of the studies in the literature are performed on an individual level, where the main focus of these studies was principally to increase the thermal conductivity of a PCM. Although some studies of cylindrical cells and the PCM with enhanced thermal conductivity are available in the literature, a detailed study of a prismatic cell with different arrangements is required. In addition, none of

these studies addresses the issue of dispersion instability of carbon nanoparticles due to agglomeration and deposition on the bottom surface with the passage of time.

3.4 Exergy Analyses of Battery Thermal Management Systems

Exergy analyses provide a better understanding of the efficiency and effectiveness of a BTMS and help to establish the areas where improvements are required. In the literature, examples of exergy analysis are very limited for BTMSs of EVs and HEVs. Javani et al. [120] completed an exergy analysis of an active conventional cooling system integrated with the PCM-based TESS. Exergy destruction at each component was calculated. The results show that exergy destruction is maximum at the compressor, followed by the evaporator and condenser. It was also observed that exergy efficiency of the system increases with an increase in the mass of the PCM. The exergy efficiency of the system increases by 5.04% with the use of the PCM compared to no PCM and the overall exergy efficiency of the developed system was 31%. The study does not include the use of PCM between the cells. Also, analysis of the effects of a change in coolant temperature on exergy destruction and exergy efficiency was not included.

A similar study was conducted by Hamut et al. [121], who performed an exergy analysis of each component in a thermal management system for the Li-ion battery. The results show that the exergy efficiency of the chiller thermal expansion valve is maximum and the evaporator has minimum efficiency. The overall exergetic coefficient of performance (COP) of the system was 0.32. Exergy destruction at each component is not discussed in this study, and the effect of parameters such as coolant temperature on exergy destruction or exergy efficiency were not included.

In another study [122], exergy analysis of a conventional BTMS was performed by considering different types of refrigerants. The authors studied five different refrigerants: R134a; dimethyl ether (DME); R1234yf (tetrafluoro propene); R600 (butane); and R600a (isobutane). The results show that the energetic and exergetic COP of the system is highest with dimethyl ether and environmental impacts are lowest. The authors also concluded that the rate of exergy destruction is highest at the compressor and lowest at the coolant pump, while the exergy efficiency of the evaporator thermal expansion valve is highest and lowest in the case of the condenser. Although

the study includes various refrigerants, it does not comment on the effect of variation in refrigerant temperature on exergy efficiency and COPs.

As previously observed, examples of the exergy analysis of BTMS are very limited and do not provide details about the effect of a change in coolant temperature on exergy destruction.

3.5 Optimisation of Battery Thermal Management Systems

Optimisation techniques are widely used in different fields. However, examples related to optimisation of BTMSs for EVs and HEVs are very limited.

Javani et al. [120] performed a multi-objective optimisation using a genetic algorithm, where the exergy efficiency of the PCM-based passive TESS integrated with BTMS is maximised, while the total cost of the system is minimised. The authors selected the genetic algorithm for optimisation due to its ability to find an optimal global solution or near optimal solution for almost any type of problem. The study was limited to TESS, and the optimum value of exergy efficiency and operational cost of the TESS obtained are 0.3351 and 1.529 \$/h, respectively.

In another study, Hamut et al. [92] completed a single and multi-objective optimisation of an HEV thermal management system using a genetic algorithm. The authors optimised the exergy efficiency, cost, and environmental impact, individually, and then performed exergoeconomic and exergoenvironmental optimisation. The results obtained from these optimisations are compared with the base case where no optimisation was performed. The result shows that through single objective optimisation, environmental impact and cost of BTMSs can be reduced by 10% and 19%, respectively, and exergy efficiency can be increased by 27%. In exergoeconomic optimisation, exergy efficiency of BTMSs can be increased by 14%, and the cost of the system can be reduced by 5%.

Both of these studies use a genetic algorithm for optimisation due to its capability to find a global or near optimal solution. Although these studies consider the various aspects of conventional BTMSs and the PCM-based TESS for optimisation, there is a lack of research related to the PCM-based passive BTMSs.

3.6 Main Gaps in the Literature

This section considers gaps in the literature and how the present research work will address these issues. From the literature, it was observed that only a few studies are available on pack level testing of the Li-ion battery and at high discharge rates. There is also a lack of experimental data related to the effect of liquid coolant temperature on capacity and the surface temperature of the battery. In this regard, pack level testing of the Li-ion battery (LiFePO_4) will be performed at different discharge rates using a liquid coolant at various temperatures. Variation in voltage, the surface temperature of the battery, and heat generation rate will be observed at various charge and discharge rates.

Studies show that PCMs can be used to manage Li-ion battery temperature. However, there is a lack of detailed experimental results of a PCM-based BTMS with prismatic Li-ion batteries. Most of the studies related to use of PCMs with Li-ion batteries are either experimental studies with cylindrical cells or a simulation of prismatic cells. In consideration of this fact, the PCM-based plates will be developed, and experiments will be performed using the Li-ion battery pack and developed PCM plates at various discharge rates.

Studies related to the use of PCMs as a BTMS do not reflect the effect of varying the thickness of a PCM layer on battery temperature. In most cases, PCMs are directly filled into a container having cylindrical cells and kept in a vertical position. The practical application of these studies to form an actual PCM-based BTMS is questionable due to various design issues. To address these issues, experiments with the Li-ion battery pack will be performed by varying the thickness of the PCM plates and observations will be made. Practical applications of developed system will be discussed.

It is important to increase the thermal conductivity of PCMs to increase their effectiveness as a passive BTMS. There exist individual studies that focus on improving the thermal conductivity of the PCM using various methods. However, experimental studies of a Li-ion battery with PCM with improved thermal conductivity are missing in the literature. Some of the studies in the literature suggest using CNTs with the PCM, as the results show a significant improvement in thermal conductivity of the PCM. However, studies show that CNTs start agglomerating once the PCM melts [14]. The various studies available in the literature do not tackle the issue of re-agglomeration. Therefore, a special technique will be used to disperse CNTs in the PCM and to

reduce re-agglomeration. PCM plates will be developed using CNTs and polyurethane, and experiments will be performed with developed plates at various discharge rates.

A detailed comparison of a conventional BTMS (liquid-based) with a PCM-based BTMS is missing in the literature. No data are available in the literature related to the application of commercially developed PCC plates with prismatic a Li-ion battery at different discharge rates. Therefore, a detailed comparison of various active (liquid-based) and passive (PCM-based) BTMSs will be conducted. Experiments will be performed with custom-made PCC plates to observe the variation in the battery pack temperature. Again, the thickness of PCC plates will be varied to observe the changes in the battery pack temperature.

Modelling and simulation are cost effective methods, and studies show that they often provide the required details of the system with reasonable accuracy. Therefore, a model will be developed and analysed in MATLAB Simulink, and simulation will be completed in ANSYS Fluent for the developed system. The developed model can be extended to the whole battery pack and can be utilised for various cooling conditions with minor modifications and input parameters.

There is no study in the literature related to the cost of a PCM-based BTMS. Limited studies are conducted in the literature to optimise the PCM-based BTMS. Although it is difficult to establish the actual cost of a PCM-based BTMS on an industrial scale due to the involvement of various factors and non-availability of reliable data, a cost analysis will be performed on a lab-scale. Optimisation techniques will be used to improve the developed system.

The overall objective of this study is to find best design conditions and parameters for the PCM-based passive BTMS. In the next chapter, details about various experiments will be provided.

Chapter 4. Experimental Setup

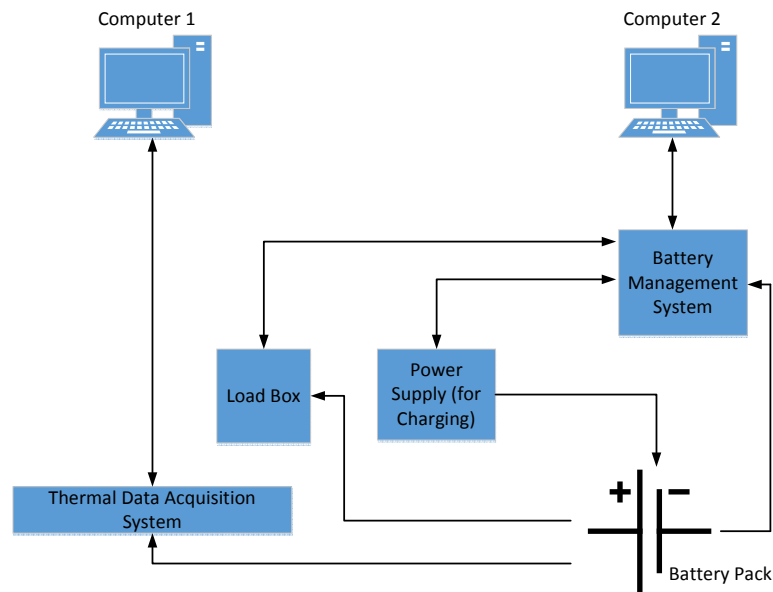
This chapter provides details about the experimental setups used in the thesis, including the instruments used, as well as the experimental plan and procedure. An experimental facility is built to test different battery packs at various discharge rates and boundary conditions. Experiments are conducted to obtain the temperature distribution, voltage variation and heat generation in the Li-ion battery pack at different operating conditions. Commercially developed PCC plates are integrated within battery pack to analyse their effects on voltage variation and temperature distribution. Plates with different combinations of PCMs, CNTs, and polyurethane foam are developed to improve the thermal conductivity of selected PCMs and to reduce the agglomeration effect in the CNTs. An experimental setup is developed to test the developed plates of the PCMs, CNTs, and polyurethane foam. Details of the microscopic study required to investigate the dispersion of nanoparticles in the PCM are also provided. Furthermore, experimental setups are developed to test the variation in internal resistance of the prismatic and cylindrical cells with a change in temperature and SOC.

4.1 Experimental Setups for Battery Pack Testing

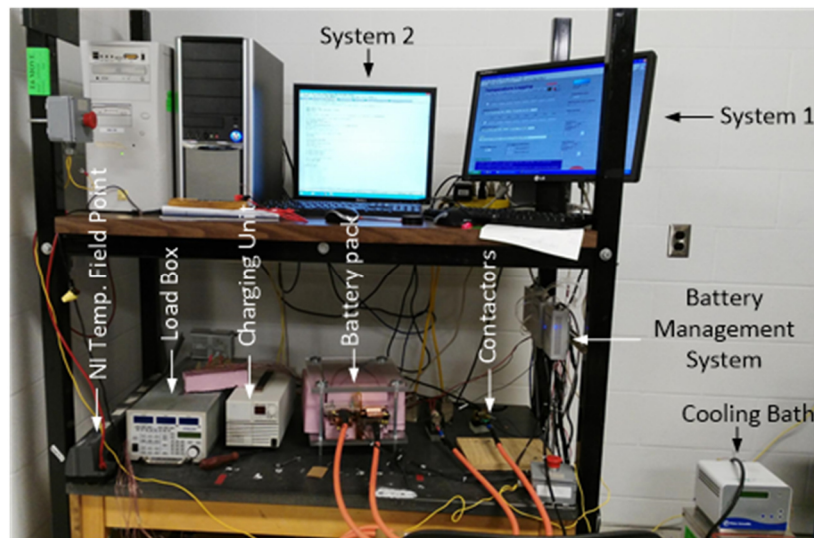
In the present study, two different test benches are used to test the battery pack due to various constraints. Figure 4.1 (a, b) shows the line diagram and actual setup of the first test bench that is used to test the battery pack. The test bench previously used for charging and discharging is modified according to the test requirements of the battery pack studied in this thesis. There are seven main components in the test bench: the load box, charging unit, battery management system (BMS), temperature measurement device, battery pack, computer 1, and computer 2. The description of these components is as follows:

T-type thermocouples, used to measure the temperature, are connected to National Instrument (NI) thermocouple input modules (FP-TC-120), which are connected to computer 1. LabVIEW 8.2 software is used to control and operate the NI temperature measurement device at computer 1. Computer 2 is used to measure the battery pack voltage, current, and SOC at one-second intervals through the BMS. The BMS is used for communication between the battery pack and computer 2, which sets the current or voltage values on the load box and power supply, depending on the experiment requirements. The BMS is connected to the load box and charging unit through a

controller, which opens/closes the circuit to charge or discharge the battery pack based on the given instructions. On the other hand, the BMS is also used to measure and control the voltage and current in the battery pack at every second. The current and voltage, measured internally at the load box and power supply, are transmitted back to computer 2.



(a)



(b)

Figure 4.1: Experimental setup 1; (a) line diagram, (b) actual setup.

Depending on the computer instructions, the power supply or load box provides power to or draws power from the battery pack. The BMS controls and balances the voltage and current

extracted/delivered from each cell in the pack. A XBL 50-150-800 Dynaload load box with a maximum capacity of 800 W is used to discharge the battery pack. TDK-Lambda power supply with a capacity of maximum 20 V and 40 A is used to charge the battery pack. Heavy duty copper cables are used to connect the battery pack with the load box and charging unit through a 100 A fuse and controller, operated through the BMS.

Figure 4.2 shows the second test bench used for experiments. The second test bench consists of five main components: an A & D cell cycler, a National Instrument (NI) temperature measurement device, a battery pack, and computer 1 and computer 2. The details of these components are as follows:

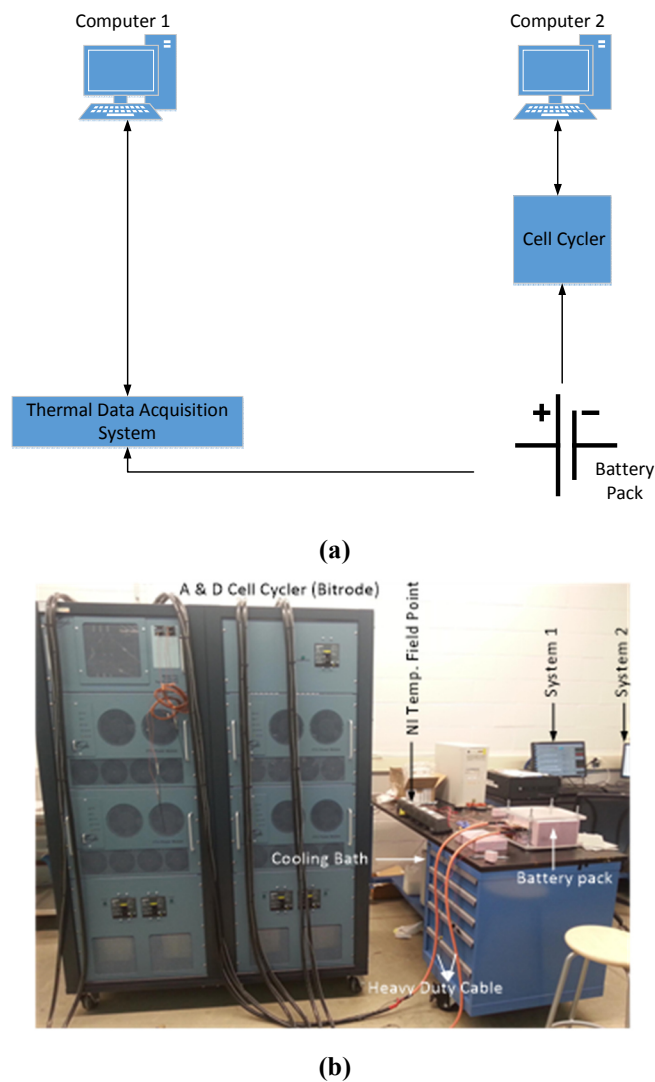


Figure 4.2: Experimental setup 2; (a) line diagram, (b) actual setup.

The arrangements of T-type thermocouples with the NI temperature measurement device are the same as in the case of test bench 1. The A & D cell cycler (Bitrode), with a maximum capacity to charge/discharge at 20V and 1200 A, is used to charge and discharge the battery pack. The cell cycler is controlled by computer 2 through VisuaLCN software. Heavy duty copper cables are used to connect the battery pack with the cell cycler. To charge and discharge the battery pack at different rates, a profile is created using a VisuaLCN program editor.

4.1.1 Prismatic Cell

In the present study, three 20Ah lithium-ion prismatic pouch cells (LiFePO_4) are used to form a battery pack. These cells are commonly used in EVs and HEVs due to their high energy density and low probability of thermal runaway at high temperatures. However, the Li-ion cells of other chemistries can also be used for the experiments. The selection of three cells and their arrangement in series is based on the capacity of the available charge-discharge unit. The pouch cell specifications are given in Table 4.1. Modified copper plates are used to connect the battery pack to the power source, voltage, and current sensing device.

4.1.2 Data Acquisition System

Three 8-channel thermocouple input modules (FP-TC-120) from the National Instruments are used to measure the temperature of the battery pack. One of the input modules is shown in Figure 4.3 (a). Figure 4.3 (b) shows the analogue input circuitry on one channel in the module. These three modules are connected through a terminal base to form a 24 channel thermocouple input module, as shown in Figure 4.3 (c). Each FieldPoint thermocouple input module has eight thermocouples or millivolt inputs. These modules have built-in linearization and cold-junction compensation for eight types of thermocouples (J, K, R, S, T, N, E, and B). These modules can operate from -40 to 70 °C.

To operate all three modules, a code is developed in LabVIEW software with a capability to measure and record the temperatures from all 24 thermocouples connected to the modules. A user interface is also created in LabVIEW software to observe the temperature and control the test, as shown in Figure 4.4. As previously discussed in section 4.1, a battery management system is used to measure and control the voltage and current in the circuit.

Table 4.1: LiFePO₄ 20Ah lithium-ion pouch cell specifications.

Parameter	Details
Type	Lithium Iron Phosphate
Cell Dimensions (mm)	$7.25 \times 160 \times 227$
Cell Weight (g)	496
Cell Capacity (minimum, Ah)	19.6
Energy Content (nominal, Wh)	65
Discharge Power (nominal, W)	1200
Voltage (nominal, V)	3.3
Specific Power (nominal, W/kg)	2400
Specific Energy (nominal, Wh/kg)	131
Energy Density (nominal, Wh/L)	247
Operating Temperature (°C)	-30 to 50
Cycle Life (Cycle)	> 500
Specific Heat (J/kg.K)	1027
Thermal Conductivity of Cell in x and y-Direction (W/m. K)	25
Thermal Conductivity of Cell in z-Direction (W/m. K)	1
Rate of Heat Generation (kW/m ³)	22.8
Density of Cell (kg/m ³)	4035
Max Discharge (SOC & Temperature Dependent) (A)	300
Max Charge (SOC & Temperature Dependent) (A)	300
Internal Resistance (mΩ)	0.5
Volume (L)	0.263
Cathode Material	LiFePO ₄
Anode Material	Graphite
Electrolyte	Carbonate-Based

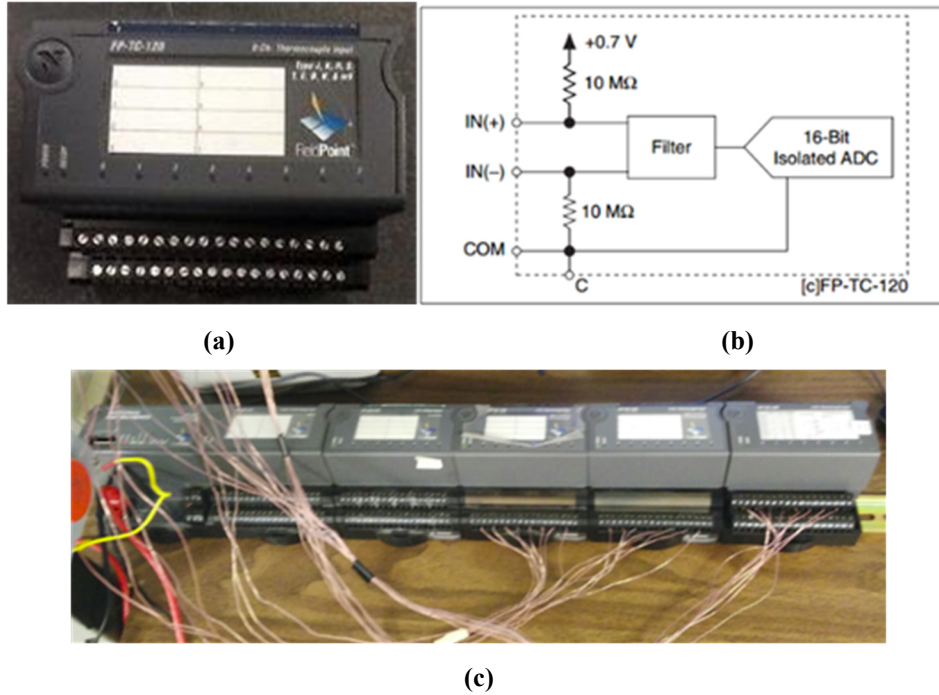


Figure 4.3: Thermal data acquisition system; (a) 8-channel thermocouple input module (FP-TC-120), (b) analogue input circuitry on one channel, (c) actual system with 3 modules and 18 thermocouples.

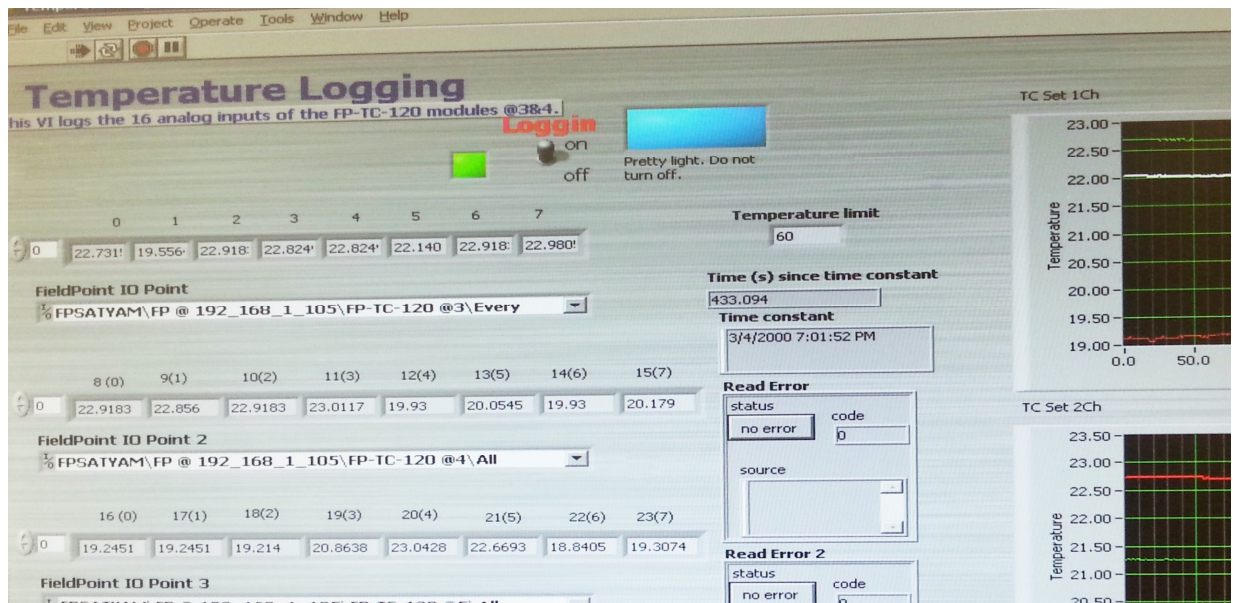


Figure 4.4: User interface developed in LabVIEW for thermal data acquisition.

4.1.3 Thermocouple Locations

To measure the temperature variation, a total of 18 thermocouples are installed on the principle surface of all three cells. T-type 30 gauge, special limits of error thermocouple wires with an

uncertainty of 0.5°C (according to the manufacturer's specifications) are used due to their low uncertainty and wide operating temperature range. Six thermocouples are installed on every cell, three on each side. From each the set of three thermocouples, the first thermocouple is placed near the cathode, the second near the anode, and the third at the mid-surface of the cell, as shown in Figure 4.5. The selection of three thermocouples on each side of a cell and their location is based on the temperature variation tests of a single cell and the limitation of available equipment. Tests are conducted on a single cell to check the variation in temperature across the cell surface. From the tests on the single cell, it is found that three thermocouples are enough to measure the temperature of the cell surface, with minor errors. The thermocouples are attached to the cell surface with a special thermal tape.

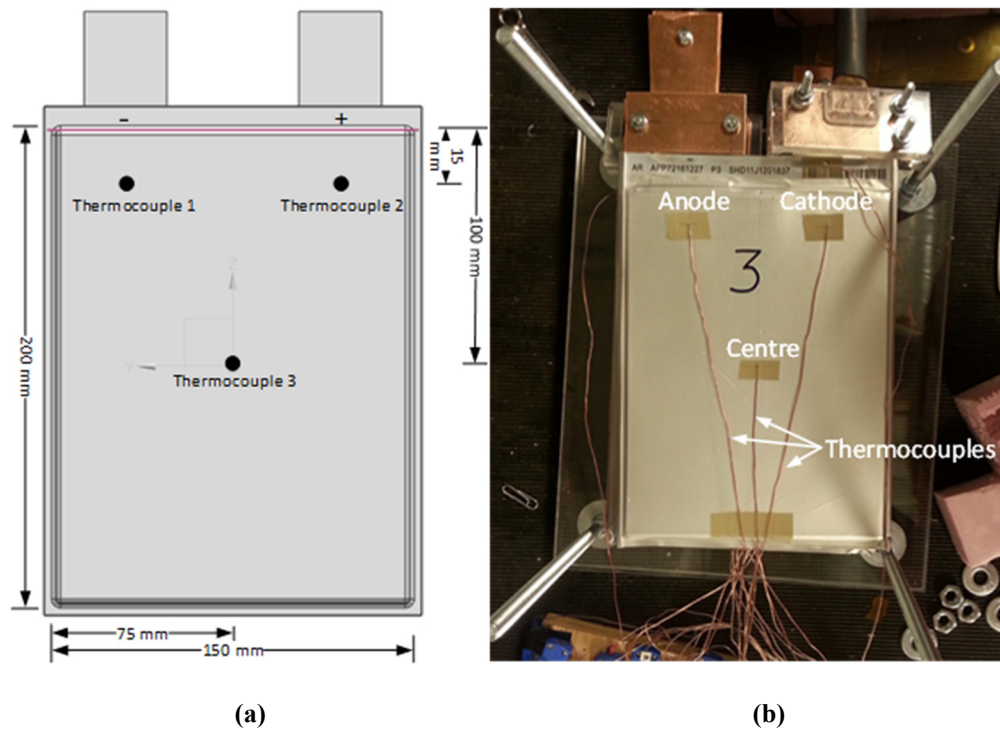
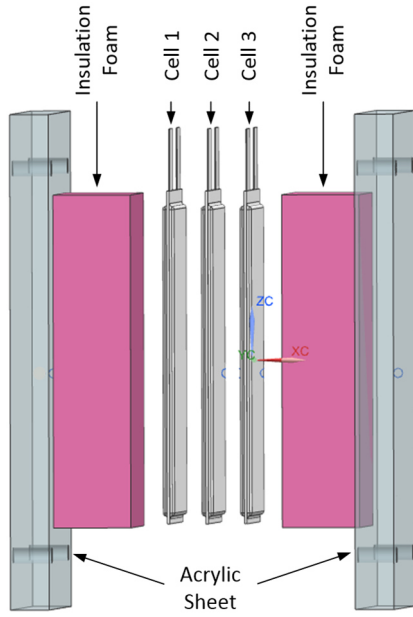


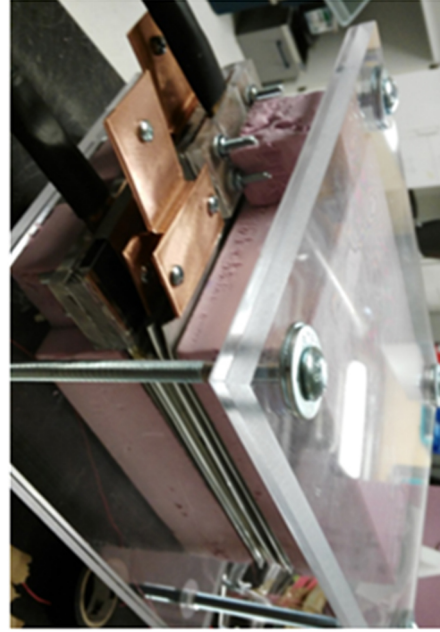
Figure 4.5: Thermocouple locations; (a) drawing with dimensions, (b) actual cell with the thermocouple.

4.2 Battery Pack with No Cooling

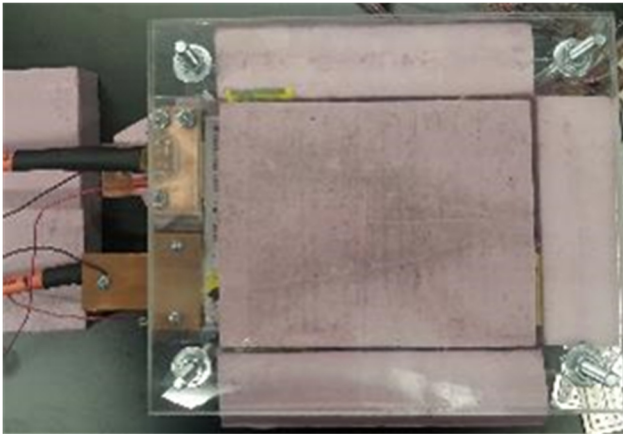
In EV applications, the battery system consists of a number of single cells connected either in series or parallel to achieve the power and capacity requirements. The battery pack, as shown in Figure 4.6, consists of three 20Ah LiFePO₄ cells electrically connected in series through copper plates.



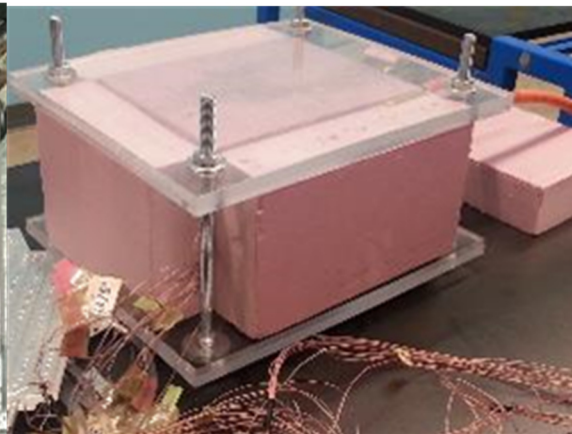
(a)



(b)



(c)



(d)

Figure 4.6: Arrangement of cells in the battery pack; (a) expanded view, (b) actual battery pack, (c) top view, (d) rear view.

Figure 4.6 (a) shows the expanded view of the battery pack created in a design software with no thermal management system. The actual battery pack without side and back insulation foams is shown in Figure 4.6 (b). Figure 4.6 (c, d) shows the top and side view of the complete battery pack. As explained in the previous paragraph, the battery pack is connected with T-type thermocouples, as well as with current and voltage sensors. In this study, each cell is experimentally characterised,

to predict the cell voltage and capacity during discharging and charging at an ambient temperature ($\sim 22^{\circ}\text{C}$). In all the experiments conducted, the cells are initially charged, then utilised until completely discharged.

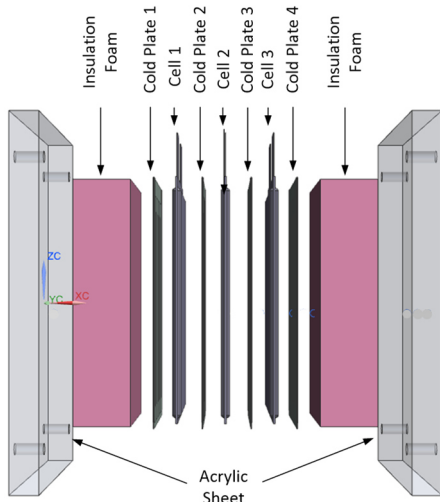
The three cells connected in series are enclosed between two-inch thick foam to provide insulation. The same foam is used on both sides and at the back to ensure proper insulation. To make a secure and tight connection, the cells along with the insulation foam are tightened between a 12 mm thick acrylic sheet by using $\frac{1}{2} \times 8$ -inch nuts and bolts.

4.3 Battery Pack with Conventional Liquid Cooling

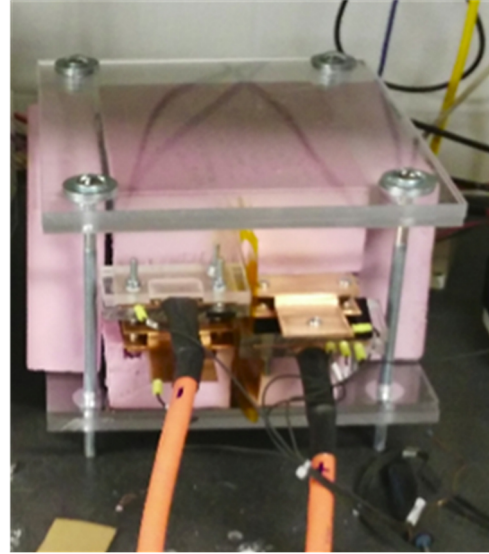
Four commercially available cold plates are selected for the present study to test the battery pack at various boundary conditions, using water as a coolant. The cold plates are placed at the top and bottom of a pouch cell (one on each side), with similar arrangements for the other cells. To prevent heat transfer to/from the surrounding environment, insulation is provided from all three sides of the Li-ion battery pack by using polystyrene. The battery pack and cooling plate arrangements are shown in Figure 4.7. Figure 4.7 (a) shows the expanded view of the battery pack created in a design software with cold plates. The front view of the actual battery pack is shown in Figure 4.7 (b). Figure 4.7 (c, d) shows the side and rear view of the battery pack.

4.3.1 Cold Plate

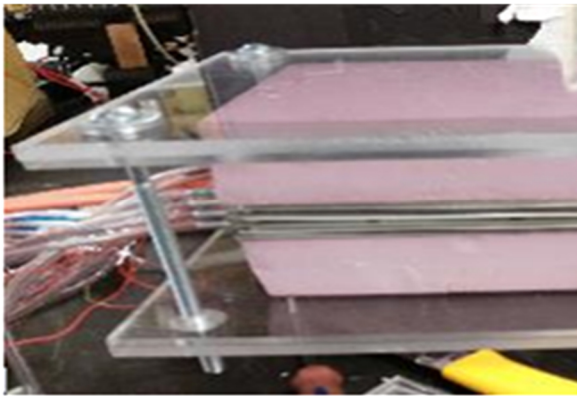
The cold plates used in the present study are manufactured using two stamped aluminium plates, joined through a nickel brazing process, as shown in Figure 4.8. Characterization of these “zig-zag turn” type cold plates is achieved through a single flow channel. These plates are commonly used in conventional BTMS of EVs and HEVs. Various thermophysical properties, such as specific heat, density and thermal conductivity of aluminium, are considered and given below in Table 4.2. Some corrections need to be applied for the thermal convection effect [51].



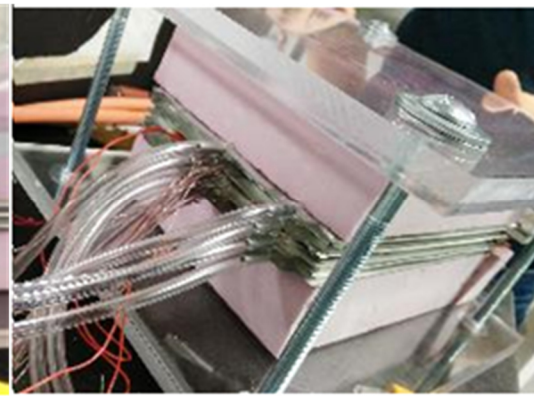
(a)



(b)



(c)



(d)

Figure 4.7: Battery pack arrangement with liquid cooling; (a) expanded view, (b) front view of the actual battery pack, (c) side view and (d) rear view.

Table 4.2: Cold plate parameters.

Parameter	Value
Material	Aluminium
Type	Zig-Zag Turn
Specific Heat (C_p)	871 J/kg K
Density (ρ)	2719 kg/m ³
Thermal Conductivity (K)	202.4 W/m K

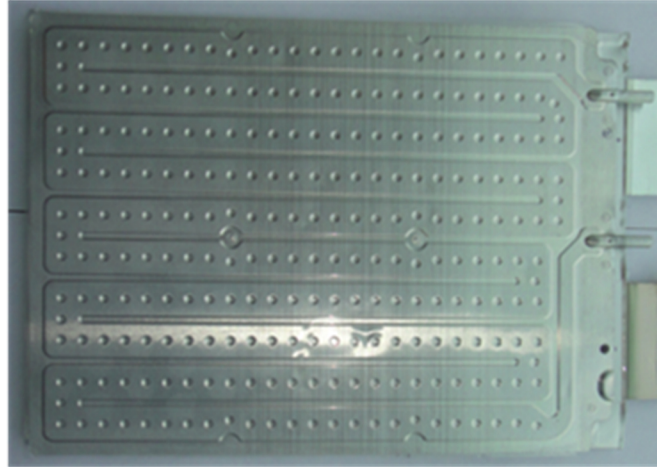


Figure 4.8: Aluminium cold plate used in experiments.

4.3.2 Battery Cooling System

The battery cooling system consists of four cooling plates (P1, P2, P3, P4) connected to a Fisher Scientific Isotemp 3016 fluid bath through tubes. Sensors are placed along the flow path to record the properties of the fluid. A schematic of the system is shown in Figure 4.9 (a). The fluid bath is capable of ensuring a constant inlet temperature of the coolant. The cooling plates are compressed against the principal surfaces of all three cells through an acrylic sheet, such that the heat generated within the cells is principally removed by conduction to the surfaces of the cooling plates.

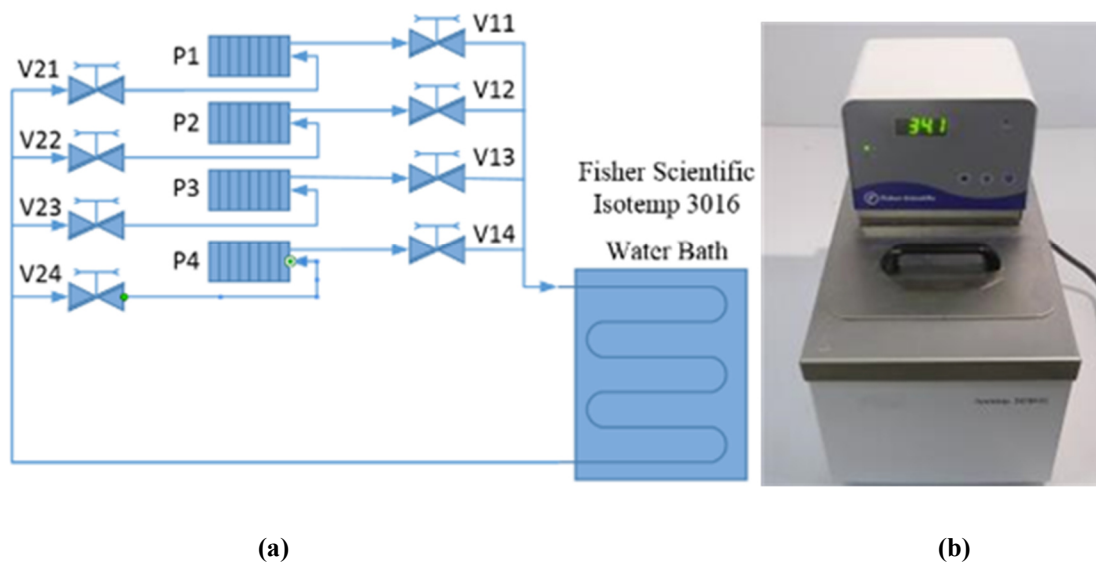


Figure 4.9: Battery liquid cooling system; (a) line diagram of cooling system along with cold plates and valves, (b) actual cooling system.

4.4 Battery Pack with Phase Change Composite Material

For the present study, custom made phase change composite (PCC) material plates with different thicknesses are used to develop the passive thermal management for the battery pack. These PCC plates are rigid and can hold the load of the cells even beyond the melting point of the PCM inside these plates. The composite material remains solid even at extremely high temperatures, and nothing leaks out from the plates. The battery pack with no cooling system is modified, and four PCC plates are placed between the cells. Figure 4.10 (a) shows the exploded view, and Figure 4.10 (b) shows the actual battery pack with PCC plates.

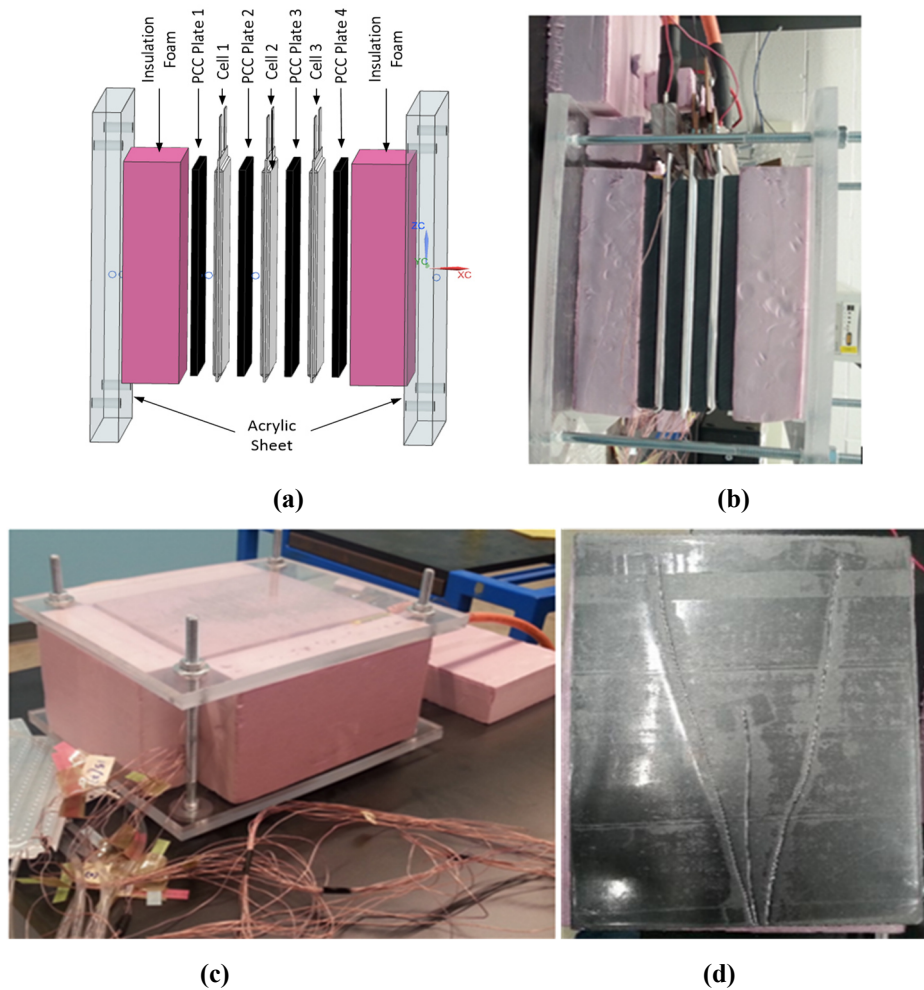


Figure 4.10: Battery pack with PCC plates; (a) expanded view, (b) actual setup, (c) actual setup with all side insulation, (d) PCC plate.

Figure 4.10 (c) shows the side view of the battery pack with PCC plates. One of the PCC plates used in the battery pack is shown in Figure 4.10 (d). One PCC plate is placed on the top side of

cells and one on the bottom side. The same arrangement is used in the other two cells, as shown in Figure 4.10. Again, to ensure proper insulation, two-inch thick insulation foam is placed on the top, bottom and sides of the battery pack. PCC plates with three different thicknesses (6, 9, and 12 mm) are used for the present study. The selection of the thickness of the PCC plates is based on a study conducted in the literature [54] and according to availability. The dimension of each PCC plate is 200×150 mm.

4.4.1 Phase Change Composite Material

The phase change composite is a commercially developed material that is a combination of the PCM and graphene [Figure 4.10 (d)]. Graphene is used to increase the thermal conductivity of PCM. Out of three different options for the type of PCC, as given in Table 4.3, PCC37 is selected for the present study because its melting point is nearest to an optimal operating temperature of the Li-ion cells. The melting point of the selected PCC is 37°C with a latent heat of 160 J/g. The length and width of the PCC plates are kept the same as those of the cell (200×150 mm).

Table 4.3: Properties of different type of PCC materials.

Specification	PCC37-1000	PCC48-1000	PCC55-1000	Detail
Melting Point (°C)	37	48	55	
Melting Range (°C)	32 – 38	45 – 50	48 – 57	
Density (kg/m³)	895	890	875	Room Temperature
Thermal Expansion - Solid Phase (%/°C)	0.1	0.074	0.146	Measured from Room Temperature to Melting Onset
Thermal Expansion During Melting (%/°C)	0.841	0.839	0.494	Measured during Melting
Thermal Expansion - Liquid Phase (%/°C)	0.075	0.051	0.075	Measured after Melting to 75°C
Thermal Conductivity (W/m K)	10 – 25	10 – 25	10 – 25	XY-Plane
	6 – 12	6 – 12	6 – 12	Z-Plane
Latent Heat (J/g)	160	170	165	
Specific Heat (J/g K)	1.91	1.82	1.96	Specific Heat-Solid
	2.25	1.96	2.2	Specific Heat-Liquid
Electrical Resistance (10⁻³ Ωm)	0.41	0.33	0.37	XY-Plane
	0.19	0.14	0.16	Z-Plane
Thermal Cycle Life (Number of Cycle)	>10,000	>10,000	>10,000	Number of Melting Cycles

4.5 Battery Pack with Phase Change Materials

A passive thermal management system is developed using phase change materials. A pure and technical grade of n-Octadecane PCM is selected for the study. An open cell, non-rigid polyurethane foam is used to absorb the PCM and form PCM plates. As the selected polyurethane foam is non-rigid and incapable of holding the weight of the cells after PCM starts melting, a special experimental setup is developed.

To hold the weight of the cells and avoid leakage, a cavity is made by using 3 mm and 6 mm thick and 20 mm wide gaskets around the periphery of all three cells. The inactive area of the cell cover is sandwiched between the gasket and used as a main support to handle the weight of the cell. A special double-sided tape, capable of handling high temperatures, is used to attach the gasket to the periphery of the cell. Silicon glue is used inside the cavity to fill the gap and form leak-proof joints. Solid PCM and foam plates are placed inside these cavities with a similar arrangement as in the case of PCC plates. The bottom cell cavity is sealed using a gasket with dimensions 3×190×240 mm, while a similar sized gasket is placed on the top cell cavity. Figure 4.11 shows the step-by-step process of assembling the battery pack. Cell 1 at the bottom, having a cavity on both sides, is placed over the insulation foam and PCM plates are placed inside the cavities, as shown in Figure 4.11 (a). Cell 2 is then placed over cell 1 and the PCM plates are placed inside the cavity [Figure 4.11 (b)]. The steps for cell 2 are repeated for cell 3 [Figure 4.11 (c)]. As previously explained, the top cell (cell 3) is sealed with a 3 mm thick gasket [Figure 4.11 (d)] and, again, an insulation foam is placed over the gasket [Figure 4.11 (e)]. All the three cells, along with insulation foam, are tightened using nuts, bolts and an acrylic sheet, as shown in Figure 4.11 (f).

4.5.1 Selection of Phase Change Material

Selection of the type of a PCM is critical from an application point of view. In the present study, n-Octadecane PCM is selected by considering the optimum operating temperature of the battery and latent heat of a PCM. The melting point of a PCM depends on the purity of the material. Based on the literature and as provided by the manufacturer, the melting of pure n-Octadecane is 28°C. Two types of PCMs are used in the present study: pure and technical grades of n-Octadecane. Pure n-Octadecane is 99% pure, while technical grade is 90% pure. The cost of technical grade n-

Octadecane is significantly lower than pure. Therefore, both pure and technical grade n-Octadecane are selected for experiments in order to find the better option.

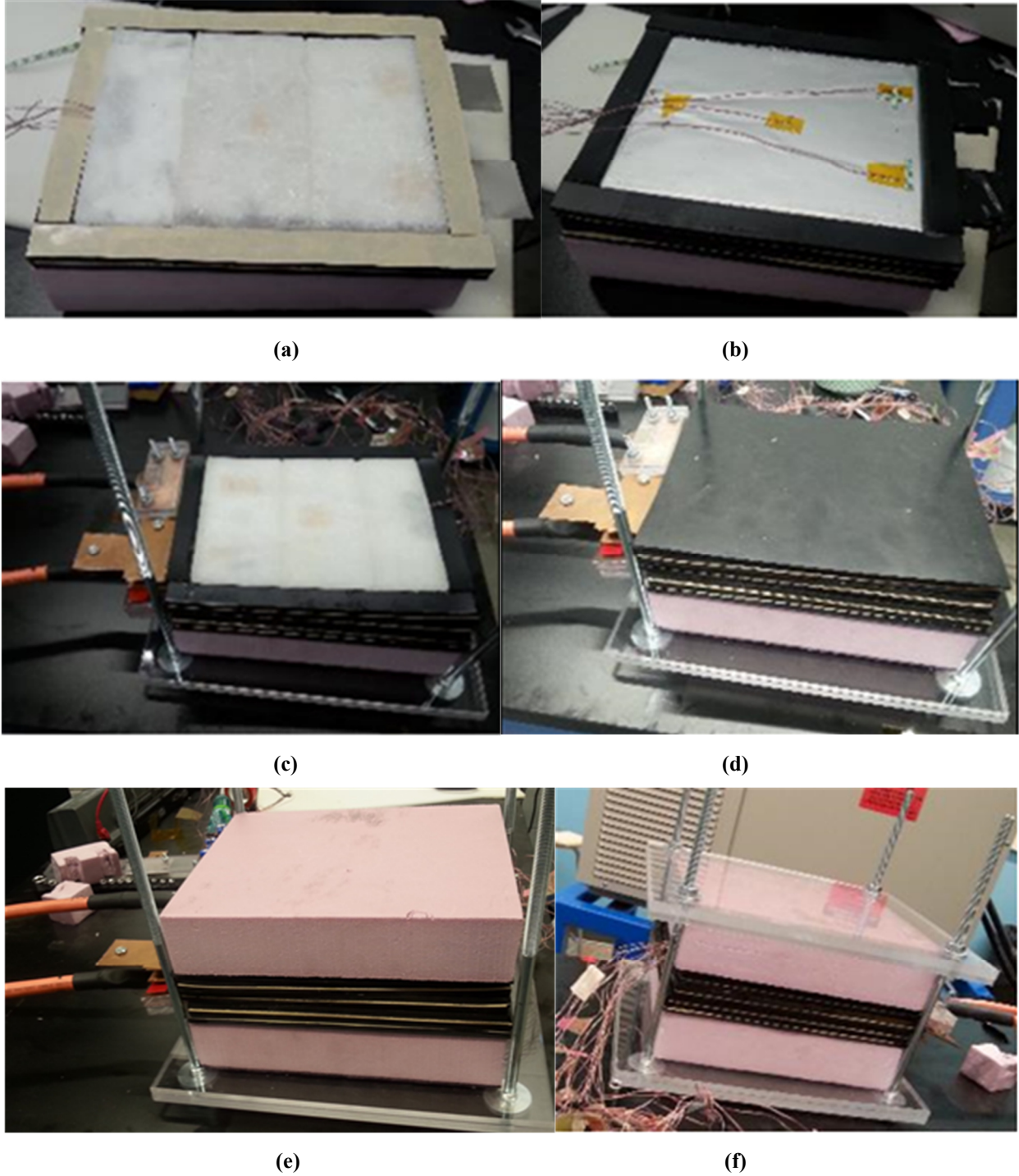


Figure 4.11: Step by step process of assembling the prismatic battery pack with the PCM cooling jacket.

The various properties of the pure and technical grades of the selected PCM are given in Table 4.4. The type of PCM can be changed according to the operating temperature of the battery and melting point of the PCM. The melting temperature of the PCM should be close to the optimum operating temperature of the battery.

Table 4.4: Properties of the selected PCMs.

Parameter	Pure n-Octadecane	Technical Grade n-Octadecane
Purity (%)	99	90
Melting Point (°C)	28.2	28
Boiling Point (°C)	316.7	317
Density (kg/m ³)	778.8	778.8
Heat of Fusion (J/g)	243.5	230
Thermal Conductivity (W/m K)	0.083	0.083

4.5.2 Selection of Foam

The foam used with a PCM in the battery pack needs to be lightweight and have higher thermal stability, longer life, and high porosity. A polyurethane foam with these properties was selected for the present study. The foam is used to disperse CNTs in the PCM and keep them in their place when the phase change process occurs. Although various methods are available to disperse CNTs into PCMs, these methods are not capable of avoiding re-agglomeration. For the present study an open cell, non-rigid polyurethane foam is selected. The properties of selected polyurethane foam are given in Table 4.5.

Table 4.5: Properties of open cell polyurethane foam.

Parameter	Value
Name	Polyurethane
Type	Non-Rigid
Specific Heat (J/kg K)	1500
Thermal Conductivity (W/m K)	0.083
Density (kg/m ³)	22.43
Porosity (%)	96.9

The porosity of the foam is calculated based on the density and volume of foam. As shown in Figure 4.12, a roll of 3 mm thick foam [Figure 4.12 (a)] and a sheet of 6 mm thick foam [Figure 4.12 (b)] is used to prepare the foam plate. Several 3 mm thick plates with dimension 75×152 mm are made from the 3 mm thick roll, as shown in Figure 4.12 (c). Similarly, several 6 mm thick plates with dimension 200×152 mm are made from the 6 mm thick sheet, as shown in Figure 4.12 (d).

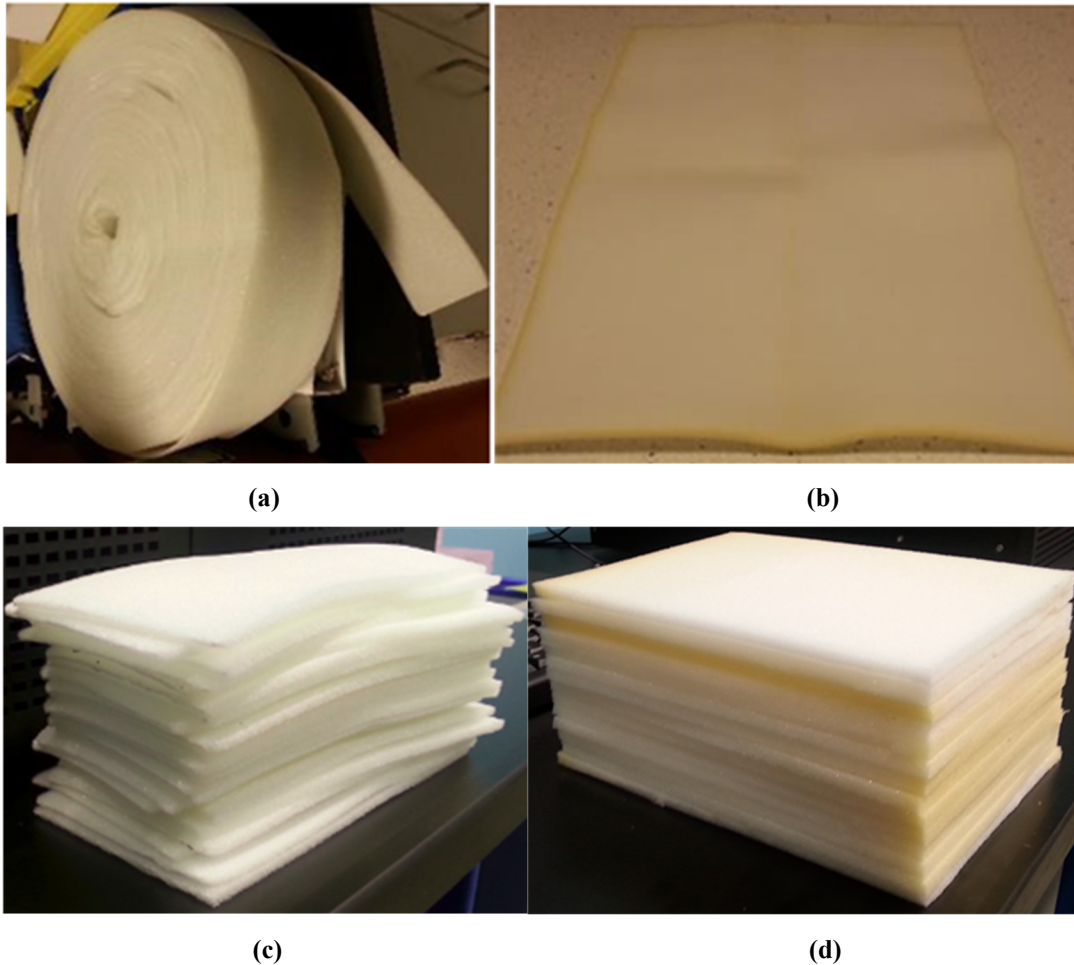


Figure 4.12: Open cell polyurethane foam; (a) roll for 3 mm thick foam, (b) sheet of 6 mm thick foam, (c) 3 mm thick plates, (d) 6 mm thick plates.

4.5.3 Phase Change Material Plates

A process is developed to prepare plates of the PCM and polyurethane foam. A weighting unit, specially developed steel trays with covers, a thermal chamber, cooling bath and Porex glass tube are used to make the PCM plates.

4.5.4 Trays to Prepare Plates

Three precise steel trays, along with their covers, are made using a plain 1 mm thick steel plate, as shown in Figure 4.13. These trays are used in making the PCM and polyurethane foam plates. Two holes are made in each plate for the extra material to pour out from these holes. The dimensions of the tray used to make the 6 mm thick PCM and foam plate is $200 \times 152 \times 15$ mm with 5 mm diameter holes exactly 6 mm above the bottom surface. Two different trays are made to make the 3 mm thick PCM and foam plate due to dimension constrained. The dimension of the first tray is $75 \times 152 \times 15$ mm and the second tray is $55 \times 152 \times 15$ mm with 5 mm diameter holes exactly 3 mm above the bottom surface. Figure 4.13 (a) shows the three different trays made from steel and Figure 4.13 (b) shows the polyurethane foam placed inside the trays. To ensure the equal distribution of the PCM and the thickness of the PCM and foam plate, a 1 mm thick cover for each tray is made [Figure 4.13 (c)]. Figure 4.13 (d) shows all three trays along with the polyurethane foam and covers.

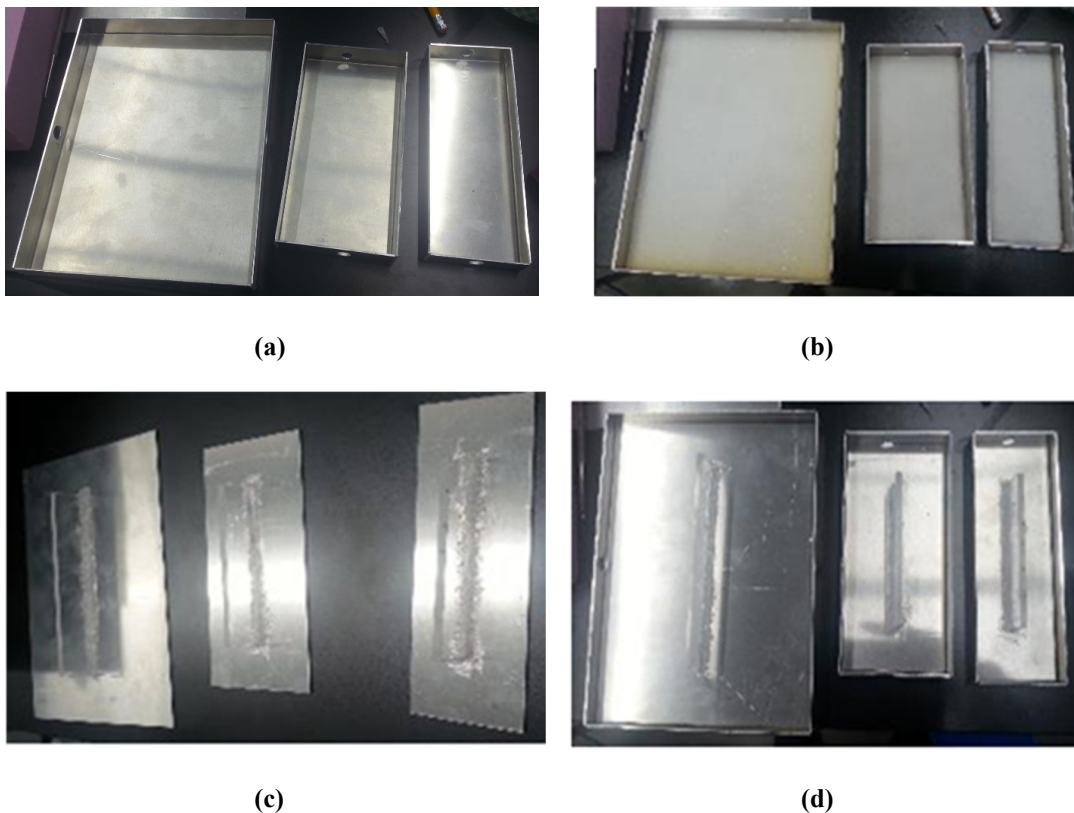


Figure 4.13: Custom made tray for making samples; (a) tray, (b) tray with foam samples, (c) tray cover, (d) tray with foam and cover.

4.5.5 Procedure to Make Phase Change Material Plates

Both pure and technical grades of n-Octadecane are used to make the 3 mm and 6 mm thick PCM and foam plates. The following steps are taken to prepare the plates:

1. The thermal chamber temperature is set to 60°C.
2. PCM in a container is placed inside the thermal chamber where it remains until it completely melts and the temperature reaches approx. 60°C.
3. Based on volume calculations for the specific plate, melted PCM is poured into a Porex beaker.
4. The PCM in the beaker is poured over the foam placed in the respective tray, as shown in Figure 4.14.
5. The respective cover is placed over the tray for equal distribution of the PCM in the foam.
6. The tray is then placed in the cooling chamber and the PCM is allowed to solidify.
7. The PCM and foam plate is removed from the tray after it is completely solidified.
8. Steps 2 to 7 are repeated for both pure and technical grades of the PCM in order to prepare the required number of 3 mm and 6 mm thick plates.

Figure 4.14 (a-c) shows the PCM plates of different dimensions prepared using developed steel trays.

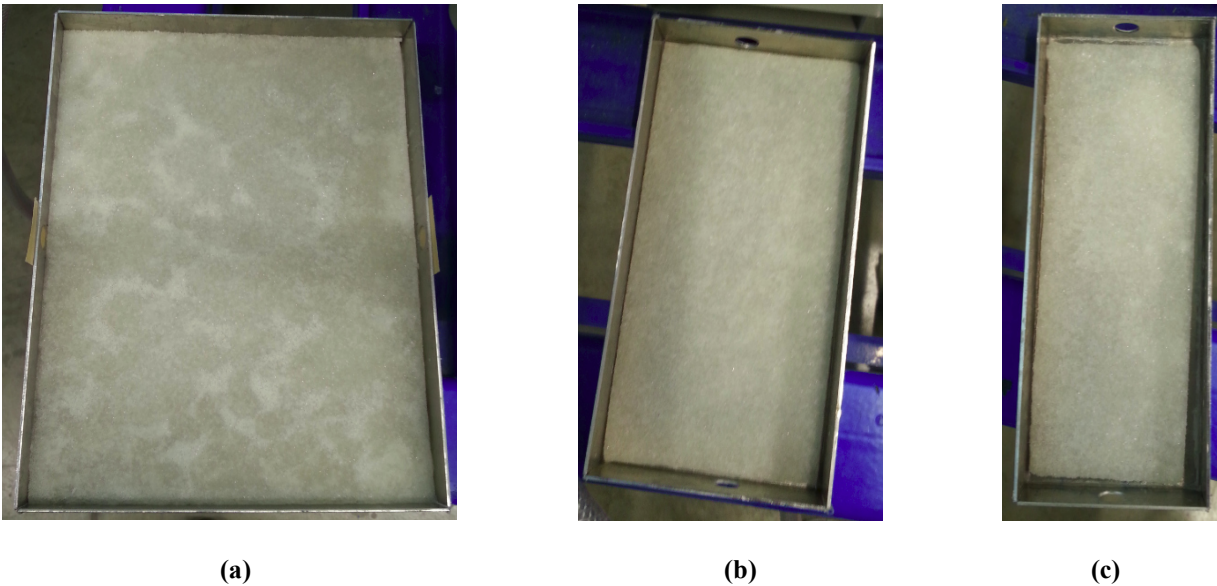


Figure 4.14: Foams after soaking in the PCM; (a) 200×152×6 mm, (b) 75×152×3 mm, (c) 55×152×3 mm.

The weight of foam is measured before and after the PCM is poured; Table 4.6 provides the dimensions of the various foams and their weight with and without the PCM.

Table 4.6: Polyurethane foam dimensions and their weight with and without PCM.

Sample	Foam Thickness (mm)	Dimension of Foam (Length × Width (mm))	Surface Area of Foam (mm ²)	Mass of Foam (g)	Mass of Foam After Soaking in PCM (g)	Mass of PCM Absorbed (g)
1	3	75 × 152	24162	0.834	26.034	25.2
2	3	75 × 152	24162	0.834	26.034	25.2
3	3	55 × 152	17962	0.6177	18.8577	18.24
4	6	200 × 152	65024	4.604	139.604	135

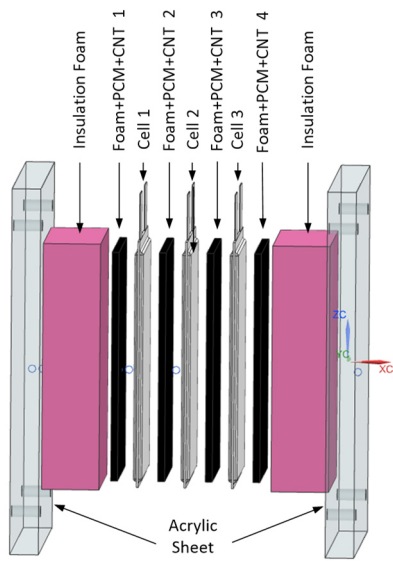
4.6 Battery Pack with Phase Change Materials and Carbon Nanotubes

The low thermal conductivity of PCMs limits its application in battery thermal management due to the high melting and solidification time. As earlier discussed in Chapter 3, various researchers have conducted substantial research to improve the thermal conductivity of PCMs [71]. Studies show that carbon nanotubes have very high thermal conductivity and can be added to PCMs to improve its thermal conductivity. Although the thermal conductivity of CNT material is very high, it is associated with the agglomeration effect. In this study, polyurethane foam is used to disperse the CNTs in PCM. Two different mass concentrations (1.5% and 3%) of CNT material are used in the present study along with both pure and technical grades of n-Octadecane. The experimental setup previously used with PCM and foam plates is modified, and the PCM plates are replaced with the PCM and CNT plates. Figure 4.15(a-d) shows the step-by-step process of assembling the battery pack with PCM and CNT plates. Figure 4.15 (a) shows the expanded view of the battery pack created in a design software with plates made from PCM and CNTs. Figure 4.15 (b, c) shows the actual battery pack while assembling and Figure 4.15 (d) shows the complete battery pack.

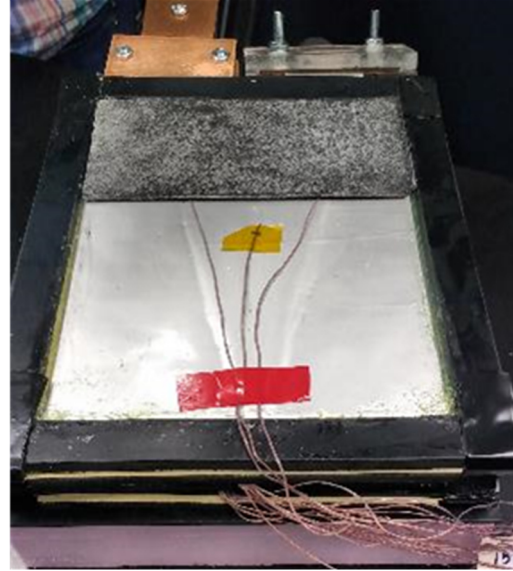
4.6.1 Carbon Nanotubes

In the present study, multi-walled carbon nanotubes are used with pure (99% purity) and technical grades (90.8%) PCM with a mass concentration of 1.5% and 3%. For concentrations greater than 10%, the mixture becomes less viscous, and the latent heat of fusion of the mixture decreases. The corresponding properties of CNTs are [123, 124]:

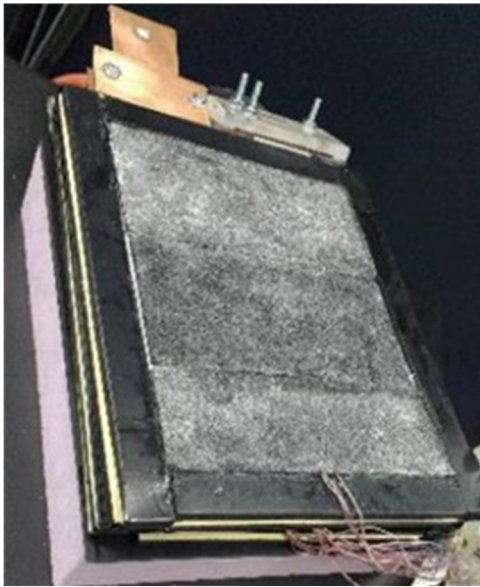
- Outer diameter: 50-80 nm
- Length: 10-50 μm
- Purity: >95 wt %



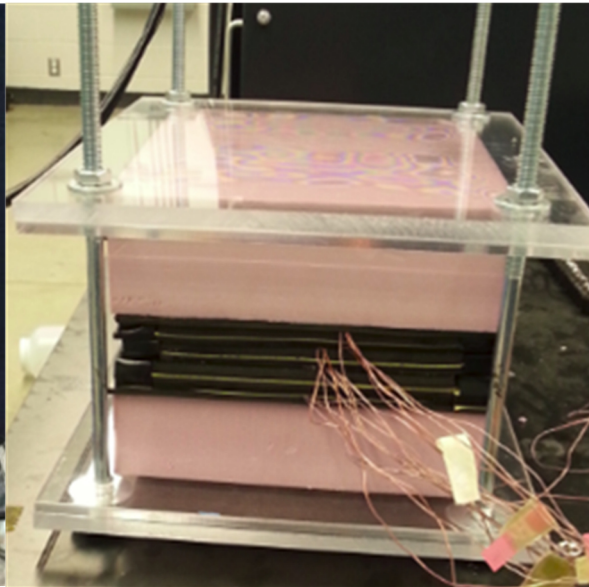
(a)



(b)



(c)



(d)

Figure 4.15: Battery pack with the PCM and CNT plates; (a) expended view, (b-c) actual battery pack while assembling, (d) complete battery pack.

4.6.2 Plates of Phase Change Materials and Carbon Nanotubes

A special process is developed to prepare the PCM and CNT plates along with the foam. CNTs are mixed with technical grade and pure n-Octadecane in different mass concentrations. The required amount of CNTs is calculated, and measurements are performed using highly accurate weighing machines. An ultrasonic water bath is used to properly disperse the nanotubes in the PCM, as shown in Figure 4.16 (a). The advantage of the ultrasonic method is the prevention of an agglomeration of nanoparticles during the phase change process. By increasing the elapsed usage time of the ultrasonic device, the thermal conductivity of the mixture also increases due to better alignment of the CNTs in series with increased elapsed time, as the thermal conductivity of CNTs is very low in parallel. The prepared samples [Figure 4.16(b)] are also used for optical microscopic studies.

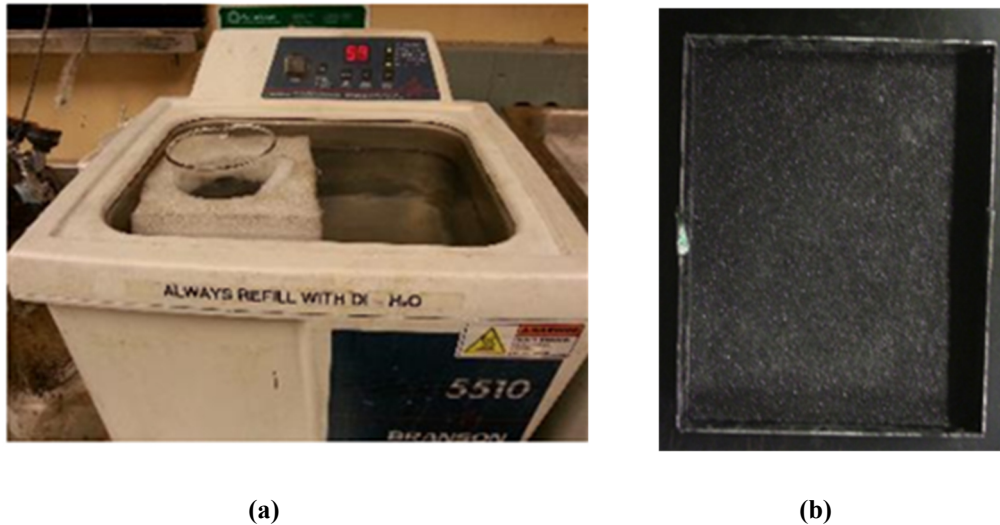


Figure 4.16: Preparation of the PCM and CNT mixture; (a) ultrasonic water bath, (b) 6 mm thick plate of PCM and CNTs in the tray.

The following steps are taken to prepare the plates:

1. After weight measurement, the PCM and CNTs are mixed in a beaker and placed in an ultrasonic water bath at a temperature of 60°C.
2. The trays used in preparing the PCM plates and Porex tubes are kept inside a thermal chamber at 60°C.

3. Based on the calculation, half of the amount of mixture required to prepare one plate is poured onto a hot plate and the foam is carefully placed in the tray to absorb the mixture equally.
4. Once the foam properly absorbs the mixture, it is removed from the tray and the other half of the mixture is poured onto the plate.
5. Again, the foam is carefully placed in the tray from the other side to absorb the mixture.
6. The respective cover is placed over the tray for equal distribution of mixture in the foam.
7. The tray is then placed in a cooling chamber and the mixture is allowed to solidify.
8. The PCM and CNT plates are removed from the tray after the mixture completely solidifies.
9. Steps 2 to 7 are repeated for both pure and technical grades of the PCM along with 1.5% CNT and 3% CNT to prepare the required number of 3 mm and 6 mm thick plates.

4.7 Experimental Procedure for Prismatic Battery Pack Testing

Experiments with the battery pack are performed with five different options: No Cooling; With Cold Plate; with PCC; with PCM; and with a combination of the PCM and CNTs. An open cell polyurethane foam is used along with the PCM and a combination of the PCM and CNTs. These five options are further classified into various combinations, as shown in Figure 4.17. To test the battery pack, four different temperatures are selected: 10°C, 20°C, 30°C, and 40°C. The selection of these temperatures are made on the basis of ambient temperature and melting point of PCC and PCM: below ambient temperature (10°C); at ambient temperature (20°C); above ambient temperature and near to melting point of PCM (30°C); and above melting point of PCM and PCC (40°C). Although all these tests are performed above the freezing point of water, further studies can be conducted at a sub-zero temperature by using a refrigerant or by adding an antifreeze solution to water. The sequence of experiments is shown in Figure 4.17.

The battery pack is charged and discharged at constant current. Four different discharge rates, i.e. 1C, 2C, 3C, and 4C, are selected to examine the effect of discharge rate on the electrical and thermal performance of the battery pack. The selection of discharge rates is based on the maximum discharge rates in the standard drive cycle. Charging is conducted at 1C for all four discharging cases. The selection of charging rate is based according to battery manufacturer guidelines and the

charging capacity of the cell cycler. The maximum charging voltage is fixed to 3.65 V, while the minimum discharge voltage is 2.0 V for each cell. As all three cells are connected in series, the maximum charging voltage for the battery pack is fixed to 10.95 V, while the minimum discharge voltage is 6.0 V.

The discharge current with respect to each discharge rate is presented in Table 4.7. A profile with several charge and discharge cycles is developed in VisuaLCN and used for all experiments. A rest period is provided in between the charge and discharge cycle to make sure that the temperature of the battery reaches close to the initial value before the next discharge cycle starts. For consistency, a similar approach is used for all other cooling options. In the case of no cooling, experiments are performed at room temperature.

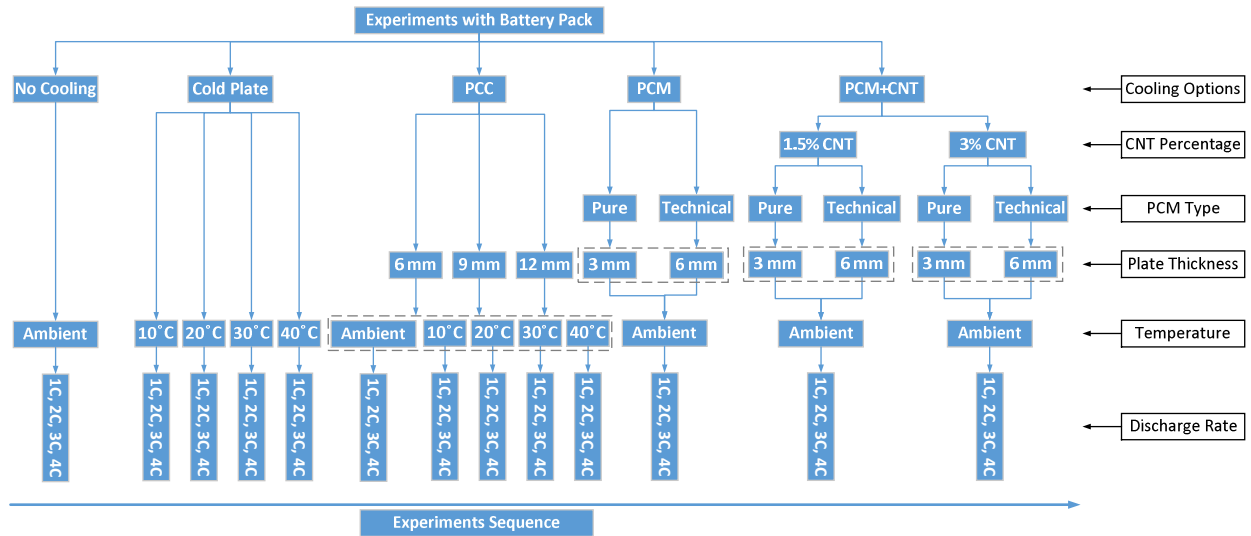


Figure 4.17: Experimental plan for prismatic battery testing.

Table 4.7: Selected discharge and charge rates along with respective currents and minimum/maximum voltages.

Discharge Rate	Constant Discharge Current (A)	Minimum Discharge Voltage (V)	Charge Rate	Constant Charge Current (A)	Maximum Charge Voltage (V)
1C	20	6	1C	20 A	10.95
2C	40				
3C	60				
4C	80				

The procedure given below is followed to initiate the battery pack cycling and thermal data collection. The procedure does not describe the steps for assembling the battery pack. This procedure assumes that the cell and all other components during the test are properly installed and fully connected to the other components as required. The general procedure, as followed during all tests with all options, is as follows:

1. The profile created in computer 2 using VisuaLCN, which includes several charge and discharge cycles along with a rest period in between, is loaded in VisuaLCN software. The following relevant test parameters are included in the program:
 - a. Charge current
 - b. Discharge current
 - c. Charge and discharge period
 - d. Rest period
 - e. Number of cycles
 - f. Drive cycle (charge and discharge cycle)
 - g. Maximum voltage at the end of the charge cycle
 - h. Minimum voltage at the end of the discharge cycle
 - i. Measurement sample time
2. The thermal data acquisition modules (FP-TC-120) connected to computer 1 are switched on through LabVIEW software and allowed to initialize through the user interface. The surface temperature of all three cells in the battery pack are recorded in computer 1 as a text file.
3. The charge-discharge test unit and thermal data acquisition system are activated at the same time so that charging/discharging and data acquisition begin simultaneously.
4. The test continues until the desired number of battery cycles is completed.
5. From each test, two text files are created:
 - a. Thermal data
 - b. Electrical charge-discharge data

In the case of cold plates, few additional steps are required other than installing the cold plate. To ensure a steady state temperature of the battery pack and cold plate, the Isotemp 3016 fluid bath is

started a minimum two hours before the test starts. The valves leading to the cold plates are observed and set to open. The mass flow rate of the coolant is measured through each cold plate. Equal mass flow rate of the coolant is ensured through each cold plates by adjusting the valves. The isothermal fluid bath is set to the desired cooling temperature or boundary conditions of 10°C, 20°C, 30°C, and 40°C for the test.

4.8 Microscopic Test for Carbon Nanotube Distribution

An optical microscope is used to identify the distribution of CNT particles in the foam along with PCM, as shown in Figure 4.18. Samples (1×1 inch) are made from 3 mm and 6 mm thick plates having various combinations of the PCM, CNTs, and foam. An optical microscope with a capacity of 1000 times magnification is used to study the structure and distribution of CNT particles. The samples are placed in the testing area, and a high-intensity beam of light is used to heat the samples. The variation in structure during melting and solidification is recorded.

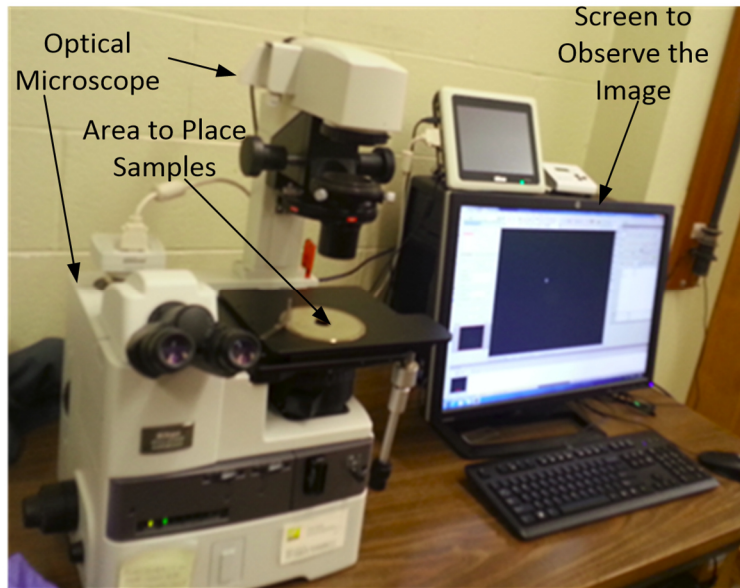


Figure 4.18: Optical microscope used for tests.

4.9 Resistance Measurement of Prismatic Li-ion Cell

A123 20Ah cell is characterised using a BioLogic VMP3B-100 multi-channel potentiostat. Open-circuit voltage curves are estimated by a C/25 charge and discharge cycle. Figure 4.19 shows the experimental setup for the internal resistance measurement of the prismatic cell.

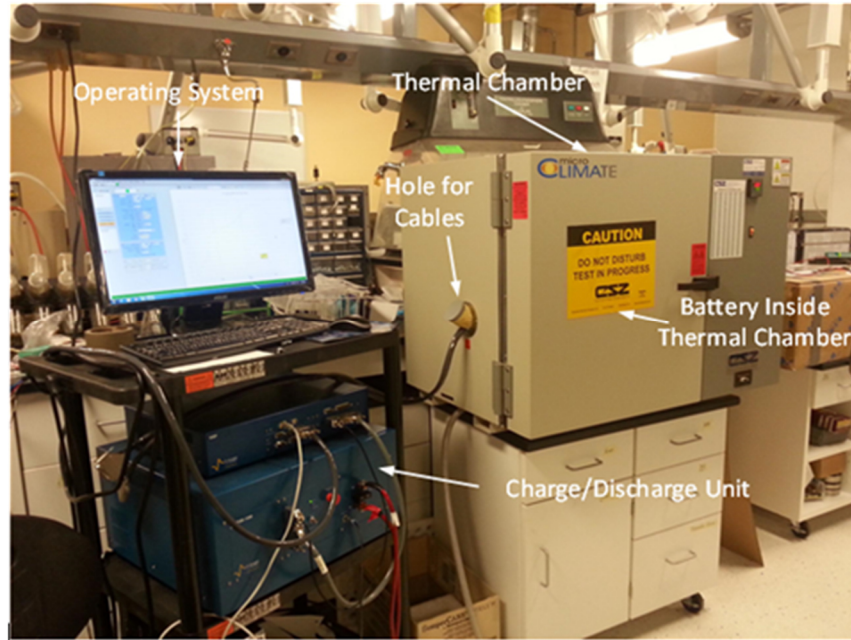


Figure 4.19: Experimental setup for internal resistance measurement of the prismatic cell.

The circuit parameters for the equivalent circuit model employed are estimated based on hybrid pulse power characterization (HPPC). HPPC procedure is followed: i.e. 1C (20A) discharge for 10 s, followed by 40 s of rest, ending with a 10 s 3C/4 (15A) charge. The HPPC test is performed at 10% intervals in SOC, from 90% to 10% SOC. A CSZ MicroClimate chamber is used to maintain the temperature of the cell during the HPPC test in order to estimate resistance under different conditions. The test is conducted at 10°C, 20°C, 30°C, 40°C, 50°C and 60°C. The discharge time between pulses to reach the next lowest SOC value is six minutes long at 1C discharge rate. An hour of rest follows each of these discharges to ensure that the battery's temperature is equilibrated at the ambient temperature before each pulse. It is assumed that the battery's internal temperature does not change during the HPPC test, due to the low current and very short time.

4.10 Resistance Measurement of Cylindrical Cell

NCR18650B cells, which are used in EVs and HEVs due to high energy density, are selected for the present study. A battery pack of seven NCR18650B cylindrical cells is used to measure internal resistance. The experimental setup for the cylindrical cells is shown in Figure 4.20. All the cells are initially characterised using a BioLogic VMP3B-100 multi-channel potentiostat. Open-circuit voltage curves are estimated by a C/25 charge and discharge cycle. The circuit parameters for the equivalent circuit model employed are estimated based on hybrid pulse power characterization

(HPPC). The experimental setup consists of four main components: an A & D cell cycler; a CSZ micro climate chamber; a cylindrical battery pack; and a computer.

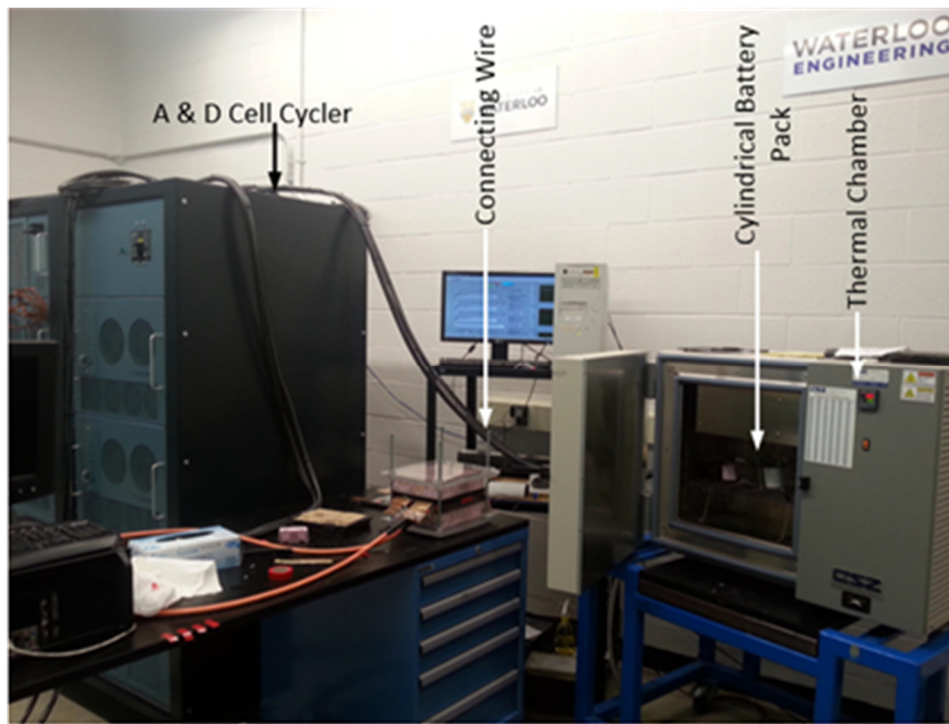


Figure 4.20: Experimental setup for internal resistance measurement of the cylindrical cell.

The battery pack is connected to the A & D cell cycler and controlled and operated through a computer. An HPPC profile is created in VisualCN software editor. A similar approach is adopted to test the cylindrical battery pack as in the case of resistance measurement of the prismatic cell. The HPPC procedure is as follows: 1C (23.8A) discharge for 10 s, followed by 40 s of rest, ending with a 10 s 3C/4 (17.85A) charge. The HPPC test is performed at 10% intervals in SOC, from 90% to 10% SOC. Again, a CSZ micro climate chamber is used to maintain the temperature of the cell during the HPPC test in order to estimate the resistance at different conditions. The temperatures selected are -10°C, 0°C, 10°C, 20°C, 30°C, 40°C, 50°C and 60°C.

4.10.1 Experimental Setup for Cylindrical Cell

Seven NCR18650 cylindrical cells are connected in parallel through a custom-made circular copper plate, as shown in Figure 4.21. The specification of the cylindrical cell is given in Table 4.8. A cell holder is 3D-printed, as shown in Figure 4.21 (a).

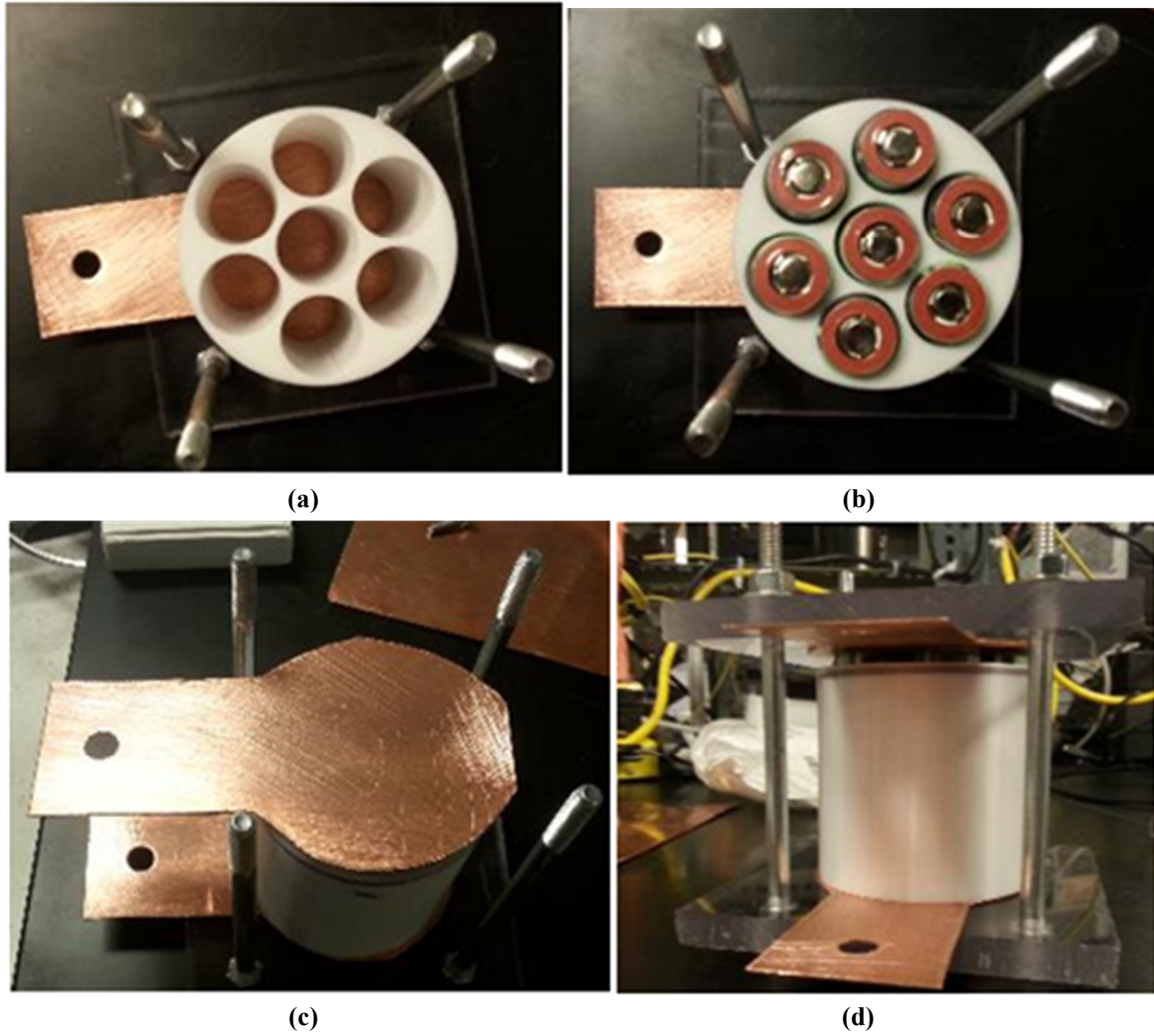


Figure 4.21: Step by step process of assembling the cylindrical cell to form a battery pack.

Table 4.8: NCR18650B, 3400mAh cylindrical cell specification.

Parameter	Details
Brand Name	NCR18650B
Cell Dimensions (mm)	70 × 18 × 18
Cell Weight (g)	49
Cell Capacity (minimum, Ah)	3.2
Voltage (nominal, V)	3.7
Gravimetric Energy Density (Wh/kg)	243
Volumetric Energy Density (Wh/L)	676
Operating Temperature (°C)	-30 - 55
Cathode Material	Nickel Oxide-based

All the cells are placed in the designed cavities inside the holder [Figure 4.21 (b)] and copper plates are placed on the top and bottom of the cells [Figure 4.21 (c)]. The cells, along with the copper plates, are sandwiched between two acrylic sheets and bolted to make secure connections.

4.11 Experimental Plan for Resistance Measurement of Prismatic and Cylindrical Cells

The increase the internal resistance has an adverse effect on battery capacity. Tests are performed on cylindrical and prismatic cells at various temperatures and SOC in order to observe the effect on internal resistance.

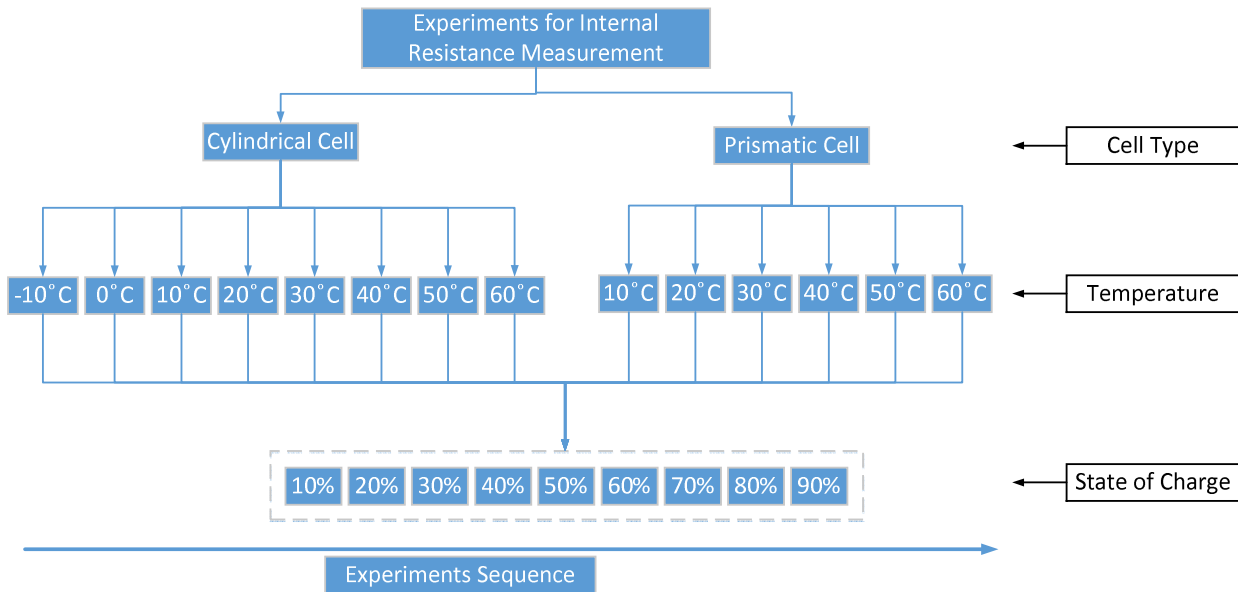


Figure 4.22: Experimental plan for internal resistance measurement of cylindrical and prismatic cells.

For both cylindrical and prismatic cells, the test is performed at 90% to 10% SOC with an interval of 10%. The ambient temperature selected for the study varies from -10°C to 60°C at an interval of 10°C. Figure 4.22 shows the experimental plan for internal resistance measurement of the cylindrical and prismatic cells. The data from these tests will be used to develop a model to understand the behaviour of the battery pack.

4.12 Uncertainty Analysis

It is almost impossible to obtain 100% accuracy in experimental results due to the involvement of various types of errors, including instrumental, observation, and calculation errors. Therefore, it is

very important to locate and calculate these uncertainties. In this section, the uncertainties in experimental measurements and derived correlations are presented.

4.12.1 Uncertainty in Temperature and Heat Generation

In this section, uncertainty in the surface temperature of the cell and the total heat generated in the battery pack is calculated.

4.12.1.1 Uncertainty in Average Temperature Measurement

The average surface temperature of the battery pack is calculated as follows:

$$T_{surf} = \frac{\sum(T_{ij}A_{ij})}{A_{total}} \quad (4.1)$$

where $A_{ij} = lw$. l and w are the length and width of the battery. T is the temperature of the battery at any point. The subscripts i and j represent a particular thermocouple. To find the uncertainty in the measurement of battery temperature, the uncertainty in average battery temperature and area measurements are required. These uncertainties are calculated as follows:

a) Surface Temperature, T_{ij}

The battery surface temperature is measured using T-type thermocouples through 8-channel thermocouple input modules. As provided by the manufacturer, the value of uncertainty in thermocouple reading is less than 1°C. The uncertainty in thermocouple reading is given in Equation 4.2.

$$\frac{\delta T}{T} = \pm \frac{1^\circ\text{C}}{T[^\circ\text{C}]} \quad (4.2)$$

b) Area, A_{ij}

An electronic digital Vernier calliper, having a resolution of 0.005 mm, is used to measure the positions of the thermocouples installed on the principle surface of the battery pack. Equation 4.3 is used to calculate the uncertainty area.

$$\frac{\delta A}{A} = \pm \left\{ \left(\frac{\delta l}{l} \right)^2 + \left(\frac{\delta w}{w} \right)^2 \right\}^{1/2} \quad (4.3)$$

Let us consider that $P_{i,j}$ represents the individual average surface temperature of the battery ($T_{ij}A_{ij}/A_{total}$) to calculate average surface temperature. Error in individual $P_{i,j}$ is calculated using Equation 4.4.

$$\frac{\delta P_{i,j}}{P_{i,j}} = \pm \left\{ \left(\frac{\delta T_{ij}}{T_{ij}} \right)^2 + \left(\frac{\delta A_{ij}}{A_{ij}} \right)^2 + \left(\frac{\delta A_{total}}{A_{total}} \right)^2 \right\}^{1/2} \quad (4.4)$$

Equation 4.5 is used to obtain the relative uncertainty in average surface temperature of the battery. The absolute error in the battery surface temperature is found to be maximum at the lowest temperature. Therefore, relative uncertainty is also maximum at the lowest temperature. The values of relative uncertainty and absolute error are shown in Table 4.9.

$$\frac{\delta T_{surf}}{T_{surf}} = \pm \left\{ \left(\frac{\delta P_{1,1}}{P_{1,1}} \right)^2 + \left(\frac{\delta P_{1,2}}{P_{1,2}} \right)^2 + \dots + \left(\frac{\delta P_{5,1}}{P_{5,1}} \right)^2 \right\}^{1/2} \quad (4.5)$$

Table 4.9: Relative and absolute uncertainty in battery surface temperature at four operating temperatures.

Operating Temperature (°C)	± Relative Uncertainty (%)	± Absolute Uncertainty (°C)
10	15.5	0.7
20	1.2	0.4
30	1.3	0.5
40	0.6	0.5

4.12.1.2 Heat Generation Uncertainty

Equation 4.6 is used to calculate the uncertainty in total heat generated, which is a combination of different components such as sensible, cooling and environmental heat.

$$\frac{\delta Q_{gen}}{Q_{gen}} = \pm \left\{ \left(\frac{\delta Q_{sen}}{Q_{sen}} \right)^2 + \left(\frac{\delta Q_{cooling}}{Q_{cooling}} \right)^2 + \left(\frac{\delta Q_{env}}{Q_{env}} \right)^2 \right\}^{1/2} \quad (4.6)$$

where Q_{gen} is total heat generated in the battery. Q_{sen} is sensible heat stored in the battery pack in the form of increase in temperature. $Q_{cooling}$ is heat transferred to the coolant and Q_{env} is heat lost

to the surroundings. Similarly, uncertainty in the rate of total heat generation is obtained using the following equation:

$$\frac{\delta \dot{Q}_{gen}}{\dot{Q}_{gen}} = \pm \left\{ \left(\frac{\delta \dot{Q}_{sen}}{\dot{Q}_{sen}} \right)^2 + \left(\frac{\delta \dot{Q}_{cool}}{\dot{Q}_{cool}} \right)^2 + \left(\frac{\delta \dot{Q}_{env}}{\dot{Q}_{env}} \right)^2 \right\}^{1/2} \quad (4.7)$$

4.12.1.3 Uncertainty in Sensible Heat

The calculation of sensible heat is based on the average surface temperature, specific heat, and mass of the battery. The specific heat and mass of the battery is provided by the manufacturer and assumed to be correct. Uncertainty in sensible heat is calculated using Equation 4.8.

$$\frac{\delta Q_{sen}}{Q_{sen}} = \pm \frac{\delta \Delta T_{surf,avg}}{\Delta T_{surf,avg}} \quad (4.8)$$

The uncertainty in the rate of sensible heat accumulation is calculated by:

$$\frac{\delta \dot{Q}_{sen}}{\dot{Q}_{sen}} = \pm \left\{ \left(\frac{\delta \Delta T_{surf,avg}}{\Delta T_{surf,avg}} \right)^2 + \left(\frac{\delta \Delta t_{disch}}{\Delta t_{disch}} \right)^2 \right\}^{1/2} \quad (4.9)$$

a) Uncertainty in Surface Temperature Difference

The uncertainty in average surface temperature differences in the battery is calculated using Equation 4.10.

$$\frac{\delta \Delta T_{surf,avg}}{\Delta T_{surf,avg}} = \pm \left\{ \left(\frac{\delta T_{surf,avg}}{T_{surf,avg}} \right)^2 + \left(\frac{\delta T_{surf,avg}}{T_{surf,avg}} \right)^2 \right\}^{1/2} \quad (4.10)$$

b) Discharge Time

As previously discussed, the charge and discharge bench is controlled by Labview software; therefore, calculation of discharge time is based on Labview output. The uncertainty in discharge time is considered equal to the time interval in measurements, which is 1 second. Equation 4.11 is used to calculate the uncertainty in discharge time.

$$\frac{\delta \Delta t_{disch}}{\Delta t_{disch}} = \pm \frac{1 \text{ sec}}{\Delta t_{disch}} \quad (4.11)$$

4.12.1.4 Uncertainty in Heat Removed by Cold Plates

The generated heat from the battery pack is rejected to the fluid through cold plates. Therefore, the amount of heat removed depends on the temperature difference between the inlet and outlet temperature of the coolant, the specific heat of the coolant and the mass flow rate of the coolant. Equation 4.12 is used to calculate the uncertainty in heat removed by cold plates.

$$\frac{\delta Q_{cool}}{Q_{cool}} = \pm \left\{ \left(\frac{\delta \dot{m}}{\dot{m}} \right)^2 + \left(\frac{\delta \Delta T}{\Delta T} \right)^2 + \left(\frac{\delta \Delta t_{disch}}{\Delta t_{disch}} \right)^2 \right\}^{1/2} \quad (4.12)$$

where \dot{m} is mass flow rate of the coolant and ΔT is the difference between the inlet and outlet temperature of the coolant. Similarly, Equation 4.13 is used to calculate the uncertainty in the rate of sensible heat accumulated.

$$\frac{\delta \dot{Q}_{cool}}{\dot{Q}_{cool}} = \pm \left\{ \left(\frac{\delta \dot{m}}{\dot{m}} \right)^2 + \left(\frac{\delta \Delta T_w}{\Delta T_w} \right)^2 \right\}^{1/2} \quad (4.13)$$

a) Flow Rate Uncertainty

As previously discussed, a Fisher Scientific Isotemp 3016 fluid bath is used to circulate the cooling fluid through the cold plate. The volumetric flow rate of the cooling fluid is measured with the help of Microtherm FS1 30-300 mL/min flow meters. The manufacturer provides the instrument's uncertainty equal to 6% on the full scale, which is ± 18 mL/min. The same uncertainty is obtained from Equation 4.14.

$$\frac{\delta \dot{m}}{\dot{m}} = \pm \frac{18 \text{ mL/min}}{\dot{m} [\text{mL/min}]} \quad (4.14)$$

b) Fluid Temperature Difference

Equation 4.15 is used to calculate the uncertainty in the inlet and outlet temperature difference of the cooling fluid at the cold plate. The uncertainty in the measurement of the inlet or outlet temperature of the fluid is equivalent to the uncertainty given in Equation 4.2. Table 4.10 provides a summary of uncertainty for different parameters.

$$\frac{\delta \Delta T_w}{\Delta T_w} = \pm \left\{ \left(\frac{1 \text{ }^\circ\text{C}}{T_{w,i} [^\circ\text{C}]} \right)^2 + \left(\frac{1 \text{ }^\circ\text{C}}{T_{w,o} [^\circ\text{C}]} \right)^2 \right\}^{1/2} \quad (4.15)$$

Table 4.10: Summary of uncertainties for various parameters.

Variable	Range	Temperature (°C)	± Relative Uncertainty (%)
$T_{i,j}(\text{°C})$	10°C – 56.5°C	–	2.1% - 15.5%
$T_{avg}(\text{°C})$	10°C – 44.5°C	–	0.48 % - 28.5%
$Q_{sen} \text{ (J)}$	2950 J – 59200J	10	30.2 %
		20	3.45 %
		30	1.49 %
		40	1.20 %
$\dot{Q}_{sen} \text{ (W)}$	0.82 W – 65.6 W	10	30.2 %
		20	3.45 %
		30	1.49 %
		40	1.20 %
$\dot{m} \text{ (mL/min)}$	300 mL/min – 360 mL/min	–	7.2% - 12.5%
$\Delta T_w(\text{°C})$	0.1°C – 4.3°C	–	0 % – 23.8%
$Q_{gen} \text{ (J)}$	9320 J – 59200 J	20	35.5 %
$\dot{Q}_{gen} \text{ (W)}$	2.59 W – 65.6 W	20	35.5 %

Chapter 5. Modelling, Analysis and Optimisation Methods

In order to conduct a numerical analysis of the system in MATLAB, ANSYS or any other software, a mathematical model, which incorporates the physics of the problem, input variables, and relationship between these parameters, is required. The model should have governing equations and their respective valid range of variation with initial and boundary conditions. Furthermore, such a model is required to achieve the determined objectives by assigning constraints for the problem and defining the corresponding methodology. Validation of simulation results with experimental data is essential. Therefore, in this chapter, a model is developed to investigate the behaviour of the Li-ion batteries at various discharge rates. Various parameters such as battery temperature, voltage, heat generation rate, and the state of charge, are calculated. An ANSYS model is developed to obtain a temperature profile across the cell with the PCM plates. Energy and exergy efficiencies are defined to better understand the developed system. A preliminary cost analysis of the existing conventional BTMS and the developed system is performed. An objective function is developed to maximise the driving range of the vehicle using optimisation techniques.

5.1 Battery Pack Modelling using MATLAB Simulink

Based on the information obtained from experiments conducted in present study on the Li-ion battery pack, a battery model is developed in MATLAB. The obtained data from the experiment is integrated into a look-up table, and a MATLAB code is used to access this look-up table. In the developed model, the battery voltage is measured by using an input current draw. Current and voltage together provide an estimation of the required power from the system. Four major battery parameters are calculated from the developed model: i.e. internal resistance, voltage, temperature, and heat generation rate.

The heat generation inside a cell takes place mainly due to the internal resistance of the cell and change in entropy [125-127]. Various parameters can affect the cell temperature, such as Joule heating, mixing effects, electrochemical reactions and possible phase change inside the cell. Such a general energy balance equation to calculate the rate of heat generation from a battery is given below [90]:

$$\dot{q} = I \left(V_{ocv} - V_a - T \frac{dV_{ocv}}{dT} \right) = h_s (T - T_a) + M_A C_p \frac{dT}{dt} \quad (5.1)$$

where h_s is the heat transfer coefficient per cell. M_A is the mass of the cell per unit area and C_p is the weight-averaged specific heat of the cell. The term $I(V_{ocv} - V_a)$ is the heat generation rate due to cell polarization, and $IT \frac{dV_{ocv}}{dT}$ is the entropy coefficient due to reversible processes in the cell. Equation 5.1 shows that the heat generated in the cell includes heat generation due to Joule's heating or Ohmic heating, and heat generation due to change in entropy because of electrochemical reactions. Equation 5.1 can be further simplified to:

$$\dot{Q} = I^2 R - T \Delta S \left[\frac{I}{n F} \right] \quad (5.2)$$

where I is the current, R is the resistance, ΔS is the change in entropy, n is the number of electrons, and F is Faraday's constant. Equations 5.1 and 5.2 are most commonly used to calculate heat generation rate. Heat generation rate in the battery can also be obtained through a calorimetry test.

In the present thesis, data collected from the HPPC tests is used to build the Thevenin equivalent circuit model shown in Figure 5.1. The Thevenin model uses an open-circuit voltage (OCV) and a series resistor (R_1) to model the bulk of battery behaviour, and the RC-pair (R_2 and C) to model transient effects [128]. The OCV in the model is correlated to SOC based on the C/25 discharge rate data. The circuit parameters, R_1 , R_2 , and C , fit to the data with a genetic algorithm, and good fits are obtained at all temperatures and SOC values. The output voltage of the battery (V_L) is estimated based on the current (I) according to Equations 5.3 to 5.5.

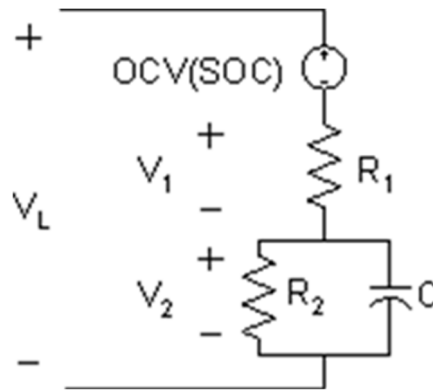


Figure 5.1: Thevenin equivalent circuit model for battery along with RC-pair.

$$V_{sim} = OCV(SOC) - V_1 - V_2 \quad (5.3)$$

$$V_1 = IR_1 \quad (5.4)$$

$$\frac{dV_2}{dt} = -\frac{V_2}{R_2C} + \frac{I}{C} \quad (5.5)$$

In the developed model, the heat generation rate in the battery pack (\dot{Q}_{gen}) is estimated according to Equation 5.6.

$$\dot{Q}_{gen} = I|V_1 + V_2| - IT \frac{dV_{OCV}}{dT} \quad (5.6)$$

The first term in Equation 5.6 is known as Joule's heating and is responsible for most of the heat generation. The second term is known as irreversible heat loss and is estimated according to a lookup table from Forgez et al. [129]. The rate of heat loss to the environment (\dot{Q}_{loss}) is estimated by a simple approach based on Newton's law of cooling, which states that the rate of heat transfer to the environment is proportional to the temperature difference between the battery pack and the surroundings. Equation 5.7 is developed to calculate the heat loss.

$$\dot{Q}_{loss} = b(T_{avg} - T_{amb}) \quad (5.7)$$

where T_{avg} is the average temperature of the battery pack, T_{amb} is the ambient temperature (18°C), and b is a constant. The estimated value of parameter b is 0.85 W/K, based on temperature data from resting periods after battery discharge events. The subsequent energy balance on the system led to Equation 5.8. The change in temperature of the battery pack (ΔT) can be estimated from this equation. The term mC_p is simply the product of the battery pack mass and heat capacity.

$$mC_p\Delta T = \dot{Q}_{gen} - \dot{Q}_{loss} \quad (5.8)$$

The change in temperature of the battery pack (ΔT) could be estimated from this equation. The term mC_p is simply the product of the battery pack mass and heat capacity. The battery pack voltage and temperature are modelled according to Equations 5.3 to 5.8 in MATLAB Simulink. Figure 5.2 shows the block diagram of the main Simulink model. The voltage subsystem estimated the voltage of a single cell according to the equivalent circuit model. It is assumed as valid to multiply the cell voltage by the number of cells in the pack to estimate the pack voltage. This assumption is made because cell-to-cell voltage variations are negligible, and extremely accurate voltage estimation is

not the scope of this work. The voltage subsystem (Figure 5.3) also has outputs V_{Res} and $T(dVoc/dT)$, which are $|V_1 + V_2|$ and $T \frac{dOCV}{dT}$ terms, respectively, in Equation 5.6.

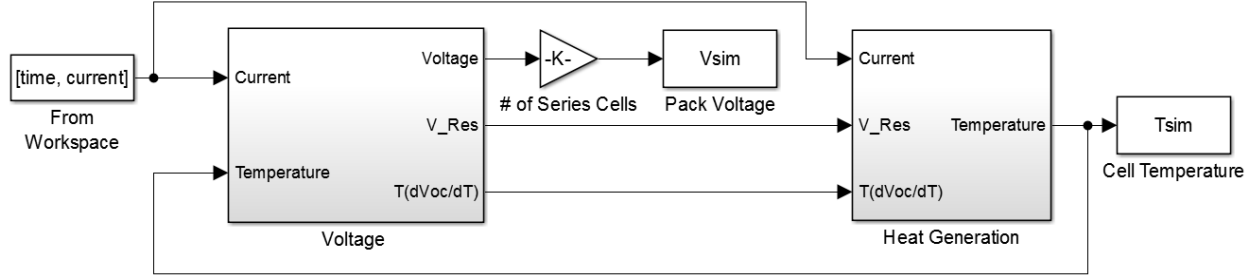


Figure 5.2: Block diagram of the Simulink battery pack model.

Other multiple subsystems inside the voltage estimation subsystem are shown in Figure 5.3. Simple coulomb counting is used to estimate the SOC. The SOC, current, and battery temperature are required as inputs to *Circuit Param Lookup*, where R_1 , R_2 and C are estimated from lookup tables based on HPPC results. The resistances are scaled, depending on C-Rate, to improve the accuracy of the heat generation rate based on the data presented by Samadani et al. [130]. The circuit equations are solved in the *Voltage Estimation* subsystem (Figure 5.3).

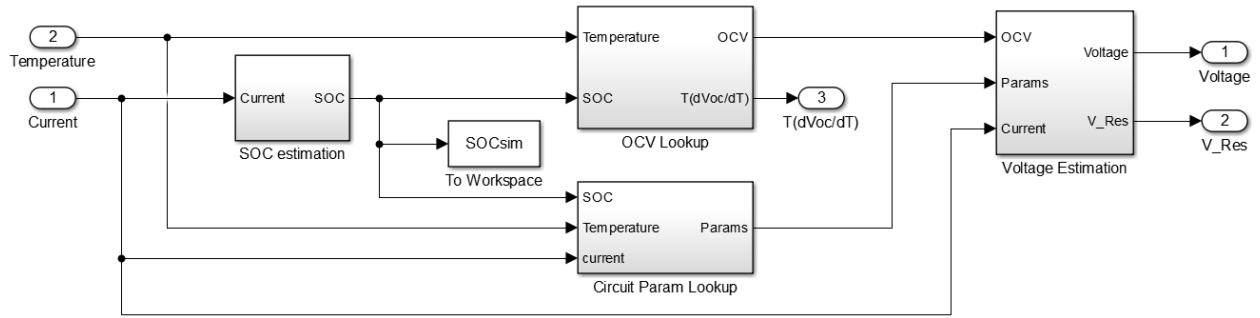


Figure 5.3: Actual view of the voltage estimation subsystem.

The heat generation subsystem as shown in Figure 5.4 takes the current as well as the $|V_1 + V_2|$ and $T \frac{dOCV}{dT}$ as inputs and solve the energy balance from Equations 5.4 to 5.7. The temperature is estimated by continuously integrating the temperature difference. Simulink's variable-step ODE45 solver is used.

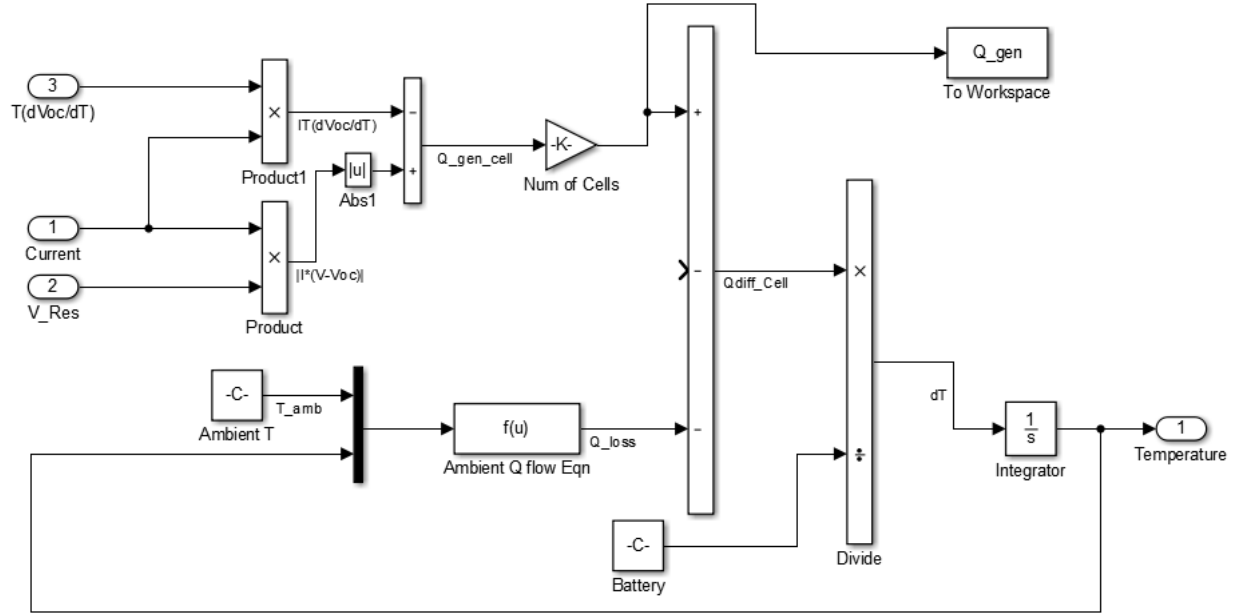


Figure 5.4: Actual view of the heat generation subsystem.

The main purpose of investigating the battery pack through MATLAB Simulink is to identify whether the developed model can sufficiently accurately predict the behaviour of the battery pack by providing only a few inputs. If good agreement is found between the experimental results and the results obtained from the developed model for no cooling conditions, the model can be further used for various cooling conditions with some modification.

5.2 Battery Simulation in ANSYS

The physical domain and geometry of the model used in ANSYS simulation are presented in this section, which also offers assumptions and details about mesh generation. The basic elements considered in the model are the Li-ion cell and the PCM plates. The developed model can be scaled-up for pack level investigation in order to observe the effect of PCM on various parameters.

5.2.1 Model for Numerical Study

A single Li-ion cell is modelled in an ANSYS DesignModeler with 6 mm thick PCM plates on both sides of the cell. Figure 5.5 illustrates the configuration of the cell along with the PCM plates. In the present study, the heat generation rate of the cell is considered as the only source of heat. Only one cell is considered for ANSYS simulation due to computational limitation and the fact that all three cells have almost the same temperature during the experiments.

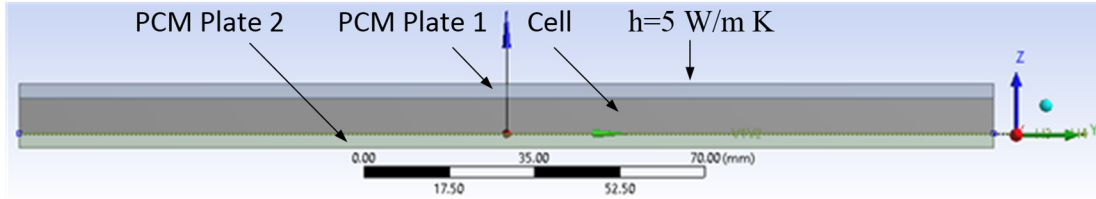


Figure 5.5: Single cell configuration along with the PCM plates considered for the study.

5.2.2 Solver and Discretization Scheme

The time consumed in the simulation process and accuracy of the result also depend on the type of solver used, and discretization scheme adopted. The obtained meshed file is processed by ANSYS Fluent solver, where the governing integral equation for conservation of energy, mass, momentum, and others can be solved by density-based or pressure-based solvers [131].

In both pressure- and density-based solvers, in the case of fluid flow, momentum equations are used to obtain the velocity field. In the pressure based solver, the pressure correction equation obtained from the manipulation of momentum and continuity equations are used to obtain the pressure field. Discretization used by both methods is similar and based on a finite volume approach. A different approach can be used to solve a discrete equation. Two algorithms, segregated and coupled, are available for the pressure-based solver in Fluent. In the case of the segregated algorithm, governing equations for the solution variables (e.g., ϵ , T , k , p , u , v , w) are solved sequentially and separated from each other, while in the case of the coupled algorithm, a coupled system of equations is solved. Furthermore, the solution convergence rate significantly improves in the coupled algorithm compared to the segregated algorithm. In coupled algorithm, the continuity and momentum equation are solved in a closely coupled manner. However, at the same time, the memory requirement also increases 1.5 to 2 times in the coupled algorithm, compared to the segregated algorithm.

In the case of the density-based solver, the governing equations of energy continuity and momentum, are determined concurrently by using either the coupled implicit or explicit formulation. In the case of the coupled-implicit method, all the variables (T , p , u , v , w) in all cells are solved at the same time, whereas in the case of the coupled-explicit method all the variables in only one cell are solved at a time [131]. An overview of the pressure and density-

based solvers available in ANSYS Fluent are shown in Figure 5.6. In the preliminary versions of Fluent software, the pressure-based solver was developed only to be used in the case of low-speed incompressible flows, while on the other hand for high-speed compressible flow, the density-based solver was developed. However, after various reformulations, the pressure as well as the density-based solver can be used for a wide range of flow conditions. SIMPLE and PISO algorithms are used to model constant and transient problems. In ANSYS Fluent, a control-based discretization technique is used to transform a general scalar transport equation to an algebraic equation. The algebraic equation obtained can be numerically solved.

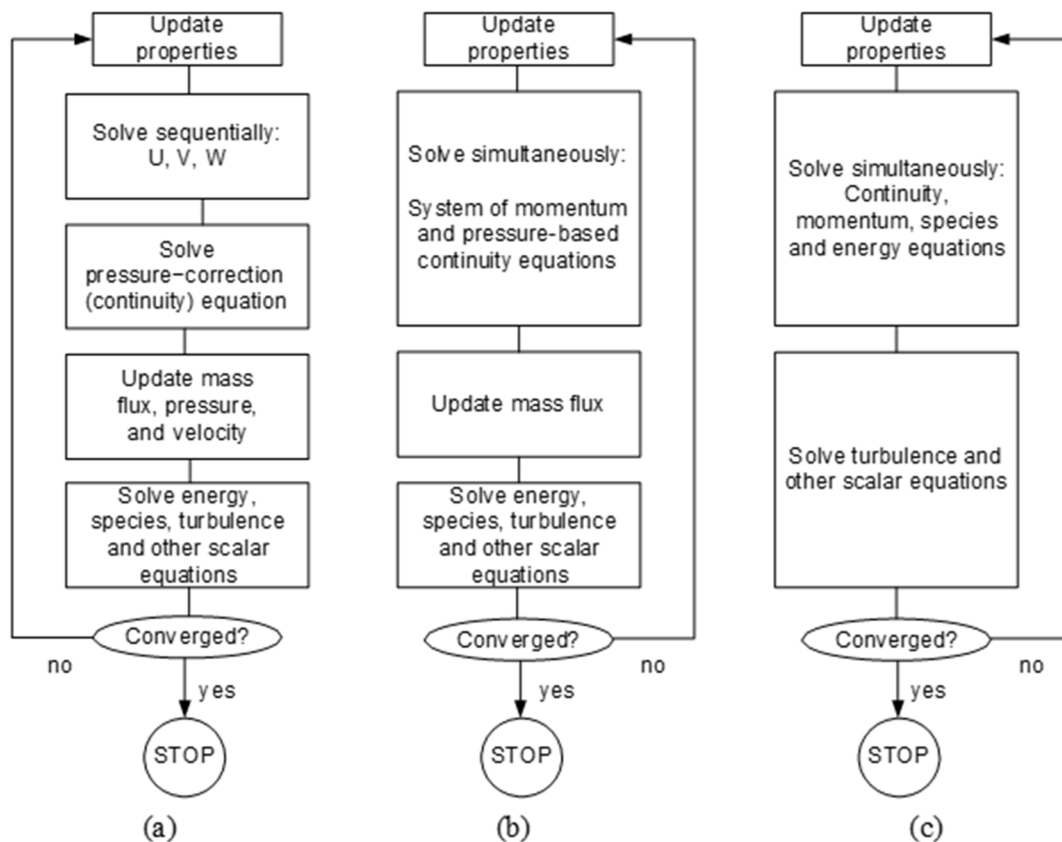


Figure 5.6: Overview of solvers available in ANSYS Fluent 14.0. (a) pressure-based segregated algorithm, (b) pressure-based coupled algorithm, (c) density-based algorithm (adapted from [132]).

The above-mentioned discretization technique leads to a discrete equation. In this way, the law of conservation on a control-volume will be expressed through a discrete equation. Discretization of governing equations for an arbitrary control volume V can be demonstrated by Equation 5.9 by considering the unsteady conservation equation.

$$\int_V \frac{\partial \rho \phi}{\partial t} dV + \oint \rho \phi \vec{v} \cdot d\vec{A} = \oint \Gamma_\phi \nabla \phi \cdot d\vec{A} + \int_V S_\phi dV \quad (5.9)$$

where ρ is density, \vec{A} is surface area vector, \vec{v} is velocity vector ($= u\hat{i} + v\hat{j}$ in 2D), Γ_ϕ is a coefficient of diffusion for ϕ , $\nabla \phi$ is the gradient coefficient of ϕ and S_ϕ is ϕ source per unit volume. In a computational domain, Equation 5.9 above applies to each cell or each control volume. Equation 5.10 shows the discretization of the equation for a given cell [133].

$$\frac{\partial \rho \phi}{\partial t} V + \sum_f^{N_{faces}} \rho_f \vec{v}_f \phi_f \cdot \vec{A}_f = \sum_f^{N_{faces}} \Gamma_\phi \nabla \phi_f \cdot \vec{A}_f + S_\phi V \quad (5.10)$$

where ϕ_f is the value of ϕ convected through face f , N_{faces} is the number of faces enclosing the cell, \vec{A}_f is the area of the face, $\nabla \phi_f$ is gradient ϕ at face f , V is the cell volume and $\rho_f \vec{v}_f \cdot \vec{A}_f$ is mass flux through the face.

Spatial and temporal methods are the two main discretization options available in ANSYS Fluent. In the case of spatial discretization, there are various schemes available, including first order upwind scheme, power-law scheme, second order upwind scheme and central scheme. The uses of the same depend on the desired accuracy as well as on the equation [134]. The governing equation should be discretized in both time and space for transient simulation.

The temporal discretization can be obtained for an arbitrary variable ϕ using Equation 5.11.

$$\frac{\partial \phi}{\partial t} = F(\phi) \quad (5.11)$$

where F is a function that incorporates a spatial discretization. A first order accurate temporal discretization using backward difference can be expressed as [135]:

$$\frac{\phi^{n+1} - \phi^n}{\Delta t} = F(\phi) \quad (5.12)$$

where ϕ is a scalar quantity, and $n+1$ and n are values at next and current time level, respectively. While using the implicit time integration, the function F can be obtained as [135]:

$$\frac{\phi^{n+1} - \phi^n}{\Delta t} = F(\phi^{n+1}) \quad (5.13)$$

From the above equation, the final implicit equation that can be resolved each time before moving forward is expressed as:

$$\phi^{n+1} = \phi^n + \Delta t F(\phi^{n+1}) \quad (5.14)$$

5.2.3 Mesh Generation

Meshing/Grid generation is very important, as the quality and accuracy of the results depend on the quality of the mesh generated. A preprocessor such as Gambit or ICEM can be used to generate the mesh/grid by defining the domains and zones that need to be analysed in detail. In the present study, meshing is performed using the meshing tool available in ANSYS. The selection of the type of mesh used for meshing is also important for the accuracy of results and processing time, which depend mainly on geometry complexity. Structured mesh is best suited for a simple geometry, while unstructured mesh is normally used in the case of complex geometry. As the present case has a simple geometry, a medium structure mesh is used for mesh generation. The size of mesh is also important as the number of grid increases with the refinement of the mesh, which increases the accuracy of the results but, at the same time, increases simulation time and cost.

5.2.3.1 Grid Independent Study

The grid independent study verifies whether the solution obtained from a numerical analysis depends on the resolution of a mesh generated. In the present study, course, medium, and fine meshes are used for a grid independent study of 6 mm thick PCM plates at 1C discharge rate. A medium mesh is used as a standard for all cases. The course and fine meshes are selected in order to investigate the effect of increase and decrease in mesh size over the cell temperature. As a result, 25 million, 37 million, and 45 million elements are obtained with course, medium, and fine mesh, respectively. The temperature profile obtained shows a slight progressive increase in temperature with the decrease in mesh size. The maximum difference in temperature with the course and the medium mesh is only 1.14%, which is within the acceptable range of error for CFD simulation. The difference in the cell temperature across the domain remain same with the change in mesh size. The average cell temperature at the end of the discharge cycle obtained with different mesh sizes is given in Table 5.1. Considering the computation time, course, medium, and fine mesh took approximately 8 hours, 12 hours, and 15 hours, respectively. Based on the computational time and accuracy of results, it is decided to keep medium mesh for all discharge rates.

Table 5.1: Grid independence results for the cell temperature.

Mesh Type	Approx. Elements (million)	Cell Temperature (°C)
Course	25	26.137
Medium	37	26.438
Fine	45	26.625

5.2.4 Initial and Boundary Conditions

Information about the dependent variable must be specified at the domain boundaries in order to achieve a unique solution for a defined modelling problem. Cell zones and boundary conditions in any simulation define the thermal and flow variable on the boundaries of the physical model. Different types of boundary condition are available in ANSYS, including flow inlet and exit boundaries, velocity inlet and outlet, pressure inlet and outlet, internal face boundaries, repeating, wall and pole boundaries. In ANSYS Fluent, the boundary condition is not associated with faces or cells, but only associated with zones. In the case of cell or faces, an internal face boundary condition having no finite thickness is applied and can be used for physical models such as thin porous membranes, fans, and radiators. Through an internal face boundary condition, step-changes in flow and properties can be obtained. Some boundary conditions, including periodic boundaries, can be used to reduce computational time and effort. Defining boundary conditions is critical from a results point of view. Poorly defined boundary conditions can have a substantial effect on simulation results [136].

The interface between the PCM plate and the cell is defined as "wall boundary conditions". The convective heat transfer coefficient is considered on all outer surfaces of the PCM and the cell as shown in Figure 5.5.

The initial conditions and boundary conditions for the single cell are as follows:

- Uniform heat generation rate is considered over the entire body of the cell.
- Ambient temperature considered equal to 293.15 K.
- The initial temperature of the battery and the PCM plate is taken as equal to the ambient temperature.
- The thermal conductivity of the cell is assumed orthotropic.
- Specific heat for the cell is assumed constant.

- Thermal conductivity and specific heat of the PCM is constant respective to its phase.
- Heat transfer through radiation is not considered.
- No flow field for the liquid phase of the PCM as shape of container does not change during the experiment.

5.2.5 Convergence Criteria

Convergence criteria provide the accuracy of the result of a numerical study [137]. Although there are no universal metrics for judging convergence, three main criteria are residual values, solution imbalances and quantities of interest [138, 139]. However, residual is a most fundamental measure of convergence, as it directly quantifies the error in the solution. In each control volume, the residual measures the local disparity of a conserved variable. Therefore, each cell in the model has its own residual value for every equation being solved. The iterations will continue until the residual level of each parameter reaches to a predefined value [138]. For energy equations, it is suggested to have residual level equal to 10^{-6} or lower [139]. Therefore, the residual in the present study is also set to 10^{-6} .

5.2.6 Model Input Parameters

The behaviour of a material with respect to a change in temperature is important for the accuracy of simulation results. The accuracy of simulation results mainly depends on the property variation defined in the simulation software through the user-defined function (UDF) or by any other method (polynomial, piecewise polynomial). Some of the input parameters, which will be used in simulations, are defined in this section.

5.2.6.1 Properties of PCM

In the present study, n-Octadecane PCM is selected by considering the operating temperature of the battery. The solid and liquid temperatures of n-Octadecane are selected as 300.2 K and 303.2 K, respectively. The specific heat of a PCM also varies with temperature, and can be considered as a step function between the solid and liquid temperature of n-Octadecane. The other values of n-Octadecane with respect to the experimented time can be obtained by using some curve fitting methods. Some of the fitting algorithms available are Gauss-Newton algorithms, Levenberg-Marquardt, least squares and Chebyshev polynomials. Gauss function is another method which

can be used to find the specific heat of the PCM with respect to change in temperature in the following form [54]:

$$C_p = 0.0088 + G(54.79 \times G(1.628e - 7/(T^4 - 3.687 \times T^3 + 5.017 \times T^2 - 3.108 \times T + 0.7144))) \quad (5.15)$$

where T is average temperature, and G is Gauss function. The above formula in Equation 5.15 for finding the specific heat is approximately 97% accurate. ANSYS Fluent allows the user to enter the input data as discrete numbers. Therefore, the values can be entered directly into ANSYS as soon as the variations in the properties of any material are known. For simulation purposes, the different values of specific heat, thermal conductivity and density of the PCM (n-Octadecane) are given below [54]:

$$C_p = \begin{cases} 2150 \text{ J/(kgK)} & T_{solid} > T \\ 243500 \text{ J/(kgK)} & T_{solid} < T < T_{liquid} \\ 2180 \text{ J/(kgK)} & T > T_{liquid} \end{cases} \begin{matrix} \text{Solid Phase} \\ \text{Mushy zone} \\ \text{Liquidus Phase} \end{matrix} \quad (5.16)$$

$$k = \begin{cases} 0.358 \text{ W/(mK)} & T_{solid} > T \\ 0.255 \text{ W/(mK)} & T_{solid} < T < T_{liquid} \\ 0.152 \text{ W/(mK)} & T > T_{liquid} \end{cases} \begin{matrix} \text{Solid Phase} \\ \text{Mushy zone} \\ \text{Liquidus Phase} \end{matrix} \quad (5.17)$$

$$\rho = \begin{cases} 776 \text{ kg/(m}^3\text{)} & T_{solid} > T \\ 769 \text{ kg/(m}^3\text{)} & T_{solid} < T < T_{liquid} \\ 758 \text{ kg/(m}^3\text{)} & T > T_{liquid} \end{cases} \begin{matrix} \text{Solid Phase} \\ \text{Mushy zone} \\ \text{Liquidus Phase} \end{matrix} \quad (5.18)$$

These properties of n-Octadecane are provided by the manufacturer and also available in the literature.

5.2.6.2 Cell

As discussed previously in Chapter 4, in the present study, 20Ah LiFePO₄ is used for experiments. Different thermo-physical properties, such as specific heat, density, and thermal conductivity of the cell, are given in Table 4.1 (Chapter 4). The same properties of 20Ah LiFePO₄ Li-ion cell are considered for ANSYS simulation.

5.2.7 Governing Equations for Cell Testing

An energy balance equation can be applied to find the temperature distribution of the cell. The conservation of the energy equation can be defined by using the energy balance and considering

the average thermophysical properties of the cell. These equations are simply derived by the author based on assumptions and selected parameter.

Conservation of energy equation can be stated as:

$$\Delta \dot{E}_{total} = \Delta \dot{E}_{cond} + \Delta \dot{E}_{conv} + \dot{W}_{net} \quad (5.19)$$

where $\Delta \dot{E}_{total}$ is the net rate of change for internal and kinetic energy [54].

$$\Delta \dot{E}_{total} = \frac{\partial}{\partial t} \left[\rho \left(\hat{u} + \frac{v^2}{2} \right) \right] dx dy dz \quad (5.20)$$

Here, $\Delta \dot{E}_{cond}$ is the net rate of energy change through conduction (heat), as given below [54]:

$$\Delta \dot{E}_{cond} = -(\nabla \cdot \dot{q}) dx dy dz \quad (5.21)$$

Here, $\Delta \dot{E}_{conv}$ the net rate of energy change through convection (fluid flow), as given below:

$$\Delta \dot{E}_{conv} = - \left\{ \nabla \cdot \left[\left(\hat{u} + \frac{v^2}{2} \right) \rho V \right] \right\} dx dy dz \quad (5.22)$$

Here, \dot{W}_{net} is the net rate of work by body forces and surface forces (work by element on surrounding), as given below:

$$\begin{aligned} \dot{W}_{net} = & -\rho (V \cdot g) dx dy + \left[\frac{\partial}{\partial x} (u\sigma_{xx} + v\tau_{xy} + w\tau_{xz}) + \frac{\partial}{\partial y} (u\tau_{yx} + v\sigma_{yy} + \right. \\ & \left. w\tau_{yz}) + \frac{\partial}{\partial z} (u\tau_{zx} + v\tau_{zy} + w\sigma_{zz}) \right] dx dy dz \end{aligned} \quad (5.23)$$

By substituting the value of $\Delta \dot{E}_{total}$, $\Delta \dot{E}_{cond}$, $\Delta \dot{E}_{conv}$ and \dot{W}_{net} from Equations 5.20-5.23 to Equation 5.19, we will obtain:

$$\begin{aligned} \frac{\partial}{\partial t} \left[\rho \left(\hat{u} + \frac{v^2}{2} \right) \right] = & -(\nabla \cdot \dot{q}) - \nabla \cdot \left[\left(\hat{u} + \frac{v^2}{2} \right) \rho V \right] - \rho (V \cdot g) + \left[\frac{\partial}{\partial x} (u\sigma_{xx} + v\tau_{xy} + \right. \\ & \left. w\tau_{xz}) + \frac{\partial}{\partial y} (u\tau_{yx} + v\sigma_{yy} + w\tau_{yz}) + \frac{\partial}{\partial z} (u\tau_{zx} + v\tau_{zy} + w\sigma_{zz}) \right] \end{aligned} \quad (5.24)$$

The above equation can be simplified by extracting stress tensor having symmetry (9 normal and shear stresses). A simplified equation is represented as given below:

$$\rho \frac{D\hat{u}}{Dt} = -\nabla \cdot \dot{q} + \left(\sigma_{xx} \frac{\partial u}{\partial x} + \tau_{xy} \frac{\partial v}{\partial x} + \tau_{xz} \frac{\partial w}{\partial x} \right) + \left(\tau_{yx} \frac{\partial u}{\partial y} + \sigma_{yy} \frac{\partial v}{\partial y} + \tau_{yz} \frac{\partial w}{\partial y} \right) + \frac{\partial u}{\partial z} \left(\tau_{zx} \frac{\partial u}{\partial z} + \tau_{zy} \frac{\partial v}{\partial z} + \sigma_{zz} \frac{\partial w}{\partial z} \right) \quad (5.25)$$

where D/Dt is a symbol of substantial derivative and physically the time rate of change. φ is the energy dissipation rate. A constitutive equation is required to eliminate normal and shear stress and to co-relate heat flux \dot{q} to the temperature field. For the temperature field, the Fourier law equation can be used, as given below:

$$\dot{q}_n = -k_n \frac{\partial T}{\partial n} \quad (5.26)$$

Assuming the material is isotropic and $k_x = k_y = k_z = k$, Equation 5.26 changes to $\dot{q} = -k\nabla T$.

A Newtonian approximation as another constitutive equation can relate the stresses and velocity fields, as given below [140]:

$$\tau_{xy} = \tau_{yx} = \mu \left(\frac{\partial v}{\partial x} + \frac{\partial u}{\partial y} \right) \quad (5.27)$$

By using Equations 5.26 and 5.27, the main energy conservation equation can be rearranged as:

$$-\rho \frac{D\hat{u}}{Dt} = -\nabla \cdot k\nabla T - p\nabla \cdot V + \mu\varphi \quad (5.28)$$

In the above equation, the value of enthalpy $\hat{h} = \hat{u} + \frac{p}{\rho}$, by differentiating this relation with respect to time and introducing the same in Equation 5.28, we will obtain:

$$\rho \frac{D\hat{h}}{Dt} = \nabla \cdot k\nabla T + \frac{Dp}{Dt} + \mu\varphi \quad (5.29)$$

In the case where the point of interest is temperature, then enthalpy can be replaced by temperature as given below:

$$D\hat{h} = C_p dT + \frac{1}{\rho} (1 - \beta) dp \quad (5.30)$$

where β is the thermal expansion coefficient, as given below [140]:

$$\beta = -\frac{1}{\rho} \left(\frac{\partial \rho}{\partial T} \right)_p \quad (5.31)$$

Using Equations 5.30 and 5.31, Equation 5.29 can be rearranged, and the resulting energy conservation equation is given below:

$$\rho C_p \frac{DT}{Dt} = \nabla \cdot k \nabla T + \beta T \frac{Dp}{Dt} + \mu \varphi \quad (5.32)$$

During charging and discharging cycle, heat generation takes place in the battery pack; the heat can be stored in the PCM as sensible heat as well as latent heat when the phase change occurs.

$$Q = m_{PCM} \times C_{eff}(T_f - T_i) + m_{PCM} \times \text{latent heat} \quad (5.33)$$

where m_{PCM} is mass of the PCM, C_{eff} is the effective specific heat of the PCM, T_i and T_f are the initial and final temperatures of the PCM, respectively.

5.2.8 Heat Generation Rate in Cell

In the present study, the heat generation rate is calculated according to the experimental data. An average volumetric heat generation rate is calculated from the available data. Table 5.2 provides the heat generation rate and volumetric heat generation rate for a single cell.

Table 5.2: Heat generation rate and volumetric heat generation rate considered for the study.

Discharge Rate	Heat Generation Rate (W)	Volumetric Heat Generation Rate (W/m ³)
1C	3.85	14850
2C	8.4	32200
3C	14.4	55400
4C	20.85	80200

5.3 Energy Efficiency of the Battery Pack

In this study, the energy efficiency of the battery is defined in various ways. The most relevant energy efficiency definition is in terms of the amount of electrical energy that the battery can provide. Therefore, the energy efficiency of the battery pack is defined as the ratio of electrical energy delivered by the battery and the theoretical Gibbs free energy of the fully-charged battery. Theoretically, the electrical energy present in the battery can be calculated as shown in Equation 5.34. The integral in Equation 5.34 can be experimentally expressed as a finite sum of measured data points, as shown in Equation 5.35. The Gibbs free energy of the battery can be calculated as

shown in Equation 5.36. Finally, the efficiency of the battery can be calculated as shown in Equation 5.37.

$$E_{ele} = \int I(t) \cdot V(t) dt \quad (5.34)$$

$$E_{ele,exp} = \sum I(t) \cdot V(t) \cdot \Delta t \quad (5.35)$$

$$\Delta G_{cell} = -nFE_{cell} \quad (5.36)$$

$$\eta_{Gibbs} = \frac{\text{Electrical Energy}}{\text{Gibbs Free Energy}} = \frac{E_{ele,exp}}{G_{cell}} \quad (5.37)$$

The efficiency of the battery can also be defined as the ratio of electrical energy that is experimentally delivered by the battery to the theoretical electrical energy stored in the battery. In this calculation, the theoretical electrical energy stored in the battery can be calculated using the nominal voltage and rated capacity of the battery, as shown in Equation 5.38. The efficiency of the battery can be calculated as shown in Equation 5.39.

$$E_{ele,theo} = V_{cell}^o \cdot \text{Capacity} \quad (5.38)$$

$$\eta_{ele} = \frac{\text{Electrical Energy}}{\text{Theoretical Electrical Energy}} = \frac{E_{ele,exp}}{E_{ele,theo}} \quad (5.39)$$

The efficiency of the battery pack can be defined based on the heat generation during battery operation. This criterion considers the efficiency of the battery from the perspective of energy lost in the form of heat generation. The heat generated during the operation is the sum of heat accumulated in the battery and the heat lost to the coolant. The heat generation is calculated as shown in Equations 5.40, 5.41, and 5.42. The efficiency of the battery can be calculated as shown in Equation 5.43.

$$Q_{total} = Q_{water} + Q_{batt} \quad (5.40)$$

where Q_{water} is the total heat transferred to the coolant, which is de-ionised water in the present study. Q_{batt} is heat stored in the battery pack as sensible heat. Q_{water} can be calculated as follows:

$$Q_{water} = m_{water} c_{water} \sum_{i=1}^n (T_{w,i} - T_{w,i-1}) \quad (5.41)$$

where m_{water} is the mass of deionised water flow through the cold plates and c_{water} is the specific heat of water. T_w is the temperature of the water at any instant. Q_{batt} can be calculated from:

$$Q_{batt} = m_{pack} c_{cell} \sum_{i=1}^n (T_{b,i} - T_{b,i-1}) \quad (5.42)$$

where m_{pack} is the total mass of all three cells used in the experiment setup and c_{cell} is the specific heat of a cell. T_b is the temperature of a cell at any instant. The efficiency of the battery pack can be calculated as:

$$\eta_{heat} = 1 - \frac{Heat}{Gibbs \text{ Free Energy}} = 1 - \frac{Q_{total}}{G_{cell}} \quad (5.43)$$

The efficiency of the battery is calculated by varying different operating parameters such as discharge rate, the thickness of the PCC plates and coolant temperature. A summary of the test scenarios conducted in this study is given in Table 5.3.

Table 5.3: Summary of experimental conditions analysed.

Discharge Rate	Cooling Conditions with Various Thicknesses of PCC Plates (mm)				
	10°C	20°C	30°C	40°C	No Cooling
1C	None	None	None	None	None
	6	6	6	6	6
	9	9	9	9	9
	12	12	12	12	12
2C	None	None	None	None	None
	6	6	6	6	6
	9	9	9	9	9
	12	12	12	12	12
3C	None	None	None	None	None
	6	6	6	6	6
	9	9	9	9	9
	12	12	12	12	12
4C	None	None	None	None	None
	6	6	6	6	6
	9	9	9	9	9
	12	12	12	12	12

5.4 Thermal Conductivity of PCM and CNT Mixture

The CNT can be used to overcome the low thermal conductivity associated with a PCM. The properties of the PCM are altered by mixing the nanotube material. Equations are derived to identify the properties of the combination of the PCM and CNTs by considering the PCM as carrying fluid and CNTs as an additive. For the theoretical analysis, different volumetric concentrations of CNTs are considered for analysis.

$$c = \frac{v_{PCM}}{v_{Tot}} = \frac{v_{PCM}}{v_{PCM} + v_{CNT}} \quad (5.44)$$

where c is the ratio of the volume of a PCM to the total volume of a PCM and CNT.

The thermal conductivity of CNTs significantly depends on their series and parallel arrangement. The thermal conductivity of CNT is very high if they are aligned in series and very low if they are aligned parallel to each other. The effective thermal conductivity of a PCM and CNT mixture for both series and parallel arrangement of CNT is given below, respectively [141].

$$k_{eff,series} = ck_{PCM} + (1 - c)k_{CNT} \quad (5.45)$$

$$k_{eff,parallel} = \left(\frac{c}{k_{PCM}} + 1 - \frac{c}{k_{CNT}} \right)^{-1} \quad (5.46)$$

where $k_{eff,series}$ and $k_{eff,parallel}$ is effective thermal conductivity of a PCM and CNT mixture when CNTs are arranged in series and parallel, respectively. k_{PCM} and k_{CNT} are the overall thermal conductivity of PCM and CNTs, respectively. The ratio of actual effective thermal conductivity to thermal conductivity with respect to series and parallel arrangement of CNT are given below:

$$\frac{k_{eff,series}}{k_{CNT}} = c \frac{k_{PCM}}{k_{CNT}} + (1 - c) \quad (5.47)$$

$$\frac{k_{eff,parallel}}{k_{CNT}} = \left(c \frac{k_{CNT}}{k_{PCM}} + (1 - c) \right)^{-1} \quad (5.48)$$

At any instant, it is not possible to have all CNTs aligned in series or parallel. Therefore, different weightage to series and parallel arrangements of CNTs in a mixture is given. If P is defined as the

probability of a series arrangement (best case), then the following equations can be obtained to identify the overall thermal conductivity of the mixture [141].

$$k_{mix} = P \times k_{eff,series} + (1 - P) \times k_{eff,parallel} \quad (5.49)$$

$$k_{mix} = P(c \cdot k_{PCM} + (1 - c)k_{CNT} + (1 - P) \left(\frac{c}{k_{CNT}} + \frac{1 - c}{k_{CNT}} \right)^{-1} \quad (5.50)$$

where k_{mix} is thermal conductivity of a PCM and CNT mixture having a probability of a series arrangement of CNTs.

5.5 Exergy Analyses of Battery Thermal Management Systems

The efficiency of a TMS of EVs and HEVs plays a critical role in vehicle performance, operational cost and environmental impact due to limited onboard energy resources. Therefore, it is essential to properly measure the efficiencies associated with the TMS and its components. At the same time, an energy efficiency of the system may be misleading and draw an inadequate conclusion that will not offer a clear picture. Unlike exergy, energy efficiency does not consider the direction of energy flow and state of the environment, as exergy is not conserved. Exergy of a system can be defined as the maximum work that can be obtained from a system at a specified reference environment [142]. When writing in generalised form for a control volume, the exergy balance can be defined as:

$$\sum_k \dot{Q}_k \left(1 - \frac{T_0}{T_s} \right) + \sum_i \dot{m}_i ex_i = \dot{W} + \sum_e \dot{m}_e ex_e + \dot{E}x_D \quad (5.51)$$

where \dot{Q} , T , \dot{m} , ex , \dot{W} , and $\dot{E}x_D$ are the heat transfer rate, temperature, mass flow rate, specific exergy, rate of work completed and exergy destruction rate, respectively. The subscripts k and 0 represent the property at any state k and at reference condition, respectively. At any given state, the physical specific exergy, ex , is defined as:

$$ex_k = (h_k - h_0) - T_0(s_k - s_0) + \frac{v_k^2 - v_0^2}{2} + g(z_k - z_0) \quad (5.52)$$

where h is specific enthalpy, v is velocity, g is gravity and z is elevation. In the case of BTMS, heat transfer takes place at a finite temperature in the system or between the system and surroundings,

which is mainly responsible for creating irreversibilities for a system. Irreversibilities make the available amount of energy unusable by reducing work potential. Entropy generation plays an important role in measuring the effect of irreversibilities in the system during a process.

For any component or system, mass, energy, entropy and exergy balances are required for exergy analysis. These balance equations are used to determine the rate of entropy generation, heat input, and exergy destruction. By using these equations, the energy and exergy efficiencies of a component or system are calculated.

For a steady state process, mass, energy, entropy and exergy balance equations can be written as:

$$\text{M.B.E} \quad \dot{m}_{in} = \dot{m}_{out} \quad (5.53)$$

$$\text{E.B.E} \quad \dot{E}_{in} = \dot{E}_{out} \quad (5.54)$$

$$\text{En.B.E} \quad \dot{S}_{in} + \dot{S}_{gen} = \dot{S}_{out} \quad (5.55)$$

$$\text{Ex.B.E} \quad \dot{Ex}_{in} = \dot{Ex}_{out} + \dot{Ex}_D \quad (5.56)$$

where the exergy destruction rate $\dot{Ex}_D = T_0 \dot{S}_{gen} = T_0 \dot{m} \Delta S$, \dot{E} , and \dot{m} are the energy transfer rate and mass flow rate, respectively. \dot{S} is the entropy flow rate or generation rate.

In the present study, exergy analysis of a developed system with a cold plate is performed, and exergy destruction and exergy efficiencies are calculated. The mass, energy, entropy and exergy balance equation for a battery with a cold plate are written below.

$$\text{M.B.E} \quad \dot{m}_{in} = \dot{m}_{out} = \dot{m}_{cool} \quad (5.57)$$

$$\text{E.B.E} \quad \dot{m}_{in} h_{in} + \dot{Q}_{batt} = \dot{m}_e h_e \quad (5.58)$$

$$\text{En.B.E} \quad \dot{m}_{in} s_{in} + \frac{\dot{Q}_{batt}}{T_0} + \dot{S}_{gen} = \dot{m}_e s_e \quad (5.59)$$

$$\text{Ex.B.E} \quad \dot{m}_{in} ex_{in} + \dot{Ex}_{\dot{Q}_{batt}} = \dot{m}_e ex_e + \dot{Ex}_{D,batt} \quad (5.60)$$

where $\dot{E}x_{\dot{Q}_{batt}} = \dot{Q}_{batt} \left(1 - \frac{T_0}{T_s}\right)$. \dot{Q}_{batt} is rate of heat generation in the battery pack.

However, in most cases, energy and exergy efficiencies of an electrical system become the same. In the present study, the exergy destruction is defined from heat stored in the battery pack and heat transfer to the cold plate. The calculations are performed using Equations 5.61 and 5.62.

$$Exd_{pack} = \sum Q_{batt}(t) \cdot \left(1 - \frac{T_0(t)}{T_{pack}(t)}\right) \cdot \Delta t \quad (5.61)$$

$$Exd_{cooling} = \sum Q_{cool}(t) \cdot \left(1 - \frac{T_0(t)}{T_{cool}(t)}\right) \cdot \Delta t \quad (5.62)$$

5.6 Economic Analyses of Battery Thermal Management Systems

In EVs and HEVs, liquid cooling is most widely used for battery thermal management. Normally, a vapour compression refrigeration cycle is used to maintain the battery temperature. To remove heat, a refrigerant or other liquid circulates through the cold plate between the cells. A heater is used to heat the battery in cold weather. In the present study, a simplified approach is used to analyse only the cooling cycle. Two main costs are associated with a vapour compression refrigeration cycle-based battery cooling system: i.e. capital cost and operational cost. The capital cost consists of the cost of major components such as the compressor, condenser, expansion valve and evaporator. It is difficult to establish the actual capital cost of BTMS in EVs and HEVs due to non-disclosure by automobile manufacturers. Therefore, the cost of the refrigeration cycle available in the literature is considered for the present study. Chevy Volt is considered to have determined the operational cost of BTMS, which can be divided into two sections:

1. Operational cost due to energy consumption in running the BTMS ($C_{o,Cycle}$)
2. Operational cost due to energy consumption in carrying the weight of BTMS ($C_{o,weight}$)

The cost of conventional BTMS can be calculated using Equation 5.63.

$$C_{BTMS} = C_{capital,BTMS} + C_{o,BTMS} \quad (5.63)$$

where the operational cost of BTMS is

$$C_{o,BTMS} = C_{o,Cycle} + C_{o,weight} \quad (5.64)$$

It is important to analyse the cost associated with developed passive BTMS to establish the feasibility of the system. In the present work, several processes are involved in developing the passive BTMS. There are various costs associated with developing the present system, as given in Equation 5.65.

$$C_T = C_d + C_p + C_m + C_o \quad (5.65)$$

where C_T is the total cost, C_d is design cost, C_p is manufacturing cost, C_m is material cost and C_o is operational cost.

The design cost involves cost related to the design of the battery pack with PCM or PCC plates such as space requirement and vehicle aerodynamics. Manufacturing cost involves cost related to the different types of equipment, energy, and labour used to develop the PCM or PCC plates. The material cost involves the cost of different materials used to develop the plates and system, including. PCM, CNTs, foam, gasket, and special glue. The operating cost is essentially related to energy consumed by a vehicle in carrying the extra weight associated with the developed system.

All these costs vary significantly with the scale (size) and type of process or method used to develop the passive BTMS. In the present thesis, the entire system will be developed within a laboratory and by using some case specific methods/processes. It is difficult to calculate the actual cost involved in developing the present passive BTMS due to non-availability of the cost of design and manufacturing. Therefore, only material costs involved in developing PCM-based plates is considered for the present study. The material cost for PCM-based plates is given in Equation 5.66.

$$C_m = m_{PCM} \times C_{PCM} + m_{CNT} \times C_{CNT} + m_{foam} \times C_{foam} \quad (5.66)$$

where C_m is total material cost. C_{PCM} , C_{CNT} , C_{foam} are the unit cost of PCM, CNT, and polyurethane foam, respectively. m_{PCM} , m_{CNT} , m_{foam} are the mass of PCM, CNT, and polyurethane foam, respectively, and can be calculated as:

$$m_{PCM} = (N_{cell} + 1) \times \rho_{PCM} \times L_{PCM} \times W_{PCM} \times T_{PCM} \quad (5.67)$$

$$m_{CNT} = (N_{cell} + 1) \times m_{PCM} \times CNT_{conc.} \quad (5.68)$$

$$m_{foam} = (N_{cell} + 1) \times m_{foam} \quad (5.69)$$

where ρ_{PCM} is density of PCM. L_{PCM} , W_{PCM} , T_{PCM} are the length, width, and thickness of the PCM plate, respectively. N_{cell} is the number of Li-ion cells in the battery pack. $CNT_{conc.}$ is the concentration of CNTs in the PCM. These costs may vary significantly as only a small amount of material is purchased for the experiments, while the cost of material on an industrial scale will be low due to bulk purchase. PCC plates are commercially developed and the cost of a plate can vary with the number of plates required. Based on the details provided by a PCC plate manufacturer, the capital cost of PCC-based BTMS can be calculated from Equation 5.70.

$$C_{PCC} = C_{m,PCC} + C_{non,rec} + C_{batch} \quad (5.70)$$

where $C_{m,PCC}$ is material cost. $C_{non,rec}$ is the non-recurring engineering fee and C_{batch} is the batch fee charged by the manufacturer. The material cost ($C_{m,PCC}$) can be calculated using the per PCC plate cost charged by the manufacturer and the number of PCC plates required.

5.7 Optimisation of Battery Thermal Management Systems

The objective of this optimisation study is to maximize the driving range of a vehicle. One of the major reasons for using passive BTMS is to reduce the cooling load from the battery, which will improve the driving range of the vehicle due to the availability of extra energy. The results show that both commercially developed PCC material-based BTMS and PCM-based BTMS are capable of managing the battery pack temperature within the required limits. Therefore, for the present optimisation study, PCC-based BTMS is selected. The length and width of PCC plates depend on the dimension of the Li-ion cell. However, the thickness depends on the required temperature of the cell; as the results show that the temperature of the cell decreases with an increase in PCC plate thickness. As already discussed, the thickness of PCC plates varies from 6 mm to 12 mm with an interval of 3 mm. It is observed that the capacity of the battery pack varies with the change in PCC plate thickness, which can be linked to a change in temperature. At the same time, a change in PCC plate thickness changes the power required to move the vehicle, as the mass of a vehicle changes with the change in PCC plate thickness. The power requirement to move the vehicle affects the driving range of the vehicle. Therefore, it is important to determine the required

thickness of PCC plates along with other parameters to maximise the driving range of the vehicle. Although the battery pack temperature changes with the change in PCC plate thickness, it remains in the optimum temperature range of the Li-ion battery with all three PCC plates (6 mm, 9 mm, 12 mm).

Therefore, an objective function is defined, where the driving range of the vehicle is maximised. In this study, the optimisation is limited to maximising the driving range of the vehicle with PCC-based BTMS only. However, the same approach can be used for optimising the driving range for PCM-based BTMS. Also, the cost of the developed system is not included in the optimisation as it does not change with a change in PCC plate thickness for the present case.

Although there are numerous optimisation techniques available in the literature, a genetic algorithm is selected for the present study. This selection is based on the various advantages previously discussed in the background and literature review. Also, genetic algorithm is readily available in the commonly used software Engineering Equations Solver (EES), which saves time and effort.

5.7.1 Objective Function

The driving range of a vehicle mainly depends upon battery capacity, the power required to move the vehicle, the efficiency of the battery and other components. The capacity of the battery depends on temperature and discharge rate. The power required to move the vehicle can be calculated based on operating conditions and weight of the vehicle. According to the fundamental theory of vehicle dynamics, the instantaneous power of EVs and HEVs can be determined by using roadway grade, vehicle speed, and acceleration. Therefore, an analysis is conducted to establish the relation between vehicle power, roadway grade, velocity, and acceleration.

In the first part, certain driving conditions are selected, and some assumptions are made to calculate the tractive effort of EVs or HEVs. Three major resistances are selected and described by the following equation:

$$F = ma + R_{ae} + R_{rr} + R_g \quad (5.71)$$

where F is tractive effort, m is the mass of the vehicle, a is acceleration, and R_{ae} , R_{rr} , R_g are aerodynamic, rolling, and grade resistances, respectively. Roadway grade R_{ae} , R_{rr} , and R_g can be calculated by the following equation:

$$R_{ae} = \frac{\rho}{2} C_D A_f v^2 \quad (5.72)$$

$$R_{rr} = f_{rr} m g \quad (5.73)$$

$$R_g = m g \sin \theta \quad (5.74)$$

where ρ is air density, A_f is a frontal area of the vehicle; C_D is drag coefficient; v is vehicle velocity; f_{rr} is rolling resistance constant, and g is gravity. Using Equations 5.72-5.74, in Equation 5.71, we obtain:

$$F = ma + \frac{\rho}{2} C_D A_f v^2 + f_{rr} m g + m g \sin \theta \quad (5.75)$$

The above equation about tractive effort can be used for both conventional and electric vehicles. The required power to generate tractive force for a vehicle travelling at velocity v can be estimated using the following equation:

$$P_{ideal} = F \cdot v = \left(ma + \frac{\rho}{2} C_D A_f v^2 + f_{rr} m g + m g \sin \theta \right) v \quad (5.76)$$

Here, P_{ideal} is the power required at the wheel to drive the vehicle at a given speed, which is provided by the input power (P_{Actual}). In the case of conventional ICE vehicles, P_{Actual} is generated by combustion of the fuel, but in the case of EVs, P_{Actual} is power generated by an electric motor. In the case of PHEVs, P_{Actual} can be power generated by an electric motor or by combustion of the fuel. EVs and HEVs are much more efficient compared to conventional ICE vehicles due to lower power losses in an electric motor. If we assume the efficiency of an electrical motor and transmission system, Equation 5.77 can be used to find actual power. Then:

$$P_{Actal} = P_{ideal} / (\eta_{motor} \times \eta_{trans}). \quad (5.77)$$

Power consumption by a vehicle also depends on the mass of the vehicle. In the present study, the mass of the vehicle is divided into three sections: a mass of battery, the mass of PCM and mass of all remaining components.

$$m_{vehicle} = m_{battery} + m_{PCC} + m_{rest} \quad (5.78)$$

Mass of PCC used in the vehicle battery depends on the length, width, and thickness of the PCC plates and the density of the PCC and can be calculated from Equation 5.79.

$$m_{PCC} = PCC_N \times \rho_{PCC} \times PCC_L \times PCC_W \times PCC_{thick} \quad (5.79)$$

where PCC_N is the number of PCC plates. ρ_{PCC} is the density of the PCC material. PCC_L , PCC_W and PCC_{thick} are the length, width, and thickness of the PCC plate, respectively. The number of PCC plates in a battery pack depends on the number of cells.

$$N_{PCC} = (N_{cell} + 1) \quad (5.80)$$

The mass of battery is calculated by:

$$m_{battery} = N_{cell} \times m_{cell} + m_{other} \quad (5.81)$$

where m_{other} includes the mass of insulation, the mass of battery cover and other components related to the battery. A relation is developed between the capacity of the cell and thickness of the PCC plates using the langrage method.

$$P_{cell} = 10630 PCC_{thick}^2 \times 149.46 PCC_{thick} + 18.826 \quad (5.82)$$

where P_{cell} is the capacity of the cell. As previously discussed in section 5.7, the objective of the present optimisation study is to maximise the driving range of the vehicle while keeping the battery temperature in the optimum operating temperature range. Various parameters can affect the driving range of the vehicle. Therefore, an objective function is defined by considering all these parameters:

$$DR = (Cell\ Capacity \times Number\ of\ Cells) / (P_{Actal}) \quad (5.83)$$

Using Equations 5.76-5.78, and 5.82 in Equation 5.83, we obtain:

$$\begin{aligned} \text{Objective function} &= DR \\ &= \frac{(10630 PCC_{thick}^2 \times 149.46 PCC_{thick} + 18.826) \times Number\ of\ Cells}{\left(\left(m_{vehicle} a + \frac{\rho}{2} C_D A_f v^2 + f_{rr} m_{vehicle} g + m_{vehicle} g \sin \theta \right) v \right) / (\eta_{motor} \times \eta_{trans})} \end{aligned} \quad (5.84)$$

The following assumptions are made to perform the optimisation:

- There is enough space in the vehicle to place the battery along with the PCC plates.
- Extra space acquired by PCC plates does not affect the aerodynamics of the vehicle.
- Ambient temperature and pressure are 293.15 K and 101.325 kPa.
- PCC plates alone can manage the battery temperature in the optimum range.

Other than these assumptions, the values of some of the parameters used in the objective function are given in Table 5.4. Although not all these parameters affect the battery the battery pack temperature directly, they are mandatory in order to calculate the objective function.

Table 5.4: Fixed parameters in the objective function.

Parameter	Symbol	Value
Drag Coefficient	C_D	0.8
Vehicle Frontal Area (m ²)	A_f	2.225
Density of PCC Material (kg/m ³)	ρ	895
Number of Cells	N_{cell}	288
Length of PCC Plate (m)	PCC_L	0.15
Width of PCC Plate (m)	PCC_w	0.2

5.7.2 Decision Variables and Constraints

In an objective function, there can be several decision variables, which can affect the results. These decision variables can have thermodynamic, manufacturing or other constraints. Therefore, they should be carefully selected in order to identify optimum design and to save time. In the present study, all the decision variables are selected along with their constraints. The different decision variables selected are as follows:

- PCC plate thickness
- Number of cells
- Vehicle speed
- Discharge rate

The range of all decision variables is selected based on the experimental and simulation results.

Chapter 6. Results and Discussion

The purpose of this thesis is to investigate the passive thermal management of Li-ion batteries using phase change materials. Introducing the PCM into the vehicle cooling cycle can reduce the cooling load from the battery pack. Energy used by the compressor in conventional active cooling systems can be saved in order to extend the driving range of the vehicle. Also, the life of the battery can be improved by reducing the temperature gradient and keeping the battery temperature within the required range. It is also important to determine the effectiveness of a PCM-based cooling system compared to air and liquid cooling. In this chapter, the results obtained from the battery pack at various operating conditions, such as no cooling, with the cold plate, with PCC, and with PCM, are presented and discussed. The effect of using CNTs on the thermal conductivity of PCM are presented in terms of temperature drop in the battery pack. The internal resistance of the prismatic and cylindrical Li-ion cells is calculated based on the experimental data. The results obtained from the developed models are presented in this chapter, and validated by the experimental results. The results of energy and exergy analyses of the battery pack are also presented, along with results from the optical microscopic study, economic analysis, and optimisation.

6.1 Experimental Results for No Cooling Case

In this section, the results obtained from pack level testing of the Li-ion battery pack at room temperature are presented. The voltage, current and the surface temperature of the battery pack are measured at various discharge rates.

6.1.1 Temperature Profile

Figure 6.1 shows the average surface temperature of cell 1, cell 2, and cell 3 obtained at different constant current discharge rates of 1C, 2C, 3C, and 4C. A profile is created in VisualCN program editor for charging and discharging the battery pack at different C-rates, including a rest period in between. To refresh the reader, thermocouple (TC) 1 is located near the cathode, TC 2 is located near the anode, and TC 3 is located in the middle of the cell along the height. The results show that the temperature of all three cells is almost equal throughout the complete experiment, which also confirms that the battery pack is highly insulated. The cell temperature mainly depends upon the current and internal resistance. From Figure 6.1, it can be seen that as the discharge rate increases,

the average surface temperature of all three cells also increases. The highest temperature of the battery pack obtained at 4C discharge rate is 56.50°C and the lowest is 33°C at 1C discharge rate. Considering the optimum temperature range for Li-ion cells, i.e. 25°C-40°C [99, 143], it can be concluded that there is no need for a thermal management system at 1C discharge rate. However, an efficient thermal management system is suggested at and above 2C discharge rate. The variation in the battery pack surface temperature at different discharge rates is plotted against time, as shown in Figure 6.2.

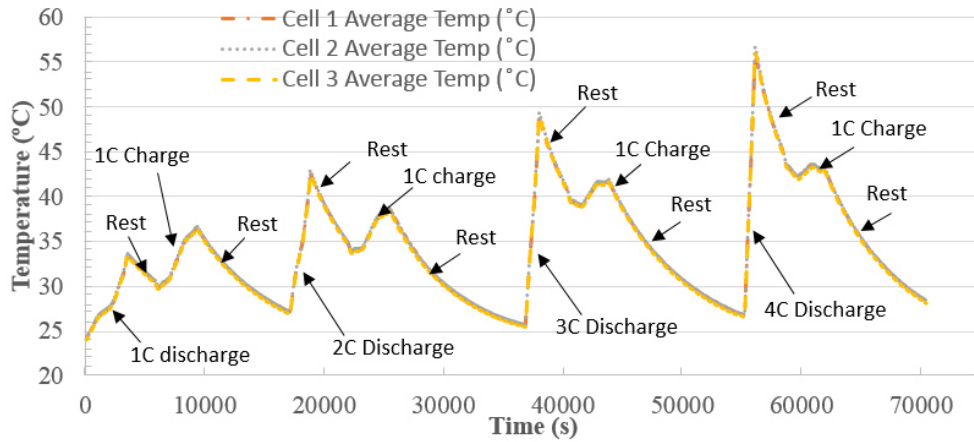


Figure 6.1: The temperature profiles of cell 1, 2, and 3 obtained from the experiments at various charge and discharge rates.

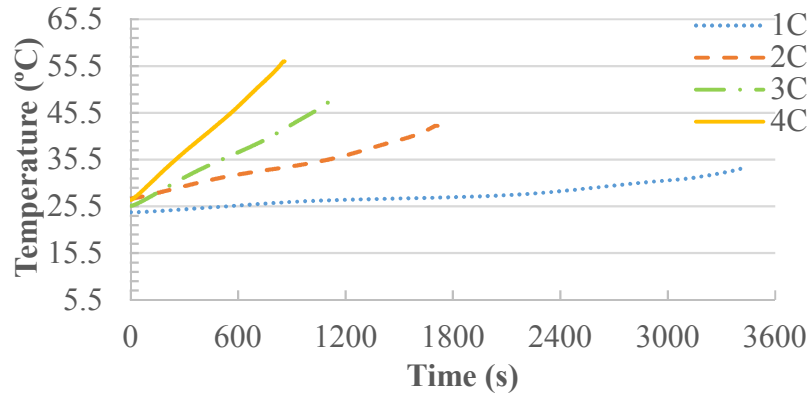


Figure 6.2: Variation in the surface temperature of the battery pack with time at various discharge rates.

The maximum and average surface temperatures of the battery pack at various discharge rates is given in Table 6.1. The average temperature of the Li-ion battery pack at 1C, 2C and 3C is within the optimum operating temperature range, i.e. 25°C-40°C, but at 4C discharge rate, the temperature is beyond the optimum operating range.

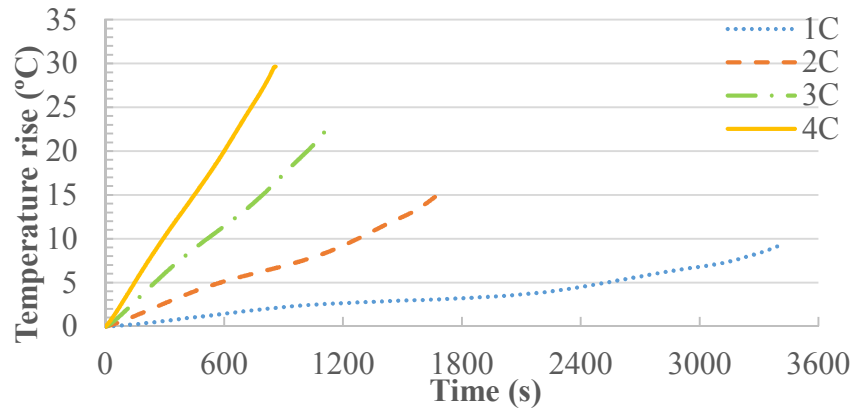


Figure 6.3: Rise in the battery pack temperature at various discharge rates.

Figure 6.3 shows the rise in surface temperature of the battery pack at various discharge rates. It can be seen from Figure 6.3 that there is a sharp increase in temperature with an increase in discharge rate. The rise in the surface temperature of the battery pack at 1C, 2C, 3C, and 4C is 9.3 °C, 16.5 °C, 23.5°C, and 29.6°C, respectively.

Table 6.1: Maximum temperature, average temperature, and rise in temperature of the battery pack for various discharge rates with no cooling case.

Discharge Rate	Maximum Temperature (°C)	Average Temperature (°C)	Temperature Rise (°C)
1C	33	27.9	9.3
2C	42.7	34.5	16.5
3C	48.6	37	23.5
4C	56.5	41.7	29.6

6.1.2 Voltage Profile

The nominal voltage of each cell in the battery pack is 3.3 V. The voltage window for each cell is kept between 2.0 V to 3.65 V. As three cells are connected in series, and the voltage window of the battery pack is kept between 6.0 to 10.95 V (Figure 6.4). The battery pack is charged with constant current (CC) protocol until the voltage of an individual cell reaches 3.65 V and discharges at constant current (CC) until the voltage drops to 2.0 V in each cell. Figure 6.5 shows the discharge voltage profile of the battery pack at 1C, 2C, 3C and 4C discharge rates. It can be seen that the voltage drop increases with an increase in discharge rate due to the flow of high current across the circuit.

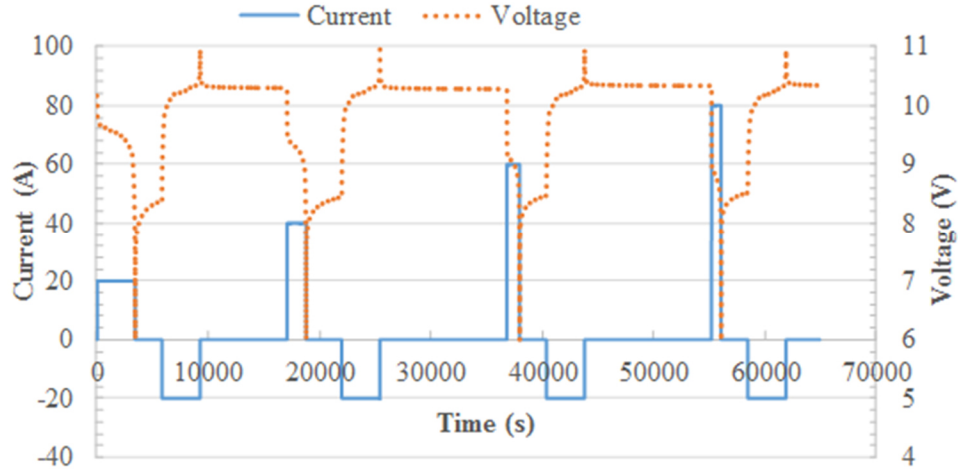


Figure 6.4: Experimental voltages and currents at various charging and discharging rates.

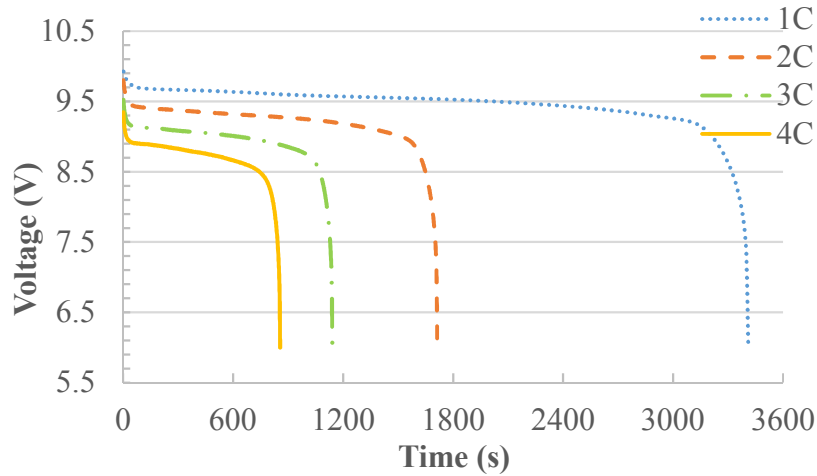


Figure 6.5: Variation in the battery pack voltage observed during experiments at various discharge rates.

6.1.3 Heat Generation Rate

The heat generation rate at various discharge rates is calculated according to the experimental data. In order to calculate the heat generation rate of the battery pack, two main factors, i.e. heat stored in the cell and heat loss to surroundings, are considered. Heat generation mainly depends on the internal resistance of the cell. The results show that the heat generation rate increases with time and reaches maximum towards the end of the cycle, as shown in Figure 6.6, due to an increase in internal resistance with the decrease in SOC towards the end of the cycle. From Figure 6.6, it can be observed that the heat generation rate increases with an increase in the discharge rate and fluctuates with respect to time. The heat generation rate is calculated on the basis of the battery

surface temperature. The reason for the fluctuation in heat generation rate is the delay in the reflection of heat generation on the battery surface in terms of increase in temperature. The average heat generation rate in the battery pack at 1C, 2C, 3C, and 4C discharge rate is 12.2 W, 27.7 W, 47.2 W, and 69.4 W, respectively. Similarly, total heat generation in the battery pack at 1C, 2C, 3C and 4C discharge rate is 41.70 kJ, 47.50 kJ, 54.50 kJ, and 59.20 kJ, respectively.

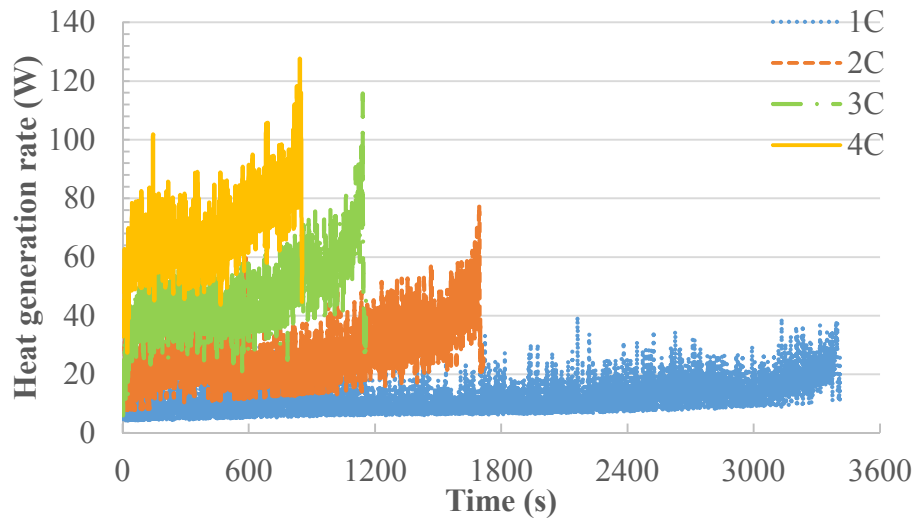


Figure 6.6: Heat generation rate in the battery pack with respect to time at various discharge rates.

6.2 Experimental Results with Liquid Cooling at Various Coolant Temperatures

In this section, the experimental results of the battery pack obtained with a cold plate at various temperatures and discharge rates are presented. Four temperatures of the coolant, i.e. 10°C, 20°C, 30°C and 40°C, are selected to test the battery pack at various discharge rates. The selection of these temperatures is based on various parameters such as ambient temperature, the melting point of the PCM, and the water exit temperature from the radiator in HEVs. The same current profile as in the case of no cooling is used to observe the behaviour of the battery pack at different discharge rates.

6.2.1 Coolant at 10°C

The ambient temperature is assumed to be 20°C. To investigate the electrical and thermal behaviour of the battery pack at lower than ambient temperature, the coolant temperature is kept at 10°C. The de-ionized water is used as the coolant. Figure 6.7 shows the variation in the battery pack voltage at 10°C coolant temperature for various discharge rates. Although the trend of voltage

variation in the battery pack at 10°C coolant temperature is similar to no cooling case, greater voltage drop is observed in the first phase of each cycle due to the increase in internal resistance of the battery pack at 10°C coolant temperature.

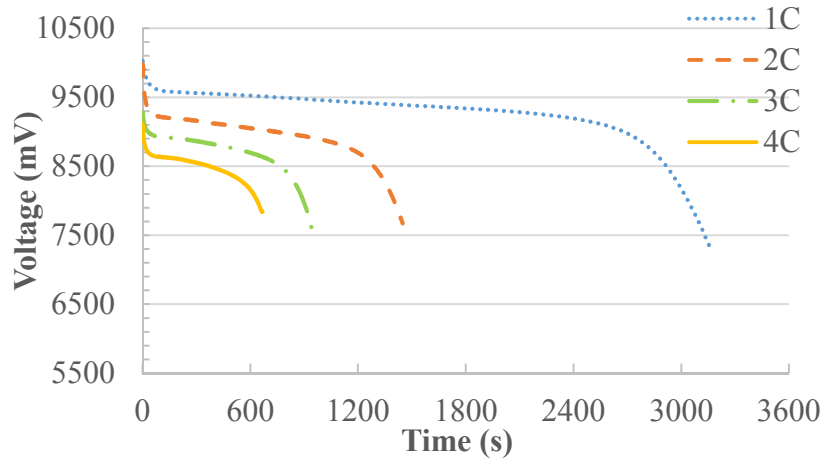


Figure 6.7: Variation in voltage at 10°C coolant temperature for various discharge rates.

The bathtub temperature is fixed at 10°C. However, due to heat gain from the atmosphere through the pipes, the temperature of the water observed at the cold plate inlet is higher than 10°C. Figure 6.8 shows the variation and rise in the battery pack temperature at various discharge rates. There is minor variation in the battery pack temperature at 1C discharge rate as the temperature is raised by 2.2°C. At 2C, 3C and 4C discharge rates, the rise in battery pack temperature obtained is 4.04°C, 7.35°C, and 9.3°C, respectively as shown in Figure 5.8 (b).

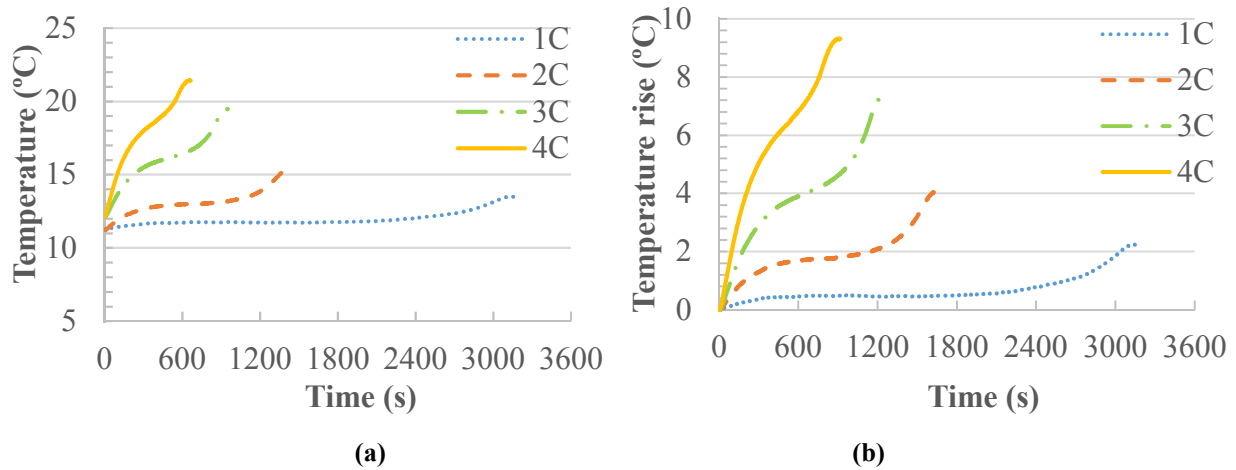


Figure 6.8: Battery pack temperature; (a) variation, (b) rise, at various discharge rates.

The maximum temperature, average temperature, and increase in temperature of the battery with 10°C coolant temperature are given in Table 6.2. One important observation that can be made from Table 6.2 is that the average and maximum temperatures of the battery pack remain below the optimum operating temperature range of the Li-ion battery, i.e. 25°C-40°C with the coolant temperature at 10°C. This may lead to a decrease in the capacity and life of the battery.

Table 6.2: Maximum temperature, average temperature, and rise in temperature of the battery pack with 10°C coolant temperature at various discharge rates.

Discharge Rate	Maximum Temperature (°C)	Average Temperature (°C)	Temperature Rise (°C)
1C	13.5	12	2.2
2C	15.3	12.2	4
3C	19.5	16	7.3
4C	21.4	17.8	9.3

As previously discussed, a constant current profile is created and used for the battery pack in the present study. However, the voltage and current of the battery continuously fluctuate according to the operating conditions of the vehicle. Therefore, a real world drive cycle is used to observe the behaviour of the battery pack. The voltage and current of the actual drive cycle of a vehicle is reduced to the scale of a battery pack having three cells. Figure 6.9 shows the variation in voltage and temperature during an actual drive cycle when the coolant temperature is 10°C.

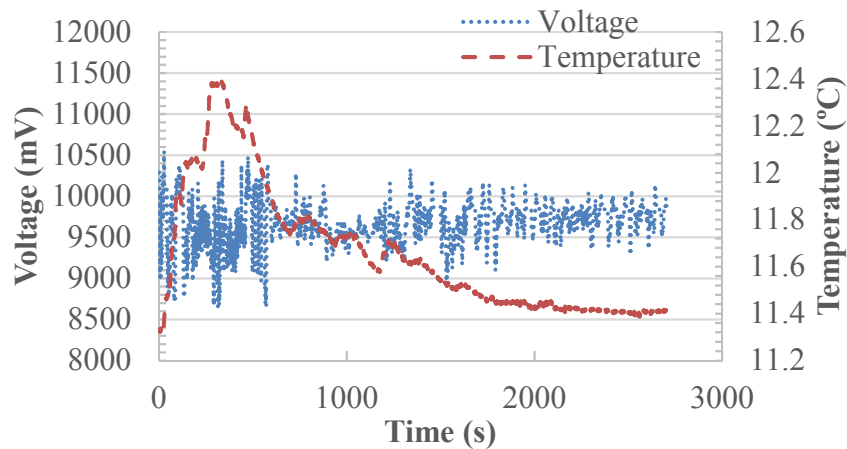


Figure 6.9: Variation in voltage and temperature with respect to time for the selected drive cycle.

The temperature of the battery pack sharply increases in the initial period of the drive cycle and then decreases, as shown in Figure 6.9. This is due to a high discharge rate in the start of the drive

cycle and a low discharge rate during the rest of the cycle. Again, the maximum and average temperatures of the battery pack remains lower than the optimum operating temperature range of the battery, i.e. 25°C-40°C.

6.2.2 Coolant at 20°C

To investigate the electrical and thermal behaviour of the battery pack at ambient temperature, the coolant temperature is kept at 20°C. Figure 6.10 shows the variation in the battery pack voltage at 20°C coolant temperature for various discharge rates. Minor improvements are observed in the battery pack voltage in terms of voltage drop with respect to time compared to the voltage drop at 10°C coolant temperature.

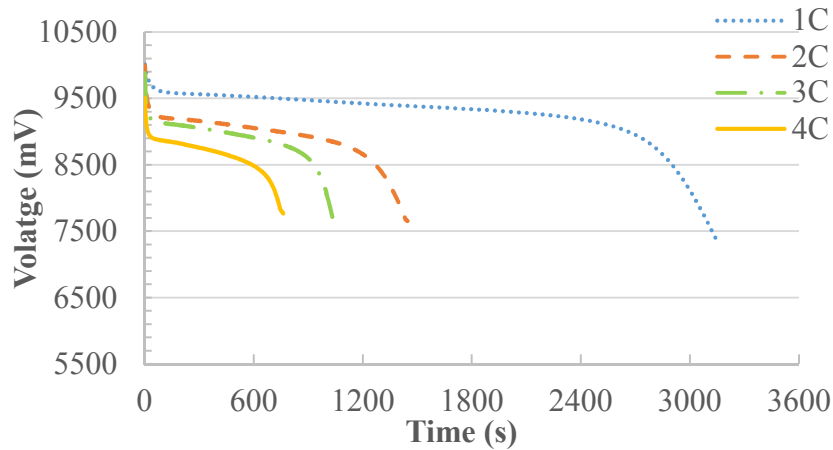


Figure 6.10: Variation in voltage at 20°C coolant temperature for various discharge rates.

The bathtub temperature is fixed at 20°C. Similar to the previous case, there is minor variation in the battery pack temperature at 1C discharge rate as the temperature is increased by 1.7°C. At 2C, 3C and 4C discharge rates, the resulting rise in battery pack temperature is 3.3°C, 6°C, and 7.8°C, respectively, as shown in Figure 6.11 (b). The same drive cycle is used to test the battery pack at 20°C coolant temperature. Figure 6.11 (c) shows the variation in voltage and temperature during an actual drive cycle when the coolant temperature is 20°C. Similar to the previous case, the temperature of the battery pack sharply increases in the initial period of the drive cycle and then decreases.

The maximum temperature, average temperature, and rise in temperature of the battery with 20°C coolant temperature are given in Table 6.3. With a coolant temperature of 20°C, the maximum

temperature of the battery pack remains lower than the optimum operating temperature range, i.e. 25°C-40°C at 1C and 2C discharge rates, and within the range at 3C and 4C discharge rates. The average temperature of the battery pack remains lower than the optimum operating temperature range, i.e. 25°C-40°C at all discharge rates.

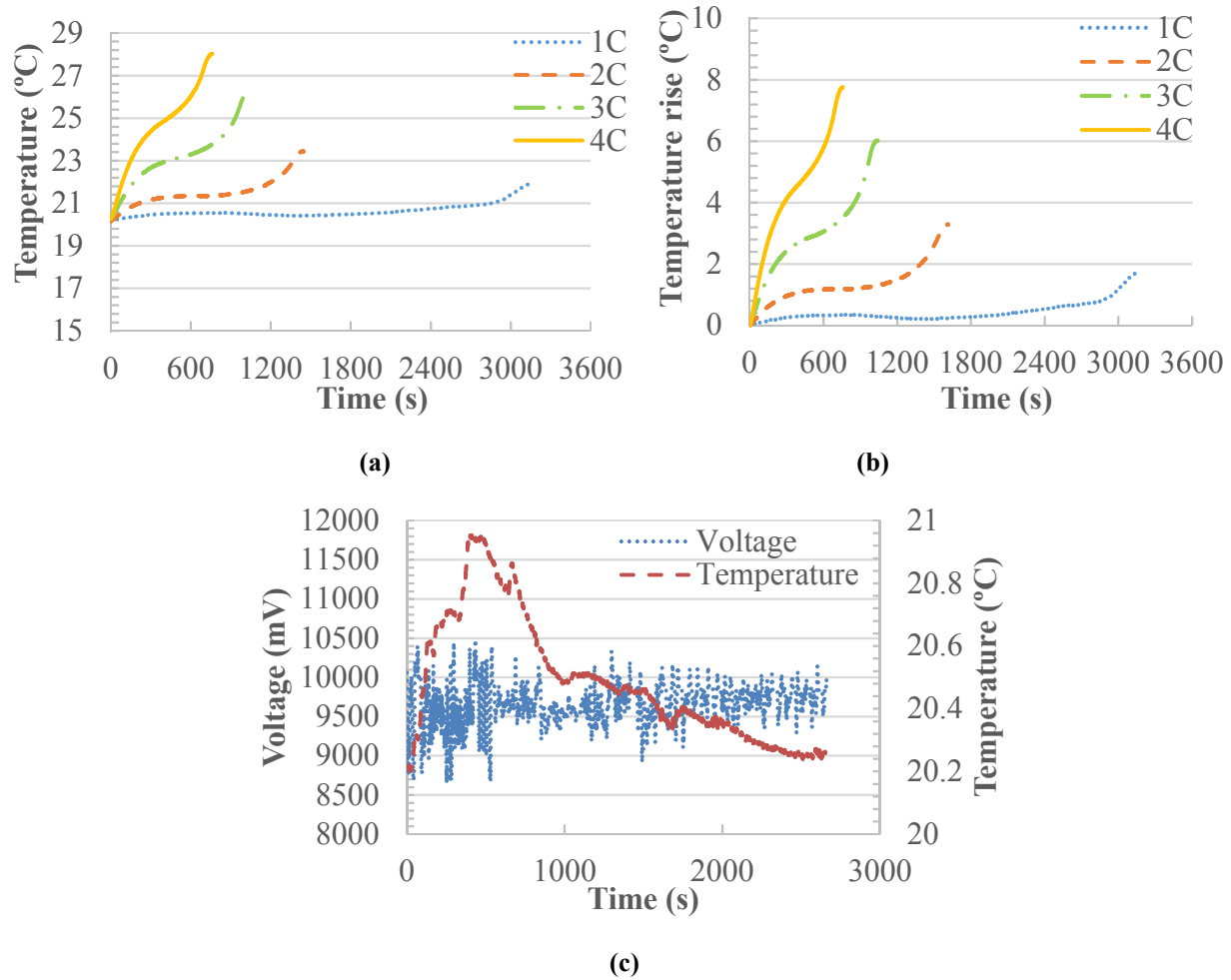


Figure 6.11: At 20°C coolant temperature; (a) variation in temperature at various discharge rates, (b) rise in temperature at various discharge rates, (c) variation in voltage and temperature during the drive cycle.

Table 6.3: Maximum temperature, average temperature, and rise in temperature of the battery pack with 20°C coolant temperature at various discharge rates.

Discharge Rate	Maximum Temperature (°C)	Average Temperature (°C)	Temperature Rise (°C)
1C	21.9	20.6	1.7
2C	23.4	21.5	3.3
3C	26.3	23.2	6
4C	28	24.6	7.8

6.2.3 Coolant at 30°C

To investigate the electrical and thermal behaviour of the battery pack close to melting temperature of the selected PCM, the coolant temperature is kept at 30°C. Again, the battery pack is charged and discharged using a constant current profile to study the behaviour of the battery pack at various discharge rates. Figure 6.12 shows the variation in the battery pack voltage at 30°C coolant temperature for various discharge rates. The trend of voltage variation is the same as that of previous cases, with small improvements.

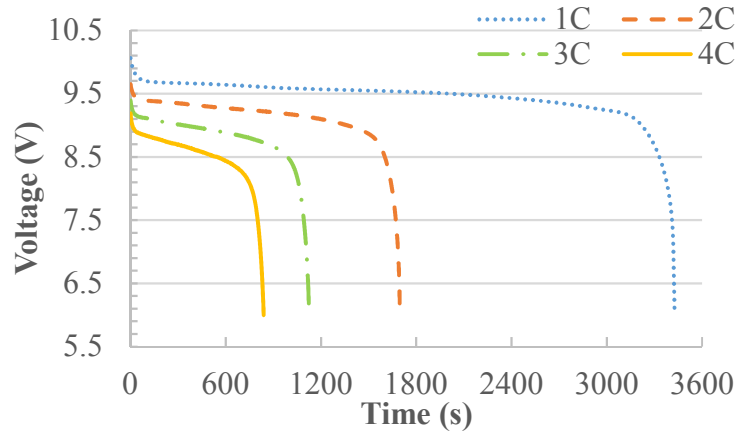


Figure 6.12: Variation in voltage at 30°C coolant temperature for various discharge rates.

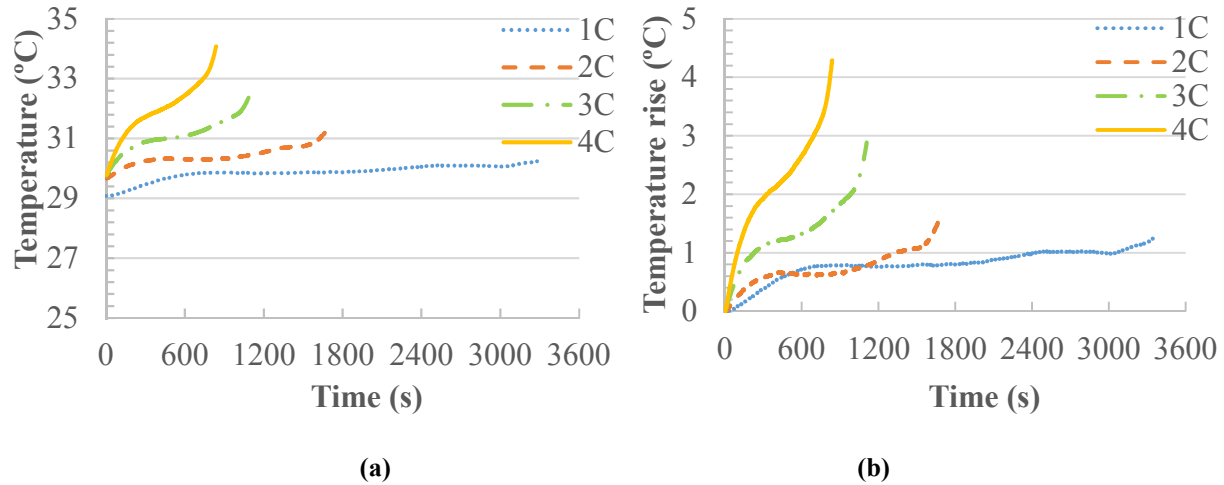


Figure 6.13: Battery pack temperature; (a) variation, (b) rise, at various discharge rates.

Similar to the previous case, there is minor variation in the battery pack temperature at 1C discharge rate as the temperature is increased by 1.3°C. At 2C, 3C and 4C discharge rates, the

resulting rise in battery pack temperature is 1.7°C, 2.9°C and 4.3°C, respectively, as shown in Figure 5.13 (b). The maximum temperature of the battery pack, i.e. 34.1°C, is found at 4C discharge rate. Although, there is a small variation in the inlet temperature at the battery pack and bath temperature at 1C discharge cycle, it is almost equal at the start of the remaining cycles. The small variation in temperature of the coolant in the starting at 1C discharge cycle may be due to a change in ambient temperature. Figure 5.14 shows the variation in the battery pack temperature and coolant outlet temperature at various charge and discharge rates. It can be clearly seen that the coolant outlet temperature follows the trend of the battery pack temperature. However, there is a significant difference in the battery pack and coolant outlet temperature at various discharge rates. The coolant outlet temperature always remains lower than the battery pack temperature, which shows that the cold plates are less effective in absorbing heat from the battery pack. The maximum coolant outlet temperature of 32.5°C is found at 4C discharge rate.

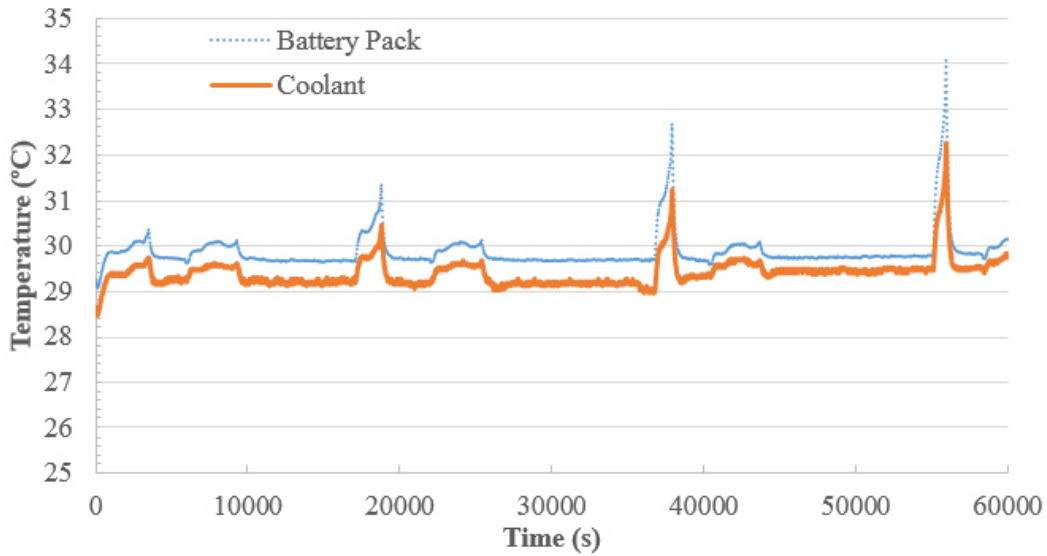


Figure 6.14: Variation in the battery pack and coolant outlet temperatures at various discharge rates.

The maximum temperature, average temperature, and rise in temperature of the battery pack at various discharge rates are given in Table 6.4. An interesting observation can be made from Table 5.4, where the maximum and average temperatures of the battery pack remain within the optimum operating temperature range of the Li-ion battery, i.e. 25°C-40°C, at all discharge rates.

Table 6.4: Maximum temperature, average temperature, and rise in temperature of the battery pack with 30°C coolant temperature at various discharge rates.

Discharge Rate	Maximum Temperature (°C)	Average Temperature (°C)	Temperature Rise (°C)
1C	30.4	29.4	1.3
2C	31.3	30.4	1.7
3C	32.7	31.1	2.9
4C	34.1	32	4.3

6.2.4 Coolant at 40°C

The selection of 40°C coolant temperature is based on the fact that 40°C is the upper limit of the optimum operating temperature of the Li-ion battery. Also, another objective is to observe if the coolant in the ICE engine of an HEV at 40°C can be reused to remove the heat from the battery pack. Figure 6.15 shows the variation in voltage at 40°C coolant temperature for various discharge rates; a similar trend can be observed as in previous cases.

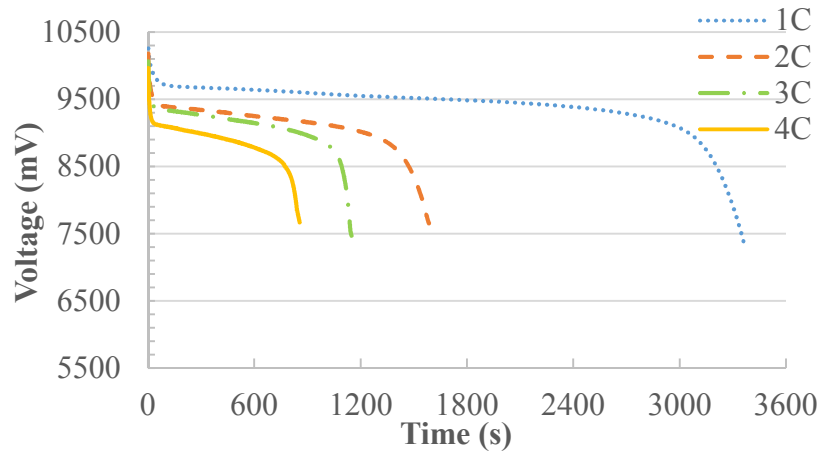


Figure 6.15: Variation in voltage at 40°C coolant temperature for various discharge rates.

The bath tube temperature is fixed at 40°C. However, due to heat loss to the atmosphere through the pipes, the temperature of the water observed at the cold plate inlet is lower than 40°C. Figure 6.15 shows the variation and rise in the battery pack temperature with respect to time at various discharge rates when the coolant temperature is 40°C. The temperature of the battery pack is found to be a maximum of 43.1°C at 4C discharge rate. Similar to previous cases, there is minor variation in the battery pack temperature at 1C discharge rate as the temperature is increased by 0.7°C. At

2C, 3C and 4C discharge rates, the resulting rise in battery pack temperature is 1.9°C, 3.8°C and 5.8°C, respectively.

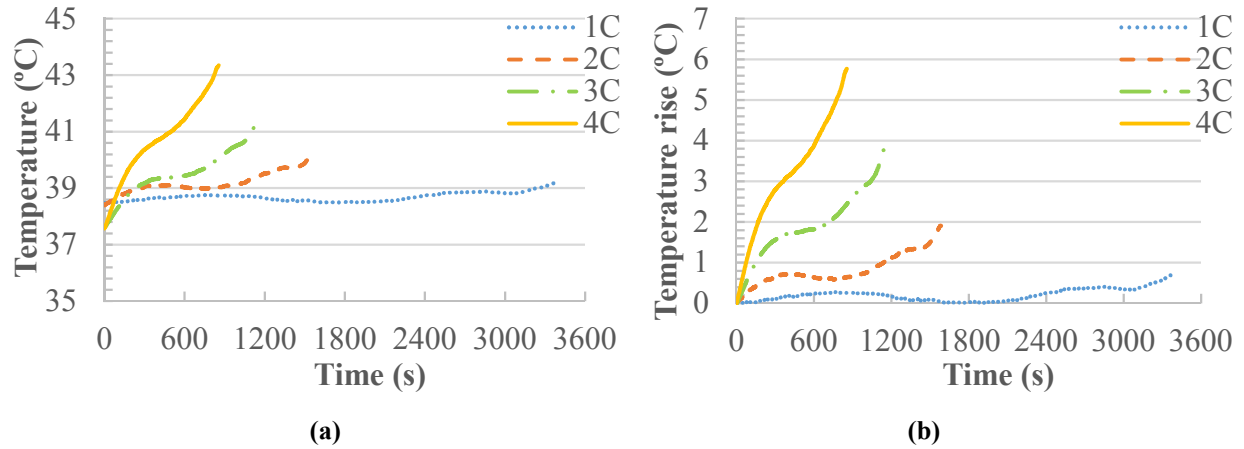


Figure 6.16: Battery pack temperature; (a) variation, (b) rise, at various discharge rates.

The maximum temperature, average temperature, and rise in temperature of the battery pack with 40°C cooling bath temperature at various discharge rates are given in Table 6.5. From Table 6.5, it can be observed that the maximum temperature of the battery pack at 1C discharge rate and the average temperature of the battery pack at 1C, 2C, and 3C discharge rate remain within the optimum operating temperature range of the Li-ion battery. The maximum temperature of the battery pack at 2C, 3C, and 4C discharge rates is slightly higher than the optimum operating temperature range of the Li-ion battery. However, it should be noted that, in each discharge cycle, the inlet temperature is lower than 40°C due to heat loss to the surroundings through pipes carrying the coolant (water).

Table 6.5: Maximum temperature, average temperature, and rise in temperature of the battery pack with 40°C cooling bath temperature at various discharge rates.

Discharge Rate	Maximum Temperature (°C)	Average Temperature (°C)	Temperature Rise (°C)
1C	39.2	38.7	0.7
2C	40.3	39.2	1.9
3C	41.4	39.5	3.8
4C	43.3	40.7	5.8

6.2.5 Comparison of No Cooling and Liquid Cooling Results

A comparison is made between the results obtained with no cooling case and with liquid cooling at various coolant temperatures. Table 6.6 provides a comparison of the battery capacity at various discharge rates with and without a cold plate. The results show that the capacity of the Li-ion battery increases with an increase in coolant temperature and a maximum of 19.13Ah at 40°C at 1C discharge rate. However, the average capacity at all discharge rates is highest with a 30°C coolant temperature. From Table 6.6, it can be seen that the battery capacity significantly reduces with an increase in discharge rate, found to be a minimum of 14.82 Ah at 4C discharge rate and 10°C coolant temperature.

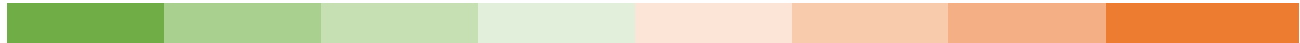
Table 6.6: Battery pack capacity at various cooling conditions.

Discharge Rate	Battery Pack Capacity at Various Cooling Conditions (Ah)				
	No Cooling	10°C	20°C	30°C	40°C
1C	19.04	17.58	17.51	19.04	19.13
2C	19.02	16.09	17.38	18.86	19.00
3C	19.02	15.85	16.91	18.77	18.71
4C	18.95	14.82	16.07	18.64	17.61

In the literature, there is no perfect boundary on battery temperature above or below battery degradation rate increases. However, studies show that approximately 31°C is the optimum temperature for Li-batteries [144]. It is very difficult to maintain the entire battery pack temperature at 31°C. Therefore, an optimum operating temperature range for a Li-ion battery, i.e. 25°C-40°C, is selected for the present study on the basis of the various studies available in the literature. Based on the range, a colour coding is applied to experimentally obtained battery pack temperatures at various discharge rates and with various cooling options. The scale is provided at the bottom of Table 6.7, where a green colour indicates a good or most suitable temperature for the Li-ion battery while a purple colour means poor or not suitable temperature. As the temperature deviates from 31°C, the colour changes from dark green to dull green, and once the range of 25°C-40°C is crossed, the colour changes towards purple. To differentiate each colour shade in terms of temperature, a range is provided in Table 6.7 against each colour shade.

Table 6.7: Temperature range with colour shade.

Temperature (°C)	<13	13-16	16-19	19-22	22-25	25-27	27-29	29-31	31-33	33-35	35-37	37-40	40-43	43-46	46-49	49-52	52<
Colour Shade																	



Good Poor

Although not a universal colour scale for observing battery temperature, by using this colour scheme the author wants to distinguish the obtained temperature of the battery pack with different cooling options. Table 6.8 provide a comparison between the maximum and average temperature of the battery pack at various cooling conditions. Based on the colour scheme, it can be clearly seen from Table 6.8 that the coolant temperature at 30°C is most suitable for keeping the battery pack temperature within the optimum operating temperature range, i.e. 25°C-40°C, at various discharge rates.

Table 6.8: Maximum and average temperatures of the battery pack at no cooling and liquid cooling.

Discharge Rate	Maximum Temperature at Various Cooling Conditions (°C)					Average Temperature at Various Cooling Conditions (°C)				
	No Cooling	10°C	20°C	30°C	40°C	No Cooling	10°C	20°C	30°C	40°C
1C	33	13.5	21.9	30.4	39.2	27.9	12	20.6	29.4	38.7
2C	42.7	15.3	23.4	31.3	40.3	34.5	12.2	21.5	30.4	39.2
3C	48.6	19.5	26.3	32.7	41.4	37	16	23.2	31.1	39.5
4C	56.5	21.4	28	34.1	43.3	41.7	17.8	24.6	32	40.7

6.3 Experimental Results with Phase Change Composite Material

In this section, experimental results of the battery pack with the PCC-based passive thermal management system are presented. Plates of phase change composite material are used to absorb the heat generated in the battery pack. Plates of three thicknesses, i.e. 6 mm, 9 mm and 12 mm are used in the experiments.

6.3.1 6 mm Thick Plates of Phase Change Composite Material

The PCC plates consist of phase change material and graphene, having high latent heat. Four plates are placed between the Li-ion cells. Figure 6.17 (a) shows the variation in temperature with respect to time at various discharge rates with 6 mm thick PCC plates. At 1C discharge rate, the maximum

temperature of the battery pack reaches 29.1°C. At 2C, 3C and 4C, the maximum temperature of the battery pack reaches to 34.1°C, 35.6°C, and 36.1°C, respectively as shown in Figure 6.17 (a). Figure 6.17 (b) shows the rise in battery pack temperature at various discharge rates. At 1C discharge rate, the temperature of the battery pack remains lower than the melting temperature of PCC. Therefore, the heat absorbed by PCC is only in the form of sensible heat. At 1C discharge rate, the temperature rise is 5.8 °C. At 2C, 3C and 4C discharge rates, as the temperature of the battery pack reaches the melting point of PCC, the phase change process starts and heat is also absorbed as latent heat. The rise in temperature at 2C, 3C, and 4C is 6.8°C, 8.2°C and 7.4°C, respectively. The reason for the low-temperature rise at 4C discharge rate compared to 3C discharge may be due to the high initial temperature of the battery pack at 4C discharge rate. Another reason may be an increase in the effectiveness of the PCC plates due to a quick rise in the battery pack temperature.

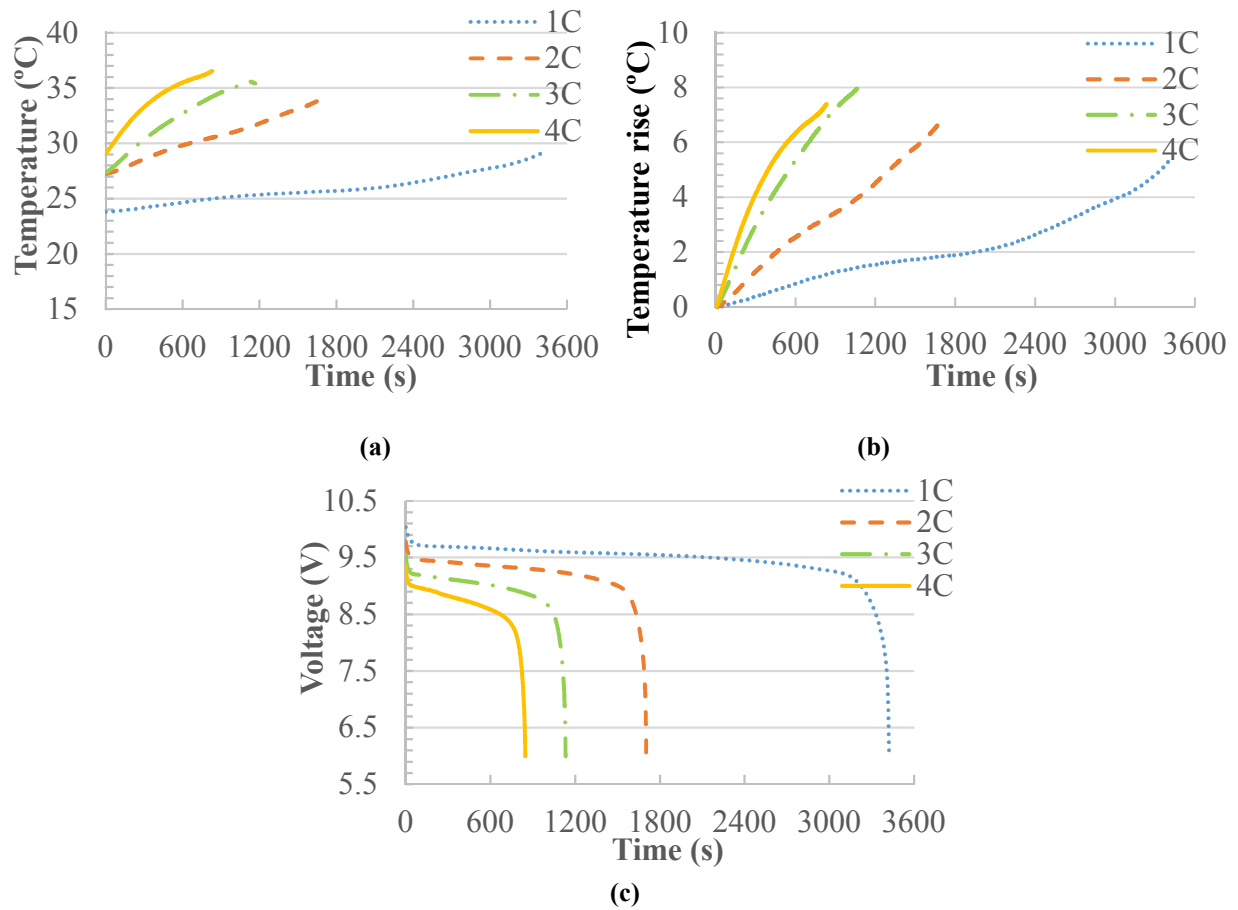


Figure 6.17: With 6 mm thick PCC plate; (a) variation in temperature, (b) rise in temperature, (c) variation in voltage, at various discharge rates.

Figure 6.17 (c) shows the variation in voltage with 6 mm thick PCC plates at various discharge rates. The trends of voltage variation at various discharge rates with 6 mm thick PCC plates are similar to previous cases. The maximum temperature, average temperature, and rise in temperature of the battery pack with 6 mm thick PCC plates are given in Table 6.9. From Table 6.9, an interesting observation may be made: the maximum and average temperatures of the battery pack with 6 mm thick PCC plates remain within the optimum temperature range of the Li-ion battery, i.e. 25°C-40°C, at all discharge rates.

Table 6.9: Maximum temperature, average temperature, and rise in temperature of the battery pack with 6 mm thick PCC plates at various discharge rates.

Discharge Rate	Maximum Temperature (°C)	Average Temperature (°C)	Temperature Rise (°C)
1C	29.1	25.9	5.4
2C	34.1	30.6	6.8
3C	35.6	32.2	8.2
4C	36.5	33.8	7.4

It is a major finding in this study that the developed passive thermal management system can keep the battery temperature within the required range. Although the PCC plates are rigid and remain solid even at high temperatures, some leakage of PCM is observed from the PCC plates at high discharge rates. Therefore, further improvements are required in the design of battery pack to ensure that PCM does not flow from PCC plates.

6.3.2 9 mm Thick Plates of Phase Change Composite Material

The thickness of the PCC plates is varied, from 6 mm to 12 mm with an interval of 3 mm, in order to identify the effect on the battery pack voltage, temperature, and other parameters. Figure 6.18 (a) and (b) shows the variation and rise in the battery pack temperatures with 9 mm thick PCC plates at various discharge rates, respectively. Similar to the previous case, at 1C discharge rate, the maximum temperature of the battery pack reaches 28.6°C. At 2C, 3C and 4C, the maximum temperature of the battery pack reaches 33.2°C, 34.9°C, and 36°C, respectively, as shown in Figure 6.18 (a).

Figure 6.18 (b) shows the rise in the battery pack temperature at various discharge rates. Similar to the previous case, heat is absorbed in the PCC plates as sensible and latent heat. The rise in the

battery pack temperature at 1C, 2C, 3C and 4C is 4.7°C, 6.0°C, 7.8°C and 7.5°C, respectively. The reason for the low temperature rise at 4C compared to 3C discharge rate is the same as that discussed in the previous section. Figure 6.18 (c) shows the variation in voltage with 9 mm thick PCC plates at various discharge rates. The trends of voltage variation at various discharge rates are similar to previous cases.

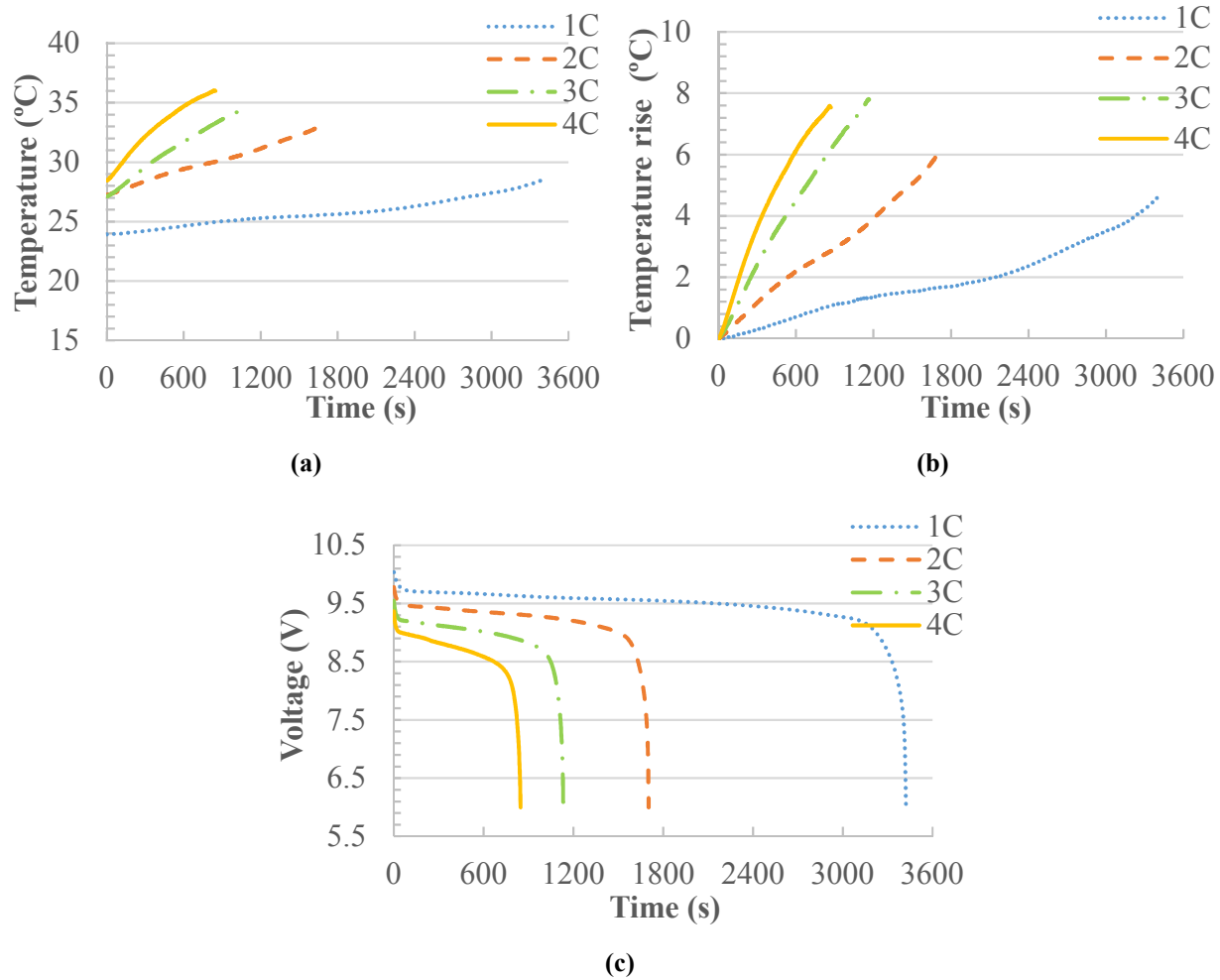


Figure 6.18: With 9 mm thick PCC plates; (a) variation in temperature, (b) rise in temperature, (c) variation in voltage, at various discharge rates.

The maximum temperature, average temperature, and rise in temperature of the battery pack are given in Table 6.10. Similar observations can be made as in the case of the 6 mm thick plate from Table 6.10, where the maximum and average temperatures of the battery pack with 9 mm thick PCC plates remain within the optimum operating temperature range of the battery at all discharge rates.

Table 6.10: Maximum temperature, average temperature, and rise in temperature of the battery pack with 9 mm thick PCC plates at various discharge rates.

Discharge Rate	Maximum Temperature (°C)	Average Temperature (°C)	Temperature Rise (°C)
1C	28.7	25.8	4.7
2C	33.2	30.1	6.0
3C	34.9	31.3	7.8
4C	36.0	32.9	7.5

6.3.3 12 mm Thick Plates of Phase Change Composite Material

Figure 6.19 (a) and (b) shows the variation and rise in temperature of the battery pack with 12 mm thick PCC plates at various discharge rates, respectively. The maximum temperature of the battery pack is found to be 36.4°C at 4C discharge rate.

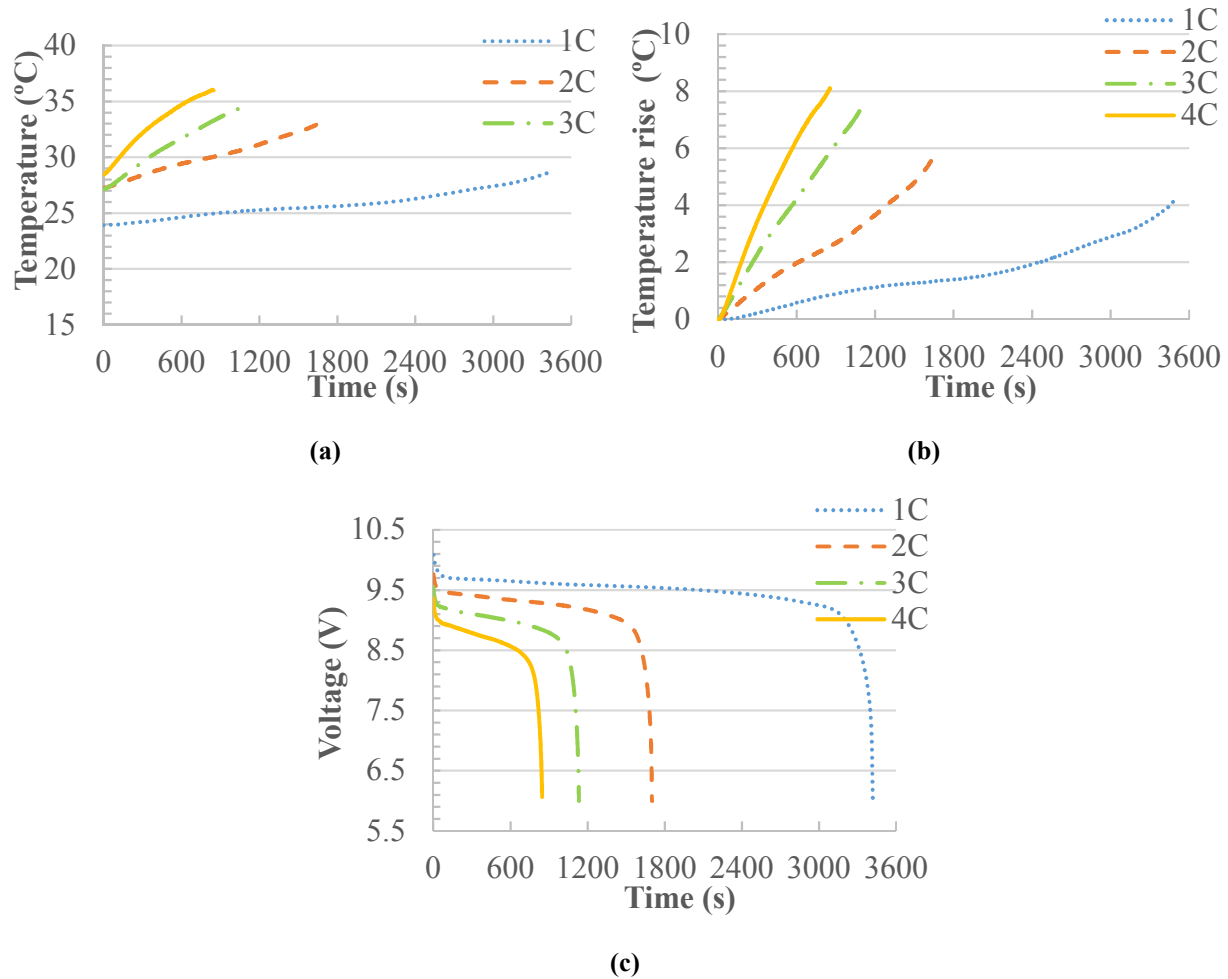


Figure 6.19: With 12 mm thick PCC plates; (a) variation in temperature, (b) rise in temperature, (c) variation in voltage, at various discharge rates.

The rise in the battery pack temperature at 1C, 2C, 3C and 4C is 4.7°C, 6.0°C, 7.8°C and 7.5°C, respectively. Figure 6.19 (c) shows the variation in voltage with 12 mm thick PCC plates at various discharge rates. Again, the trends of voltage variation at various discharge rates with 12 mm thick PCC plates are similar to previous cases.

The maximum temperature, average temperature, and rise in temperature of the battery pack with 12 mm thick PCC plates are given in Table 6.11. Again, similar observations can be made from Table 6.11, where the maximum and average temperature of the battery pack with 12 mm thick PCC plates remain within the optimum temperature range of the Li-ion battery, i.e. 25°C-40°C, at all discharge rates.

Table 6.11: Maximum temperature, average temperature, and rise in temperature of the battery pack with 12 mm thick PCC plates at various discharge rates.

Discharge Rate	Maximum Temperature (°C)	Average Temperature (°C)	Temperature Rise (°C)
1C	28.0	25.3	4.1
2C	32.8	29.3	5.6
3C	34.9	30.6	7.6
4C	36.4	32.0	8.1

6.3.4 Comparison of No Cooling and with Phase Change Composite Plates Results

In this section, a comparison is made between the results obtained with no cooling option and with PCC plates of various thicknesses.

Table 6.12 provides a comparison of the battery capacity at various discharge rates with and without a PCC plate. The capacity of the battery pack is found to be a maximum of 19.34Ah with 6 mm thick PCC plates at 1C discharge rate. From Table 6.12, it can be seen that the battery capacity significantly reduces with an increase in discharge rate, found to be a minimum of 17.80 Ah with 9 mm thick PCC plates at 4C discharge rate. The capacity drop in the battery pack is relatively small with 12 mm thick PCC plates with an increase in discharge rate. However, a small decrease in the capacity of the battery pack is observed with an increase in PCC plate thickness other than 4C discharge rate with 12 mm thick PCC plates. This may be due to the fact that the temperature drops with an increase in PCC plate thickness, which affects the battery capacity.

Table 6.12: Battery pack capacity with and without PCC plates.

Discharge Rate	Battery Pack Capacity at Various Cooling Conditions (Ah)			
	No Cooling	With 6 mm PCC	With 9 mm PCC	With 12 mm PCC
1C	19.04	19.34	19.31	18.99
2C	19.02	19.18	19.00	18.90
3C	19.02	19.03	18.92	18.88
4C	18.95	17.89	17.80	18.82

Figure 6.20 shows a comparison of the temperature profile of the battery pack with and without PCC plates at various charge and discharge rates with respect to time. It can be seen that there is a significant drop in the battery pack temperature with PCC plates compared to without PCC plates. The battery pack temperature with PCC plates remains within the required range at all discharge rates.

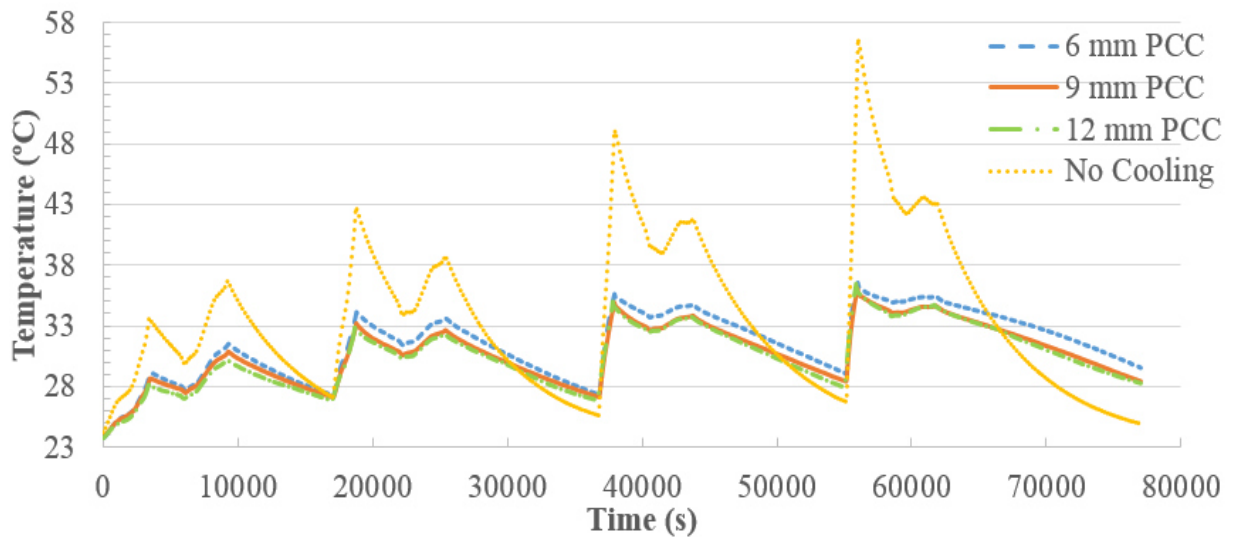


Figure 6.20: Temperature profile of the battery pack with and without PCC plates.

Table 6.13 shows the drop in maximum and average temperatures of the battery pack with PCC plates compared to no cooling case. At 1C discharge rate, there is a temperature drop of 3.9°C in the maximum temperature of the battery pack with 6 mm thick PCC plates compared to no cooling case. The drop in temperature increases with an increase in discharge rate, as more heat is stored as latent heat when the temperature of the battery pack reaches the melting point of PCC at a higher discharge rate. Therefore, at 4C discharge rate, the drop in maximum temperature of the battery

pack is 20°C with 6 mm thick PCC plates compared to no cooling case. Overall, the highest drop in maximum temperature of the battery is found to be 20.5°C with 9 mm thick PCC plates compared to the no cooling case at 4C discharge rate. The temperature drop in the average temperature of the battery pack is found to be the maximum of 9.7°C at 4C discharge rate with 12 mm thick PCC plates.

Table 6.13: Temperature drop in maximum and average temperatures of the battery pack by using PCC plates compared to no cooling case.

Discharge Rate	Temperature Drop in Maximum Temperature of Battery Pack with PCC Plates (°C)			Temperature Drop in Average Temperature of Battery Pack with PCC Plates (°C)		
	With 6 mm PCC	With 9 mm PCC	With 12 mm PCC	With 6 mm PCC	With 9 mm PCC	With 12 mm PCC
1C	3.9	4.4	5.0	2.0	2.1	2.6
2C	8.6	9.5	10.0	3.9	4.4	5.2
3C	13.0	13.7	13.7	4.8	5.7	6.4
4C	20.0	20.5	20.1	7.9	8.8	9.7

Figure 6.21 provides a comparison between the temperature profile of the battery pack at various discharge rates with and without PCC plates. From Figure 6.21, it can be clearly seen that there is a significant temperature drop in the battery pack temperature with the use of PCC plates at all discharge rates compared to no cooling case. At 1C discharge rate, the maximum battery temperature drops from 33°C to 29.1°C and, at 4C discharge rate, the temperature drops from 56.5°C to 36.5°C with 6 mm thick PCC plates compared to no cooling case.

Figure 6.22 provides a comparison between a rise in battery pack temperature at various discharge rates with and without PCC plates. Again, a significant drop in temperature rise can be seen from Figure 6.22 with PCC plates compared to no cooling case. The rise in battery pack temperature at 1C discharge rate is 5.4°C with 6 mm thick PCC plates and 9.3°C with no cooling case. Similarly, the rise in battery pack temperature at 4C discharge rate is 7.4°C with 6 mm thick PCC plates and 29.6°C with no cooling case.

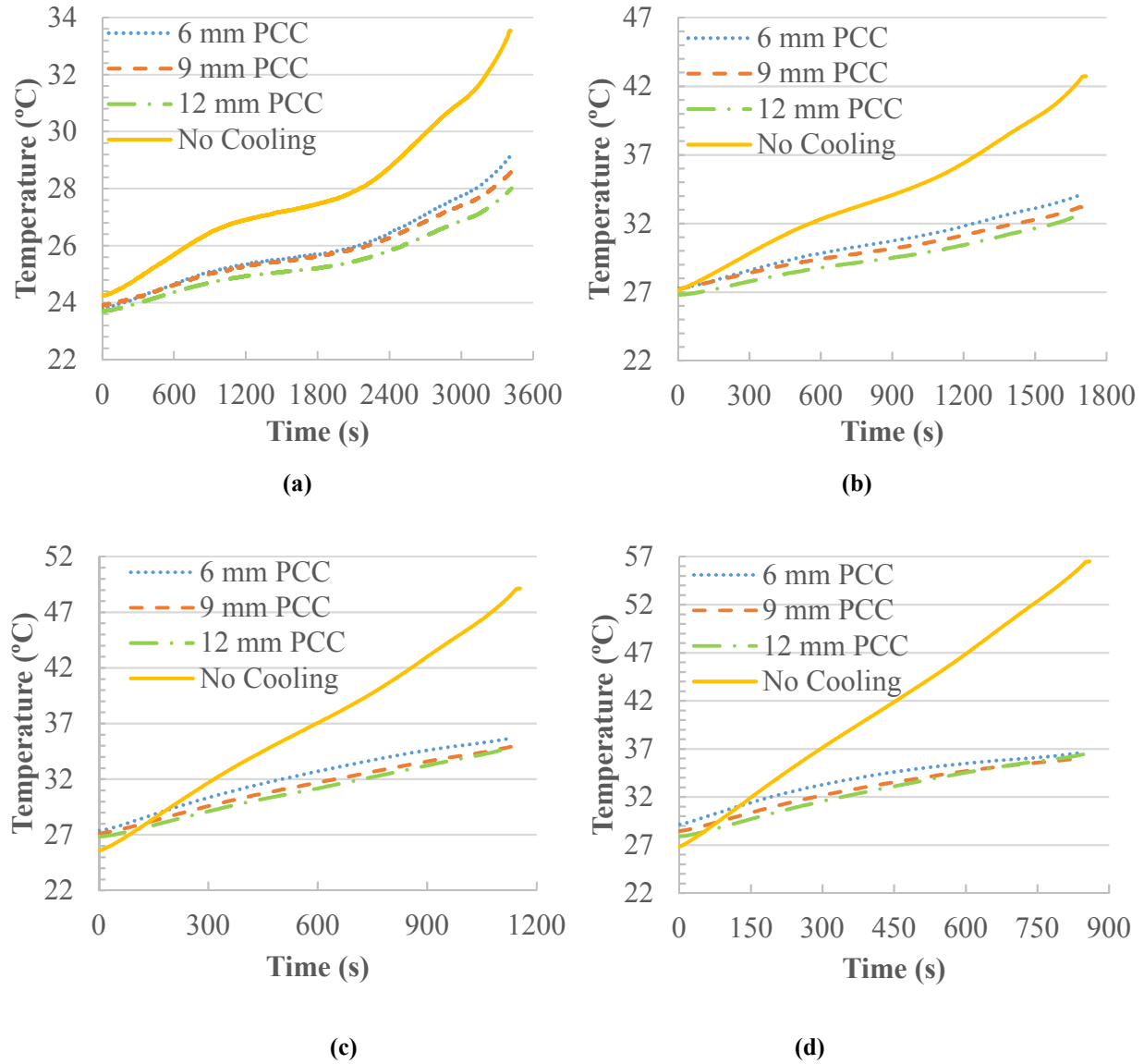
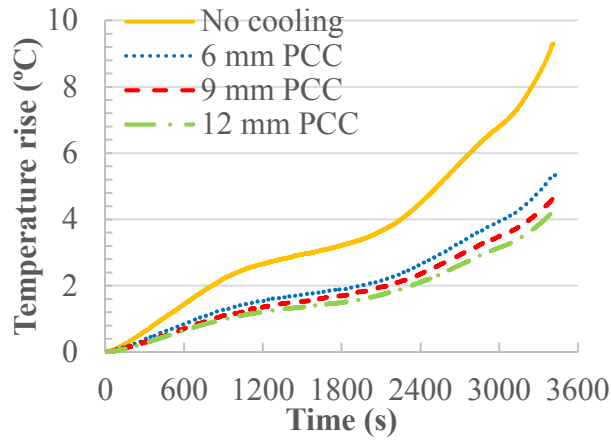
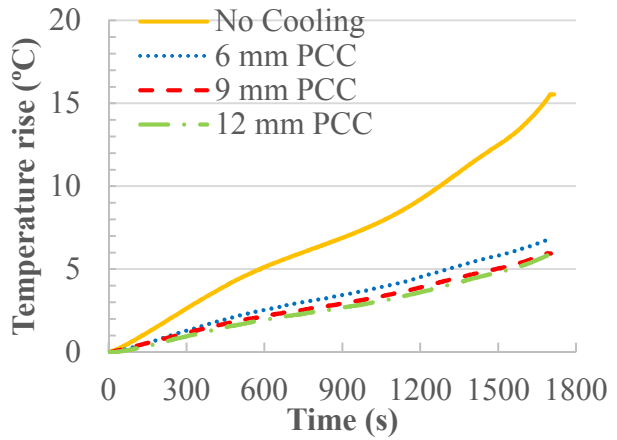


Figure 6.21: Variation in the battery pack temperature with and without PCC plates at; (a) 1C, (b) 2C, (c) 3C, (d) 4C, discharge rates.

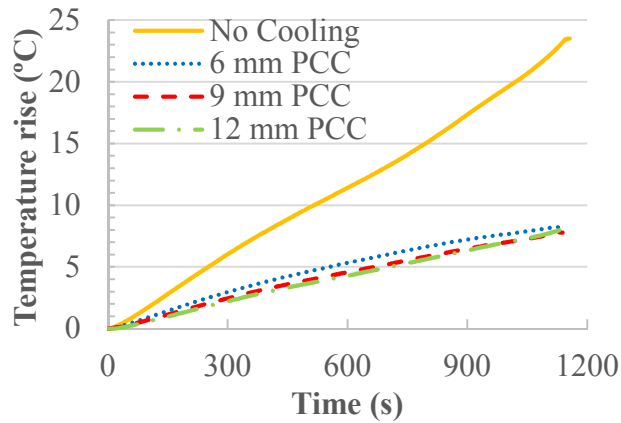
Table 6.14 provides a comparison between the maximum and average temperatures of the battery pack with and without PCC plates. Again, the colour coding is done based on the optimum operating temperature range of the Li-ion battery i.e. 25°C-40°C. It can be clearly seen from Table 6.14 that PCC plates are capable of managing the battery pack temperature within the required temperature range even at high discharge rates. There is slight variation in the battery pack temperature with an increase in PCC plate thickness.



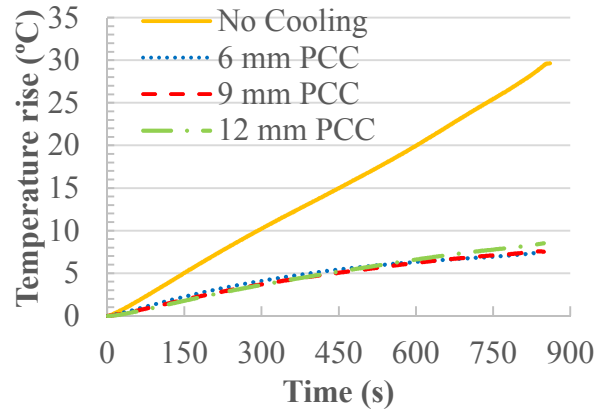
(a)



(b)



(c)



(d)

Figure 6.22: Rise in the battery pack temperature with and without PCC plates at; (a) 1C, (b) 2C, (c) 3C, (d) 4C, discharge rates.

Table 6.14: Maximum and average temperatures of the battery pack with and without PCC plates at various discharge rates.

Discharge Rate	Maximum Temperature at Various Cooling Conditions (°C)				Average Temperature at Various Cooling Conditions (°C)			
	No Cooling	With 6 mm PCC	With 9 mm PCC	With 12 mm PCC	No Cooling	With 6 mm PCC	With 9 mm PCC	With 12 mm PCC
1C	33	29.1	28.7	28	27.9	25.9	25.8	25.3
2C	42.7	34.1	33.2	32.8	34.5	30.6	30.1	29.3
3C	48.6	35.6	34.9	34.9	37	32.2	31.3	30.6
4C	56.5	36.5	36	36.4	41.7	33.8	32.9	32

It is important to compare the obtained results from developed passive BTMS using PCC plates to a conventional BTMS. Conventionally, liquid cooling is used to extract the heat from the battery pack. In a conventional BTMS, liquid flows through cold plates along the cells in the battery pack, absorbs the heat and rejects it to the condenser. The temperature and mass flow rate of liquid varies according to the battery pack temperature. In the present study, a coolant at four different temperatures is used to extract the heat from the developed battery pack. De-ionized water circulates through cold plates placed between the cells. The results obtained with cold plates and with PCC plates are compared.

As previously discussed, the temperature of the battery pack remains close to the optimum temperature of the battery with coolant at 30°C temperature at all discharge rates. The battery pack temperature with PCC plates is higher compared to liquid cooling at 30°C but remains within the optimum temperature range of the battery. This demonstrates that the liquid cooling can be replaced with PCC plates.

In the case of the cold plate, the inlet temperature of the water is kept constant during the entire experiment using a cooling bath. With PCC plates, all the experiments are performed at room temperature. Therefore, it is not worth comparing the variation of the battery pack temperature at different discharge rates with the cold plate and PCC plate, due to the different inlet temperature of the coolant in the cold plates. However, a comparison of the rise in the battery pack temperature with the cold plates and PCC plates can be made due to the same initial point (zero), as shown in Figure 6.23.

Compared to liquid cooling, the rise in the battery pack temperature at 1C, 2C and 3C is highest with the PCC plates but the gap in the temperature rise decreases with an increase in discharge rate. At 1C discharge rate, the rise in the battery pack temperature is lowest with liquid cooling at 40°C, as shown in Figure 6.23. At all other discharge rates, i.e. 2C, 3C, and 4C, the rise in the battery pack temperature remains lowest with liquid cooling at 30°C. The maximum rise in the battery pack temperature at 4C discharge rate is found to be 9.3°C with liquid cooling at 10°C.

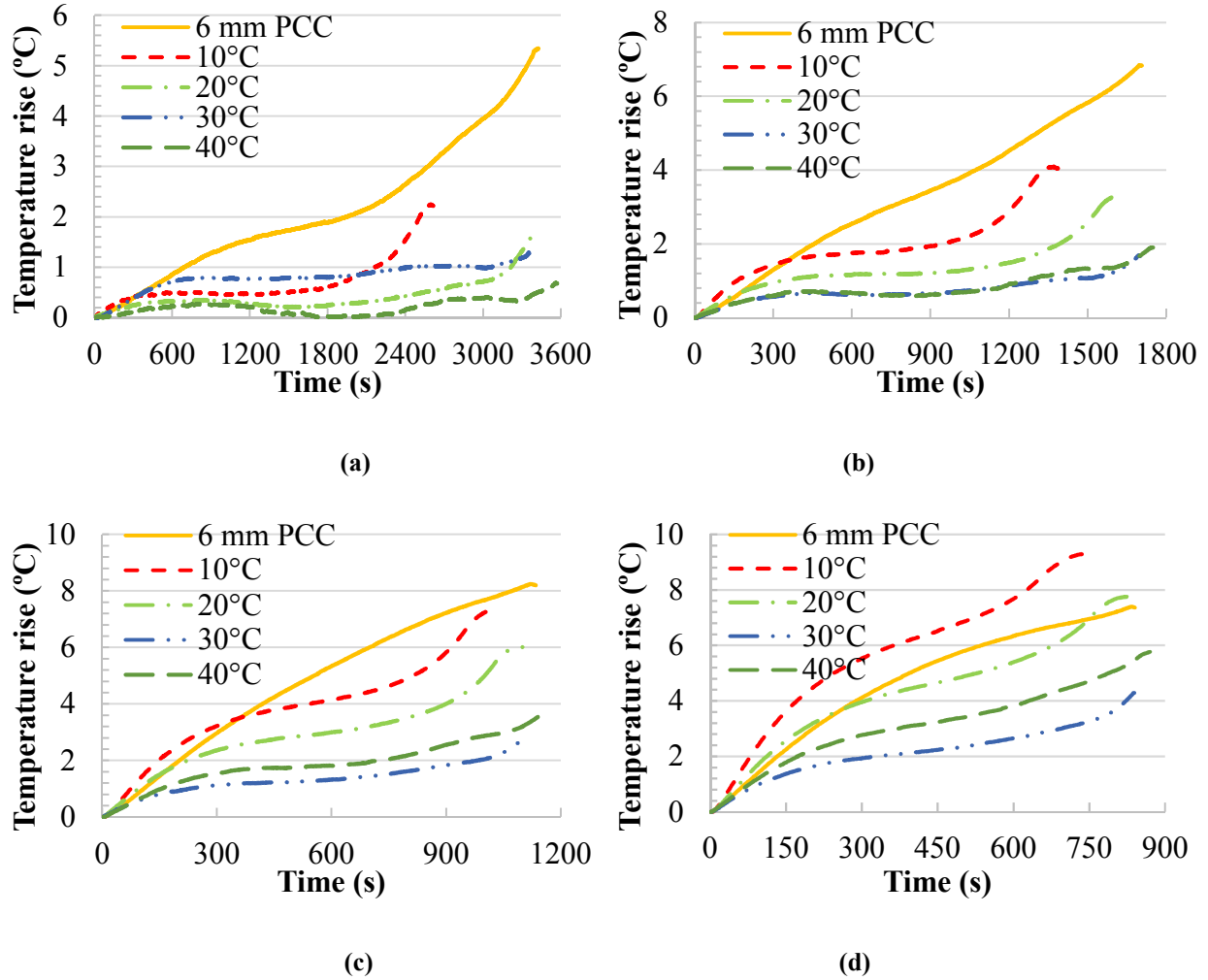


Figure 6.23: Comparison of the rise in the battery pack temperature with 6 mm thick PCC plates, and with liquid cooling at; (a) 1C, (b) 2C, (c) 3C, (d) 4C, discharge rates.

6.4 Experimental Results with Phase Change Composite Material and Liquid Cooling

Cold plates are used along with PCC plates of various thicknesses. This section describes the results obtained with cold plates at various coolant temperature along with PCC plates of various thicknesses.

6.4.1 Coolant at 10°C with Phase Change Composite Material Plates

Similar to the previous case, the ambient temperature is assumed to 20°C, and de-ionized water is used as a coolant. The criteria for the selection of 10°C temperature is the same as previously discussed in section 6.2.1. Figure 6.24(a-c) shows the variation in the battery pack voltage at 10°C

coolant temperature for various discharge rates and with various thicknesses of PCC plates; and trends are similar to the previous case when only coolant is used.

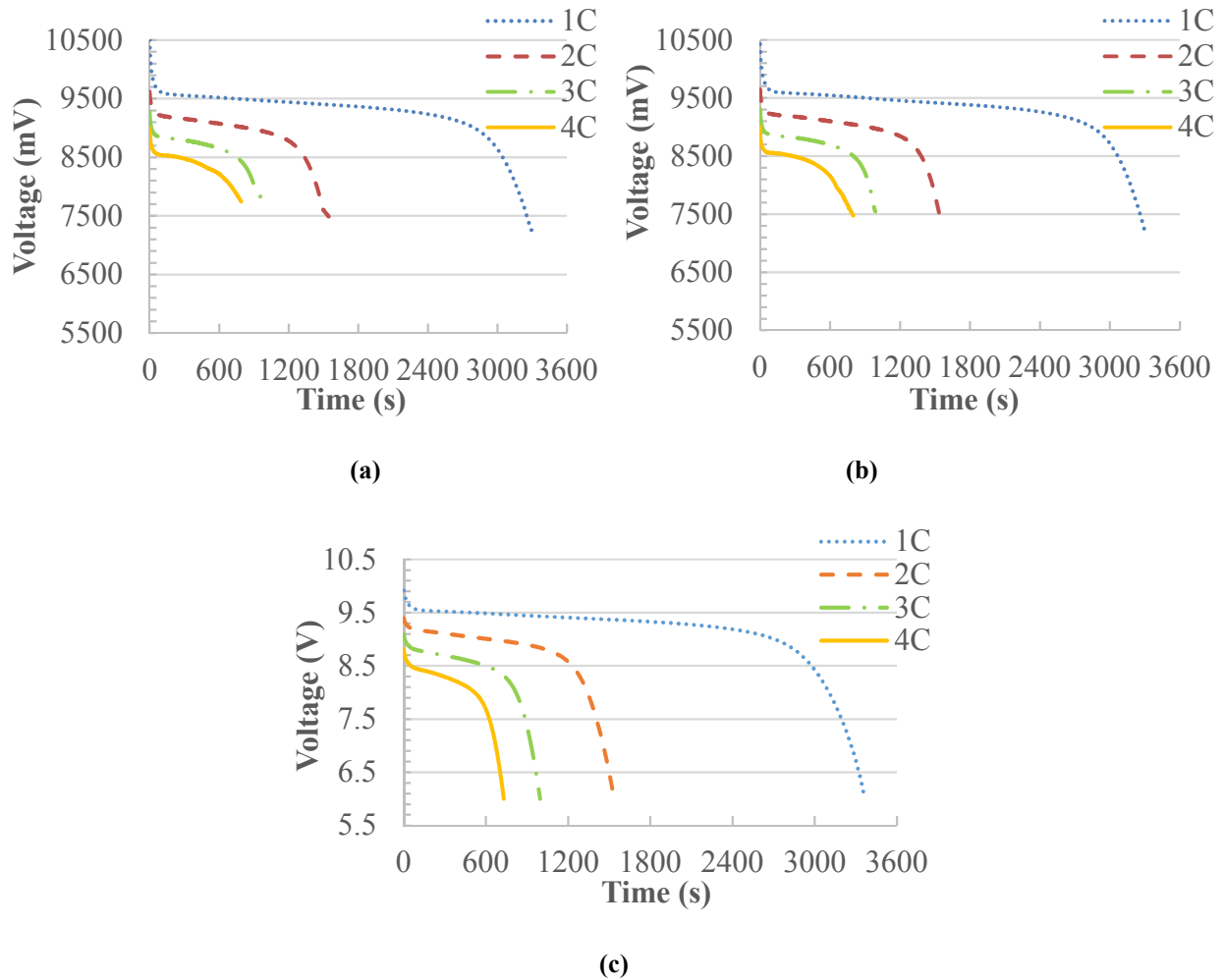


Figure 6.24: Variation in voltage with 10°C coolant temperature at various discharge rates with; (a) 6 mm, (b) 9 mm, (c) 12 mm, thick PCC plates.

Although the bath temperature is fixed to 10°C, the inlet temperature of water at the cold plate is higher than 10°C. Again, this occurs because the ambient temperature is higher than the coolant temperature. Therefore, heat transfers from the atmosphere to the pipes carrying the coolant at 10°C. Figure 6.25(a-c) shows the variation in the battery pack temperature with the coolant at 10°C and PCC plates for various discharge rates.

An interesting observation can be made from Figure 6.25, which shows that the temperature of the battery pack increases with an increase in the PCC plate's thickness. These trends are opposite

from the case where only PCC plates are used. As in the case of PCC plates only, the temperature of the battery pack decreases with the increase in plate thickness. The possible explanation for the change in trends may be the decrease in heat transfer rate to cold plates due to the increase in thickness of the PCC plates. As in this case, PCC plates are used on one side of the cells, and cold plates are used on the other side of the cells in the battery pack. The battery pack has a maximum temperature of 24°C with 12 mm thick PCC plates at a 4C discharge rate.

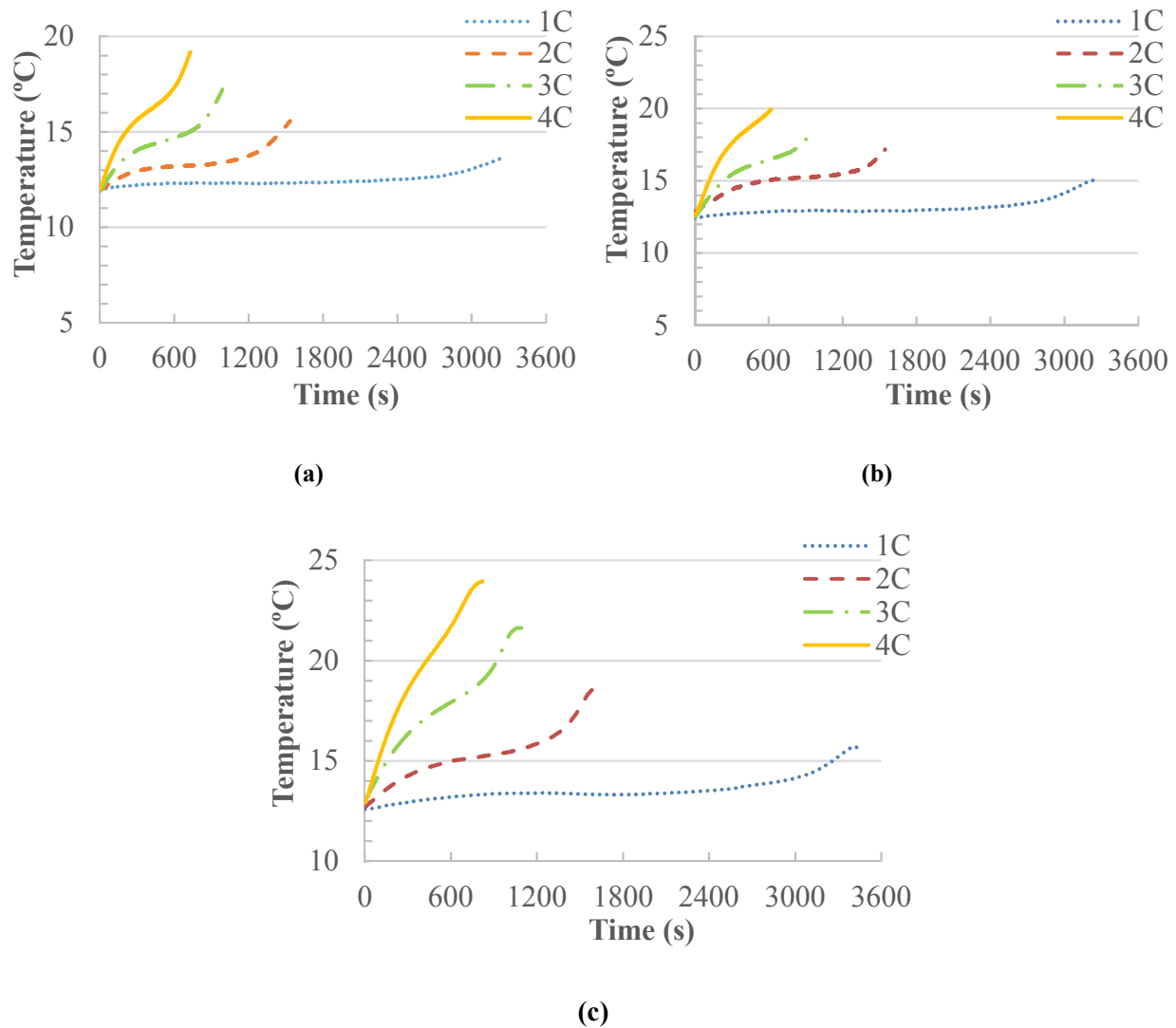


Figure 6.25: Variation in temperature of the battery pack with 10°C coolant temperature at various discharge rates with; (a) 6 mm, (b) 9 mm, (c) 12 mm, thick PCC plates.

Figure 6.26 shows the rise in temperature at various discharge rates and with various thicknesses of PCC plates with coolant temperature at 10°C. The maximum rise of 11.2°C in the battery pack temperature is obtained with 12 mm thick PCC plates at 4C discharge rates.

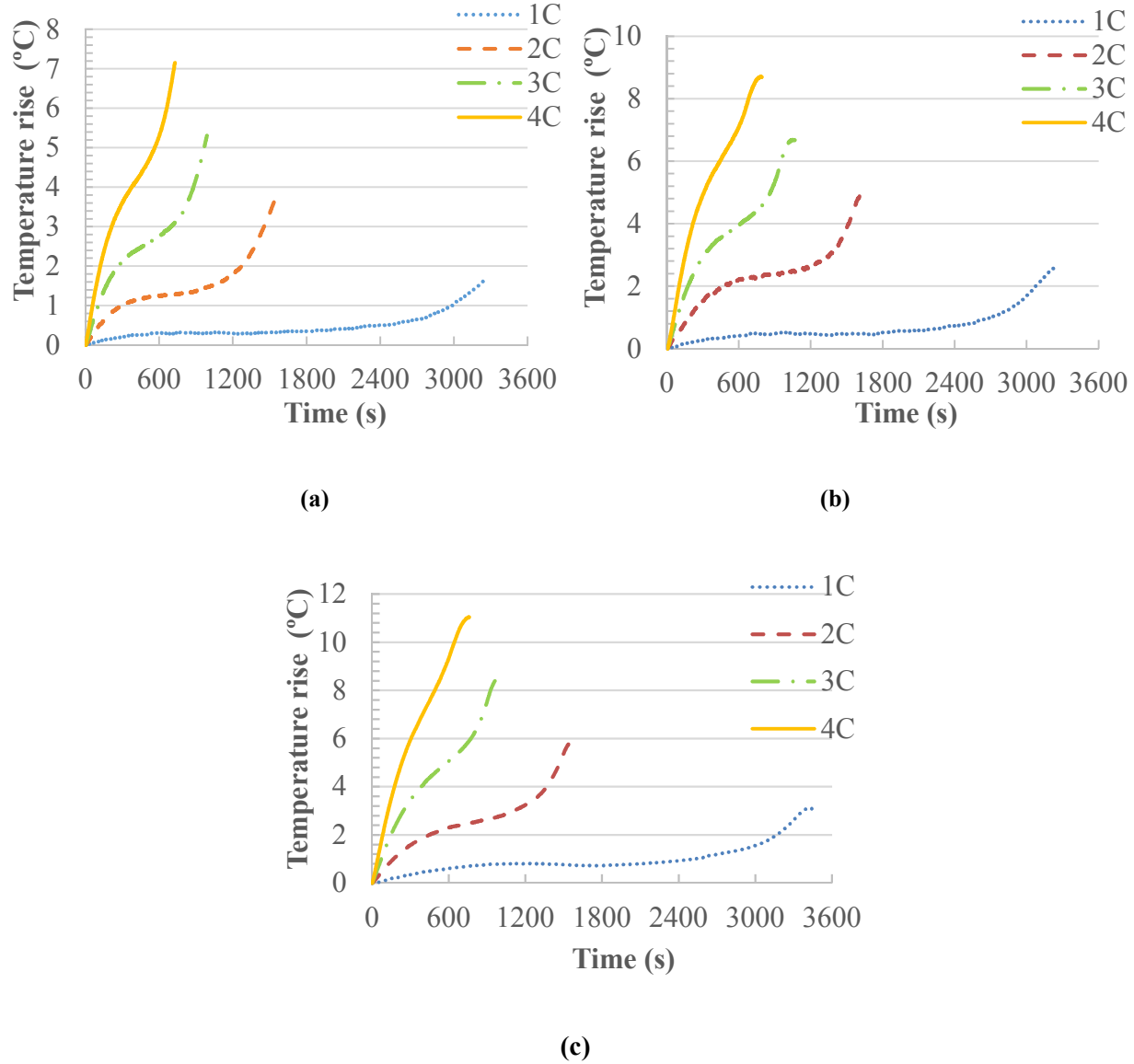


Figure 6.26: Temperature rise in the battery pack with 10°C coolant temperature at various discharge rates with; (a) 6 mm, (b) 9 mm, (c) 12 mm, thick PCC plates.

6.4.2 Coolant at 20°C with Phase Change Composite Material Plates

The criteria for the selection of 20°C coolant temperature is the same as previously described in section 6.2.2. Figure 6.27 shows the variation in voltage at 20°C temperature for various discharge

rates. A similar trend in voltage variation can be seen as compared to no cooling and with 10°C coolant temperature with some improvement in voltage.

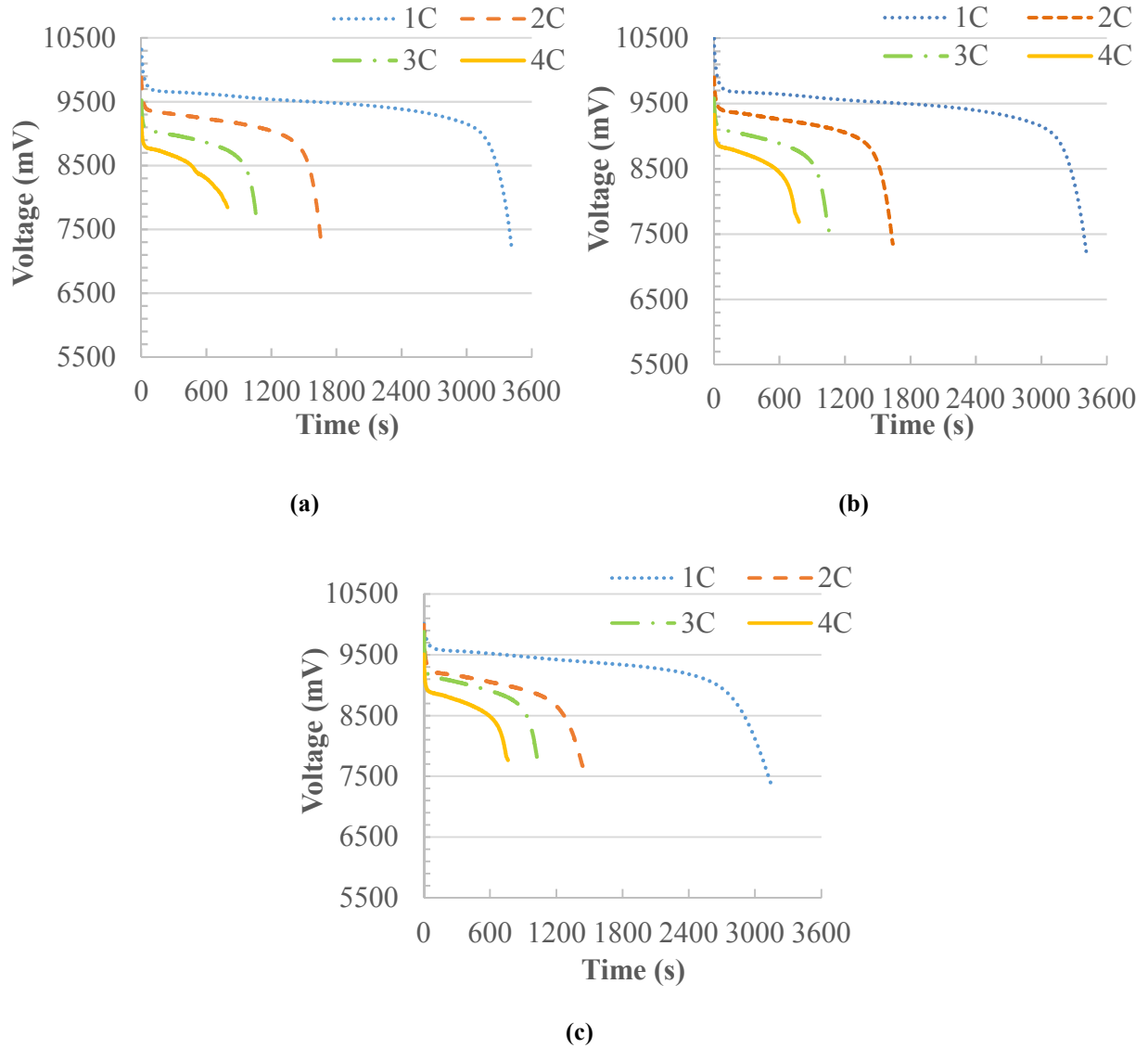


Figure 6.27: Variation in voltage with 20°C coolant temperature at various discharge rates with; (a) 6 mm, (b) 9 mm, (c) 12 mm, thick PCC plates.

Figure 6.28(a-c) shows the variation in the battery pack temperature at various discharge rates and with various PCC plates and coolant at 20°C. Similar trends in the rise of the battery pack temperature are observed with coolant at 10°C temperature, as in the previous case. Again, the temperature of the battery pack increases with an increase in PCC plate thickness. These trends are opposite from the case where only PCC plates are used. The possible explanation is the same

as previously described in section 6.4.1. The battery pack has a maximum temperature of 30.3°C with 12 mm thick PCC plates at 4C discharge rate.

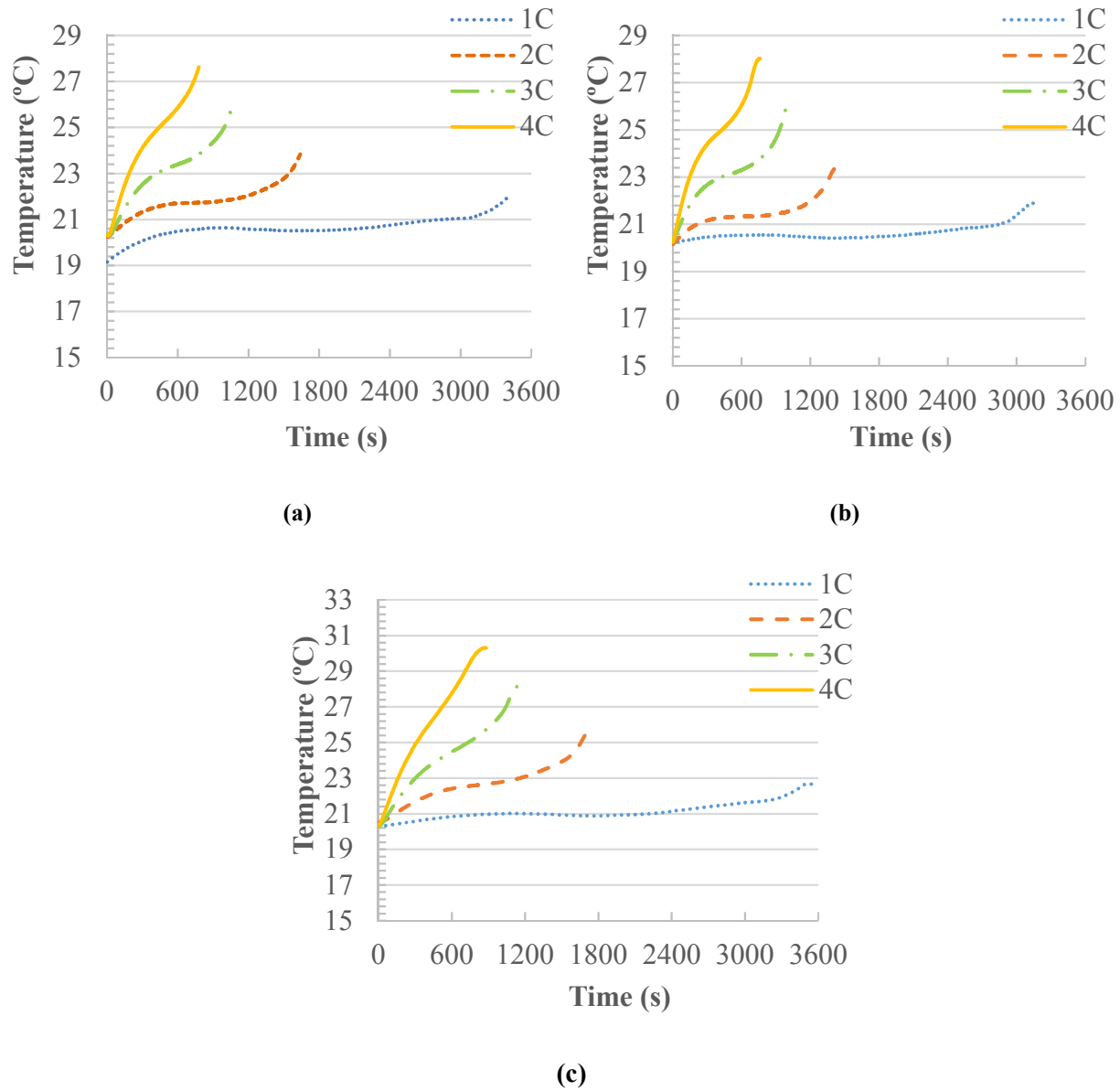


Figure 6.28: Variation in temperature of the battery pack with 20°C coolant temperature at various discharge rates with; (a) 6 mm, (b) 9 mm, (c) 12 mm, thick PCC plates.

Figure 6.29 shows the rise in the battery pack temperature at various discharge rates and at various thicknesses of PCC plates when the coolant inlet temperature is 20°C. The trends in the temperature of the battery obtained are similar to when the coolant inlet temperature was 10°C. A

maximum rise of 9.9°C in the battery pack temperature is obtained with the 12 mm thick PCC plates at 4C discharge rates.

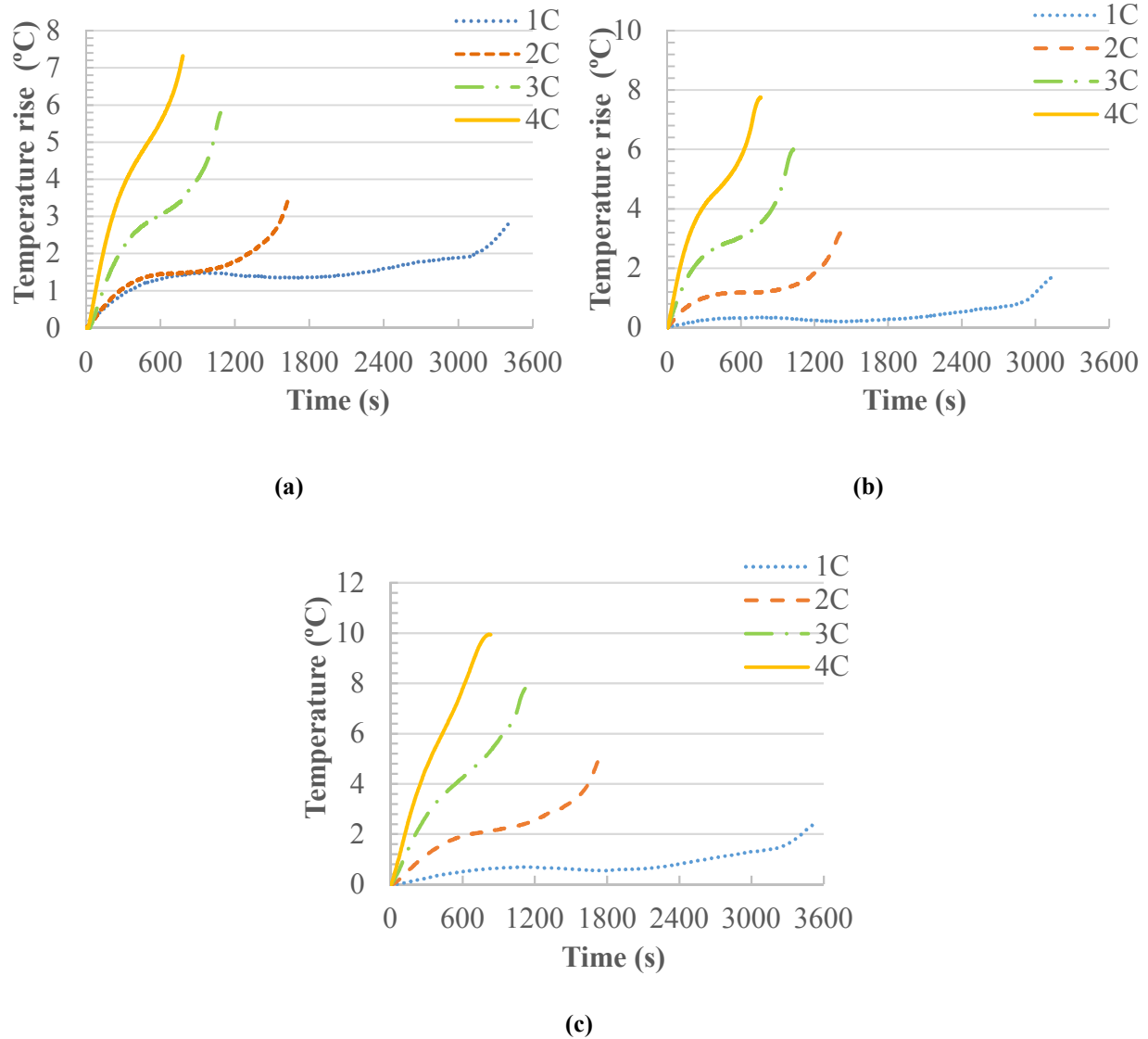


Figure 6.29: Temperature rise in the battery pack with 20°C coolant temperature at various discharge rates with; (a) 6 mm, (b) 9 mm, (c) 12 mm, thick PCC plates.

6.4.3 Coolant at 30°C with Phase Change Composite Material Plates

The selection criteria of 30°C coolant temperature is the same as previously described in section 6.2.3. Figure 6.30 shows the variation in voltage at 30°C temperature for various discharge rates. Although trends are similar to previous cases, an improvement in voltage at all discharge rates can

be seen from Figure 6.30. The variation in voltage in the case of 12 mm thick PCC plates is different from the other two cases as that experiment is conducted using the second test bench.

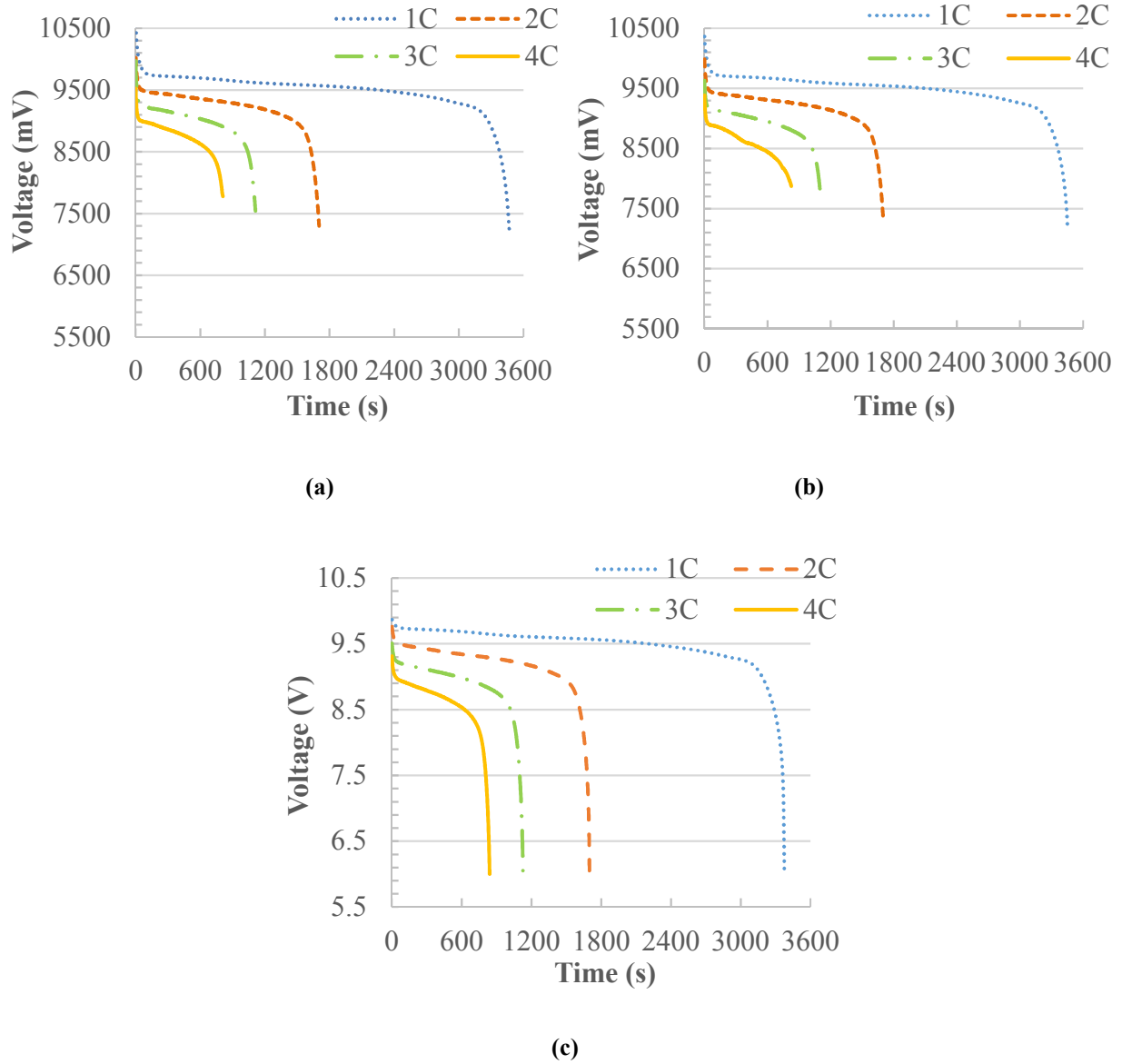


Figure 6.30: Variation in voltage with 30°C coolant temperature at various discharge rates with; (a) 6 mm, (b) 9 mm, (c) 12 mm, thick PCC plates.

Figure 6.31(a-c) shows the variation in the battery pack temperature at various discharge rates and with various PCC plates and 30°C coolant temperature. Minor changes in the battery pack temperature are observed at 1C discharge with all PCC plates. It can be observed from Figure 6.31 that the battery pack temperature remains in the optimum temperature range of the Li-ion battery

with 30°C coolant temperature. The battery pack has a maximum temperature of 35.5°C with 12 mm thick PCC plates at 4C discharge rate.

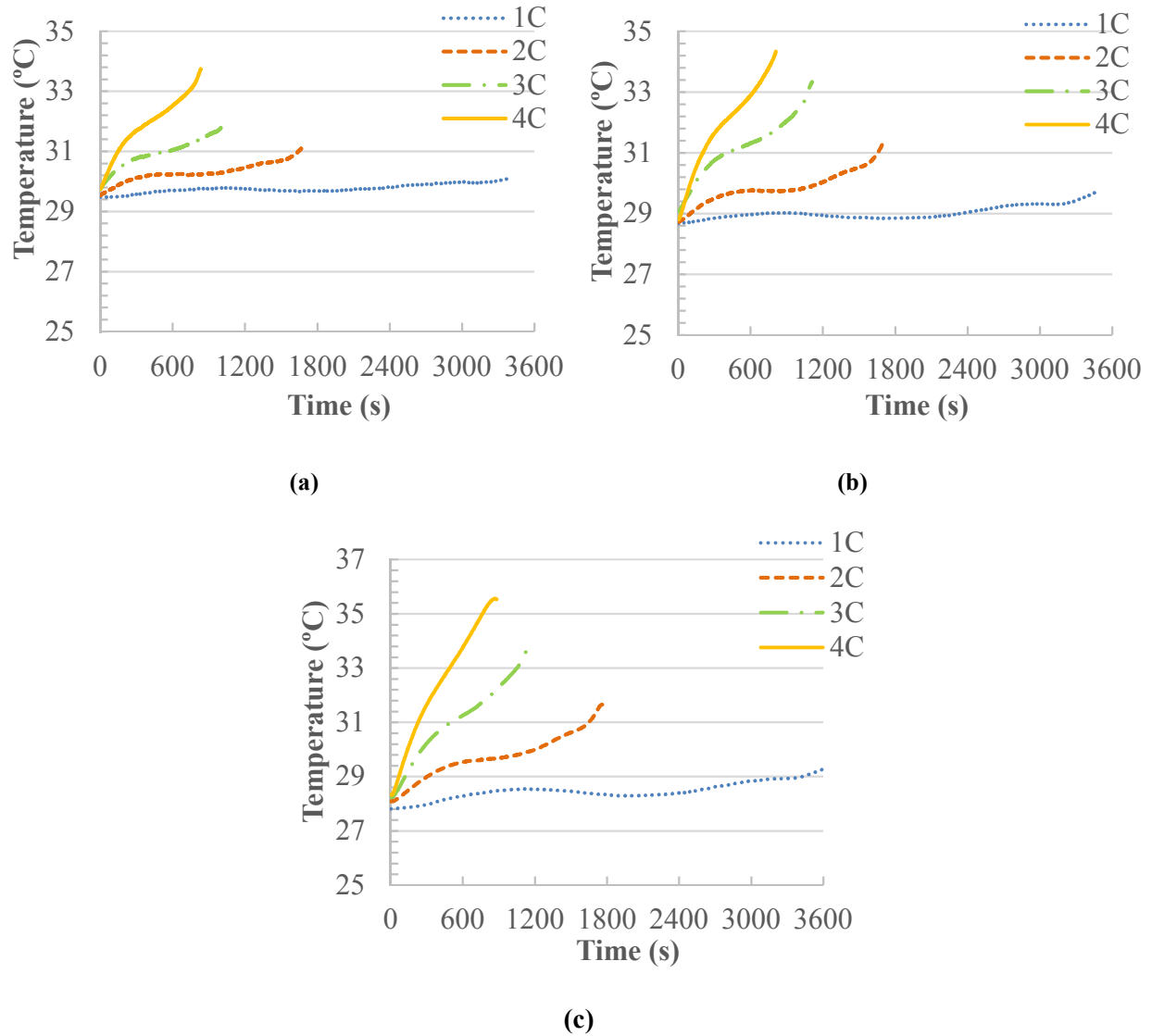


Figure 6.31: Variation in temperature of the battery pack with 30°C coolant temperature at various discharge rates with; (a) 6 mm, (b) 9 mm, (c) 12 mm, thick PCC plates.

Figure 6.32 shows the rise in the battery pack temperature at various discharge rates and with PCC plates of various thicknesses when the coolant inlet temperature is 30°C. Similar trends in the temperature of the battery pack are obtained with the PCC plate and coolant at 30°C as in the case when the coolant inlet temperature is 30°C. A maximum rise of 7.2°C in the battery pack temperature is obtained at 4C discharge rate with 12 mm thick plates.

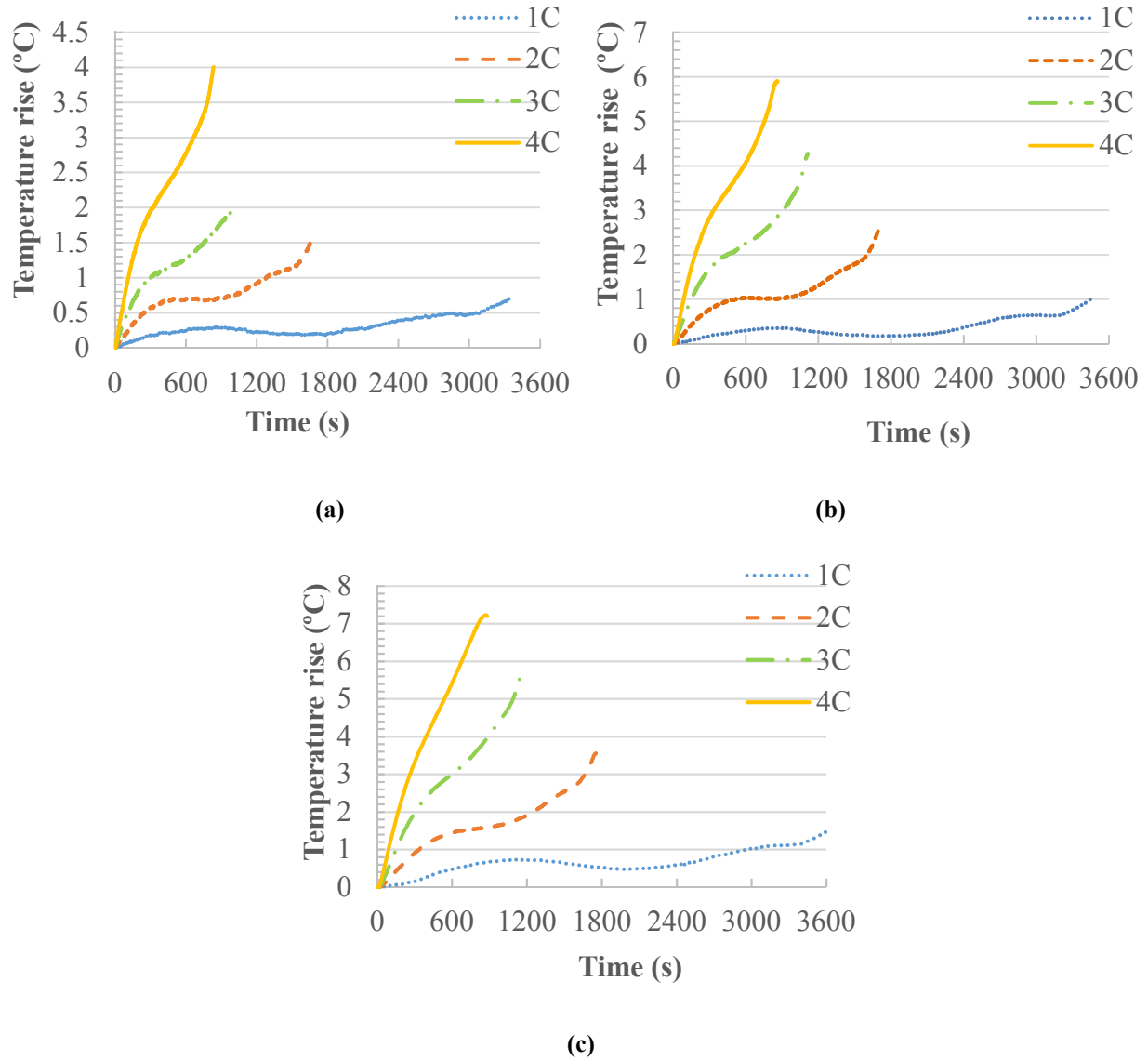


Figure 6.32: Temperature rise in the battery pack voltage with 30°C coolant temperature at various discharge rates with; (a) 6 mm, (b) 9 mm, (c) 12 mm, thick PCC plates.

6.4.4 Coolant at 40°C with Phase Change Composite Material Plates

Figure 6.33 shows the variation in voltage at 40°C temperature for various discharge rates and a similar trend can be seen as in previous cases. The lowest value of the voltage in this case is different than previous cases due to the use of a second experimental setup for testing.

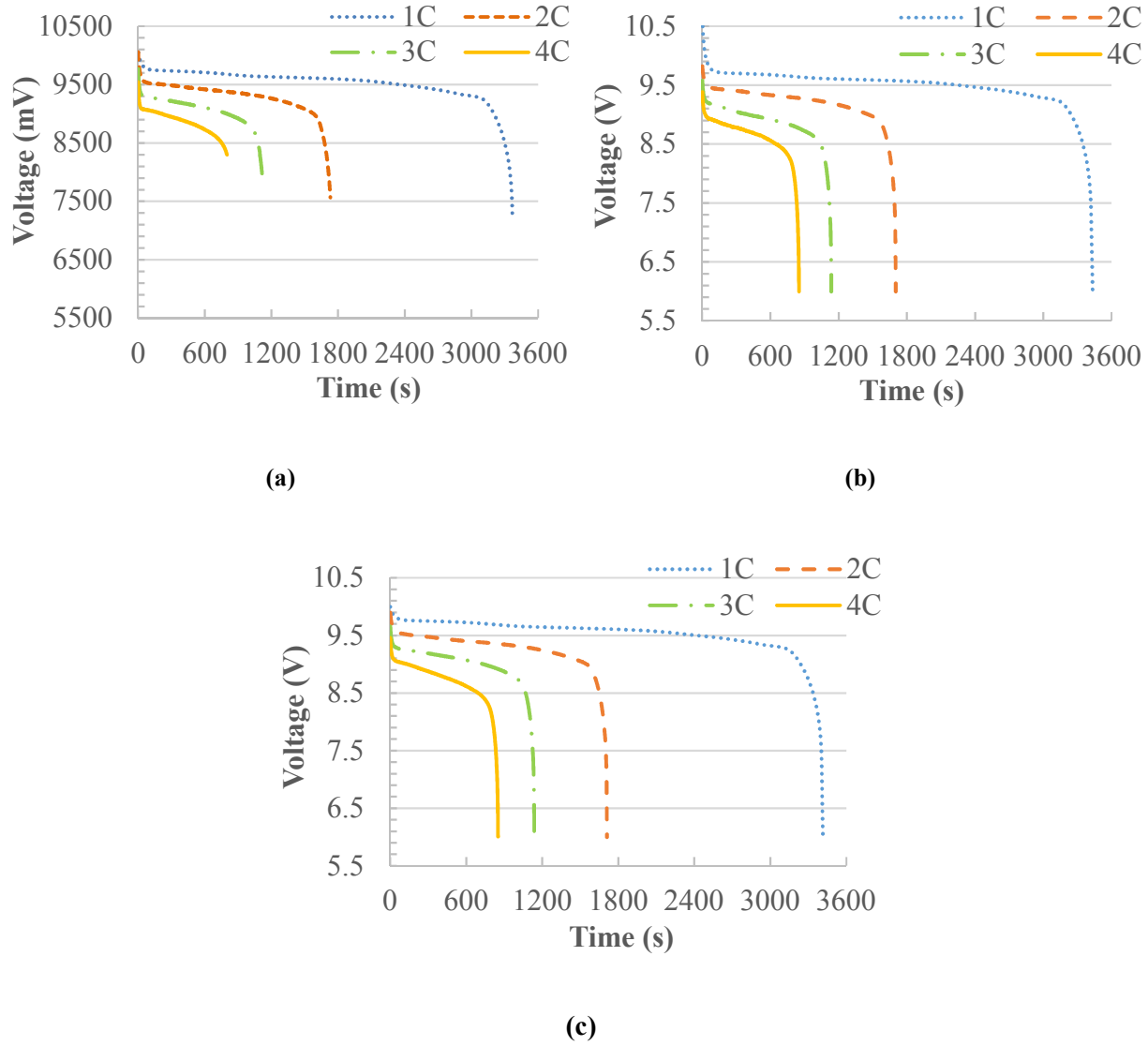


Figure 6.33: Variation in the battery pack voltage with 40°C coolant temperature at various discharge rates with; (a) 6 mm, (b) 9 mm, (c) 12 mm, thick PCC plates.

Although the bath temperature is fixed at 40°C, again the inlet temperature of the water in the cold plate is lower than 40°C due to the same reason discussed earlier in section 6.2.4. Figure 6.35 shows the variation and rise in the battery pack temperature with the coolant at 40°C and PCC plates at various discharge rates. In this case, the temperature trends are different than previous one with 30°C coolant temperature. The temperature of the battery pack decreases with an increase in PCC plate thickness. The possible explanation for the change in temperature trends can be due to the fact that, at 40°C coolant temperature, the PCC starts melting and reverse heat transfer may

occur. Therefore, PCC plates are more effective in removing the heat from cells compared to cold plates. The initial temperature of the battery pack at 1C discharge rate with 9 mm PCC is higher than other discharge rates, as the experiment is conducted separately and may be affected by ambient temperature. The battery pack has a maximum temperature of 42.3°C with 6 mm thick PCC plates at 4C discharge rate.

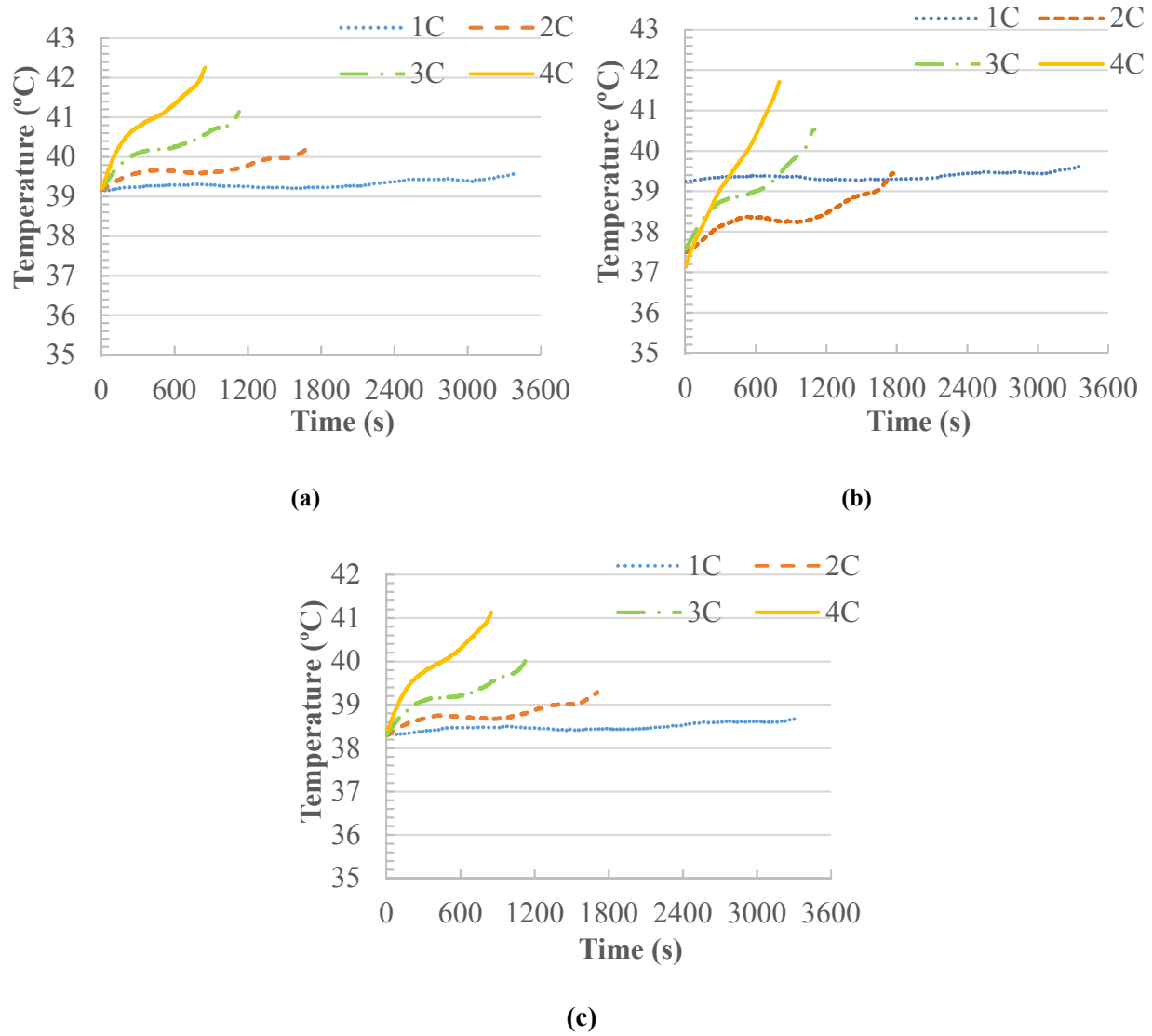


Figure 6.34: Variation in temperature of the battery pack with 40°C coolant temperature at various discharge rates with; (a) 6 mm, (b) 9 mm, (c) 12 mm, thick PCC plates.

Figure 6.35 shows the rise in the battery pack temperature at various discharge rates with PCC plates when the coolant inlet temperature is 40°C. A maximum rise of 4.5°C in the battery pack temperature is obtained with 6 mm thick PCC plates at 4C discharge rates.

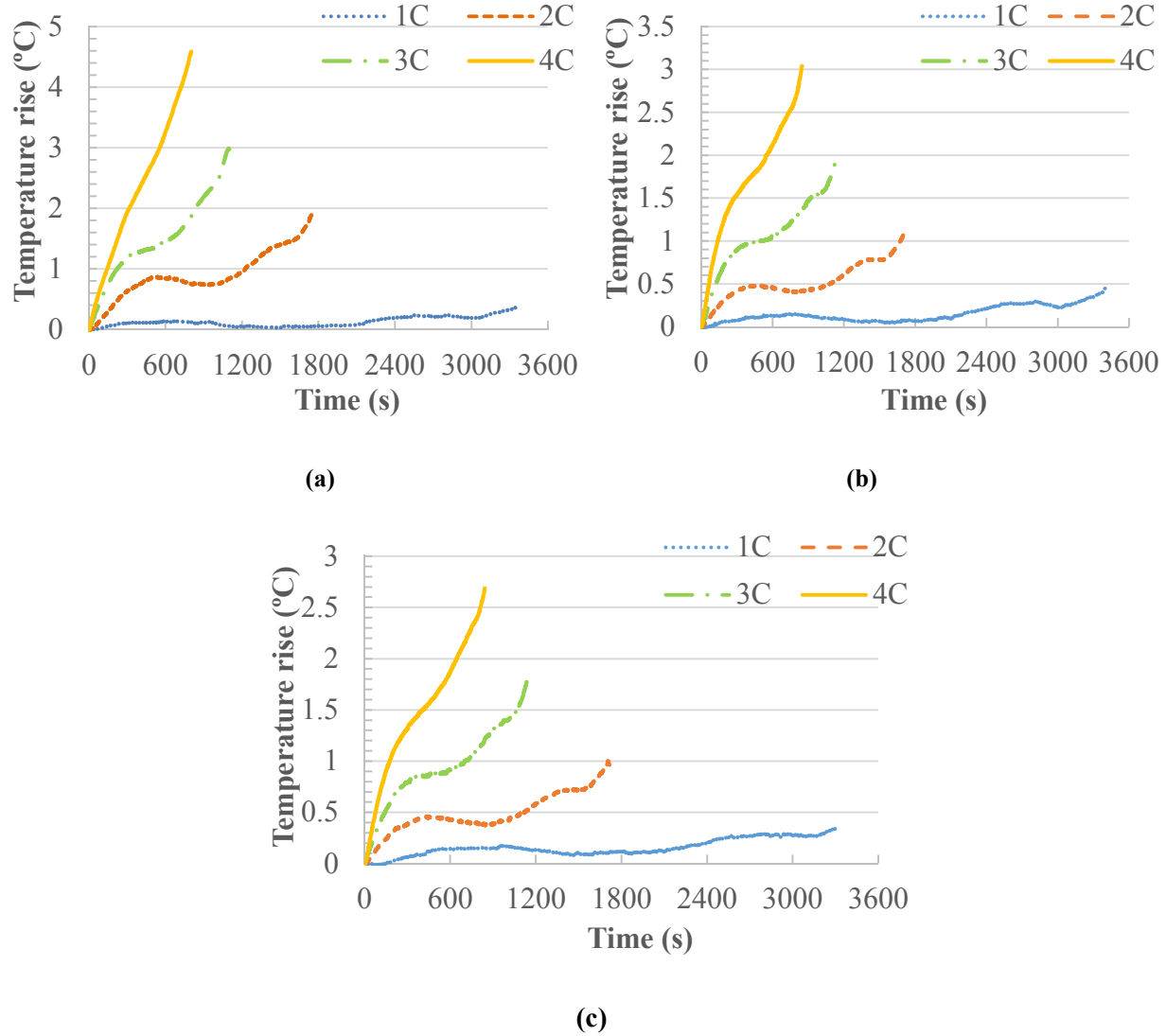


Figure 6.35: Temperature rise in the battery pack with 40°C coolant temperature at various discharge rates with; (a) 6 mm, (b) 9 mm, (c) 12 mm, thick PCC plates.

Table 6.15 provides the maximum and average temperatures of the battery at various discharge rates and with PCC plates of various thicknesses. Again, it can be seen from Table 6.15 that the maximum and average temperatures of the battery pack remain within the optimum operating range of the Li-ion battery pack with 30°C coolant temperature.

Table 6.15: Maximum and average temperatures of the battery pack with PCC plates at various discharge rates.

Thickness of PCC plate (mm)	Coolant Inlet Temperature (°C)	Maximum Temperature of Battery Pack at Various Discharge Rates (°C)				Average Temperature of Battery Pack at Various Discharge Rates (°C)			
		1C	2C	3C	4C	1C	2C	3C	4C
6	10	13.6	15.5	17.2	19.1	12.5	13.4	14.5	15.8
	20	21.9	23.4	25.5	26.6	21.1	21.8	23.1	24.4
	30	29.5	31.1	31.8	33.7	28.5	29.7	30.9	31.9
	40	39.6	40.3	41.1	42.3	39.3	39.3	40.2	40.9
9	10	15.0	17.9	19.2	21.4	13.2	15.2	16.2	17.9
	20	22.0	23.8	26.1	27.6	20.6	22.8	24	25.9
	30	29.7	31.4	33.3	34.7	29.0	29.9	31.2	32.1
	40	39.6	39.4	40.5	41.7	39.4	38.4	39.2	39.5
12	10	15.7	18.6	21.6	24.0	13.6	15.3	17.6	19.4
	20	22.6	25.7	26.3	28.0	20.6	23.2	24.2	26
	30	30.2	31.7	33.9	35.5	29.8	30.3	31.3	32.5
	40	38.7	39.3	40	41.1	38.5	38.8	39	39.5

6.5 Experimental Results with Phase Change Materials and Carbon Nanotubes

In this section, the results obtained with pure and technical grades of PCM plates at various discharge rates and various thicknesses are presented. Furthermore, the results obtained with plates made with various combinations of the PCM, CNTs and polyurethane foam are presented for various discharge rates.

6.5.1 3 mm Thick Plates of Technical Grade Phase Change Material

PCM plates made with technical grade PCM along with polyurethane foam are used with the battery pack to investigate the thermal and electrical behaviour of the Li-ion battery. This section deals with the results obtained with 3 mm thick plates of polyurethane foam and various combinations of technical grade PCM and CNTs. The melting point of technical grade PCM is 28°C. Figure 6.36 (a) shows the variation in temperature at various discharge rates with 3 mm thick plates of polyurethane foam and technical grade PCM. At 1C discharge rate, the maximum temperature of the battery pack reaches 25.9°C. At 2C, 3C and 4C discharge rates, the maximum temperature of the battery pack reaches 31.5°C, 39.4°C and 45.1°C, respectively. At 1C discharge

rate, the temperature of the battery pack remains lower than the melting temperature of PCM. This means that all the heat absorbed by the PCM is in the form of sensible heat. Figure 6.36 (b) shows the rise in the battery pack temperature at various discharge rates. At 1C discharge rate, the temperature rise is only 2.7°C. At 2C, 3C and 4C, the rise in temperature of the battery pack is 6.1°C, 13.6°C, and 19.2°C, respectively. The high rise in temperature of the battery pack at 3C and 4C shows that the 3 mm thick PCM plates are not capable of completely and quickly absorbing all the heat at high discharge rates. Figure 6.36 (c) shows the variation in voltage with 3 mm thick PCM and polyurethane foam plates at various discharge rates. The trend of voltage variation in the battery pack at various discharge rates is similar to previous cases discussed in section 6.3. A small improvement in battery pack voltage can be observed at 1C discharge rate.

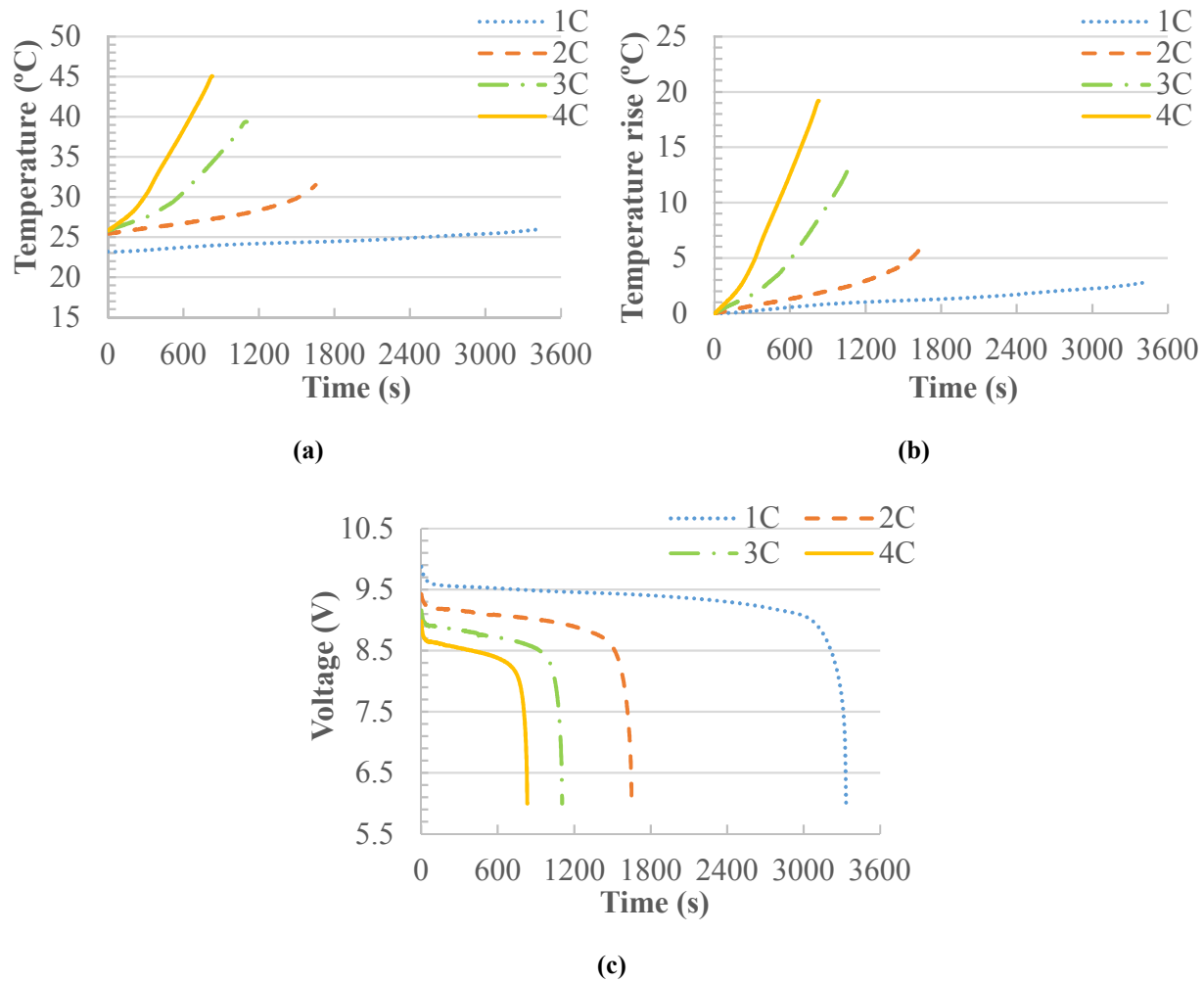


Figure 6.36: With 3 mm thick technical grade PCM plates; (a) variation in temperature, (b) rise in temperature, (c) variation in voltage, at various discharge rates.

The maximum temperature, average temperature, and rise in temperature of the battery pack with 3 mm thick technical grade PCM plates at various discharge rates are given in Table 6.16. From Table 6.16, it can be observed that the maximum temperature of the battery pack at 1C, 2C, and 3C discharge rates remains within the optimum temperature range of the Li-ion battery, i.e. 25°C-40°C, while at 4C discharge rate, the maximum temperature of the battery pack is beyond the required temperature range of the battery. The average temperature of the battery pack at all discharge rates remains within the optimum operating temperature range with 3 mm thick technical grade PCM plates.

Table 6.16: Maximum temperature, average temperature, and rise in temperature of the battery pack with 3 mm thick technical grade PCM plates at various discharge rates.

Discharge Rate	Maximum Temperature (°C)	Average Temperature (°C)	Temperature Rise (°C)
1C	25.9	24.5	2.7
2C	31.5	27.5	6.1
3C	39.4	31.0	13.6
4C	45.1	34.0	19.2

To improve the effectiveness of PCM through enhancement in thermal conductivity, 3 mm thick plates are made using technical grade PCM, polyurethane foam and 1.5% (wt.) CNT. The concentration of CNTs in PCM is in weight percentage in all the experiments. These plates are used to investigate the thermal and electrical behaviour of the battery pack at various discharge rates. Figure 6.37 (a) shows the variation in temperature with respect to time at various discharge rates with the 3 mm thick plates consisting of technical grade PCM, polyurethane foam, and 1.5% CNT. A small improvement in thermal conductivity of technical grade PCM can be seen in terms of temperature drop in the maximum temperature of the battery pack with the use of 1.5% CNT. At 1C discharge rate, the maximum temperature of the battery pack reaches 26.1°C. At 2C, 3C and 4C discharge rate, the maximum temperature of the battery pack reaches 31.2°C, 39°C, and 44.1°C, respectively. Figure 6.37 (c) shows the variation in voltage with 3 mm thick plates made of PCM, polyurethane foam and 1.5% CNT at various discharge rates.

The maximum temperature, average temperature, and rise in temperature of the battery pack with the 3 mm thick plates made of technical grade PCM, polyurethane foam, and 1.5% CNT are given in Table 6.17. From Table 6.17, it can be seen that the maximum temperature of the battery pack

at 1C, 2C, and 3C discharge rates remains within the optimum temperature range of the Li-ion battery, i.e. 25°C-40°C. Again, at 4C discharge rate, the maximum temperature of the battery pack is beyond the required temperature range. The average temperature of the battery pack at all selected discharge rates remains within the required temperature range of the battery.

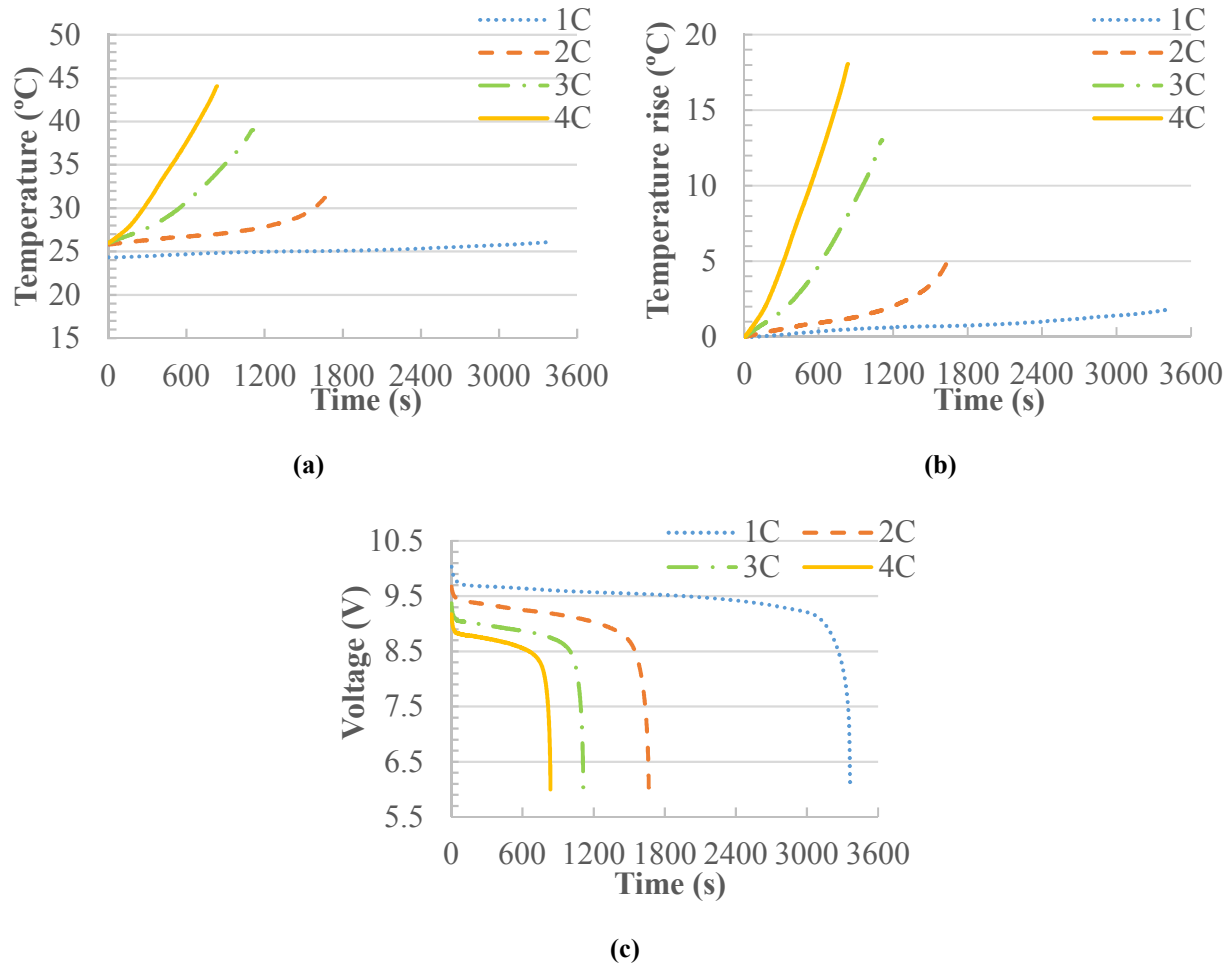


Figure 6.37: With 3 mm thick technical grade PCM and 1.5% CNT plates; (a) variation in temperature, (b) rise in temperature, (c) variation in voltage, at various discharge rates.

Table 6.17: Maximum temperature, average temperature and rise in temperature of the battery pack with 3 mm thick technical grade PCM and 1.5 % CNT plates at various discharge rates.

Discharge Rate	Maximum Temperature (°C)	Average Temperature (°C)	Temperature Rise (°C)
1C	26.1	25.1	1.8
2C	31.2	27.4	5.4
3C	39.0	31.0	13.0
4C	44.1	33.8	18.1

To investigate the effect of an increase in CNT concentration on the thermal behaviour of the battery, 3 mm thick plates are made up of technical grade PCM, polyurethane foam and 3% CNT. Figure 6.38 (a) shows the variation in the battery pack temperature at various discharge rates with the 3 mm thick plates of PCM, polyurethane foam and 3% CNT. A small improvement in thermal conductivity of PCM can be observed from Figure 6.38, in terms of temperature drop in the maximum temperature of the battery pack. At 1C discharge rate, the maximum temperature of the battery pack reaches 25.9°C. At 2C, 3C and 4C, the maximum temperature of the battery pack reaches 30.5°C, 38.1°C and 43.5°C, respectively. Further improvement can be observed in thermal conductivity of PCM in terms of a temperature drop in the maximum temperature of the battery pack with the use of 3% CNT. Figure 6.38 (c) shows the variation in voltage with 3 mm thick plates of technical grade PCM, polyurethane foam and 3% CNT at various discharge rates. The trend of voltage variation in the battery pack is the same as in the previous case.

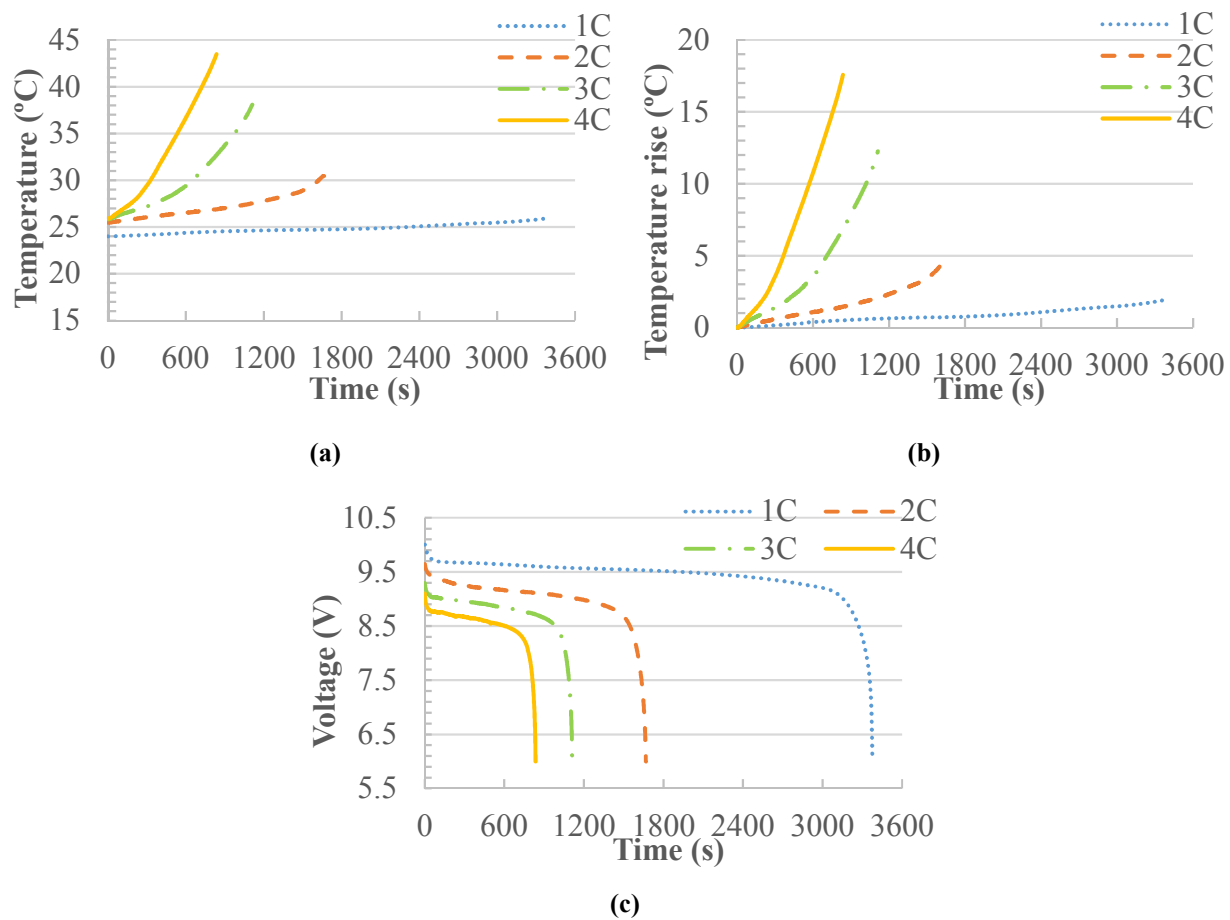


Figure 6.38: With 3 mm thick technical grade PCM and 3% CNT plates; (a) variation in temperature, (b) rise in temperature, (c) variation in voltage, at various discharge rates.

The maximum temperature, average temperature, and rise in temperature of the battery pack with the 3 mm thick plates made of technical grade PCM, polyurethane foam, and 3% CNT are given in Table 6.18. Similar to the previous case, from Table 6.18, it can be seen that the maximum temperature of the battery pack at 1C, 2C, and 3C discharge rates remains within the required temperature range of the battery, i.e. 25°C-40°C, while at 4C discharge rate, the maximum temperature of the battery pack is beyond the optimum operating temperature range of the battery. The average temperature of the battery rates remains within the required range with the 3 mm thick plates made of technical grade PCM, polyurethane foam, and 3% CNT at all discharge rates.

Table 6.18: Maximum temperature, average temperature, and rise in temperature of the battery pack with 3 mm thick technical grade PCM and 3% CNT plates at various discharge rates.

Discharge Rate	Maximum Temperature (°C)	Average Temperature (°C)	Temperature Rise (°C)
1C	25.9	24.8	1.9
2C	30.5	27.2	5.0
3C	38.1	30.0	12.3
4C	43.5	32.9	17.6

Figure 6.39 shows a comparison of variation in temperature of the battery pack with and without technical grade PCM plates. It can be clearly seen that use of PCM-based plates significantly reduces the temperature of the battery pack. However, the effect of using CNTs with a technical grade of PCM is not quite visible.

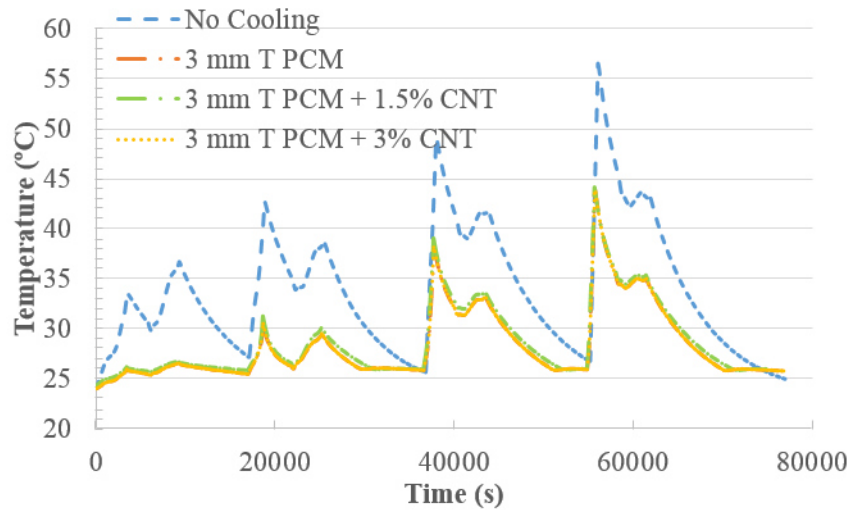


Figure 6.39: Temperature profile of the battery pack with 3 mm thick technical grade PCM based plates at various charge and discharge rates.

6.5.2 3 mm Thick Plates of Pure Phase Change Material

In this section, the results obtained from the battery pack with 3 mm thick plates made from pure PCM, polyurethane foam and different concentrations of CNTs are presented. The melting temperature of pure PCM is 28.2°C. Figure 6.40 (a) shows the variation in the battery pack temperature with 3 mm thick plates of polyurethane foam and pure PCM at various discharge rates. At 1C discharge rate, the maximum temperature of the battery pack reaches 27.4°C. At 2C, 3C and 4C, the maximum temperature of the battery pack reaches 29.3°C, 35.2°C and 42.1°C, respectively. At 1C discharge rate, as the temperature of the battery pack remains lower than the melting temperature of PCM, the heat absorbed by PCM is in the form of sensible heat. Figure 6.40 (b) shows the rise in the battery pack temperature at various discharge rates with 3 mm thick plates of polyurethane foam and pure PCM.

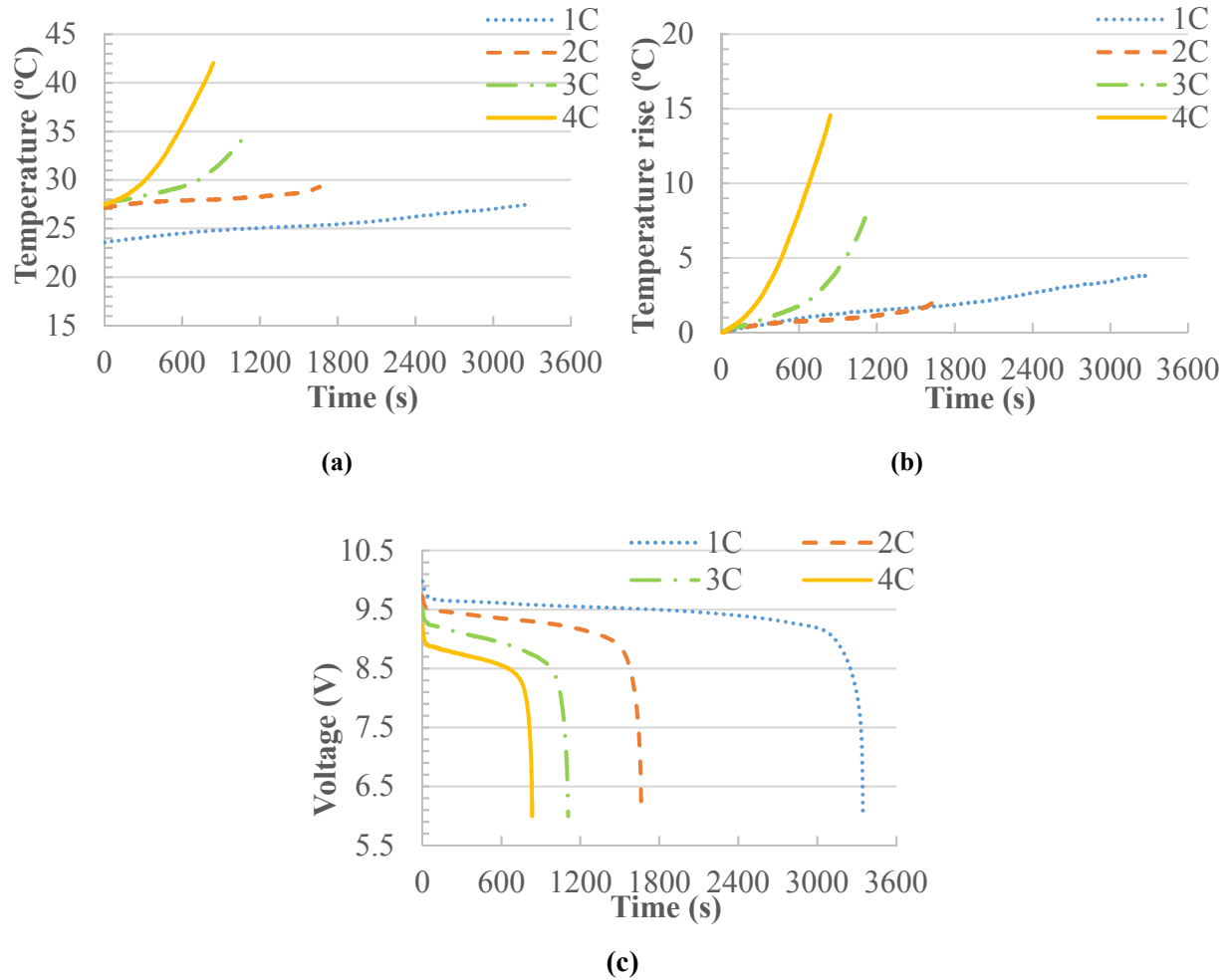


Figure 6.40: With 3 mm thick pure PCM plates; (a) variation in temperature, (b) rise in temperature, (c) variation in voltage, at various discharge rates.

At 1C discharge rate, the temperature rise is only 3.8°C. At 2C, 3C and 4C, the rise in temperature of the battery pack is 2.2°C, 7.7°C and 14.6°C. In this case, PCM can effectively absorb the heat at 1C, 2C and 3C discharge rates. However, at 4C discharge rate, pure PCM plates are not capable of completely and quickly absorbing all the heat. Figure 6.40 (c) shows the variation in voltage with 3 mm thick pure PCM and polyurethane foam plates at various discharge rates. The trend of voltage variation at various discharge rates is similar to previous cases.

Table 6.19: Maximum temperature, average temperature, and rise in temperature of the battery pack with 3 mm thick pure PCM plates at various discharge rates.

Discharge Rate	Maximum Temperature (°C)	Average Temperature (°C)	Temperature Rise (°C)
1C	27.4	25.5	3.8
2C	29.3	28.1	2.2
3C	35.2	29.9	7.7
4C	42.1	32.8	14.6

Similar to the previous case, to improve the effectiveness of pure PCM through enhancement in thermal conductivity, 1.5% CNT is added with pure PCM and polyurethane foam to make 3 mm thick plates. Again, tests are conducted with these plates to investigate the thermal and electrical behaviour of the battery pack at various discharge rates. Figure 6.41 (a) shows the variation in the battery pack temperature at various discharge rates with 3 mm thick plates of pure PCM, polyurethane foam and 1.5% CNT. In this case, a significant improvement in thermal conductivity of pure PCM is observed in terms of the temperature drop in the maximum temperature of the battery pack. The effect of using CNTs is more clearly visible at higher discharge rates. At 1C discharge rate, the maximum temperature of the battery pack reaches 27.1°C. At 2C, 3C and 4C, the maximum temperature of the battery pack reaches 29.3°C, 32.3°C and 37.6°C, respectively. Figure 6.41 (c) shows the variation in voltage with 3 mm thick plates of pure PCM, polyurethane foam and 1.5% CNT at various discharge rates.

The maximum temperature, average temperature, and rise in temperature of the battery pack with the 3 mm thick plates made of pure PCM, polyurethane foam, and 1.5% CNT are given in Table 6.20. An interesting observation can be made from Table 6.20: the maximum and average temperatures of the battery pack remains within the optimum temperature range of a Li-ion battery,

i.e. 25°C-40°C, at all discharge. The battery pack temperature can be managed within the required range with pure PCM by using 1.5% CNT is another major finding of the present study.

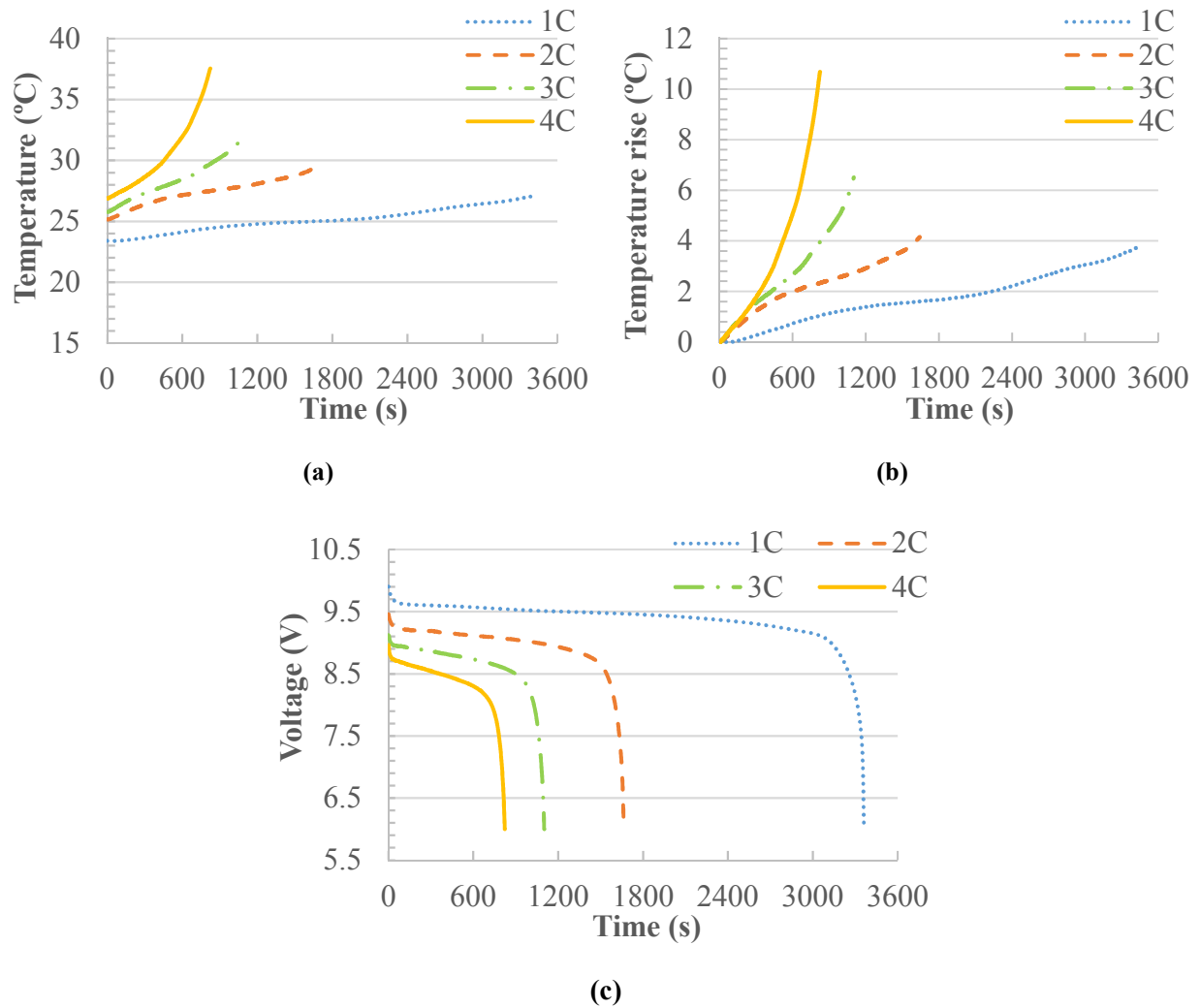


Figure 6.41: With 3 mm thick pure PCM and 1.5% CNT plates; (a) variation in temperature, (b) rise in temperature, (c) variation in voltage, at various discharge rates.

Table 6.20: Maximum temperature, average temperature, and rise in temperature of the battery pack with 3 mm thick pure PCM and 1.5% CNT plates at various discharge rates.

Discharge Rate	Maximum Temperature (°C)	Average Temperature (°C)	Temperature Rise (°C)
1C	27.1	25.1	3.7
2C	29.3	27.4	4.1
3C	32.3	28.4	6.5
4C	37.6	30.4	10.7

Similarly, to investigate the effect of an increase in CNT concentration on thermal behaviour of the battery pack, 3 mm thick plates are made using pure PCM, polyurethane foam and 3% CNT. Figure 6.42 (a) shows the variation in temperature with respect to time at various discharge rates with 3 mm thick plates made of pure PCM, polyurethane foam and 3% CNT. Further improvement in thermal conductivity of PCM can be observed in terms of temperature drop in the maximum temperature of the battery pack with an increase in CNT concentration to 3%. At 1C, 2C, 3C and 4C discharge rates, the maximum temperature of the battery pack reaches 27.2°C, 29.3°C, 32.3°C, and 36.2°C. Figure 6.42 (c) shows the variation in voltage with 3 mm thick plates of pure PCM, polyurethane foam and 3% CNT at various discharge rates.

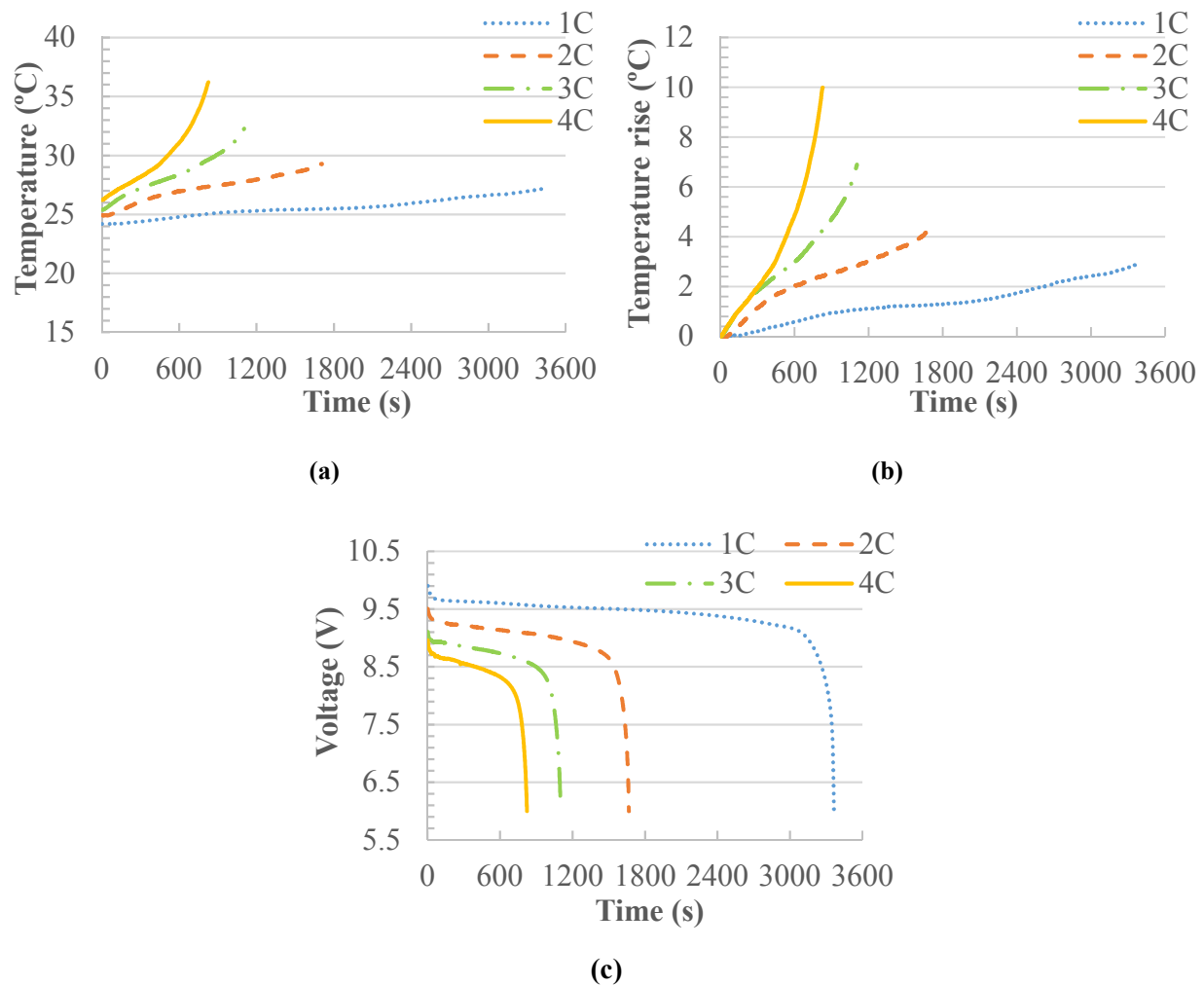


Figure 6.42: With 3 mm thick pure PCM and 3% CNT plates; (a) variation in temperature, (b) rise in temperature, (c) variation in voltage, at various discharge rates.

The maximum temperature, average temperature, and rise in temperature of the battery pack with the 3 mm thick plates made of pure PCM, polyurethane foam, and 3% CNT are given in Table 6.21. Similar to the previous case, it can be observed from Table 6.21, that the maximum and average temperatures of the battery pack remain within the optimum temperature range of a battery, i.e. 25°C-40°C, at all discharge rates. However, there is no visible effect of an increase in mass concentration of CNTs from 1.5% to 3%, on the maximum temperature of the battery pack at 1C, 2C and 3C discharge rates.

Table 6.21: Maximum temperature, average temperature, and rise in temperature of the battery pack with 3 mm thick pure PCM and 3% CNT plates at various discharge rates.

Discharge Rate	Maximum Temperature (°C)	Average Temperature (°C)	Temperature Rise (°C)
1C	27.2	25.6	2.9
2C	29.3	27.3	4.3
3C	32.3	28.4	6.9
4C	36.2	29.7	10.0

Figure 6.43 shows a comparison of variation in temperature of the battery pack with and without pure PCM plates. Again, it can be clearly seen that the use of PCM-based plates significantly reduces the temperature of the battery pack. Also, the effect of using CNTs with a pure PCM is clearly visible in terms of temperature drop in the battery pack. With the use of 1.5% CNT with pure PCM, the maximum temperature of the battery pack decrease from 41.2°C to 36.4°C at 4C discharge rate as shown in Figure 6.43.

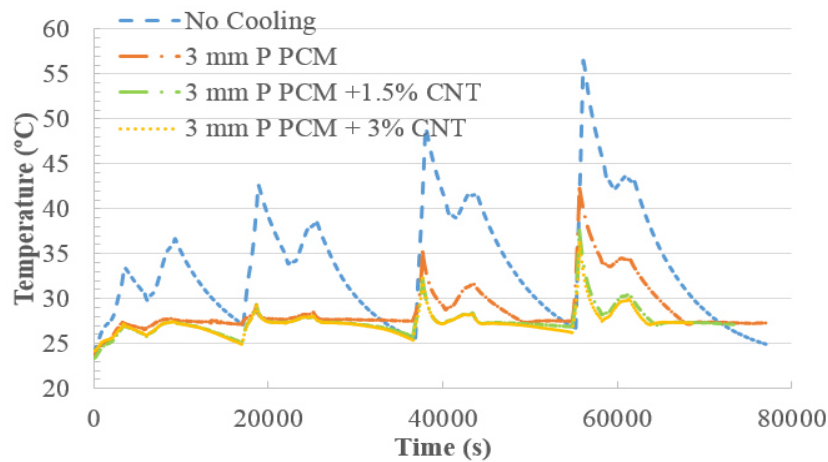


Figure 6.43: Temperature profile of the battery pack with 3 mm thick pure PCM based plates at various charge and discharge rates.

6.5.3 6 mm Thick Plates of Technical Grade Phase Change Material

PCM-based plates of two different thicknesses i.e. 3 mm and 6 mm, are used to investigate the effect of change in the thickness of PCM-based plates on the battery pack voltage, temperature, and other parameters. In this section, the results obtained from the battery pack with 6 mm thick PCM based plates are presented. Again, the technical grade of PCM is used to make the 6 mm thick plates. With respect to time, variation in the battery pack temperature with 6 mm thick technical grade PCM plates is shown in Figure 6.44 (a). At 1C, 2C, 3C and 4C discharge rate, the maximum temperature of the battery pack reaches 25.4°C, 28.2°C, 32.7°C, and 40.4°C, respectively. At 1C discharge rate, the temperature of the battery pack remains lower than the melting temperature of the PCM and almost equal at 2C discharge rate, meaning that most of the heat absorbed by the PCM is in the form of sensible heat at 1C and 2C discharge rate.

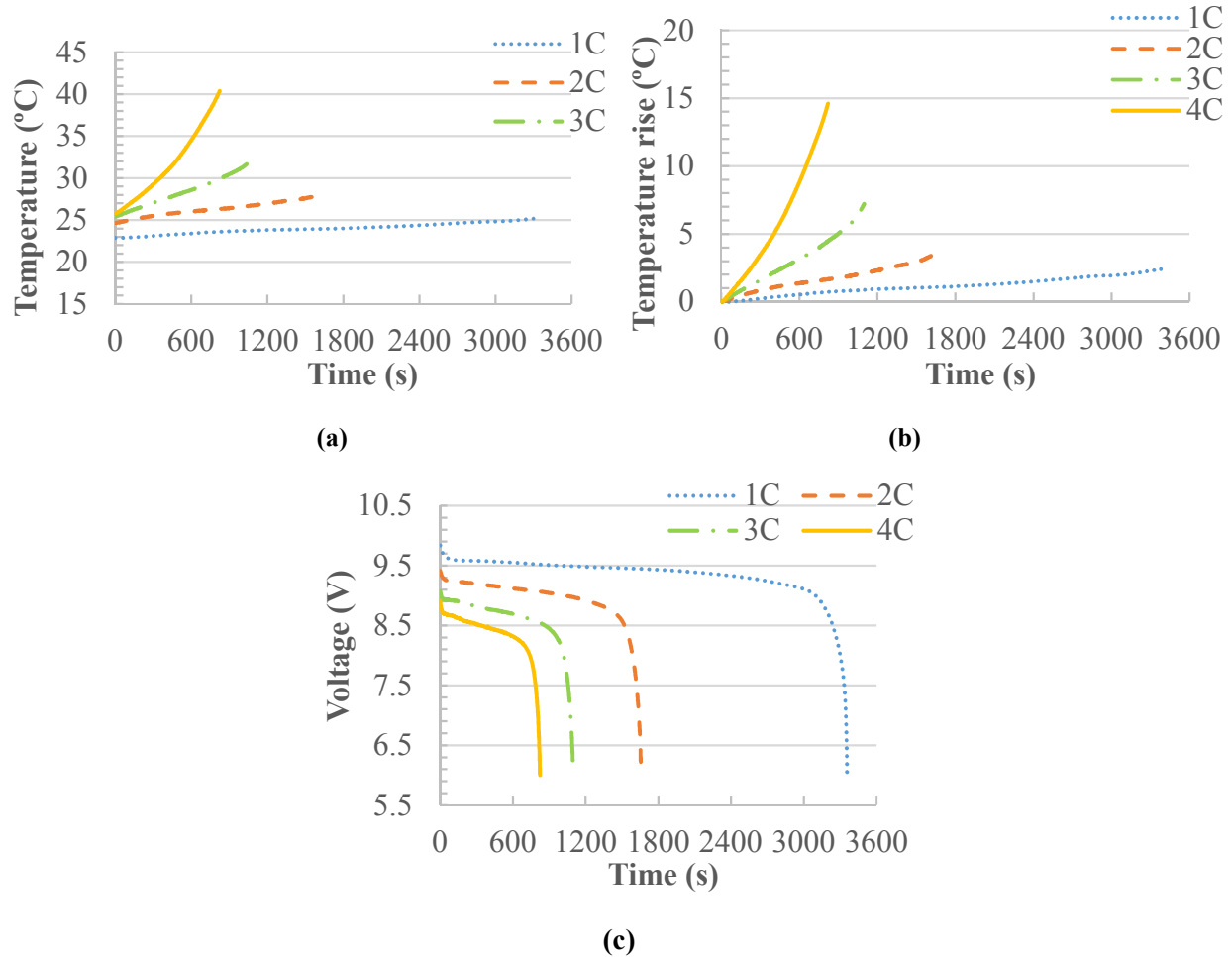


Figure 6.44: With 6 mm thick technical grade PCM plates; (a) variation in temperature, (b) rise in temperature, (c) variation in voltage, at various discharge rates.

Figure 6.44 (b) shows the rise in the battery pack temperature at various discharge rates. At 1C, 2C and 3C discharge rate, the temperature increase is only 2.5°C, 3.6°C and 7.2°C, respectively, while at 4C, there is a sharp rise of 14°C. Figure 6.44 (c) shows the variation in voltage with 6 mm thick technical grade PCM and polyurethane foam plates at various discharge rates.

The maximum temperature, average temperature, and rise in temperature of the battery pack with 6 mm thick plates of polyurethane foam and technical grade PCM at various discharge rates are given in Table 6.22. From Table 6.22, it can be observed that the maximum temperature of the battery pack at 1C, 2C and 3C discharge rates, and average temperature at all discharge rates, remain within the required range, i.e. 25°C-40°C, while at 4C discharge rate, the maximum temperature of the battery pack is just beyond the required temperature range. These trends are similar to the results obtained with 3 mm thick technical grade PCM plates.

Table 6.22: Maximum temperature, average temperature, and rise in temperature of the battery pack with 6 mm thick technical grade PCM plates at various discharge rates.

Discharge Rate	Maximum Temperature (°C)	Average Temperature (°C)	Temperature Rise (°C)
1C	25.4	24.0	2.5
2C	28.2	26.4	3.6
3C	32.7	28.5	7.2
4C	40.4	31.6	14.6

Similar to the previous cases, to enhance the thermal conductivity of PCM, 1.5% (wt.) CNT is added to technical grade PCM and polyurethane foam to form 6 mm thick plates. The experiments are performed with 6 mm thick PCM and CNT-based plates. Figure 6.45 (a) shows the variation in the battery pack temperature with 6 mm thick plates of polyurethane foam, technical grade PCM and 1.5% CNT at various discharge rates. At 1C discharge rate, the maximum temperature of the battery pack reaches 24.5°C. At 2C, 3C and 4C discharge rates, the maximum temperature of the battery pack reaches 27.9°C, 31.5°C, and 37.9°C, respectively.

Figure 6.45 (b) shows the rise in the battery pack temperature with 6 mm thick plates of polyurethane foam, technical grade PCM and 1.5% CNT at various discharge rates. At 1C, 2C and 3C discharge rates, the temperature rise is only 3.2°C, 4.1°C, and 6.7°C, respectively. Again, at 4C discharge rate, there is a high temperature rise of 12.3°C. Figure 6.45 (c) shows the variation

in voltage with 6 mm thick plates of polyurethane foam, technical grade PCM and 1.5% CNT at various discharge rates.

The maximum temperature, average temperature, and rise in temperature of the battery pack with 6 mm thick plates of technical grade PCM and 1.5% CNT are given in Table 6.23. From Table 6.23, it can be observed that the maximum and average temperatures of the battery pack remain within the required temperature range, i.e. 25°C-40°C, at all discharge rates.

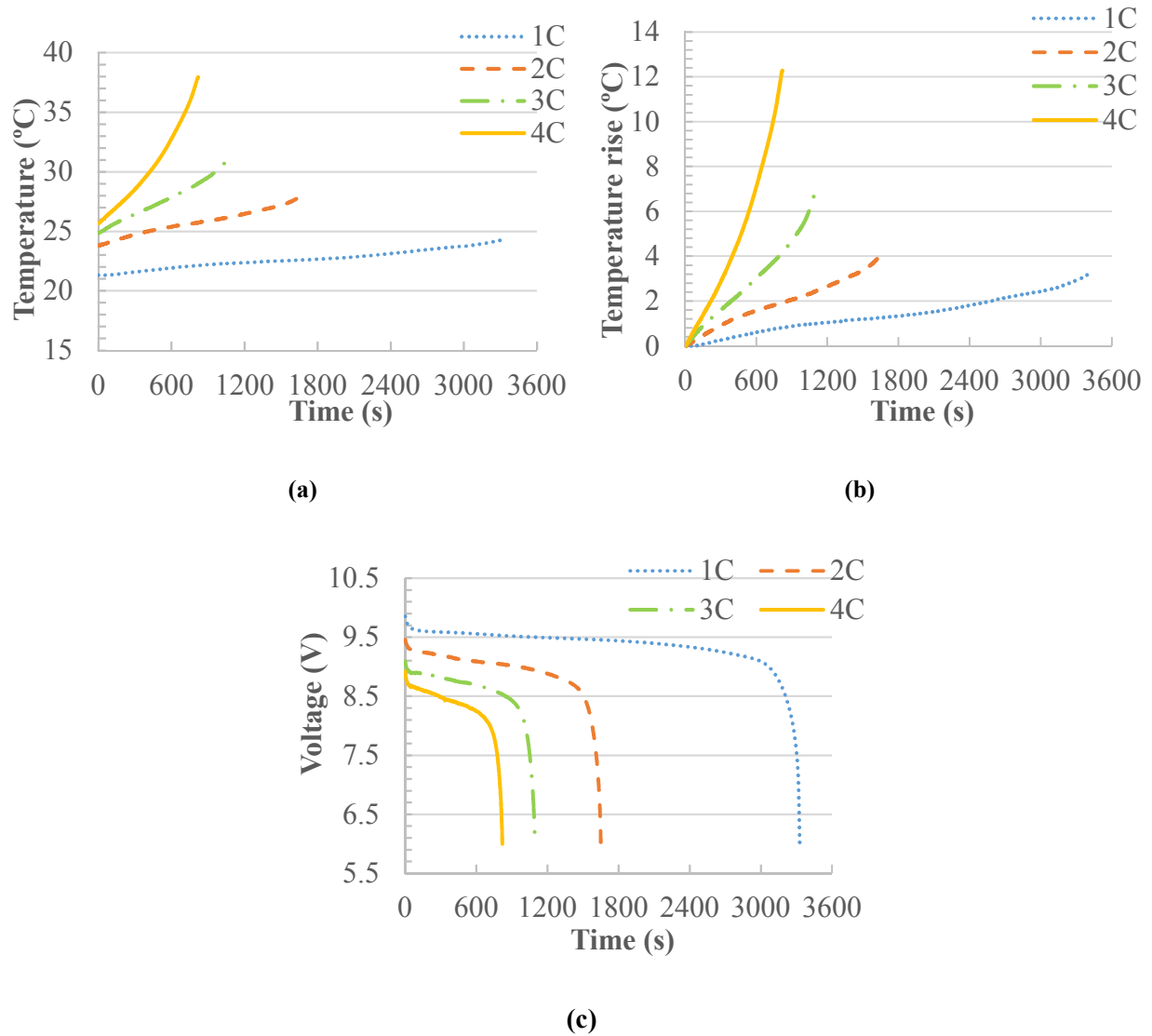


Figure 6.45: With 6 mm thick technical grade PCM and 1.5% CNT plates; (a) variation in temperature, (b) rise in temperature, (c) variation in voltage, at various discharge rates.

Table 6.23: Maximum temperature, average temperature, and rise in temperature of the battery pack with 6 mm thick technical grade PCM and 1.5% CNT plates at various discharge rates.

Discharge Rate	Maximum Temperature (°C)	Average Temperature (°C)	Temperature Rise (°C)
1C	24.5	22.7	3.2
2C	27.9	25.8	4.1
3C	31.5	27.7	6.7
4C	37.9	30.5	12.3

Similar to the previous case, 6 mm thick plates are made using technical grade PCM, polyurethane foam and 3% CNT to investigate the effect of an increase in CNT concentration on the thermal behaviour of the battery. Figure 6.46 shows the variation in temperature, voltage and increase in the temperature of the battery pack at various discharge rates with the 6 mm thick plates of PCM, polyurethane foam and 3% CNT.

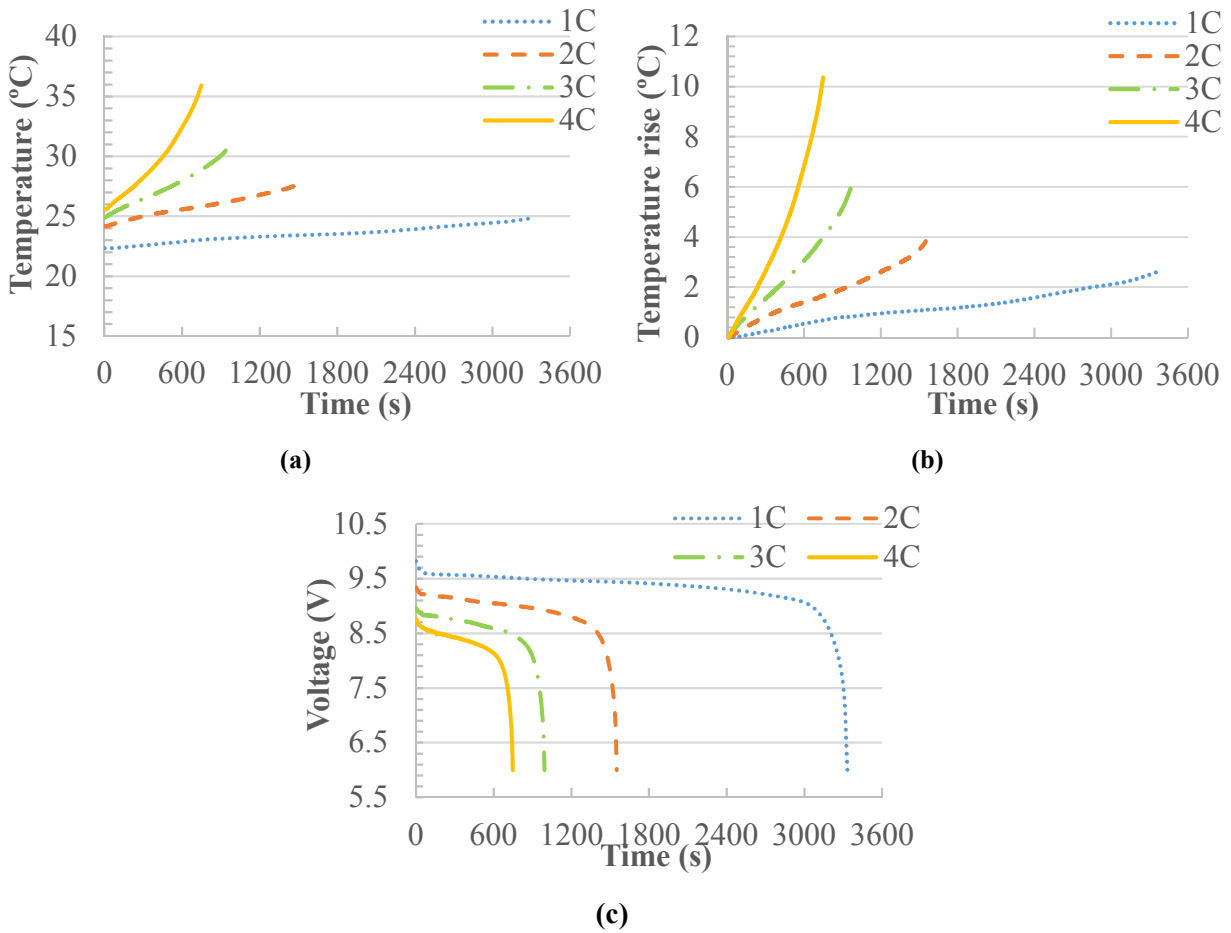


Figure 6.46: With 6 mm thick technical grade PCM and 3% CNT plates; (a) variation in temperature, (b) rise in temperature, (c) variation in voltage, at various discharge rates.

A small improvement in thermal conductivity of PCM can be seen in terms of temperature drop in the maximum temperature of the battery pack with 3% CNT compared to 1.5% CNT. The maximum temperature, average temperature, and rise in temperature of the battery pack with 6 mm thick plates of technical grade PCM and 1.5% CNT are given in Table 6.24. Similar to the previous case, it can be seen from Table 6.24, that the maximum and average temperatures of the battery pack remains within the required temperature range, i.e. 25°C-40°C, at all discharge rates.

Table 6.24: Maximum temperature, average temperature, and rise in temperature of the battery pack with 6 mm thick technical grade PCM and 3% CNT plates at various discharge rates.

Discharge Rate	Maximum Temperature (°C)	Average Temperature (°C)	Temperature Rise (°C)
1C	25.1	23.5	2.7
2C	28.0	25.9	3.8
3C	31.3	27.6	6.4
4C	35.9	29.6	10.4

Figure 6.47 shows a comparison of variation in the temperature of the battery pack with and without technical grade PCM-based plates. Again, it can be clearly seen that use of PCM-based plates significantly reduces the temperature of the battery pack. However, the effect of using CNTs with a technical grade of PCM is not clearly visible at 1C and 2C discharge rates, but can be seen at 3C and 4C discharge rates.

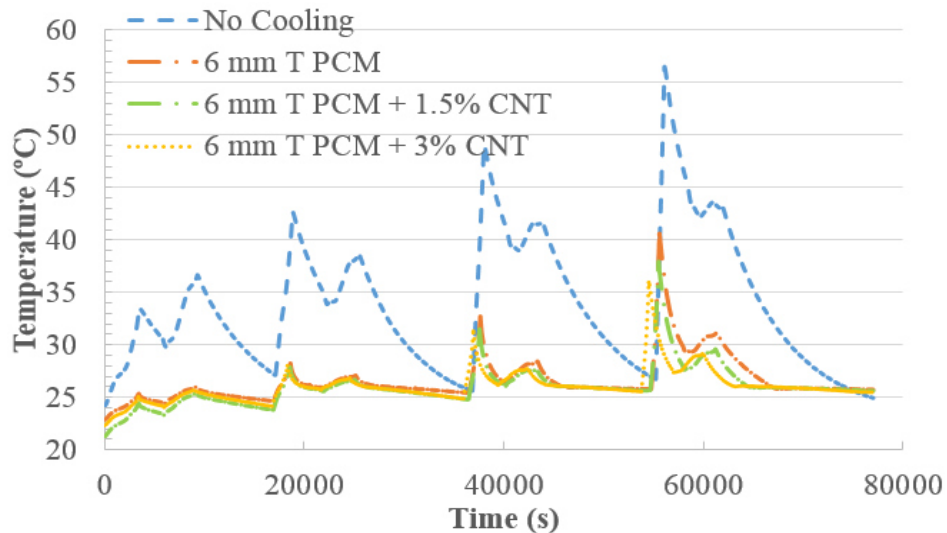


Figure 6.47: Temperature profile of the battery pack with 6 mm thick technical grade PCM based plates at various charge and discharge rates.

6.5.4 6 mm Thick Plates of Pure Phase Change Material

In this section, the results obtained from the battery pack with 6 mm thick plates made from pure PCM, polyurethane foam and various concentrations of CNT are presented. Figure 6.48 (a) shows the variation in the battery pack temperature with 6 mm thick plates of polyurethane foam and pure PCM at various discharge rates. At 1C discharge rate, the maximum temperature of the battery pack reaches 26.3°C. At 2C, 3C and 4C, the maximum temperature of the battery pack reaches 28.6°C, 29.8°C, and 31.7°C, respectively. Again, at 1C discharge rate, as the temperature of the battery pack remains lower than the melting temperature of PCM, the heat absorbed by PCM is in the form of sensible heat. Figure 6.48 (b) shows the rise in the battery pack temperature with 6 mm thick plates of polyurethane foam and pure PC at various discharge rates.

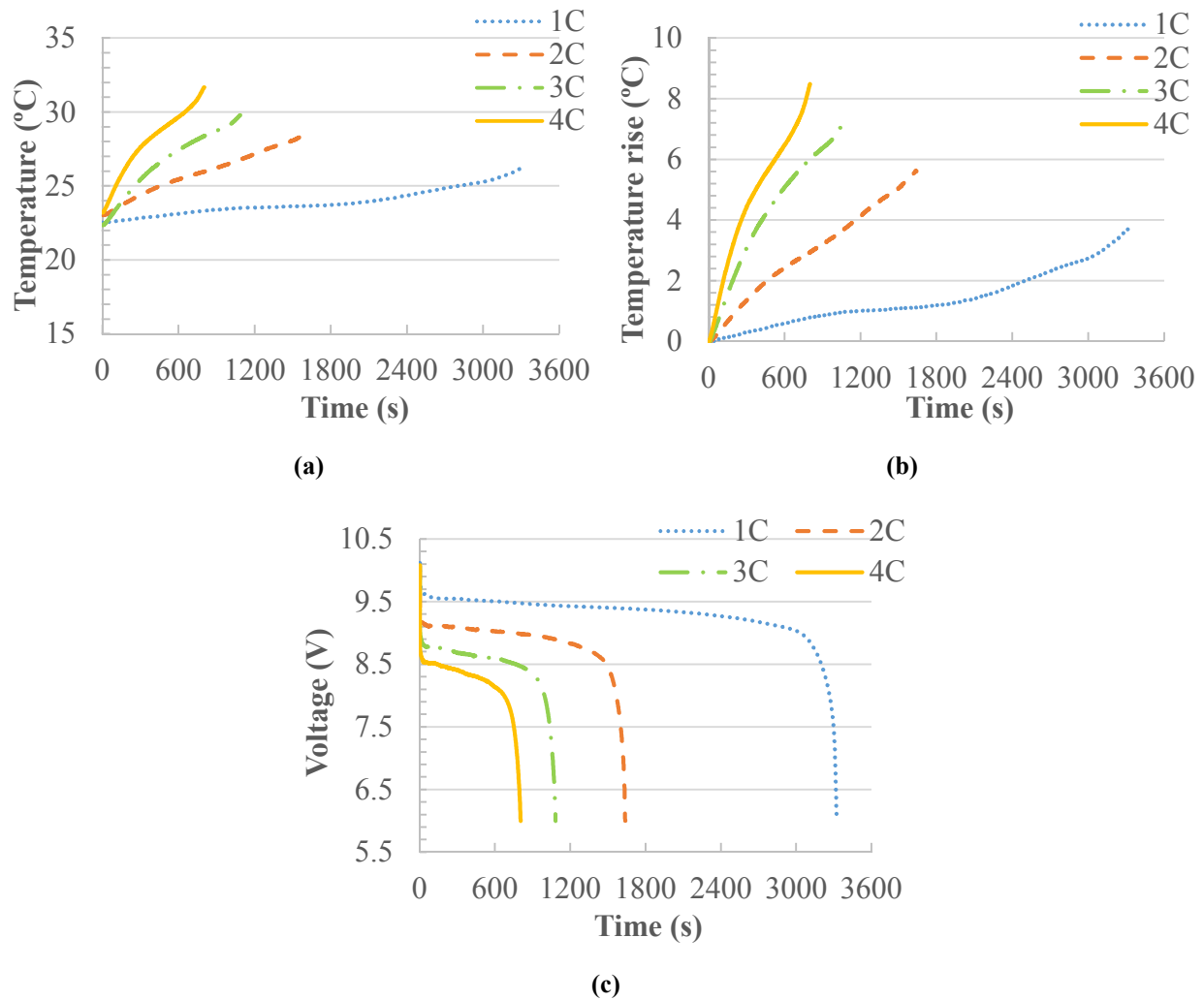


Figure 6.48: With 6 mm thick pure PCM plates; (a) variation in temperature, (b) rise in temperature, (c) variation in voltage, at various discharge rates.

At 1C discharge rate, the temperature rise is only 3.7°C. At 2C, 3C and 4C, the rise in the battery pack temperature is 5.6°C, 7.4°C and 8.5°C, respectively. An interesting observation can be made from the results that the temperature rise at 4C with 6 mm pure PCM plates is significantly lower compared to all other cases discussed.

Figure 6.48(c) shows the variation in voltage with 3 mm thick pure PCM and polyurethane foam plates at various discharge rates. The trend of voltage variation at various discharge rates is similar to previous cases.

The maximum temperature, average temperature, and rise in temperature of the battery pack with 6 mm thick pure PCM plates are given in Table 6.25. From Table 6.25, it can be observed that the maximum and average temperatures of the battery pack at all discharge rates remain within the required temperature range of the battery, i.e. 25°C-40°C, except the average temperature at 1C discharge rate. It can be concluded that the temperature of the battery pack can be maintained within optimum limits without using CNTs with 6 mm thick pure PCM plates. However, solidification time of PCM will be different with the use of CNTs.

Table 6.25: Maximum temperature, average temperature, and rise in temperature of the battery pack with 6 mm thick pure PCM plates at various discharge rates.

Discharge Rate	Maximum Temperature (°C)	Average Temperature (°C)	Temperature Rise (°C)
1C	26.3	23.9	3.7
2C	28.6	26	5.6
3C	29.8	26.7	7.4
4C	31.7	28	8.5

The battery pack temperature further decreases with the use of CNTs along with pure PCM between cells. However, the relative effect of using CNTs is not quite visible, as the rise in the battery back temperature with 6 mm thick pure PCM plates is already small.

Figure 6.49(a,b) shows the variation and rise in the battery pack temperature at various discharge rates with 6 mm thick plates of pure PCM, polyurethane foam and 1.5% CNT, respectively. At 1C, 2C, 3C and 4C discharge rates, the maximum temperature of the battery pack reaches 25.4°C, 28.5°C, 29.6°C and 33.3°C, respectively. Figure 6.49 (c) shows the variation in voltage with 6 mm thick plates of pure PCM, polyurethane foam and 1.5% CNT at various discharge rates.

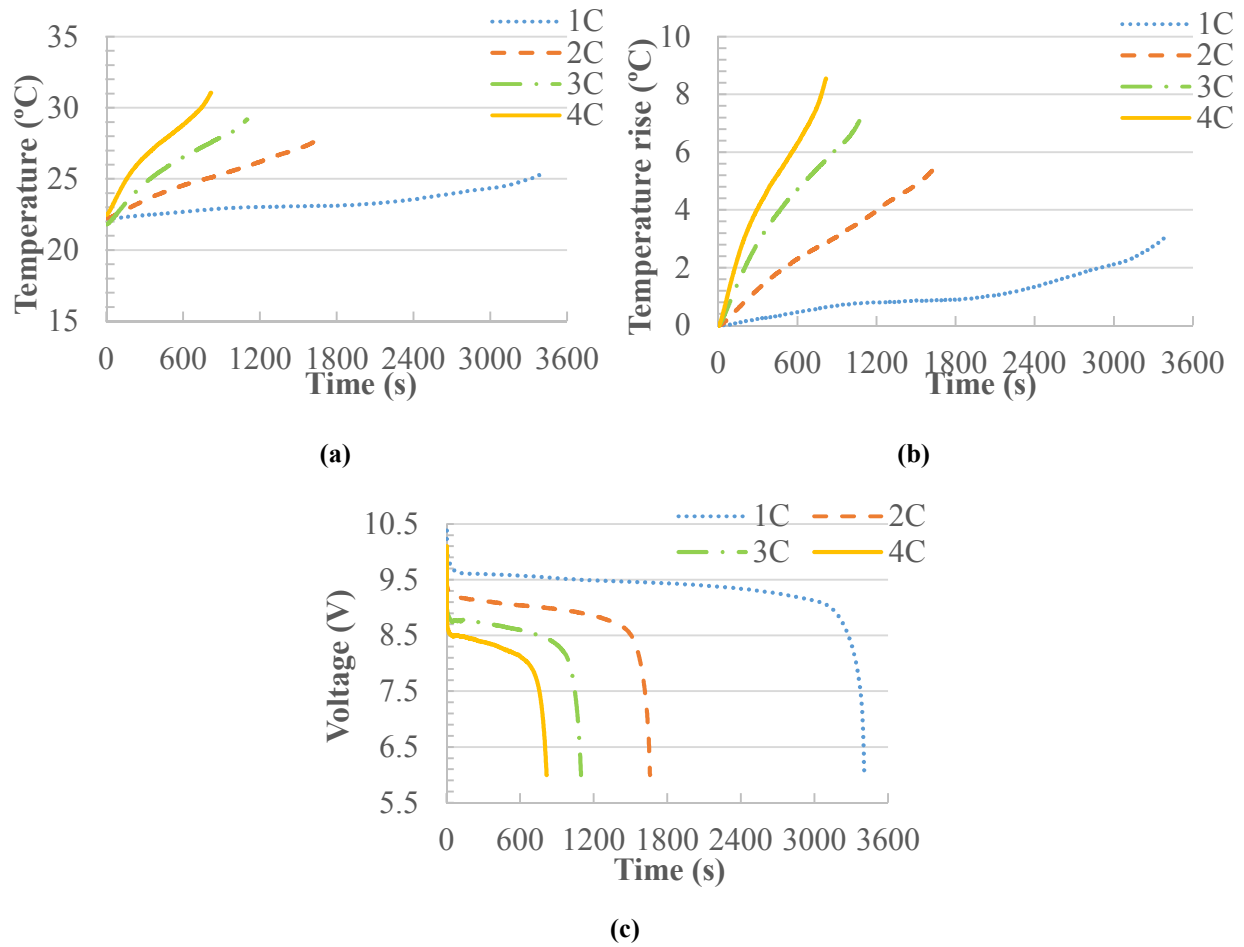


Figure 6.49: With 6 mm thick pure PCM and 1.5% CNT plates; (a) variation in temperature, (b) rise in temperature, (c) variation in voltage, at various discharge rates.

The maximum temperature, average temperature, and rise in the temperature of the battery pack with 6 mm thick plates of pure PCM, polyurethane foam and 1.5% CNT, at various discharge rates are given in Table 6.26. Similar to the previous case, the maximum and average temperatures of the battery pack at all discharge rates remain within the required temperature range of the battery, except the average temperature at 1C discharge rate.

Table 6.26: Maximum temperature, average temperature, and rise in temperature of the battery pack with 6 mm thick pure PCM and 1.5% CNT plates at various discharge rates.

Discharge Rate	Maximum Temperature (°C)	Average Temperature (°C)	Temperature Rise (°C)
1C	25.4	22.8	4.4
2C	28.5	25.7	6
3C	29.6	26.4	7.7
4C	31.3	27.5	8.7

A small decrease in battery pack temperature can be seen from Figure 6.50(a) with 6 mm thick plates of pure PCM and 3% CNT, compared to 6 mm thick plates of pure PCM and 1.5% CNT. However, the rise in the battery pack temperature with plates having 3% CNT is a little higher compared to the plates having 1.5% CNT. This may be due to a lower initial temperature of the battery before the discharge cycle starts. Figure 6.50(c) shows the variation in voltage with 6 mm thick plates of pure PCM, polyurethane foam and 3% CNT at various discharge rates. As usual, the trend of voltage variation in the battery pack is the same as in previous cases.

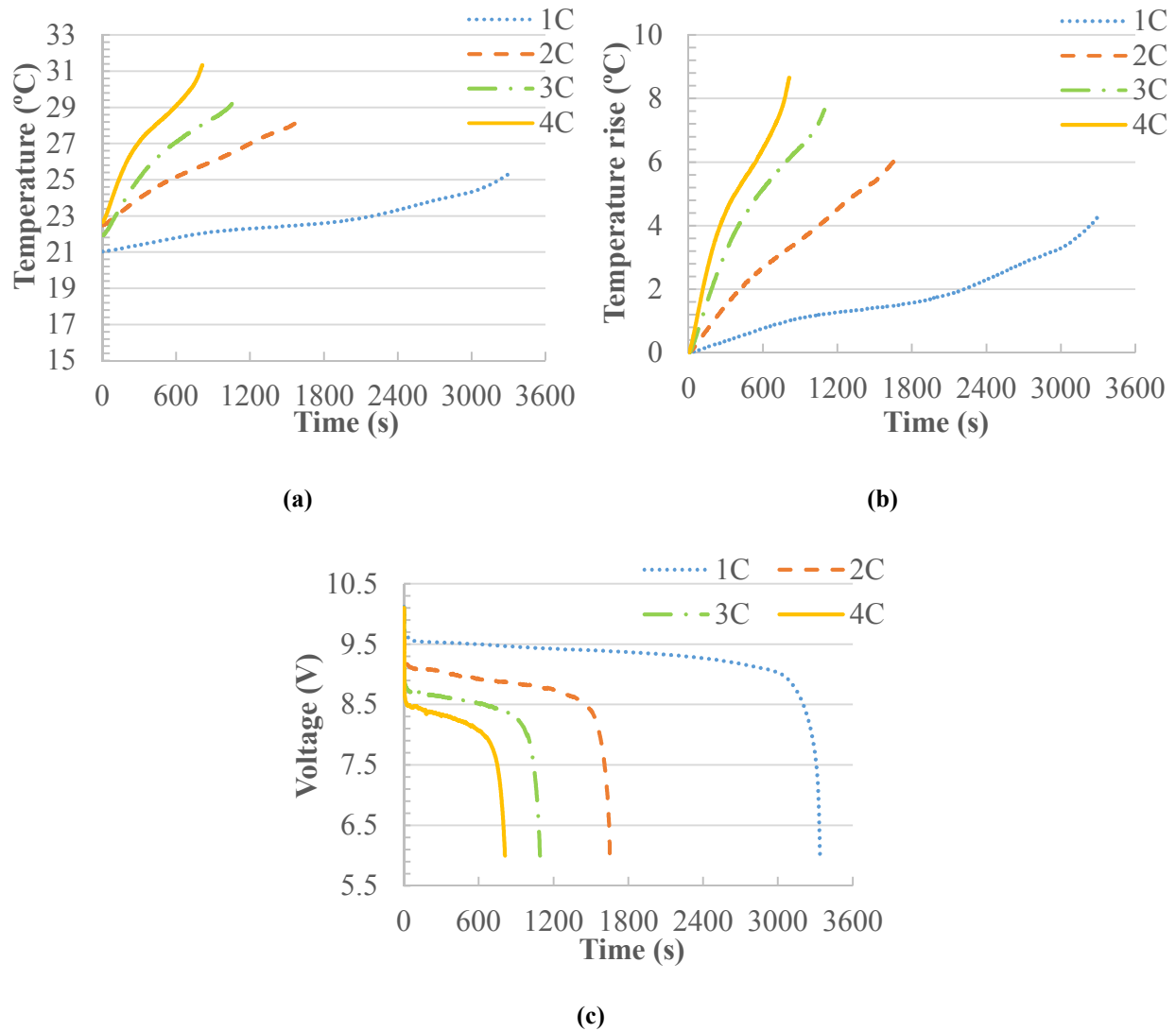


Figure 6.50: With 6 mm thick pure PCM and 3% CNT plates; (a) variation in temperature, (b) rise in temperature, (c) variation in voltage, at various discharge rates.

The maximum temperature, average temperature, and rise in the temperature of the battery pack with 6 mm thick plates of pure PCM, polyurethane foam and 1.5% CNT at various discharge rates are given in Table 6.27. Similar to the previous case, the maximum and average temperatures of the battery pack at all discharge rates remain within the required temperature range of the battery, except the average temperature at 1C.

Table 6.27: Maximum temperature, average temperature and rise in temperature of the battery pack with 6 mm thick pure PCM and 3 % CNT plates at various discharge rates.

Discharge Rate	Maximum Temperature (°C)	Average Temperature (°C)	Temperature Rise (°C)
1C	25.29	23.33	3.05
2C	27.81	25.12	5.56
3C	29.18	25.97	7.36
4C	31.07	27.19	8.55

Figure 6.51 shows the comparison of the battery pack temperature with no cooling and 6 mm thick plate made with a different combination of pure PCM and CNTs. It can be clearly seen that battery temperature significantly reduces with 6 mm thick pure PCM-based plates and remains within the required temperature range at various discharge rates.

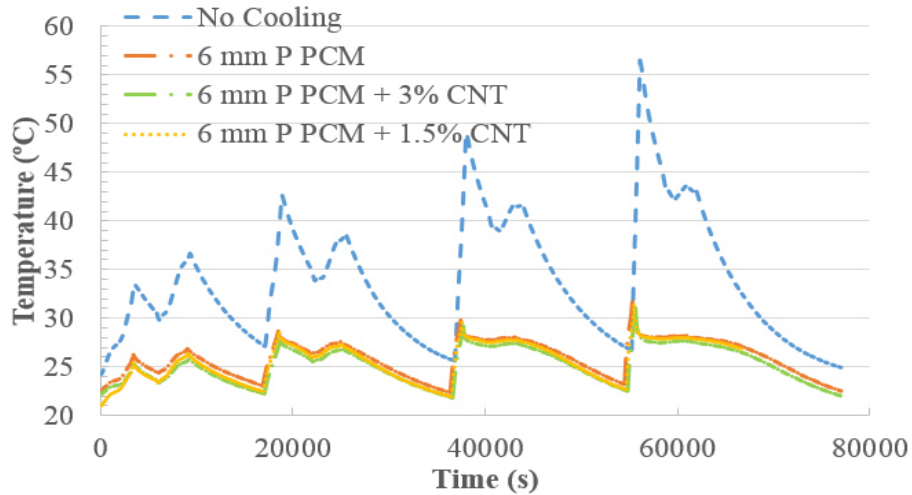


Figure 6.51: Comparison of the battery pack temperature with no cooling and 6 mm thick plates made with different combinations of pure PCM and CNTs at various discharge rates.

6.5.5 Comparison of No Cooling and with Phase Change Material Results

This section provides a comparison between the results obtained with no cooling case, and with 3 mm and 6 mm thick plates made from various combinations of PCM, polyurethane foam, and

CNTs. Figure 6.52 shows a comparison of the temperature profile of the battery pack with and without PCM-based plates at various charge and discharge rates. It can be clearly seen that there is a significant temperature drop in the battery pack temperature with PCM-based plates compared to no cooling case.

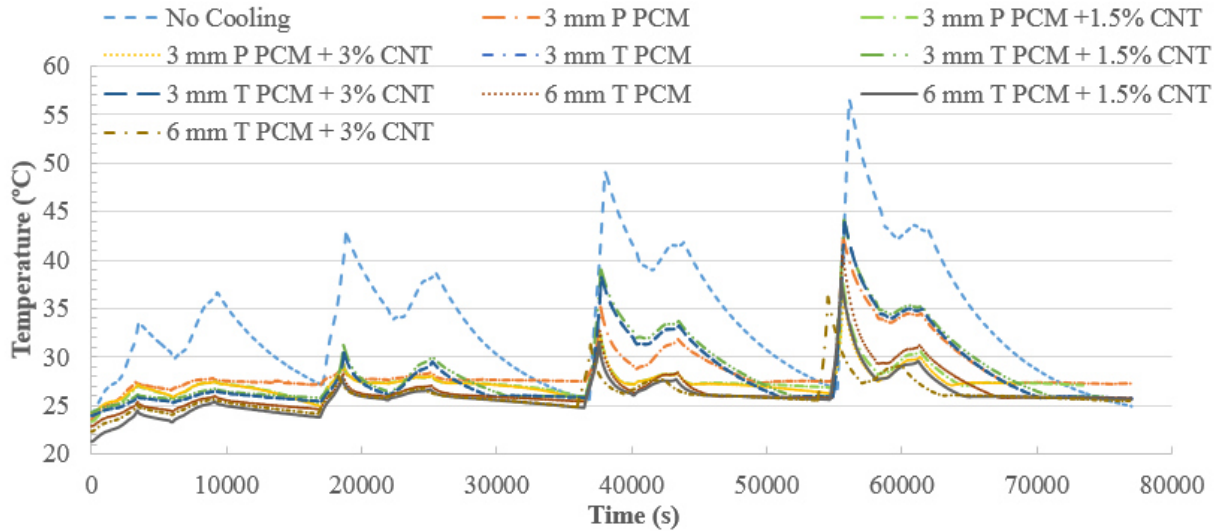


Figure 6.52: Temperature profiles of the battery pack with no cooling and with PCM and CNT-based plates.

Table 6.28 provide a comparison between the maximum and average temperatures of the battery pack with and without PCM based plates. Again, the colour coding is based on the selection of the optimum operating temperature range of the Li-ion battery. It can be seen from Table 6.28 that 3 mm and 6 mm thick plates of technical grade PCM are capable of managing the battery pack temperature in its optimum temperature range, i.e. 25°C-40°C, at 1C, 2C, and 3C, but fail to do so at 4C discharge rate. A small effect of CNTs is observed with the technical grade of PCM, but is still not capable of managing the required temperature range.

Similarly, 3 mm thick pure PCM plates are capable of managing the battery pack temperature to within the optimum operating temperature range for 1C, 2C, and 3C discharge rates, but fail to do so at 4C discharge rate. A significant effect of using CNTs with pure PCM is observed. With 1.5% or 3% of CNT with pure PCM, the temperature of the battery can be managed within the required temperature range of the battery with 3 mm thick plates. Similarly, the temperature of the battery can be managed within the required temperature range of the battery with 6 mm thick plates of technical grade PCM by using CNTs. However, the temperature of the battery pack can be

managed within the required temperature range of the battery pack with 6 mm thick pure PCM plates, even without using CNTs.

Table 6.28: Maximum and average temperatures of the battery pack with and without PCM based plates at various discharge rates.

Thickness of Plate (mm)	Cooling Conditions	Maximum Temperature of Battery Pack at Various Discharge Rates (°C)				Average Temperature of Battery Pack at Various Discharge Rates (°C)			
		1C	2C	3C	4C	1C	2C	3C	4C
	No Cooling	33	42.7	48.6	56.5	27.9	34.5	37	41.7
3	Technical Grade PCM	25.9	31.5	39.4	45.1	24.5	27.5	31	34
	Technical Grade PCM +1.5% CNT	26.1	31.2	39	44.1	25.1	27.4	31	33.8
	Technical Grade PCM +3% CNT	25.9	30.5	38.1	43.5	24.8	27.2	30	32.9
	Pure PCM	27.4	29.3	35.2	42.1	25.5	28.1	29.9	32.8
	Pure PCM +1.5% CNT	27.1	29.3	32.3	37.6	25.1	27.4	28.4	30.4
	Pure PCM +3% CNT	27.2	29.3	32.3	36.2	25.6	27.3	28.4	29.7
6	Technical Grade PCM	25.4	28.2	32.7	40.4	24	26.4	28.5	31.6
	Technical Grade PCM +1.5% CNT	24.5	27.9	31.5	37.9	22.7	25.8	27.7	30.5
	Technical Grade PCM +3% CNT	25.1	28	31.3	35.9	23.5	25.9	27.6	29.6
	Pure PCM	26.3	28.6	29.8	31.7	23.9	26	26.7	28
	Pure PCM +1.5% CNT	25.4	28.5	29.6	31.3	22.8	25.7	26.4	27.5
	Pure PCM +3% CNT	25.3	27.8	29.2	31.1	23.3	25.1	26.0	27.2

6.6 Comparison of Results Obtained from No cooling and Different Cooling Methods

In this section, the results obtained at various cooling condition are compared. Five major cooling conditions are compared: no cooling; with cold plates; with PCC plates; with pure and technical grade PCM; and with a pure and technical grade of PCM along with CNTs. Figure 6.53 provides a comparison of the battery capacity at various cooling conditions and discharge rates. The results show that discharge capacity of the Li-ion cells is a maximum of 19.34 Ah with PCC plates and then at the no cooling condition. However, the maximum temperature of the battery pack goes

beyond the optimum operating temperature range of the Li-ion battery with no cooling. From Figure 6.53, it can be seen that battery capacity reduces with an increase in discharge rate.

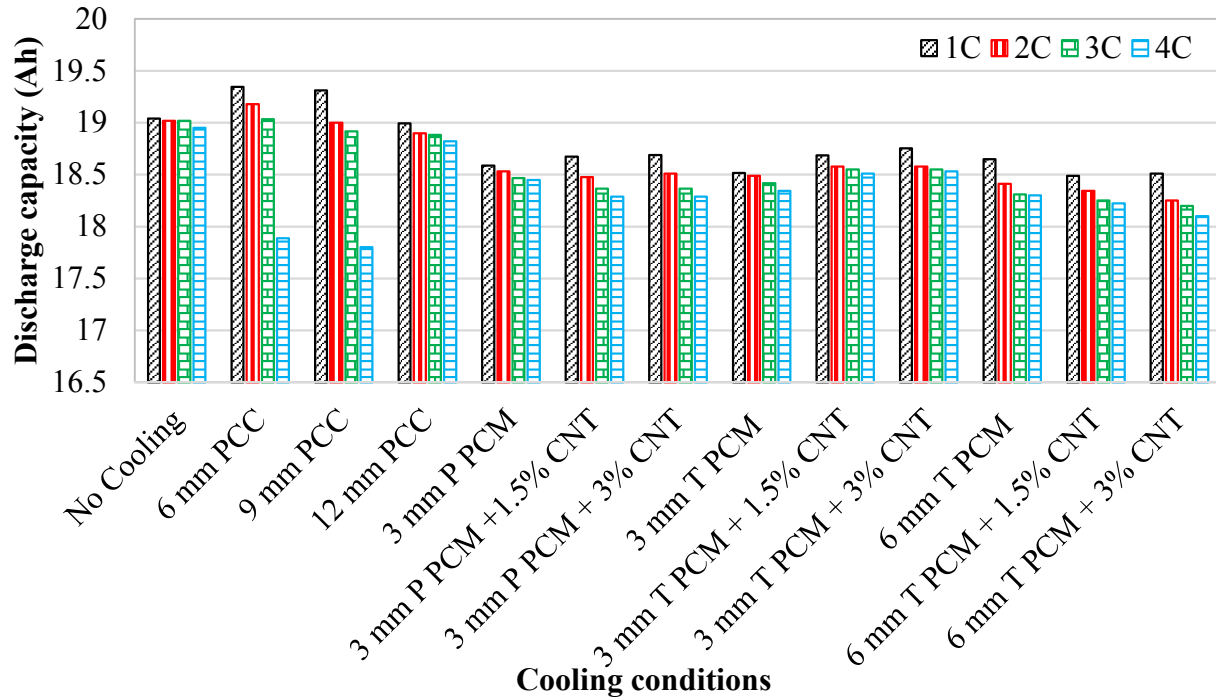


Figure 6.53: Discharge capacity of the battery pack with various cooling conditions and discharge rates.

Figure 6.54 shows the temperature profile of the battery pack with no cooling, with PCC and with PCM-based plates. A significant temperature drop in the battery pack temperature can be observed with PCC and PCM-based plates compared to no cooling case. However, at 1C and 2C discharge rates, PCM-based plates are more effective in reducing the maximum temperature of the battery pack compared to PCC plates, while at 3C and 4C discharge rates, PCC plates are more effective than technical grade PCM-based plates.

The pure PCM-based plates are more effective in controlling the battery pack temperature within the specified range compared to the technical grade PCM-based plates. Figure 6.55 shows the variation in the battery pack temperature with no cooling, PCC, and PCM-based plates at various discharge rates. It is observed that the PCM plates are more effective in reducing the battery temperature at 1C and 2C discharge rates compared to the PCC plates, as the melting point of PCM is lower than PCC.

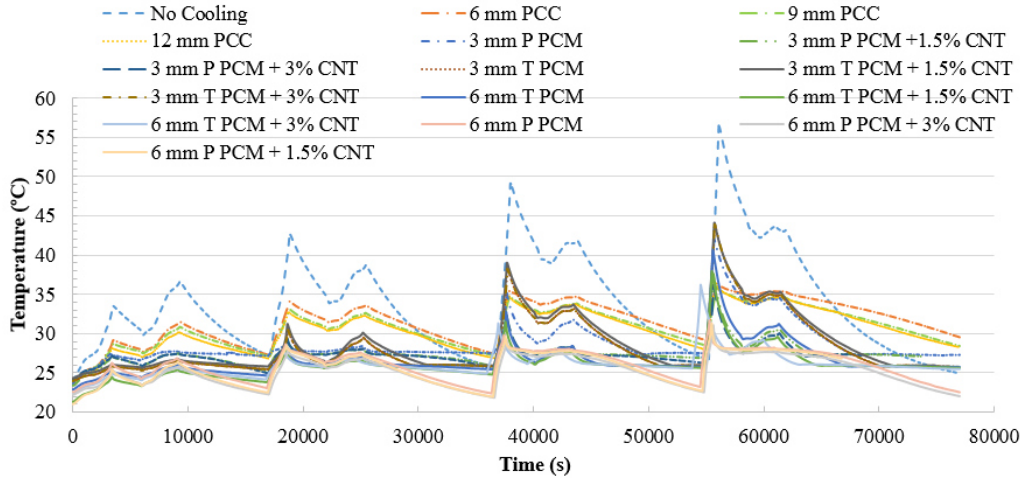


Figure 6.54: Temperature profile of the battery pack with no cooling, with PCC, and with PCM based plates.

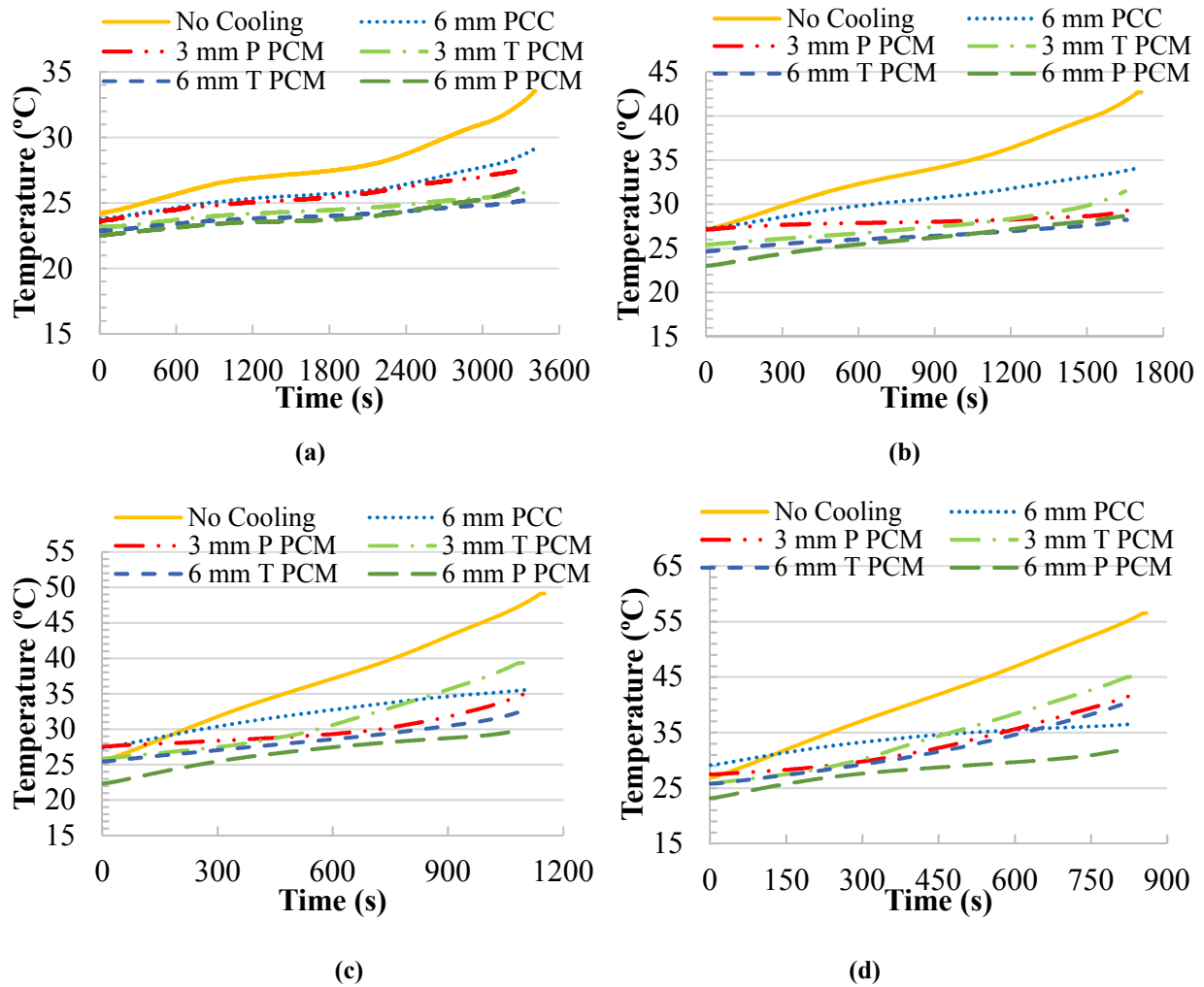


Figure 6.55: Variation in the battery pack temperature at no cooling, and with PCC, PCM plates at; (a) 1C, (b) 2C, (c) 3C, and (d) 4C, discharge rates.

PCC plates are more effective at 3C discharge rate compared to 3 mm thick technical grade PCM plates and but less effective than 3 mm thick pure PCM plates. For the same thickness, i.e. 6 mm, pure PCM plates are more effective than PCC plates in managing the battery pack temperature within the required range.

Figure 6.56 shows the variation in the battery pack temperature with no cooling, PCC, PCM and 1.5% CNT-based plates at various discharge rates. Similar trends can be seen with 1.5% CNT as in the case of the PCM-based plate only. However, the temperature drop in the battery pack with 1.5% CNT plates is higher compared to no CNTs.

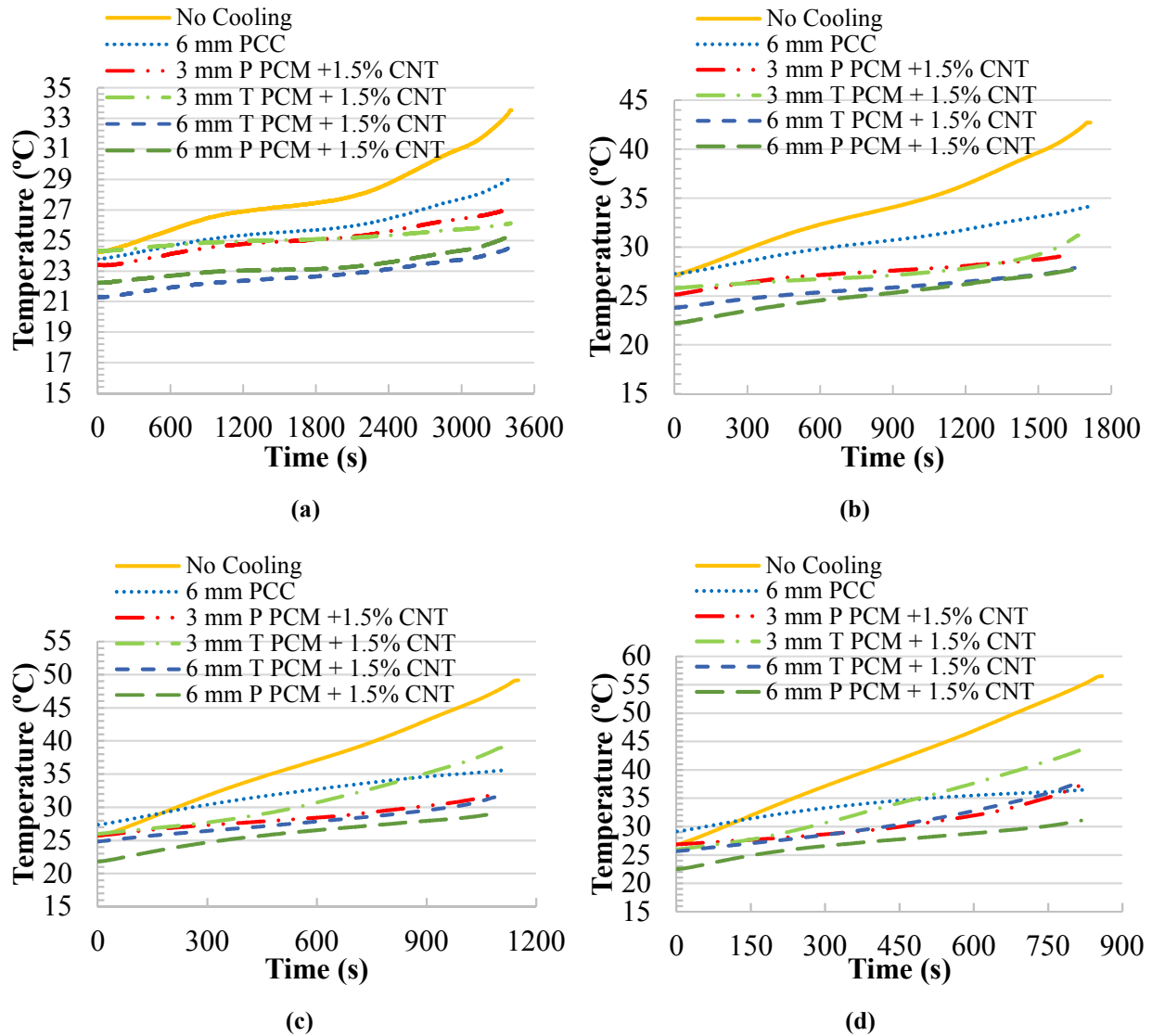


Figure 6.56: Variation in the battery pack temperature at no cooling, and PCC, PCM with 1.5% CNT plates at; (a) 1C, (b) 2C, (c) 3C, and (d) 4C, discharge rates.

Furthermore, there is a significant improvement in the effectiveness of 3 mm thick pure PCM plates with the use of CNTs in reducing the battery pack temperature. The effect of using CNTs on the battery pack temperature is more distinct at higher discharge rates.

Similar comparisons are made with the use of 3% CNT along with pure and technical grades of PCM. Figure 6.57 shows the variation in the battery pack temperature with no cooling, PCC, PCM and 3% CNT-based plates at various discharge rates. Further improvements can be seen in terms of reduction in the battery pack temperature by using 3% CNT, compared to the use of 1.5% CNT.

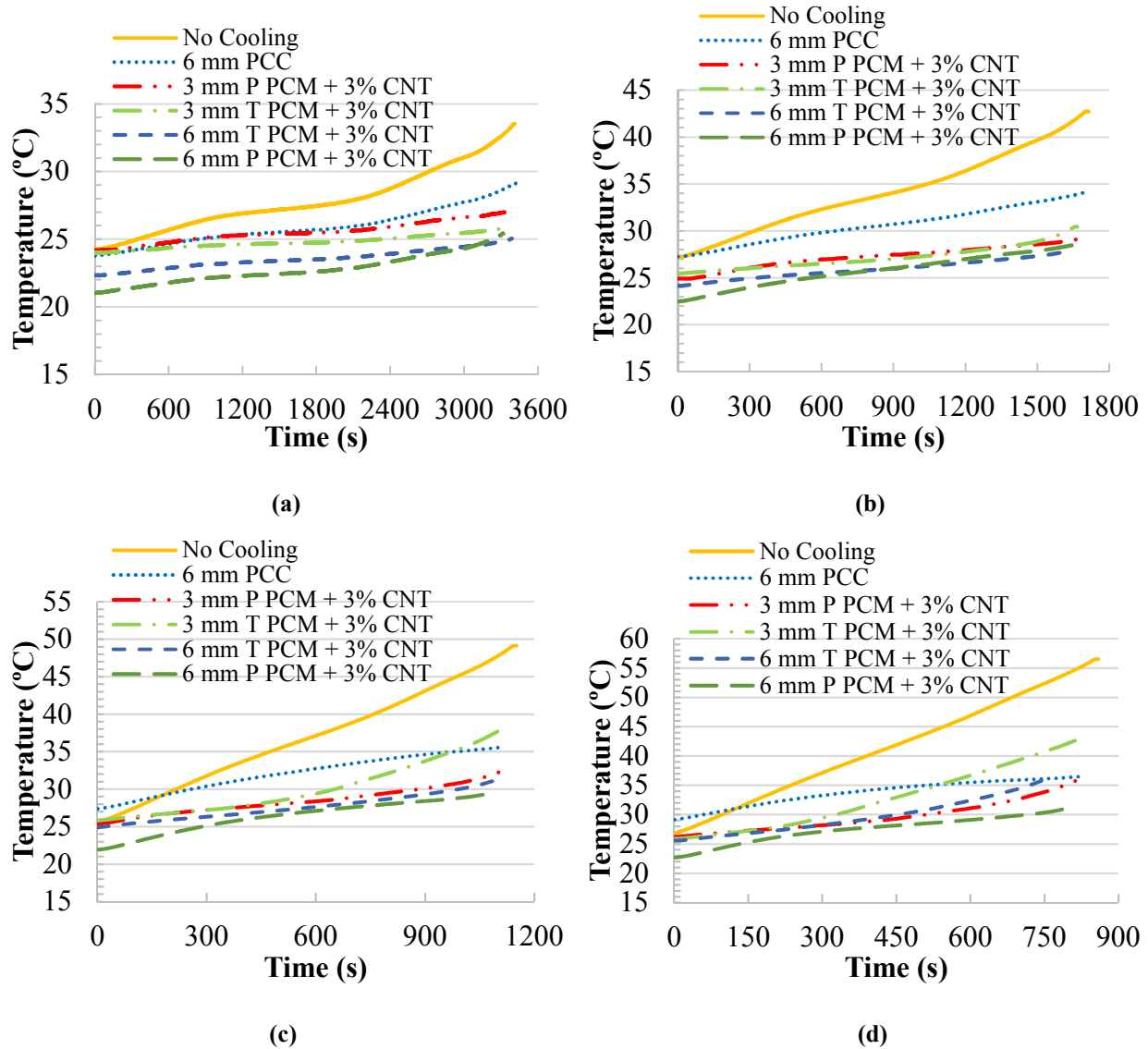


Figure 6.57: Variation in the battery pack surface temperature at no cooling, and with PCC, PCM with 3% CNT plates at; (a) 1C, (b) 2C, (c) 3C, and (d) 4C, discharge rates.

From the comparison of the obtained results, it is observed that the temperature of the battery pack remains minimum mostly with 6 mm thick pure PCM and 3% CNT plates at various discharge rates.

Figure 6.58 provides a comparison between the temperature rise in the battery pack at various discharge rates with variation cooling options. The rise in temperature is found to be a maximum 29.6 °C at 4C discharge rate with no cooling option. Again, a significant drop in temperature rise can be seen from Figure 6.58 with PCC and PCM-based plates compared to no cooling case.

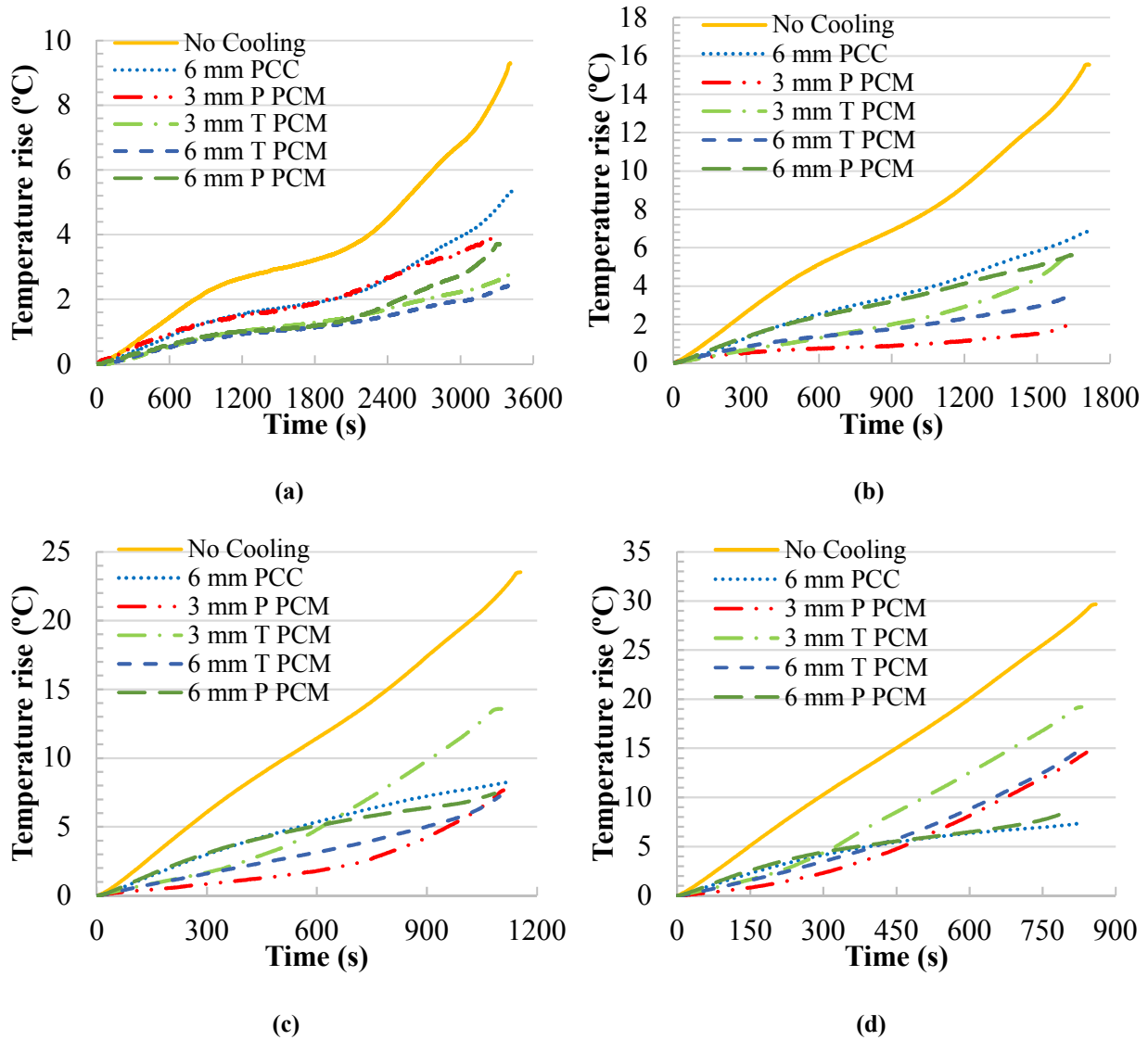


Figure 6.58: Rise in the battery pack temperature at no cooling, with PCC, and PCM plates at; (a) 1C, (b) 2C, (c) 3C, and (d) 4C, discharge rates.

At 1C discharge rate, the rise in the battery pack temperature remains a minimum of 2.5°C with 6 mm thick plates of pure PCM. At 2C discharge rate, the rise in the battery pack temperature remains a minimum of 2.15°C with 3 mm thick pure PCM plates, while at 3C discharge rate, remains minimum with 6 mm thick pure PCM plates. The rise in the battery pack temperature also depends on the environmental temperature and initial temperature of the battery pack before the discharge cycle starts. At 4C discharge rate, the rise in the battery pack temperature remains a minimum of 7.35°C with 6 mm thick PCC plates. Figure 6.59 shows the rise in the battery pack temperature with no cooling, PCC, PCM and 1.5% CNT-based plates at various discharge rates.

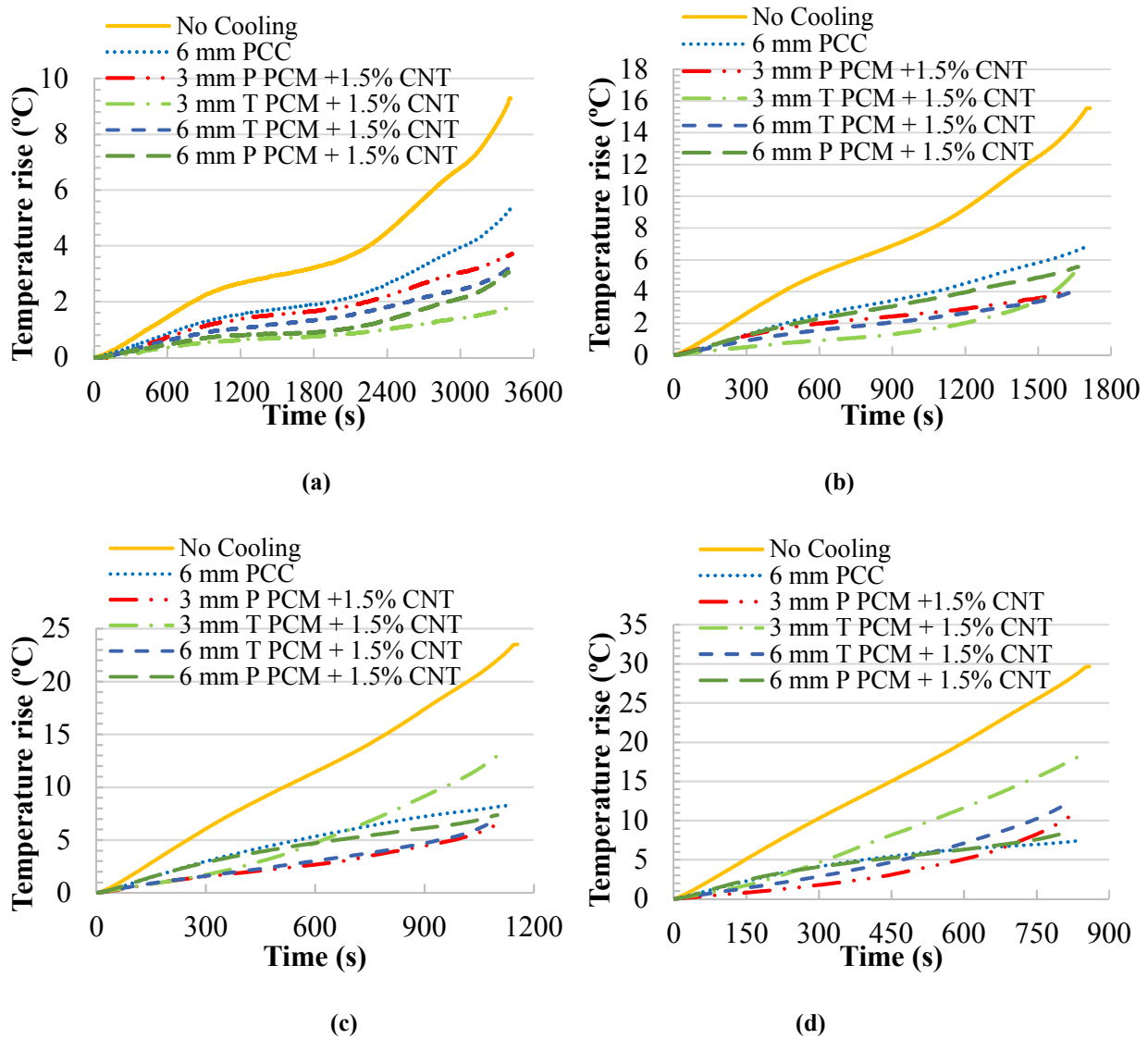


Figure 6.59: Rise in the battery pack temperature at no cooling, and with PCC, PCM with 1.5% CNT plates at; (a) 1C, (b) 2C, (c) 3C, and (d) 4C, discharge rates.

The trend of temperature rise is the same as the previous case. However, the rise in the battery pack temperature decreases with the use of 1.5% CNT. At 1C discharge rate, the rise in the battery pack temperature remains a minimum of 1.9°C with 3 mm thick plates of technical grade PCM and 1.5% CNT. Again, at 4C discharge rate, the rise in the battery pack temperature remains a minimum of 8.4°C with 6 mm thick PCC plates.

Similar comparisons of the rise in the battery pack temperature are made with the use of 3% CNT along with pure and technical grades of PCM. Figure 6.60 shows the variation in the battery pack temperature with no cooling, PCC, PCM and 3% CNT-based plates at various discharge rates. The trend of a temperature rise in the battery pack is the same as the previous case.

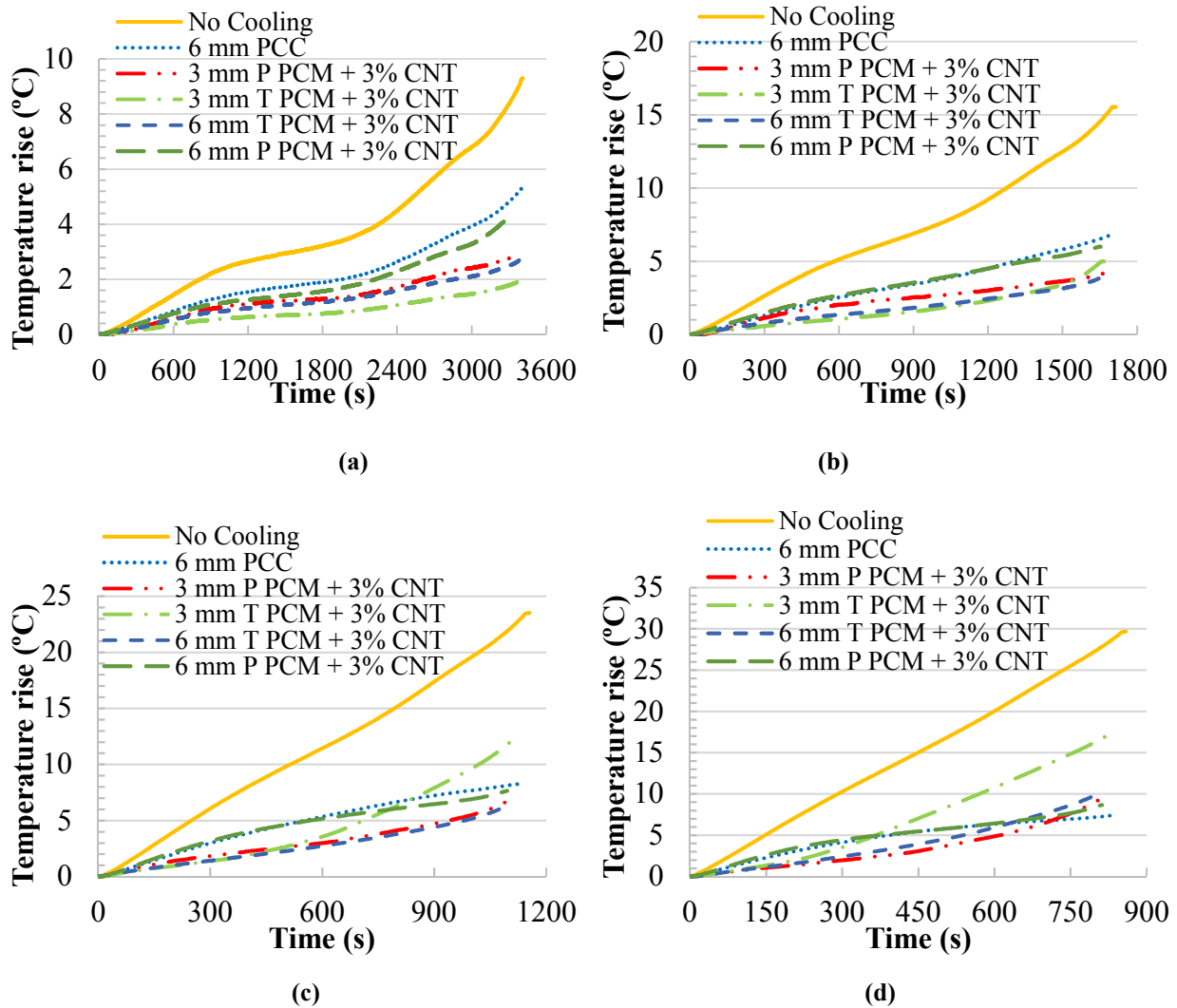


Figure 6.60: Rise in the battery pack temperature with no cooling, and PCC, PCM with 3% CNT plates at; (a) 1C, (b) 2C, (c) 3C, and (d) 4C, discharge rates.

At 1C discharge rate, the rise in the battery pack temperature remains a minimum of 1.9°C with 3 mm thick plates of technical grade PCM and 1.5% CNT. Again, at 4C discharge rate, the rise in the battery pack temperature remains a minimum of 8.2°C with 6 mm thick PCC plates.

Table 6.29 provides a comparison between the maximum and average temperatures of the battery pack with various cooling conditions. The colour coding is based on the optimum operating temperature range of the Li-ion battery. In the case of no cooling, the maximum temperature of the battery pack at 1C and the average temperature of the battery pack at 1C, 2C and 3C remains within the optimum temperature of the Li-ion battery, i.e. 25-40°C.

Table 6.29: Comparison of maximum and average temperatures of the battery pack with various cooling conditions at various discharge rates.

Thickness of Plate (mm)	Cooling Conditions	Maximum Temperature of the Battery Pack at Various Discharge Rates (°C)				Average Temperature of the Battery Pack at Various Discharge Rates (°C)			
		1C	2C	3C	4C	1C	2C	3C	4C
N/A	No Cooling	33	42.7	48.6	56.5	27.9	34.5	37	41.7
	Cold Plate at 10 °C	13.5	15.3	19.5	21.4	12	12.2	16	17.8
	Cold Plate at 20 °C	21.9	23.4	26.3	28	20.6	21.5	23.2	24.6
	Cold Plate at 30 °C	30.4	31.3	32.7	34.1	29.4	30.4	31.1	32
	Cold Plate at 40 °C	39.2	40.3	41.4	43.3	38.7	39.2	39.5	40.7
6	PCC	29.1	34.1	35.6	36.5	25.9	30.6	32.2	33.8
9	PCC	28.7	33.2	34.9	36	25.8	30.1	31.3	32.9
12	PCC	28	32.8	34.9	36.4	25.3	29.3	30.6	32
3	Technical Grade PCM	25.9	31.5	39.4	45.1	24.5	27.5	31	34
	Technical Grade PCM +1.5% CNT	26.1	31.2	39	44.1	25.1	27.4	31	33.8
	Technical Grade PCM +3% CNT	25.9	30.5	38.1	43.5	24.8	27.2	30	32.9
	Pure PCM	27.4	29.3	35.2	42.1	25.5	28.1	29.9	32.8
	Pure PCM +1.5% CNT	27.1	29.3	32.3	37.6	25.1	27.4	28.4	30.4
	Pure PCM +3% CNT	27.2	29.3	32.3	36.2	25.6	27.3	28.4	29.7
6	Technical Grade PCM	25.4	28.2	32.7	40.4	24	26.4	28.5	31.6
	Technical Grade PCM +1.5% CNT	24.5	27.9	31.5	37.9	22.7	25.8	27.7	30.5
	Technical Grade PCM +3% CNT	25.1	28	31.3	35.9	23.5	25.9	27.6	29.6
	Pure PCM	26.3	28.6	29.8	31.7	23.9	26	26.7	28
	Pure PCM +1.5% CNT	25.4	28.5	29.6	31.3	22.8	25.7	26.4	27.5
	Pure PCM +3% CNT	25.3	27.8	29.2	31.1	23.3	25.1	26	27.2

While using cold plates, the maximum and average temperatures of the battery pack remain within the required temperature range of the Li-ion battery with 30°C coolant temperature at all discharge rates. With 6 mm thick PCC plates, the maximum and average temperatures of the battery pack remain within the required temperature range of the Li-ion battery at all discharge rates. The result shows that there are minor reductions in the battery temperature with an increase in PCC thickness. With 3 mm thick plates made from pure PCM and CNTs and 6 mm thick pure PCM plates, the maximum and average temperatures of the battery pack remain within the required temperature range at all discharge rates.

6.6.1 Applications and Limitations of PCM-based BTMS

The results show that the developed PCM-based BTMS is capable of managing the battery temperature within the optimum temperature range, i.e. 25-40°C, with no liquid cooling system. However, applications of PCM-based BTMS are limited and also depend on the operating condition. The results show that once the PCM melts, it requires some time to dissipate the heat to the environment through natural convection before it can be used for the second cycle. Therefore, its stand-alone application is limited to cases which have a gap between two cycles and for smaller vehicles.

In smaller electric vehicles, such as motorcycles, lawn movers and boats, PCM can be used as a stand-alone BTMS as natural convection cooling will be sufficient to remove the heat from the PCM plates placed between the cells. If the charging and discharging cycles are continuously repeated, it is advisable to use the active cooling system with PCM-based BTMS. Also, in regions where the ambient temperature remains higher than the melting point of PCM, an active cooling system is required with PCM-based BTMS. Even when PCM is integrated with active liquid cooling, it provides freedom to remove the heat from the PCM plate during charging. Also, the amount of energy required to remove the heat from the PCM will be significantly lower compared to the amount of energy used in the continuous operation of conventional BTMS. Hence, this helps to increase the driving range of the vehicle and improve the life of the battery by keeping a more uniform temperature in the battery pack. The major issue of extra space requirement to adjust the PCM plates between the cells can be tackled through innovative design of the vehicle.

6.7 Microscopic Study for Agglomerations

The results obtained from the microscopic study of a PCM and CNT mixture with and without polyurethane foam are presented in this section. The thermal conductivity of PCM is increased with the use of CNTs, but during the phase change process, nanoparticles start agglomerating and decrease the effectiveness of CNTs in order to increase thermal conductivity. To observe the agglomeration effect in CNTs, the following sample are prepared for testing purposes:

- a) Pure PCM with 1.5% CNT
- b) Pure PCM with 3% CNT
- c) Technical grade PCM with 1.5% CNT
- d) Technical grade PCM with 3% CNT

Figure 6.61 shows the micrographs obtained from a microscope for pure PCM (99% purity) and Pure CNTs (95% purity).

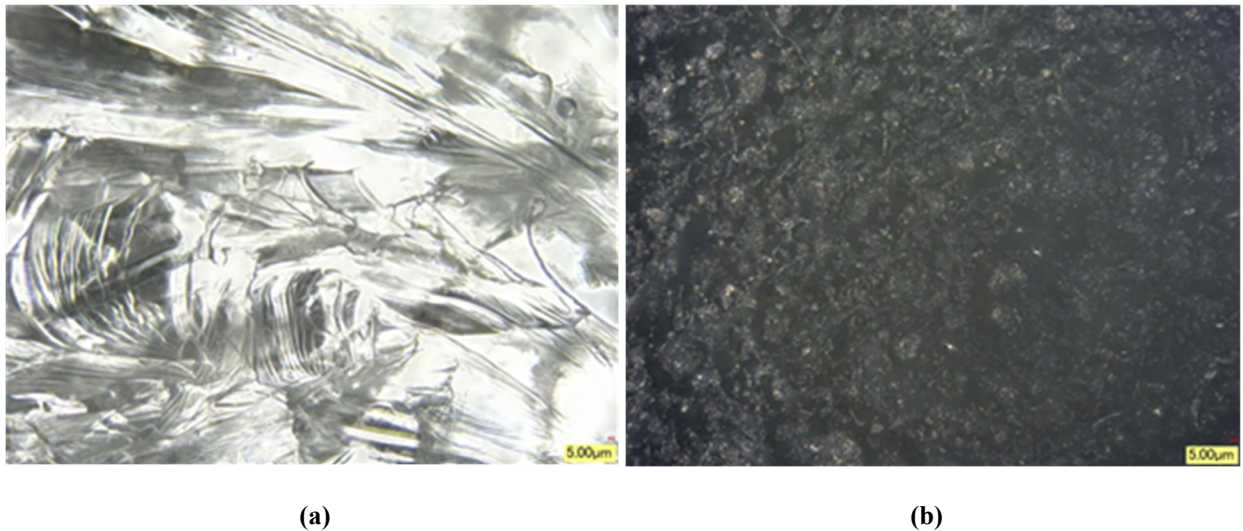


Figure 6.61: Micrographs of (a) pure PCM (n-Octadecane), (b) pure CNTs.

An ultrasonic water bath is used to disperse CNTs in PCM. The prepared sample of PCM and nanoparticles are studied using an optical microscopic. A beam of high-intensity light is used to melt the observed region of the samples. Figure 6.62(a-d) shows the micrographs obtained before and after the phase change process takes place for a sample consisting of pure PCM (n-Octadecane) and CNTs. The results clearly show that before melting of PCM, CNTs particles are properly

dispersed in PCM, but as soon as the PCM starts melting, the CNTs start agglomerating and form clusters.

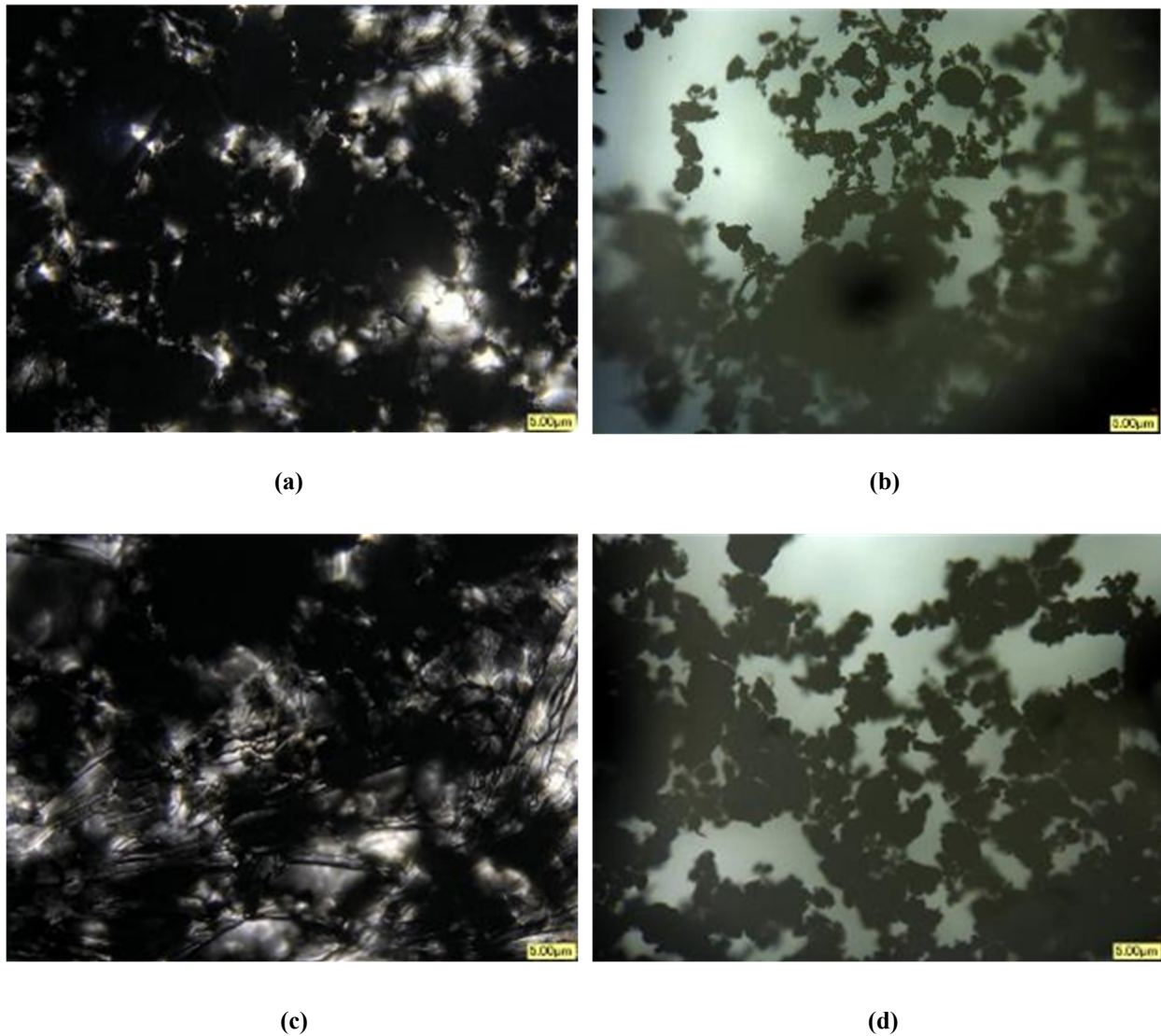


Figure 6.62 Micrographs of pure PCM with; (a) 1.5% CNT before melting, (b) 1.5% CNT after melting, (c) 3% CNT before melting, (d) 3% CNT after melting.

The formation of CNT cluster leaves areas with no CNTs in the PCM. Therefore, some areas with a cluster of CNTs have high thermal conductivity while other areas with PCM only have low thermal conductivity. Also, with the passage of time, these CNT clusters settle down at the bottom surface due to gravity, leaving no or few CNTs in the rest of the melted PCM. This reduces the effectiveness of CNTs in enhancing the thermal conductivity of PCM.

To avoid/reduce the agglomeration effect and settlement of CNTs at the bottom, an open cell polyurethane foam is used along with PCM and CNTs. The small cavities in polyurethane foam keep the CNTs in their place and do not allow them to combine or settle down on the bottom surface. Samples are made through a special process as previously discussed in the Chapter 4. To determine the effect of using foam on the agglomeration effect in CNTs, the following samples are prepared:

- a) Pure PCM and 1.5% CNT with 3 mm thick foam
- b) Pure PCM and 3% CNT with 3 mm thick foam

Similar to the previous case, a high beam of light is used to melt the observed region of the sample. Figure 6.63(a-d) shows the comparison of micrographs obtained for the mixture of PCM and CNTs, and PCM, CNTs and polyurethane foam after melting. During the microscopic test of the PCM and CNT mixture, a high beam of light passes through the sample and a clear view is obtained of the formation of the CNT cluster. In the case of the 3 mm thick sample of PCM, CNTs and polyurethane, the beam of light cannot pass through the sample due to greater thickness. Therefore, the micrograph of the sample is obtained through the reflection of light in the microscope.

During the microscopic test of the PCM and CNT mixture, a clear movement of CNTs (to agglomerate) is observed, while negligible movement is observed during the test of PCM, CNTs and polyurethane foam samples. The obtained micrograph (Figure 6.63) shows that only the PCM came out from the foam after it melts, having no or few CNTs, which shows that most of the CNT particles remain in the cavities inside the foam and do not rise to the surface. To ensure that the CNTs do not settle down at the bottom, tests are repeated with the same plates made from PCM, CNTs and polyurethane foam. Each time, the obtained results are the same and no deposition of CNTs is observed at the bottom surface.

At the end of all cycles, microscopic tests are performed on the used plates made from PCM, CNTs and polyurethane foam. These microscopic tests show the distribution of the CNT particles in the foam. However, no separate micrograph is available from these tests, as the micrographs obtained were the same as those shown in Figure 6.63 for different samples. The same micrographs were obtained due to the fact that as soon as the light from the microscope falls on samples, the PCM

start melting before the micrograph of CNT distribution over the surface can be taken. Therefore, the micrographs only show PCM and few CNT particles. Figure 6.63(a-d) shows the micrographs obtained from a microscope with and without polyurethane foam along with PCM and CNTs.

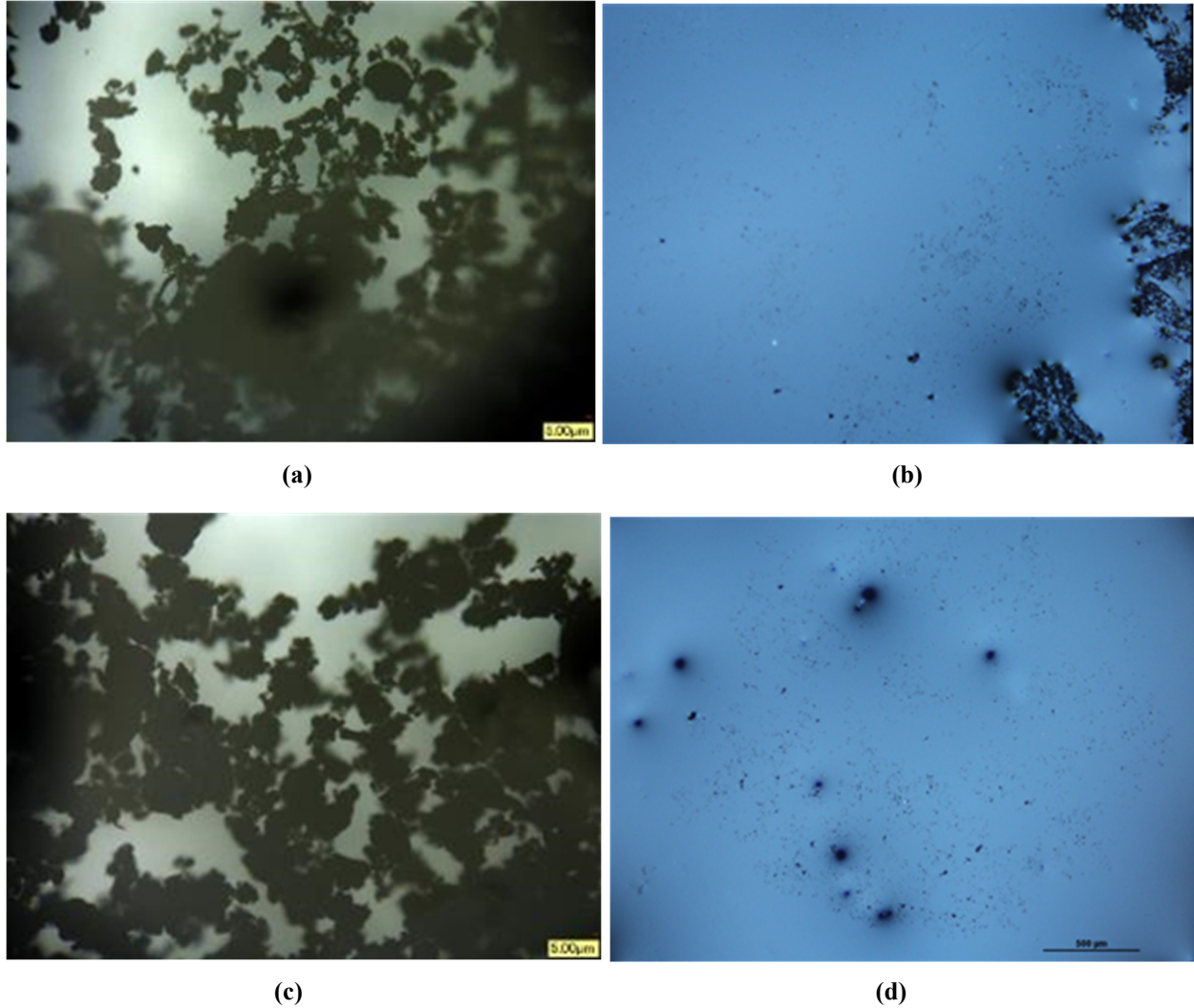


Figure 6.63: Micrographs of pure PCM after melting with; (a) 1.5% CNT without foam, (b) 1.5% CNT with foam, (c) 3% CNT without foam, (d) 3% CNT with foam.

In addition, the battery pack temperature reduces by using CNTs and foam with PCM compared to only PCM. The size of the cavity in an open cell foam can approximately vary from 90 nm - 1 mm [145] and the length of CNT particles varies from 10-50 μm [54]. In the present study, on the basis of selected foam and CNTs, the size of the foam cavity is considered as 10 μm and length of CNT particles as 20 μm . Therefore, the foam to CNTs size ratio is 1:2 and also, there are no through holes in the foam. The foam has a honeycomb/grid type structure, which means that the upper

cavity in the foam is followed by multiple cavities in the lower section. The arrangement of these cavities and size ratio does not allow CNTs to directly move to the bottom surface. As there will be no structural change in the foam during melting and solidification, the CNT particles are expected to remain in their respective locations with repetitive cycles. Based on these observations on the images and rationales, the author concludes that use of polyurethane foam reduces the agglomeration. However, further studies are required to quantify and verify the reduction in agglomeration with polyurethane foam.

6.8 Thermal Conductivity of PCMs and CNTs Mixture

It is important to experimentally investigate the overall thermal conductivity of PCM and CNTs mixture. However, the present study is limited to only theoretical analysis of mixture thermal conductivity. Therefore, in this section, the theoretical results from enhancement in thermal conductivity of PCM with the use of CNTs are presented. Previous studies show that the thermal conductivity of nanotubes depends on their arrangement. The effective thermal conductivity would be very high if the nanotubes were placed in series, but very low when arranged in parallel. Figure 6.64 shows the variation in the effective thermal conductivity of the PCM and CNT mixture with the change in CNT concentration, assuming CNTs are arranged in series and parallel.

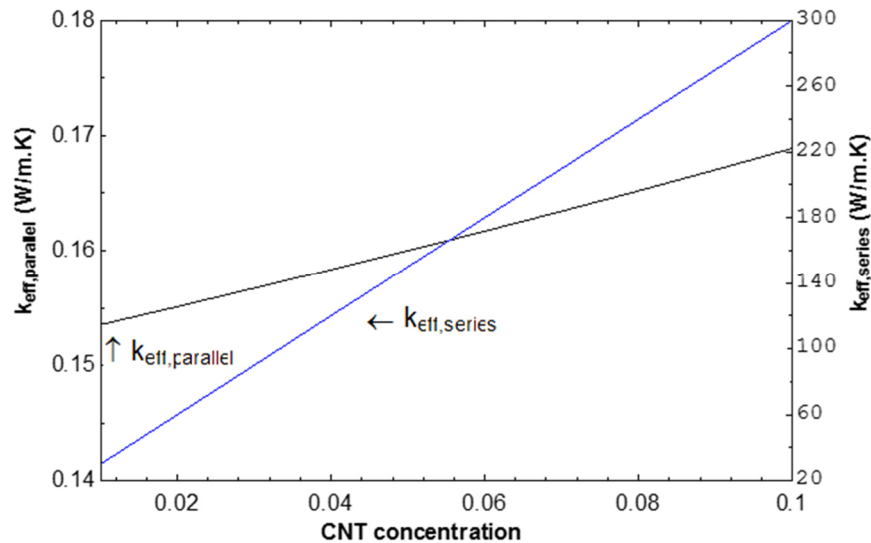


Figure 6.64: Variation in the effective thermal conductivity of PCM and CNT mixture with a change in CNTs concentration, assuming CNTs in parallel and series arrangement.

In the case of the parallel arrangement of CNTs, the effective thermal conductivity of the mixture increases from 0.153 to 0.167 W/m K, when CNT concentration increases from 1 to 10% by volume. On the other hand, in the case of series arrangement, the effective thermal conductivity of the mixture increases from 30.1 to 300.1 W/m K with the increase in CNT concentration from 1 to 10% by volume, as shown in Figure 6.64.

Although more effective if CNTs are arranged in series, from a practical perspective this is very difficult to manage. Therefore, there will be a combination of series and parallel nanotubes in the PCM. In order to understand the effect of series arrangement of CNT on thermal conductivity of mixture probability “P” can be defined as the series arrangements of the nanotubes (refer to Equation 5.50). Varying the probability varies the mixture’s thermal conductivity. A graph is plotted to investigate the effect of a change in the probability of a series arrangement of CNTs on the effective thermal conductivity of the mixture, as shown in Figure 6.65.

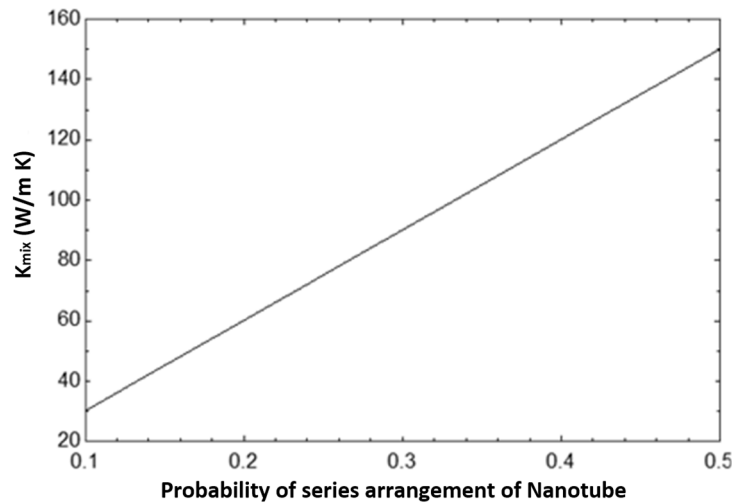


Figure 6.65: Variation in the thermal conductivity of PCM and CNT mixture with a change in the probability of series arrangement of the nanotubes.

A linear relation is obtained between the probability of a series arrangement of CNTs and improvement in thermal conductivity of PCM. It is found that effective thermal conductivity of the mixture increases from 30.2 to 150.2 W/m K with the increase in probability of the series arrangement of the nanotubes from 10 to 50 %, when CNT concentration is 10%. Further calculations are made to investigate the combined effect of variation in the probability of the series arrangement of nanotubes and CNT concentration on the effective thermal conductivity of the

mixture. Figure 6.66 shows that the effective thermal conductivity of the mixture increases from 3.153 to 150.2 W/m K when the probability increases from 10 to 50 % and CNT concentration increases from 1 to 10 %.

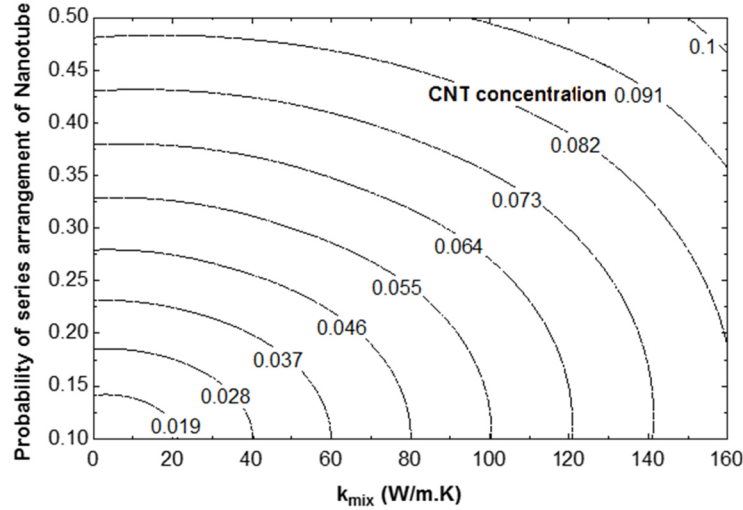


Figure 6.66: Variation in the thermal conductivity of PCM and CNT mixture with a change in the probability of series arrangement of CNTs and CNT concentration.

6.9 Resistance Measurement of Li-ion Cell

In this section, the experimental results obtained from the internal resistance of the cylindrical and prismatic cells are presented.

6.9.1 Internal Resistance of Prismatic Cell

A123 20Ah Li-ion battery is used to experimentally measure the internal resistance at different temperatures (10°C, 20°C, 30°C, 40°C, 50°C, 60°C) and different SOC (10% to 90%). A precise thermal chamber is used to simulate the required environmental temperature. The results show that internal resistance of a cell decreases with an increase in the cell temperature and increases with a decrease in SOC. The internal resistance is found to be a maximum of 11.2 mΩ at 10% SOC and 10°C, and a minimum of 2.79 mΩ at 90% SOC and 30°C. The drop in internal resistance is found to be a maximum of 2.51 mΩ at 10% SOC when the temperature changes from 20°C to 30°C and then from 30°C to 40°C (1.91 mΩ), as shown in Figure 6.67. No significant change in internal resistance is observed after 40°C. Similar trends are observed in the internal resistance of the cell with the change in SOC. A sharp increase of 2.79 mΩ in internal resistance of the cell is observed when SOC drops from 20% to 10%, as shown in Figure 6.67.

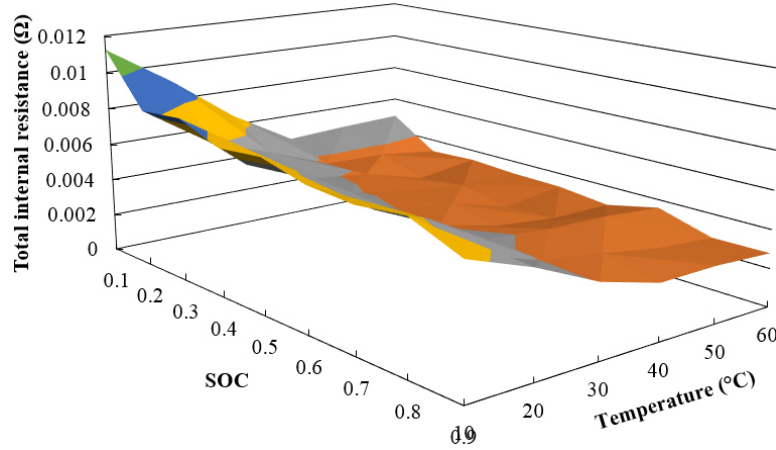


Figure 6.67: Variation in total internal resistance of the cylindrical cell with respect to change in the temperature and SOC.

6.9.2 Internal Resistance of Cylindrical Cell

A pack of seven NCR18650B 3.4 Ah Li-ion cells are used to experimentally measure the internal resistance by varying the temperature from 0°C to 60°C at different SOC (10% to 90%). Similar to the previous case of the prismatic cell, a precise thermal chamber is used to simulate the required environmental temperature. The results obtained from the experiments show that the internal resistance of the cell decreases with an increase in cell temperature and increases with the decrease in SOC.

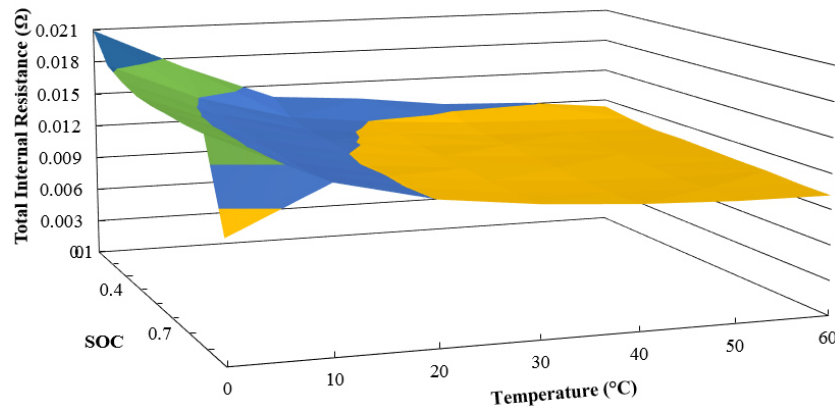


Figure 6.68: Variation in total internal resistance of prismatic cell with respect to change in the temperature and SOC.

The internal maximum resistance is found to be a maximum of 20.9 mΩ at 10% SOC and 0°C, and a minimum of 10 mΩ at 90% SOC and 60°C. The resistance drop is found to be a maximum of 3.8 mΩ when the temperature changes from 0°C to 10°C and then from 10°C to 20°C (3.2 mΩ)

at 10% SOC, as shown in Figure 6.68. No significant change is observed in internal resistance after 40°C. Similar trends are observed in the internal resistance of the cell with a change in SOC, as in the case of the prismatic cell. There is a sharp increase in the internal resistance of the cell when SOC drops from 20% to 10%. A sharp increase of 2.6 mΩ in internal resistance of the cell is observed, when SOC drops from 20% to 10%, as shown in Figure 6.68.

6.10 Results from Modelling in Simulink

Experiments are costly and time-consuming and, in some cases, it is very difficult to perform the experiments with the given constraints. Moreover, a minor change required in the experiment can change the entire experimental setup, which may incur extra cost, time and effort. On the other hand, modelling and simulations are comparatively easy to perform, are less time consuming and can be easily changed at any stage. However, experimental results are reliable, while the reliability of modelling and simulation results need to be checked. In most cases, modelling and simulation results are validated with experimental results.

Similarly, in this section, the results of temperature, voltage, and the heat generation rate of the battery pack obtained from the developed model using MATLAB Simulink are compared with experimental data to assess the accuracy of the developed model. Figure 6.69(a-d) compares the experimental and modelling results of the battery pack temperature at various discharge rates. Good agreement is observed between the experimental and modelling data, indicating the good degree of accuracy of the present model. However, at the end of the discharge cycle, some minor discrepancies are observed. Although the reasons for these discrepancies are unclear, it may be due to the fact that internal resistance used in the model is measured at an interval of 10°C in environment temperature, which may lead to some inaccuracy in the results. Also, at 1C discharge rate, the change in internal resistance is high due to the lower temperature, which again changes rapidly due to a decrease in SOC toward the end of the cycle. This affects the model accuracy in calculating the temperature towards the end of the cycle. The model predicts a lower temperature than experimentally at 1C and 4C discharge rates and a higher temperature value at a 3C discharge rate. At 2C and 3C, the experimental and model values of temperature are in good agreement.

In general, the observed trends show that the surface temperature increases as the C-rate increases. The maximum temperatures observed from modelling and experiments at various discharge rates are given in Table 6.30.

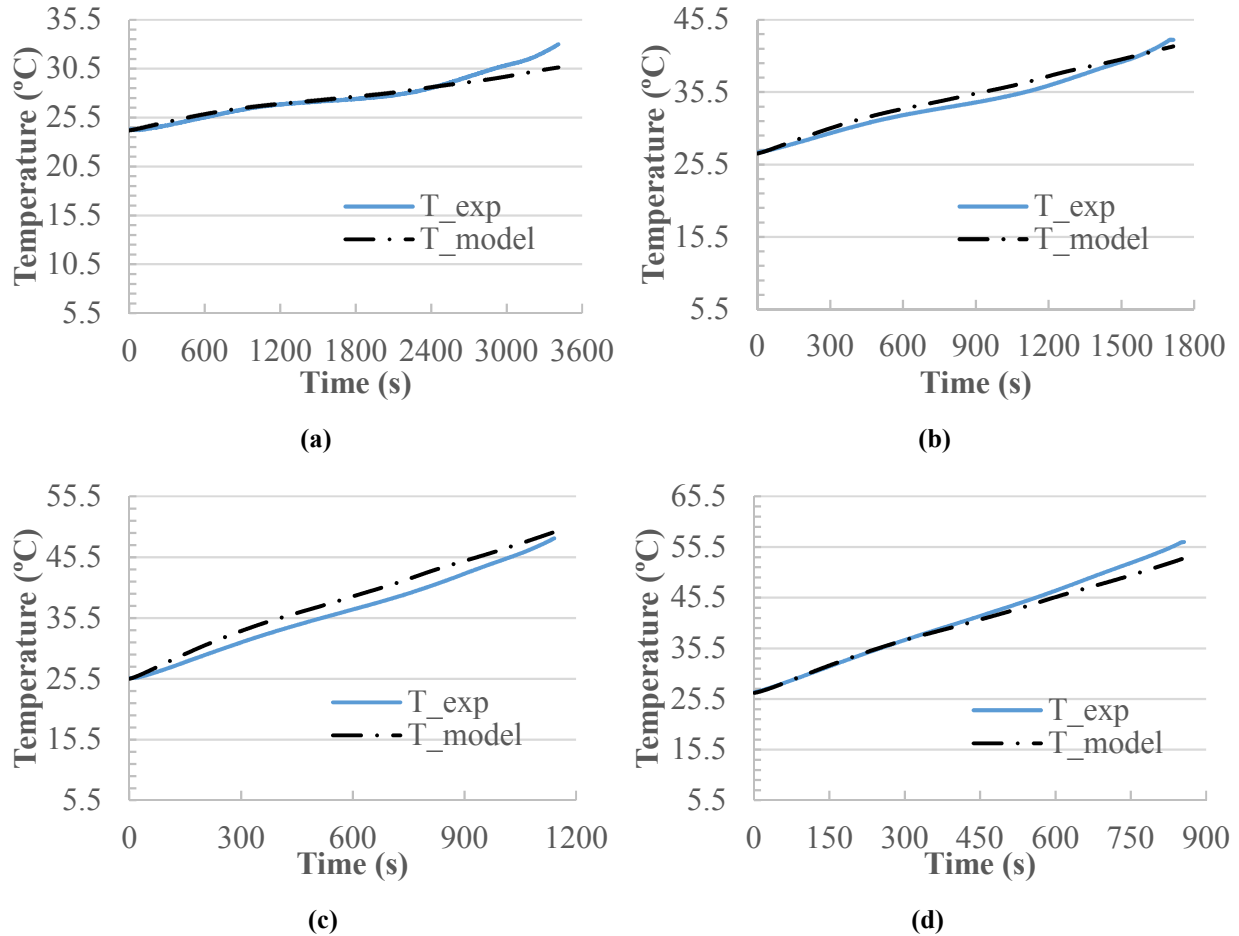


Figure 6.69: Average temperatures of the battery pack from modelling and experiments at; (a) 1C, (b) 2C, (c) 3C, (d) 4C, discharge rates.

Table 6.30: Maximum temperature obtained, and total heat generation during experiment and modelling at various discharge rates.

Discharge Rate	Maximum Temperature (°C)		Total Heat Generation (kJ)		Capacity (Ah)
	Experimental	Modelling	Experimental	Modelling	
1C	33	30.7	41.70	37.50	19.05
2C	42.7	41.8	47.50	47.20	19.04
3C	48.6	49.6	54.50	56.60	19.02
4C	56.5	53.8	59.20	57.00	19.02

Figure 6.70(a-d) compare the experimental and modelling results of the voltage at various discharge rates. All profiles are plotted against time. Good agreement can be seen between the modelling and the experimental battery pack voltages in Figure 6.70. At lower discharge rates of 1C and 2C, the modelling voltage values are comparatively lower than the values obtained experimentally, while an opposite trend can be seen at higher discharge rates (e.g., 4C). The discharge capacity of the battery pack at various discharge rates is given in Table 6.30.

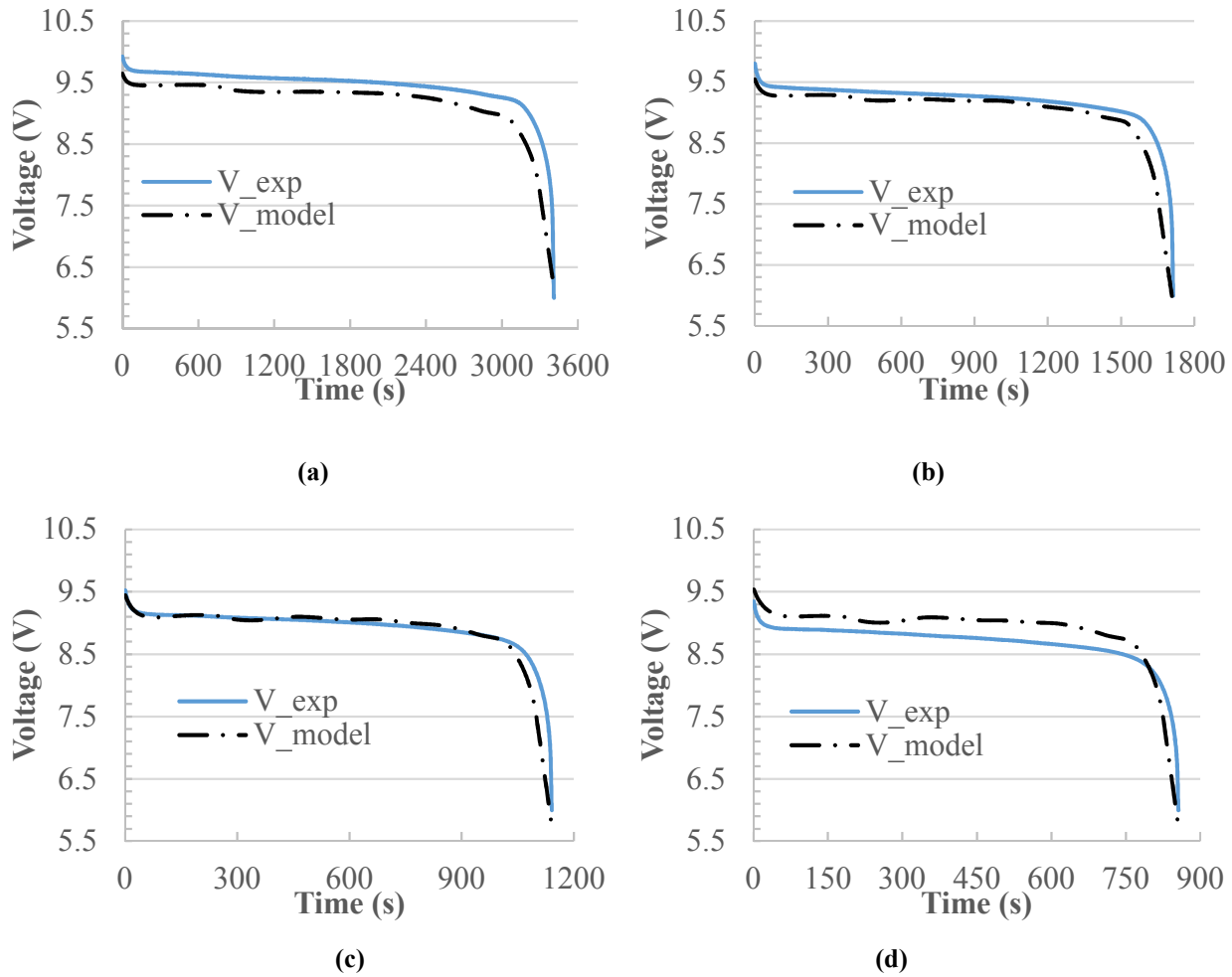


Figure 6.70: Experimental and modeling voltages of the battery pack at; (a) 1C, (b) 2C, (c) 3C, (d) 4C, discharge rates.

The rate of heat generation from the developed model is calculated using Equation 5.6. The heat generation rate during the experiments is calculated as the sum of heat stored within the battery pack and heat loss to the surroundings. Figure 6.71(a-d) compares the heat generation rate based on experimental data and modelling at several discharge rates. Good agreement between modelling

and experimental heat generation rates can be seen from Figure 6.71(a-d), but there is a fluctuation in the experimental heat generation rates. Heat generation rates obtained experimentally are based on the obtained experimental temperature using thermocouples.

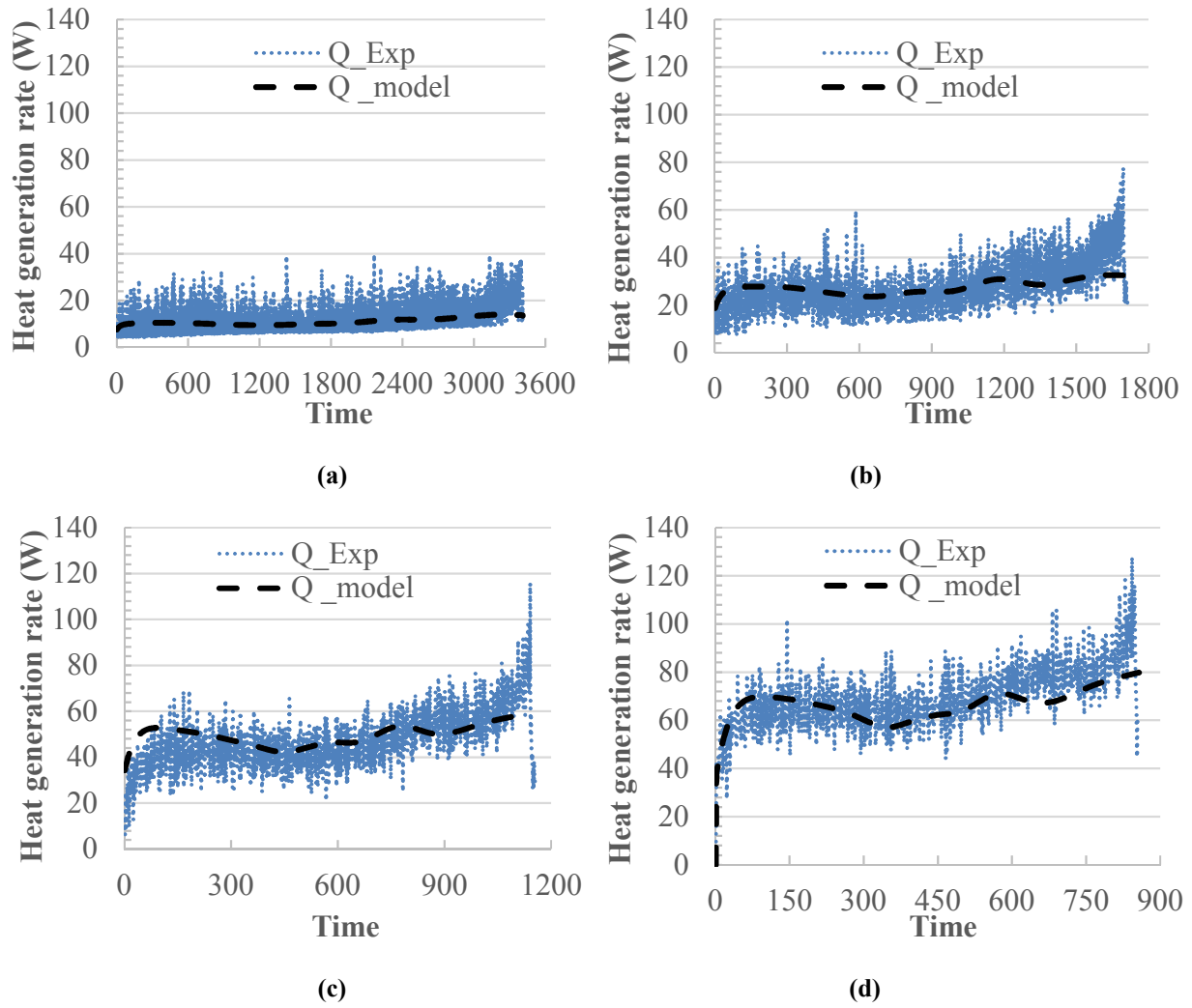


Figure 6.71: Heat generation rates in the battery pack obtained from modelling and experimental at; (a) 1C, (b) 2C, (c) 3C, (d) 4C, discharge rates.

The reason for fluctuation in experimental heat generation rate is already discussed in section 6.1.3. Some discrepancies in modelling and experimental heat generation rates can be seen towards the end of the discharge cycle. These discrepancies appear to correlate with the discrepancies in modelling and experimental temperatures. The total experimental and modelling heat generation values at various discharge rates are given in Table 6.30. The total experimental and modelling heat generation values compare well at 2C and 3C discharge rates, while some deviations exist at

the 1C and 4C discharge rates. The total heat generation is found to be a maximum of 59.2 kJ at 4C discharge rate via experiments, and a minimum of 37.50 kJ at 1C discharge rate in the case of modelling. From Table 6.30, it can be seen that the total heat generation increases with increasing discharge rate.

In the present study, all the model input parameters are experimentally determined specific to a 20Ah LiFePO₄ prismatic cell, which makes the developed model more accurate and reliable. Good agreement between the modelling and experimental result shows that the developed model is adequate to predict the battery pack behaviour at different discharge rates with acceptable error. The present model requires only a few inputs such as current, internal resistance at different temperatures and SOC, and provides the rest of the required properties of the cell. These inputs are easy to obtain through experiments, or from the literature, compared to performing entire experiments for all the properties. Testing a complete battery pack can be difficult due to various issues, including the limited capacity of the testing equipment, safety issues, and time. The developed model can be extended to a complete battery pack of an EV or HEV to obtain all the properties, such as voltage, surface temperature, and heat generation rate. The developed model can be used with other chemistries of Li-ion batteries with minor changes in input data, such as the internal resistance of that type of battery at different SOC and temperatures. The model can be further extended for various other cooling strategies with required changes and inputs.

6.11 Results from ANSYS Simulation

ANSYS simulations are performed to better understand the variation in temperature across the cell surface with 6 mm thick pure PCM plates. The rate of heat generation calculated from the experiments at different discharge rates is used as the heat source for the entire cell. In practice, the heat generation rate is not constant across the cell. However, it is observed from experimental data that the temperature of the cell over the entire surface remains almost equal, with some deviation at the corner. This happens because the thermal conductivity of the cell is very high in x and y-directions compared to the z-direction. Therefore, the rate of heat transfer in x and y-directions is higher compared to the z-direction. The same assumptions are considered for the simulations. Three different points are selected across the x-axis on the surface of the cell to measure the average temperature of the cell. The selection of these points are made by

thermocouple locations of the cell during the experiments. The obtained results from simulations are validated with experimental results. In the simulation, anode and cathode terminals are not considered since the focus of the study is limited to the temperature distribution in the battery where PCM plates are used.

Figure 6.72 shows the comparison of the cell surface temperature obtained from simulation and experiment at various discharge rates. Good agreement can be seen between the experimental and simulation temperatures at 2C and 3C discharge rate, except for some deviation towards the end of the cycle. At 1C discharge rate, there is some deviation in the experimental and simulation temperatures during the cycle. However, the final temperature in both cases is almost the same.

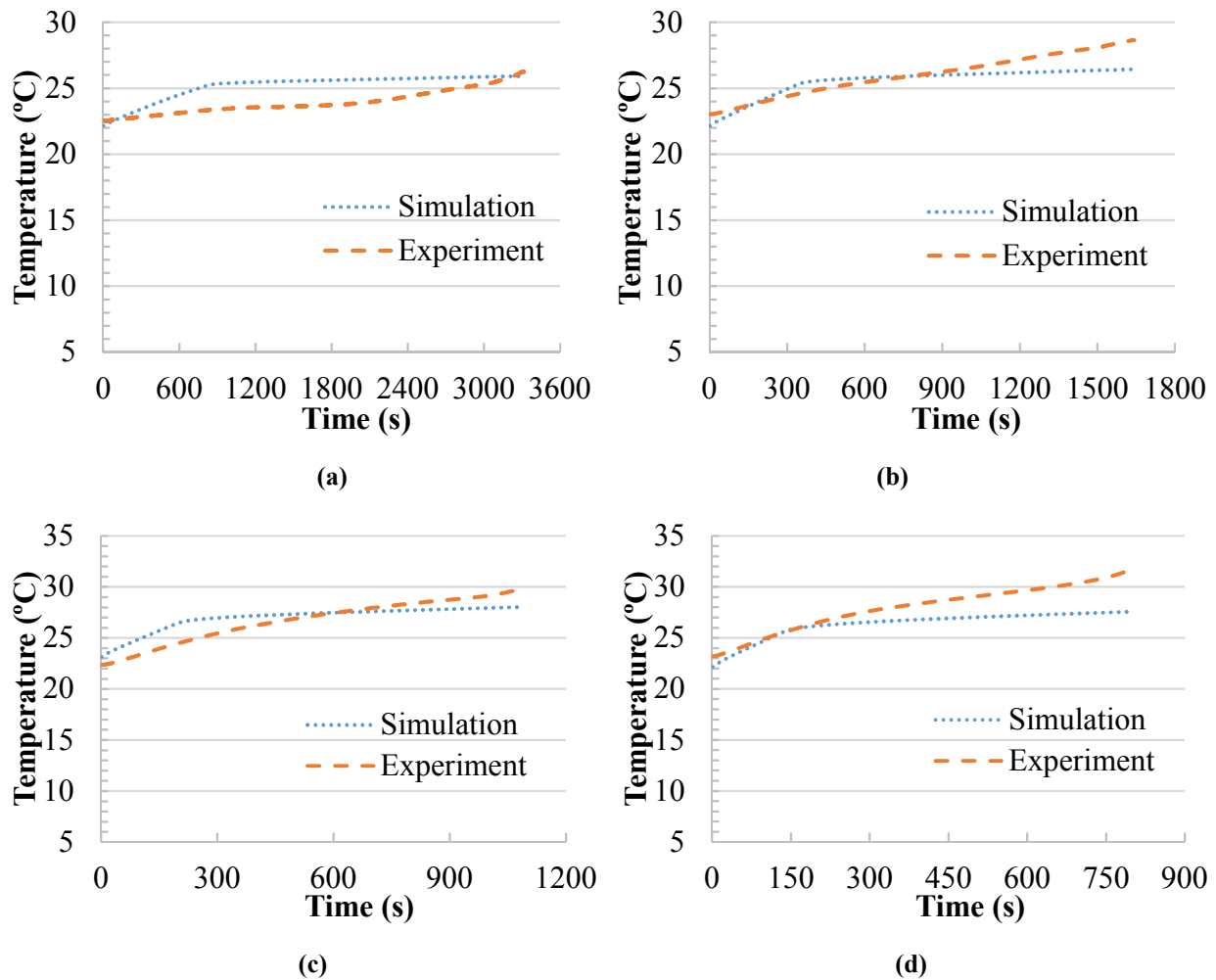


Figure 6.72: Average temperatures of the battery pack from simulation and experiments at; (a) 1C, (b) 2C, (c) 3C, (d) 4C, discharge rates.

A significant deviation is observed in the experimental and simulation temperatures of the cell towards the end of the cycle at 4C discharge rate. It is also observed that the final experimental temperature of the cell surface remains higher than the simulation temperature at all discharge rates. This may be due to the fact that, in the case of simulation, two PCM plates are used for the single cell while, in the experiment, four plates are used for three cells. Therefore, in the case of simulation, more PCM is available to absorb the heat compared to the experiment, keeping the cell surface temperature low.

From these comparisons, it can be concluded that, with some data input such as heat generation rates and basic assumptions, ANSYS simulation can be used to obtain the surface temperature of the cell with PCM plates. At low discharge rates, ANSYS simulation provides the surface temperature of the cell with reasonable accuracy while significant deviation is observed at high discharge rates. The deviation in simulation and experimental results shows that the assumption of a uniform heat generation rate is not valid at high discharge rates. Therefore, more detailed analysis is required by considering the actual variation of heat generation rate in the cell in order to improve the accuracy of the results.

Figure 6.73 shows the temperature contour on the surface of the cell and the PCM plate at the end of the 1C discharge cycle. It is observed that the temperature in the mid-surface is highest and decreases towards the corners of the cell.

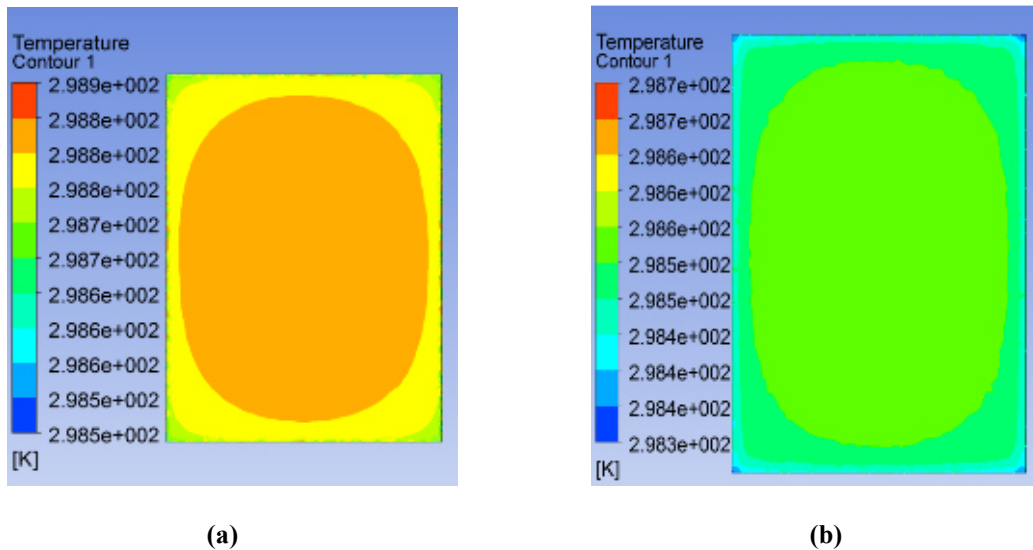


Figure 6.73: Temperature contours at the end of 1C discharge cycle; (a) cell surface, (b) PCM plate surface.

This occurs because heat transfer takes place at the corners through convection. However, the difference between the temperature at mid surface and the corners is not significant, due to the low convective heat transfer coefficient at the cell and PCM plate corners. These results confirm that the cell surface temperature remains almost equal across the surface. A similar pattern of temperature variation is obtained at 2C, 3C, and 4C discharge rates.

6.12 Energy and Exergy Analyses Result

The energy and exergy analyses result obtained from the experiments at the various cooling conditions and discharge rates are presented in this section. As discussed in Chapter 5, the energy efficiency of the battery pack is defined in two different ways. However, only minor differences are observed between both these efficiencies. Therefore, only one efficiency (electrical efficiency) is discussed here. The electrical efficiencies at various cooling conditions and discharge rates is given in Table 6.31. From Table 6.31, it is observed that the efficiency of the Li-ion battery varies significantly with coolant temperatures and discharge rates. However, an interesting observation from Table 6.31 is that the energy efficiency increases with an increase in coolant temperature and maximum with 30°C coolant temperature in most of the cases.

At 1C discharge rate, with the cold plates only, and with cold plates and 6 mm thick PCC plates, the energy efficiency of the battery pack increases from 83% to 91% and 86% to 93%, respectively, when the coolant temperature increases from 10°C to 30°C. It then starts decreasing and to 89% and 92% with the cold plates only, and with the cold plates and 6 mm thick PCC plates, respectively, at 40°C coolant temperature. The reason for the increase in energy efficiency with temperature can be explained by the fact that internal resistance of the Li-ion cells decreases with an increase in temperature. Similar trends are observed in most of the cases, as shown in Table 6.31.

The exergy destruction at the battery pack is calculated as exergy destruction at the cells and coolant (water). Table 6.32 provides the total exergy destruction at various cooling conditions and discharge rates. Only physical exergy is considered and calculated in this study. The ambient temperature is selected as 20°C for all calculations.

Table 6.31: Electrical efficiencies at various cooling conditions and discharge rates.

Discharge Rate	PCC Plate Thickness (mm)	Efficiency at Various Cooling Conditions				
		10°C	20°C	30°C	40°C	No Cooling
1C	None	0.83	0.85	0.91	0.89	0.90
	6	0.86	0.91	0.93	0.90	0.92
	9	0.87	0.91	0.92	0.91	0.93
	12	0.86	0.91	0.90	0.91	0.91
2C	None	0.73	0.75	0.87	0.81	0.88
	6	0.76	0.84	0.89	0.91	0.89
	9	0.78	0.85	0.88	0.88	0.88
	12	0.75	0.88	0.88	0.89	0.88
3C	None	0.69	0.79	0.83	0.88	0.86
	6	0.73	0.80	0.85	0.86	0.86
	9	0.72	0.80	0.84	0.85	0.85
	12	0.70	0.84	0.85	0.86	0.85
4C	None	0.64	0.73	0.80	0.84	0.83
	6	0.70	0.75	0.80	0.80	0.79
	9	0.73	0.75	0.79	0.82	0.78
	12	0.66	0.82	0.81	0.83	0.82

As presented in Table 6.32, the exergy destruction of the battery pack increases with an increase in coolant temperature and is found to be a maximum of 732.1 J at 4C discharge rate with 40°C coolant temperature, compared to other coolant temperatures. Overall, total exergy destruction is found to be a maximum of 3870.3 J at 4C discharge rate with no cooling condition. The value of exergy destruction increases with the increase in discharge rate at all cooling conditions. The negative value of exergy destruction at 10°C coolant temperature is due to the fact that the ambient temperature selected for the study in order to calculate exergy destruction is higher than the coolant temperature.

From these results, it can be concluded that energy efficiency of the battery pack increases with an increase in coolant temperature and tends to be maximum around 30°C coolant temperature. However, the exergy destruction increases with an increase in coolant temperature and reaches

maximum with no cooling condition. Based on results, it is advisable to use a BTMS and maintain the coolant temperature near to 30°C in order to have maximum energy efficiency and lower exergy destruction.

Table 6.32: Exergy destructions at various cooling conditions and discharge rates.

Discharge Rate	PCC Plate Thickness (mm)	Exergy Destruction at Various Cooling Conditions (J)								
		10°C		20°C		30°C		40°C		No Cooling
		Cell	Water	Cell	Water	Cell	Water	Cell	Water	Cell
1C	None	-30.5	-0.2	52.3	0.4	82.9	2.5	75.8	-0.2	659.7
	6	-39	-0.5	57.2	1	66.4	0.7	44.2	0.3	272.6
	9	-75.2	-0.5	95.8	0.3	271	1.3	49	0.7	229.5
	12	-33.1	-0.2	200.7	0.2	48.2	0.9	37.1	0.4	190.8
2C	None	10.4	0.1	116.5	0.5	134	0.9	210.8	1	1545.3
	6	-28.2	-0.3	102.4	0.7	177.8	1.2	241.9	1.5	547.8
	9	-40.1	-0.2	363	1.3	539.7	1.9	122.4	0.9	446.4
	12	-47.2	-0.3	393.9	0.4	110.6	0.8	105.6	0.9	368.3
3C	None	54	0.4	262.2	1.2	249.6	1.2	457.7	2	2614.8
	6	-4.2	0.0	204	1.1	314.6	1.5	428.2	2	696.7
	9	98.6	0.4	664	1.8	953.4	2.4	225.9	1.4	698.6
	12	-42	-0.2	578.4	0.1	144.6	0.8	190.3	1.1	534.8
4C	None	106.8	0.8	367	1.4	378.2	1.3	717.8	2.7	3870.3
	6	31.3	0.5	290	1.3	420.6	1.4	732.1	2.2	545.5
	9	208.4	1.3	992.1	2.3	1311	2.6	361.5	1.4	805.9
	12	-14.7	0.0	670.5	0.1	307.1	0.9	306	1.2	586

6.13 Economic Analysis Results

The capital and operational costs associated with conventional BTMS and PCM-based passive BTMS as developed in the present study are discussed in this section. The costs from both these BTMSs is compared. The BTMS of Chevy Volt HEV is selected for cost analysis. The capital cost of Chevy Volt BTMS is assumed to be approximately CAD \$1500 based on the model presented in the literature [146]. The operational cost of BTMS is calculated based on the parameters of Chevy Volt as shown in Table 6.33, from where it can be seen that, out of 16 kWh of battery capacity, approximately 1.3 kWh is used for BTMS.

Considering a scenario where the battery is completely charged and discharged every day over its life cycle, the total energy required for BTMS can be calculated as:

$$\text{Total Energy} = 1.3 \times 365 \times 8 = 3796 \text{ kWh}$$

The average price of electricity in Ontario is 13.3 ¢/kWh [147]. Based on the cost of electricity, the operational cost of the BTMS can be calculated as:

$$C_{o,cycle} = 3796 \text{ kWh} \times 13.3 \text{ ¢/kWh} = \$504.86$$

Although the cost of electricity varies with province and country, the total operational cost of the BTMS of a Chevy Volt is \$504.86.

Therefore, the total cost of the BTMS will be:

$$C_{BTMS} = \$1500 + \$504.86 = \$2004.86$$

Table 6.33: Parameters of Chevy Volt and electricity prices in Ontario [147, 148].

Parameter	Value
Total Battery Capacity of Chevy Volt (kWh)	16
Available for Vehicle Propulsion (kWh)	11
Capacity Oversize to Limit SOC (kWh)	3.5
Capacity Used for BTMS (Approx.) (kWh)	1.3
Capacity Used for Cabin Cooling (Approx.) (kWh)	0.2
Driving Range on Battery Only (km (mile))	61.2 (38)
Mileage on Battery (km/kWh)	5.56
Mileage on Gas (km/L)	15.7
Lifetime of Battery (year)	8
Off Pick Price of Electricity (¢/kWh)	8.7
Mid Pick Price of Electricity (¢/kWh)	13.2
On-Pick Price of Electricity (¢/kWh)	18
Average Price of Electricity (¢/kWh)	13.3
Average Gas Price in Ontario (¢/L)	112

* All cost in CAD as on January 28, 2017.

For an economic analysis of PCM-based passive BTMS, only those 3 mm and 6 mm thick plates are considered, where the temperature of the battery pack remains within the required range. Three materials are mainly used to develop these plates: PCM (n-Octadecane), CNTs, and polyurethane

foam. The per unit cost of these materials along with the quantity required to make one plate (pure PCM 6 mm thick plate with 1.5% CNT) is given in Table 6.34. The conventional BTMS of a Chevy Volt HEV is considered for replacement by the developed PCM-based passive BTMS. The number of cells in a Chevy Volt battery pack is 288. Therefore, 289 PCM plates need to be placed between cells to absorb the heat.

Table 6.34: Parameters used to calculate the cost of developed passive BTMS.

Parameter	Value
Number of Cell in Battery Pack	288
Number of PCM Plates	289
Thickness of PCM Plate (mm)	6
Cost of PCM (\$/kg)	98
Cost of Multi-walled CNT (\$/kg)	920
Cost of Polyurethane Foam (\$/kg)	20
Mass of PCM in One Plate (kg)	0.137
Mass of CNT in One Plate (1.5% Conc.) (kg)	0.0021
Mass of Polyurethane Foam in One Plate (kg)	0.0047

The total material cost of the developed system is given in Table 6.35. The total material cost of the developed BTMS is \$3967 without CNTs, and \$4466 and \$4967 when 1.5% and 3% CNT is used to form the 6 mm thick pure PCM plates, respectively. Although the 6 mm thick pure PCM plates are enough to manage the required temperature of the battery pack, the use of CNTs further reduces the temperature. At the same time, the use of CNTs further increases the material cost, as the cost of a pure PCM plate with 1.5% and 3% CNT is \$4466 and \$4967, respectively.

Table 6.35: The material cost of the developed systems.

Parameters	CNT Concentration in 6 mm Thick Plate (%)			CNT Concentration in 3 mm Thick Plate (%)	
	0	1.5	3	1.5	3
Cost of PCM (\$)	3940	3880	3823	1940	1912
Cost of CNT (\$)	0	558	1117	279	558
Cost of Polyurethane Foam (\$)	27	27	27	14	14
Total Cost (\$)	3967	4466	4967	2233	2484

The cost of the PCM is highest and dominates the overall cost of the developed system. Considering the fact that, with CNTs, 3 mm thick pure PCM plates can manage the required

temperature of the battery pack, the cost of the developed system can be significantly reduced. The cost of the 3 mm thick pure PCM plates with 1.5% and 3% CNT is \$2233 and \$2484, respectively. All these costs are calculated based on the purchase made on a laboratory scale. However, the cost of the developed system can be significantly reduced by bulk purchase of the material on an industrial scale.

According to the author's estimation on the basis of a bulk purchase cost of PCM and CNTs, the material cost of the developed system on an industrial scale will be approximately \$500 compared to a laboratory scale development at \$4466. The estimation is based on the cost of PCM and CNTs on an industrial scale. There will be no operational costs associated with the developed system. The total weight of developed system will be approx. 41.5 kg. It is assumed that the weight of the developed passive BTMS is almost equal to the weight of a conventional BTMS used in a Chevy Volt. Therefore, the cost associated with carrying the load of BTMS is the same in both the cases. The cost of PCC-based BTMS can be calculated by using the different costs provided by the manufacturer (Table 6.36).

Table 6.36: PCC material cost provided by the manufacturer.

Cost Type	Value (\$)
PCC Per Plate Cost	15
Non-recurring Engineering Fee	190
Batch Fee	190

Therefore, the total cost of PCC-based BTMS can be calculated as:

$$C_{PCC} = \$15/\text{plate} \times 289 \text{ plates} + \$190 + \$190 = \$4715$$

The total cost of PCC-based BTMS is \$4715, which is higher than the cost of PCM-based BTMS when 1.5% CNT is used with PCM. However, the cost of PCC-based BTMS is lower compared to PCM-based BTMS when 3% CNT is used with PCM.

Considering a scenario where a conventional BTMS is replaced with the developed PCM-based BTMS, the energy used in the conventional BTMS could be used in driving the vehicle. Therefore, the driving range of the vehicle will be higher with the same battery capacity. The total driving range that can be extended by using the developed PCM-based BTMS can be calculated as:

$$DR_{extend} = 1.3 \text{ kWh} \times 5.56 \text{ km/kWh} = 7.228 \text{ km}$$

The amount of gas required to drive 7.228 km will be 0.46 L, based on the mileage of a Chevy Volt on gas given in Table 6.33. Considering the gas price in Ontario as shown in Table 6.33, the total cost incurred due to the consumption of extra gas over the life cycle of the battery can be calculated as:

$$C_{gas} = 0.46 \text{ L} \times 1.12\$/\text{L} \times 365 \times 8 = \$1504$$

This shows that, by using the developed PCM-based thermal management system, approximately \$1504 can be saved on running costs. This saving in PCM-based BTMS is equal to the running cost of a conventional BTMS. Therefore, the actual total cost of a conventional BTMS over the lifecycle of the battery will be approximately \$3000, while the material cost of 3 mm thick PCM and CNTs based BTMS is \$2223. The comparison of results show that the PCM-based BTMS are more economical than conventional. However, it should be noted, that in the case of PCM-based BTMS, only material cost is considered on lab scale, while total cost of the conventional BTMS is considered on industrial scale.

6.14 Optimisation Results

In this section, the results obtained from optimisation of the objective function are presented. A genetic algorithm is used to maximise the objective function. To optimise the objective function, three parameters, namely thickness of PCC plates, the number of cells, and the speed of the vehicle, are selected. Design parameters and their range of variation are given in Table 6.37.

Table 6.37: Design parameters and their range.

Parameter	Lower Bound	Upper Bound
PCC Plate Thickness (mm)	6	12
Vehicle Speed (m/s)	20	30
Number of Cells	250	350

Due to space requirements and other limitations in vehicle applications, the maximum PCC plate thickness and number of cells are selected as 12 mm and 350, respectively. With an increase in the number of cells, more power will be available for the vehicle but, at the same time, this increases

the weight of the vehicle. The number of cells varies from 250 to 350 in order to find the optimum. The selection of vehicle speed is based on the normal speed of a vehicle on the highway. As the driving range of the vehicle is optimised separately at each discharge rate, the range of vehicle speed is assumed to be the same for all discharge rates. The optimisation is performed for 500 generations, using a search population size of $M = 100$ individuals, crossover probability of $p_c = 0.9$, and gene mutation probability of $p_m = 0.035$ for all discharge rates. The variation in the objective function with a number of generations is shown in Figure 6.74.

The driving range of an electric vehicle depends on the battery pack performance, which mainly depends on the battery temperature and discharge rate. The optimum value of the objective function, i.e. the driving range at 1C discharge rate, is 86.83 km with 349 cells, which decreases with an increase in discharge rate. The optimum thickness of the PCC plates at 1C discharge rate is 6.65 mm, as given in Table 6.38. The optimum speed of the vehicle remains almost equal to the lower limit for the maximum driving range as the aerodynamics resistance increases with an increase in vehicle speed. With the increase in the discharge rate, the driving range of the vehicle decreases, which can be linked to the battery capacity decrease with an increase in the discharge rate.

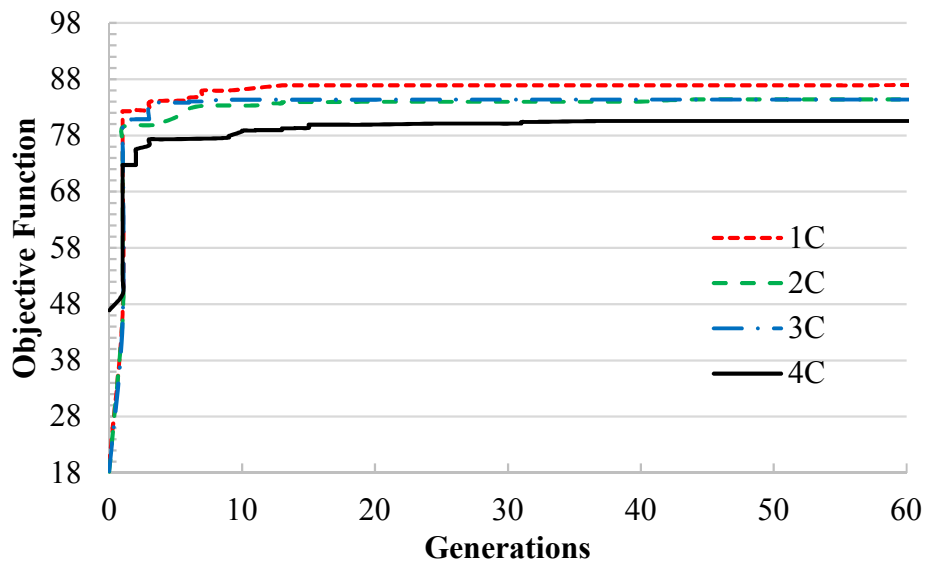


Figure 6.74: Convergences of the objective function with number of generations.

Table 6.38: Optimised parameter and objective function.

Parameter	Optimised Parameters at Various Discharge Rates			
	1C	2C	3C	4C
PCC Plate Thickness (mm)	6.56	6.2	6.06	6
Vehicle Speed (m/s)	20.01	20	20.01	20.02
Number of Cells	349	350	350	350
Objective Function (km)	86.83	84.59	84.34	80.56

The optimised value of the number of cells is equal to the upper limit provided. This shows that the effect of a change in the weight of the vehicle with an increase in the number of cells and PCC plates is small, compared to an increase in the battery pack capacity. The parameter values obtained corresponding to the optimum value of objective function are the design conditions for PCC-based BTMS. Therefore, the obtained results show that the PCC-based BTMS should be designed by using approximately 6 mm thick PCC plates and 350 cells in order to have a maximum driving range. The present optimisation is only a preliminary study of a developed BTMS, as no specific optimisation study of PCM-based BTMS is available in the literature. The trends of decision variables towards either higher or lower limits show that more detailed optimisation is required by considering various other design parameters. However, the present optimisation study provides a base for the detailed optimisation that needs to be conducted in order to improve the developed BTMS.

Chapter 7. Conclusions and Recommendations

In this chapter, the key concluding remarks of the present thesis study are presented. Some recommendations are also made for future studies.

The aim of this research work is to develop a novel PCM based thermal management system for Li-ion batteries in order to maintain a uniform temperature inside the battery and to reduce the cooling requirement of the battery. Two main requirements for any BTMS in the battery pack of EVs and HEVs are essential in order to minimise the peak temperature and prevent large temperature gradients. The main goal of using PCM in cooling systems is to reduce or remove any reliance on the active refrigeration cooling cycle which currently predominates. The use of a PCM-based thermal management system can lead to overall improvements in vehicle efficiency. Examples of stand-alone applications of the developed PCM-based BTMS include electric scooters, battery operated lawn mowers or similar machines, boats, small electric vehicles, and stationary electric energy storage batteries. Although the developed PCM-based BTMS can be used in large electric vehicles such as buses and trucks, it is advisable to integrate liquid cooling with PCM. To achieve these objectives, various combinations of cold plates, coolant temperature, PCC, PCM, and CNTs are tested with a battery pack. Different parameters, such as discharge capacity, battery surface temperature, and SOC, have been selected for the study.

In the first part of the study, an experimental facility has been developed, where cells of different chemistry and capacity can be tested. Three 20Ah A123 Li-ion cells connected in series are used to form a pack. Four discharge rates, such as 1C, 2C, 3C, and 4C, are considered to test the battery pack at lower and higher discharge rates. Initially, the battery pack is tested with no thermal management system at various discharge rates to form a base case for comparison. In the second part, an active liquid cooling system is used to remove the heat from the battery pack, where four cold plates are used along with the cooling bath. Four different temperatures are selected to test the Li-ion battery with the active cooling system.

In the third part, the battery pack is tested with a commercially developed custom-made phase change composite material plate. Similar tests are performed to investigate whether a passive thermal management system can manage the temperature of the battery pack within the required

operating temperature range. Furthermore, a combination of active and passive thermal management systems is developed and tested using PCC plates and cold plates.

In the fourth part, plates of different thicknesses are developed using various combinations of pure and technical grades of PCM with polyurethane foam and tests are performed at different discharge rates. CNTs are added to pure and technical grades of PCM along with polyurethane foam to improve the overall thermal conductivity and plates of different thicknesses are made. These plates are tested with a battery pack to investigate the effects of CNTs with PCM. An optical microscope is used to observe the agglomeration effect in CNT particles with and without polyurethane. Modelling of the battery pack is completed using MATLAB Simulink, where the battery voltage, temperature, and heat generation rate are validated with experimental results. ANSYS simulation is used to observe the temperature distribution within the cells with PCM plates. Energy and exergy analyses are performed to better understand the developed system, and an economic analysis is conducted to investigate its feasibility. An objective function is developed and optimised through a genetic algorithm.

7.1 Conclusions

The Li-ion battery pack is tested at several discharge rates by considering different cooling methods. The main conclusions of the thesis study are listed as follows:

- The developed PCM-based BTMS is capable of managing the Li-ion battery pack temperature within the required range at the selected discharge rates. The layer of PCM between the cells varies from 3 mm to 6 mm in thickness, using both pure and technical grade of PCM. The temperature remains within the required range with a 6 mm thick layer of pure PCM.
- The developed PCM-based BTMS can be placed in any position in an EV and HEV as no PCM leakage is observed from the system. The system is designed in such a way that the PCM remains in between the cells even when it melts and the vehicle is in motion. The cells also remain in their original position all the time during the experiments.
- The use of CNTs and polyurethane foam improves the effectiveness of PCM-based BTMS. With the use of CNTs (1.5% wt.) in pure PCM, the temperature of the battery pack is managed within the required range with only a 3 mm thick layer, instead of a 6 mm thick

layer without CNTs. This reduces the cost of material, the space required to adjust the PCM in between the cells, and the weight of the developed system. Although an increase in CNT concentration in the PCM further reduces the battery pack temperature, the changes observed are insignificant.

- The developed BTMS, using commercially developed PCC material, is also capable of managing the required battery pack temperature, but further improvements are required as some PCM leakage is observed at high discharge rates.
- For the same thickness, pure PCM-based BTMS is more effective than the PCC material based BTMS in keeping the battery pack temperature near the optimum value.
- The developed model in MATLAB is capable of obtaining the behaviour of the battery pack with reasonable accuracy as good agreement is obtained between modelling and experimental results. The developed model can be further modified to study the behaviour of the battery pack with different PCM-based BTMS.
- PCM is effectively utilised across the cell surface in absorbing the heat, as the temperature gradient in the cells remains very low as obtained from the ANSYS simulation. Some deviation in the simulation and experimental results shows that a more detailed ANSYS model is required to improve accuracy.
- The material cost of the PCC material based BTMS is the highest among all the developed systems, and can be significantly reduced (approximately 44%) by using CNTs and polyurethane foam. The cost reduces with the use of CNTs as less material is required to keep the battery pack temperature within the required range. Considering the bulk purchase cost of the material used in developing the PCM-based BTMS, the material cost will be further reduced, making the system more feasible.

Overall, the developed PCM-based passive BTMS is capable of maintaining the Li-ion battery pack temperature for various discharge rates selected on the basis of discharge rates in an actual electric vehicle. At all selected discharge rates, no PCM leakage is observed from the developed system, which confirms its practical application in EVs and HEVs. The use of CNTs with PCM significantly reduces the material cost, weight of the BTMS and space requirements, while keeping the required temperature. The use of polyurethane foam helps to reduce the agglomeration in CNTs. However, further studies are required to quantify and verify the effect. The developed

system can be further improved and optimised through more detailed experimental studies and analyses.

7.2 Recommendations

In this section, the main recommendations to extend, improve, and commercialise the present work are discussed. An extensive investigation has been conducted in the present study for the application of PCM-based BTMS, but still more work is required to find the feasibility and applicability of the developed system. The present work can be extended in the following ways:

- In the present study, only three cells are used to perform experiments while an actual battery pack in EVs and HEVs has hundreds of cells connected in series and in parallel. To know the feasibility of the developed system, it is important to test it with a complete battery pack of an EV or HEV.
- More detailed analysis is required in order to ascertain that use of polyurethane foam with CNTs reduces the agglomeration. Therefore, the tests need to be performed using scanning electron microscope or any other method, which can provide a clear distribution of CNT particles through the foam.
- An integration of the active liquid cooling system with the developed PCM-based passive BTMS needs to be studied for applications where stand-alone PCM-based passive BTMS will not be enough to maintain the required battery pack temperature.
- The experimental results show that the battery pack temperature reduces with the use of CNTs with PCM, which can be correlated with improvement in thermal conductivity of the mixture. However, further tests are required to find the actual thermal conductivity of the developed plates to quantify the effect of using CNTs and polyurethane foam.

The developed PCM-based passive BTMS is capable of managing the battery temperature within the required range. However, further improvements are required to make the present system more reliable and robust. The tasks required to improve the developed system are as follows:

- Alignment of CNTs in PCM has a significant effect on the thermal conductivity of the mixture. Therefore, new methods need to be developed to align the direction of CNTs in series.
- The present study shows that the temperature of the battery pack can be managed within the required range with a 3 mm thick layer of pure PCM and 1.5%, or with a 6 mm thick layer of pure PCM. However, it is not clear whether plates with a thickness between 3-6 mm will be capable of managing the battery pack temperature within the required range. Therefore, further tests are required by varying the plate thickness by smaller intervals (0.5 mm or 1 mm) to find the optimum thickness of PCM-based plates.

The present work has been completed on a research scale. The developed system can be commercialised and can have a variety of applications. The following are recommendations to commercialise the developed system:

- The effect of using PCM-based BTMS on space requirement and aerodynamic design of the vehicle needs to be studied.
- A preliminary economic analysis of the developed system is performed in the present study, where only material cost is considered. Therefore, a detailed economic analysis is required for the developed systems by considering all the associated costs on an industrial scale.

References

1. Carlowicz, M., *Global temperatures*. National Aeronautics and Space Administration (NASA), 2016 [cited 2016 December 7]; Available from: <http://earthobservatory.nasa.gov/Features/WorldOfChange/decadaltemp.php>.
2. *NOAA national centers for environmental information, state of the climate: global analysis for annual 2015*. National Oceanic and Atmospheric Administration (NOAA), 2016 [cited 2016 December 16]; Available from: <http://www.ncdc.noaa.gov/sotc/global/201513>.
3. MacMillan, A., *Global warming 101*. Natural Resources Defense Council (NRDC), 2016 [cited 2016 December 16]; Available from: <https://www.nrdc.org/stories/global-warming-101>.
4. *America's climate choices: panel on advancing the science of climate change*, in *Advancing the Science of Climate Change*, 2010: Washington, D.C.
5. *Drivers and impacts of greenhouse gas emissions*. Environment and Climate Change Canada, 2016 [cited 2016 December 16]; Available from: <https://www.ec.gc.ca/indicateurs-indicators/default.asp?lang=en&n=D4C4DBAB-1>.
6. Gordon, D., *The role of transportation in driving climate disruption, energy and climate program*. 2010, Carnegie Endowment for International Peace Program, E.A.C.: Washington.
7. *Sources of greenhouse gas emissions*. US Environmental Protection Agency, 2016 [cited 2016 December 16]; Available from: <https://www.epa.gov/ghgemissions/sources-greenhouse-gas-emissions>.
8. *2009 national inventory report: greenhouse gas sources and sinks in Canada, 1990-2007*, Environment-Canada. 2009: Ottawa.
9. *Emissions from hybrid and plug-in electric vehicles*. Alternative Fuels Data Center, 2016 [cited 2016 December 15]; Available from: http://www.afdc.energy.gov/vehicles/electric_emissions.php.
10. Khateeb, S. A., Farid, M. M., Selman, J. R., and Al-Hallaj, S., *Design and simulation of a lithium-ion battery with a phase change material thermal management system for an electric scooter*. *Journal of Power Sources*, 2004. 128(2): p. 292-307.
11. Al-Hallaj, S., Kizilel, R., Lateef, A., Sabbah, R., Farid, M., and Selman, J. R., *Passive thermal management using phase change material (PCM) for EV and HEV Li-ion batteries*, in *Vehicle Power and Propulsion, 2005 IEEE Conference*. 2005: Chicago, USA.
12. Lin, C., Xu, S., Chang, G., and Liu, J., *Experiment and simulation of a LiFePO₄ battery pack with a passive thermal management system using composite phase change material and graphite sheets*. *Journal of Power Sources*, 2015. 275: p. 742-749.
13. Han, Z. and Fina, A., *Thermal conductivity of carbon nanotubes and their polymer nanocomposites: A review*. *Progress in Polymer Science*, 2011. 36(7): p. 914-944.
14. Atif, R. and Inam, F., *Reasons and remedies for the agglomeration of multilayered graphene and carbon nanotubes in polymers*. *Beilstein Journal of Nanotechnology*, 2016. 7: p. 1174-1196.
15. Rausch, J., Zhuang, R. C., and Mäder, E., *Surfactant assisted dispersion of functionalized multi-walled carbon nanotubes in aqueous media*. *Composites Part A: Applied Science and Manufacturing*, 2010. 41(9): p. 1038-1046.

16. Gojny, F. H., Wichmann, M. H. G., Fiedler, B., Kinloch, I. A., Bauhofer, W., Windle, A. H., and Schulte, K., *Evaluation and identification of electrical and thermal conduction mechanisms in carbon nanotube/epoxy composites*. Polymer, 2006. 47(6): p. 2036-2045.
17. Ma, P. C., Siddiqui, N. A., Marom, G., and Kim, J. K., *Dispersion and functionalization of carbon nanotubes for polymer-based nanocomposites: A review*. Composites Part A: Applied Science and Manufacturing, 2010. 41(10): p. 1345-1367.
18. Høyer, K. G., *The history of alternative fuels in transportation: The case of electric and hybrid cars*. Utilities Policy, 2008. 16(2): p. 63-71.
19. Model S. Tesla, 2016 [cited 2016 December 22]; Available from: https://www.tesla.com/en_CA/models.
20. Conte, F. V., *Battery and battery management for hybrid electric vehicles: a review*. Elektrotechnik und Informationstechnik, 2006. 123(10): p. 424-431.
21. Kampman, B., Leguijt, C., Bennink, D., Wielders, L., Rijkee, X., Buck, A. D., and Braa, W., *Development of policy recommendations to harvest the potential of electric vehicle*. 2010, Transport & Environment, Friends of the Earth Europe and Greenpeace European Unit, organization, C. D.: Delft.
22. *Electric drive market snapshot: May 2015*. Electric Drive Sales Dashboard, Electric Drive Transportation Association (EDTA), 2015 [cited 2015 June 19]; Available from: <http://electricdrive.org/index.php?ht=d%2Fsp%2Fi%2F20952%2Fpid%2F20952>.
23. Malik, M., Dincer, I., and Rosen, M. A., *Review on use of phase change materials in battery thermal management for electric and hybrid electric vehicles*. International Journal of Energy Research, 2016.
24. Patterson, J., *Hybrid car types*. CarsInTrend, 2016 [cited 2016 December 22]; Available from: <https://carsintrend.com/hybrid-car-types>.
25. Lo, E. W. C., *Review on the configurations of hybrid electric vehicles*. in *2009 3rd International Conference on Power Electronics Systems and Applications (PESA)*. 2009: Hong Kong, China.
26. Bayindir, K. Ç., Gözükcük, M. A., and Teke, A., *A comprehensive overview of hybrid electric vehicle: powertrain configurations, powertrain control techniques and electronic control units*. Energy Conversion and Management, 2011. 52(2): p. 1305-1313.
27. Hodgkinson, R. and Fenton, J., *6 - Hybrid vehicle design*, in *Lightweight Electric/Hybrid Vehicle Design*. 2000, Butterworth-Heinemann: Oxford. p. 141-172.
28. Brain, M., *How electric cars work*. How Stuff Works, 2008 [cited 2014 September 5]; Available from: <http://www.howstuffworks.com/electric-car.htm>.
29. Reddy, T. B. and David, L., *Linden's handbook of batteries*. 2011, New York: McGraw-Hill.
30. Shnayerson, M., *The car that could : the inside story of GM's revolutionary electric vehicle*. 1996, New York: Random House.
31. Kalhammer, F. R., Kopf, B. M., Swan, D. H., Roan, V. P., and Walsh, M. P., *Status and prospects for zero emissions vehicle technology*. 2007, State of California Air Resources Board: California
32. Arora, P. and Zhang, Z., *Battery separators*. Chemical Review, 2004. 104: p. 4419-4468.
33. Fang, W., Kwon, O. J., and Wang, C. Y., *Electrochemical-thermal modeling of automotive Li-ion batteries and experimental validation using a three-electrode cell*. International Journal of Energy Research, 2010. 34(2): p. 107-115.

34. Brain, M., *How Lithium-ion batteries work*. How Stuff Works, 2006 [cited 2014 September 11]; Available from: <http://electronics.howstuffworks.com/everyday-tech/lithium-ion-battery1.htm>.
35. Kelty, K., *Battery*. Increasing Energy Density Means Increasing Range, Tesla Motors, 2011 [cited 2014 September 10]; Available from: <http://www.teslamotors.com/roadster/technology/battery>.
36. Wohlfahrt-Mehrens, M., and Wachtler, M., *Electrochemical energy storage systems for car applications*. HySA Systems Business Seminar, November 2009: Capetown, SA.
37. Deutsche Bank; R. Lache, P. N., D. Galves, G. Toulemonde, J. Gehrke, K. Sanger, V. ha, S. Rao, and J. Crane, *Electric Cars: Plugged In. Batteries must be included*. Deutsche Bank AG, June 2008: Frankfurt, Germany.
38. *BU-205: types of Lithium-ion*. Crash Course on Batteries, Battery-University, 2011 [cited 2014 September 14]; Available from: http://batteryuniversity.com/learn/article/types_of_lithium_ion.
39. Spotnitz, R., *Simulation of capacity fade in lithium-ion batteries*. Journal of Power Sources, 2003. 113(1): p. 72-80.
40. Dubarry, M. and Liaw, B. Y., *Identify capacity fading mechanism in a commercial LiFePO₄ cell*. Journal of Power Sources, 2009. 194(1): p. 541-549.
41. *Battery and energy technologies*. Woodbank Communications Ltd, 2016 [cited 2016 December 18]; Available from: <http://www.mpoweruk.com/chemistries.htm>.
42. Zhang, Q. and White, R. E., *Capacity fade analysis of a lithium ion cell*. Journal of Power Sources, 2008. 179(2): p. 793-798.
43. Edström, K., Gustafsson, T., and Thomas, J. O., *The cathode–electrolyte interface in the Li-ion battery*. Electrochimica Acta, 2004. 50(2–3): p. 397-403.
44. Lam, L., *A practical circuit-based model for state of health estimation of li-ion battery cells in electric vehicles*, in *Electrical Power Engineering*. 2011, University of Technology: Netherlands.
45. Smart, M. C., Ratnakumar, B. V., Whitcanack, L., Chin, K., Rodriguez, M., and Surampudi, S., *Performance characteristics of lithium ion cells at low temperatures*. IEEE Aerospace and Electronic Systems Magazine, 2002. 17(12): p. 16-20.
46. Vetter, J., Novák, P., Wagner, M. R., Veit, C., Möller, K. C., Besenhard, J. O., Winter, M., Wohlfahrt-Mehrens, M., Vogler, C., and Hammouche, A., *Ageing mechanisms in lithium-ion batteries*. Journal of Power Sources, 2005. 147(1–2): p. 269-281.
47. Mahamud, R. and Park, C., *Reciprocating air flow for Li-ion battery thermal management to improve temperature uniformity*. Journal of Power Sources, 2011. 196(13): p. 5685-5696.
48. Nelson, P., Dees, D., Amine, K., and Henriksen, G., *Modeling thermal management of Lithium-ion PNGV batteries*. Journal of Power Sources, 2002. 110: p. 349-356.
49. Sabbah, R., Kizilel, R., Selmán, J. R., and Al-Hallaj, S., *Active (air-cooled) vs. passive (phase change material) thermal management of high power lithium-ion packs: limitation of temperature rise and uniformity of temperature distribution*. Journal of Power Sources, 2008. 182(2): p. 630-638.
50. Wang, Q., Ping, P., Zhao, X., Chu, G., Sun, J., and Chen, C., *Thermal runaway caused fire and explosion of lithium ion battery*. Journal of Power Sources, 2012. 208: p. 210-224.

51. Pesaran, A. A., Burch, S., and Keyser, M., *An approach for designing thermal management systems for electric and hybrid vehicle battery packs*, in *The Fourth Vehicle Thermal Management Systems Conference and Exhibition*. 1999: London, UK.
52. Bower, G., *Tesla or GM: who has the best battery thermal management?*, Motorsport Network, 2015 [cited 2016 September 7]; Available from: <http://insideevs.com/tesla-or-gm-who-has-the-best-battery-thermal-management-bower/>.
53. *The Chevrolet Volt cooling/heating systems explained*. WopOnTour, 2009 [cited 2016 September 8]; Available from: <http://gm-volt.com/2010/12/09/the-chevrolet-volt-coolingheating-systems-explained/>.
54. Javani, N., Dincer, I., and Naterer, G. F., *Investigation of energy storage options for thermal management in hybrid electric vehicles*, in *Faculty of Engineering and Applied Science*. 2013, University of Ontario Institute of Technology (UOIT): Oshawa, Canada.
55. LeGault, M., *Chevy Volt battery pack: Rugged but precise*. Gardner Business Media Inc, 2013 [cited 2016 May 18]; Available from: <http://www.compositesworld.com/articles/chevy-volt-battery-pack-rugged-but-precise>.
56. Tennessen, P. T., Weintraub, J. C., and Hermann, W. A., *Extruded and ribbed thermal interface for use with a battery cooling system*. 2014, Google Patents.
57. Suganya, G. and Bapu, B. R., *Experimental studies on performance of latent heat thermal energy storage unit integrated with solar water heater*. International Journal of Chemical Sciences, 2016. 14(2).
58. Xu, B., Li, P., and Chan, C., *Application of phase change materials for thermal energy storage in concentrated solar thermal power plants: a review to recent developments*. Applied Energy, 2015. 160: p. 286-307.
59. Sharif, M. K. A., Al-Abidi, A. A., Mat, S., Sopian, K., Ruslan, M. H., Sulaiman, M. Y., and Rosli, M. A. M., *Review of the application of phase change material for heating and domestic hot water systems*. Renewable and Sustainable Energy Reviews, 2015. 42: p. 557-568.
60. Baetens, R., Jelle, B. P., and Gustavsen, A., *Phase change materials for building applications: a state-of-the-art review*. Energy and Buildings, 2010. 42(9): p. 1361-1368.
61. Sadrameli, S. M. and Azizi, Y., *Application of phase change materials for the safety and thermal management of the lithium-ion batteries at high temperature climate conditions*. in *Meeting Abstracts*. 2016. The Electrochemical Society.
62. Abhat, A., *Low temperature latent heat thermal energy storage heat storage*. Solar Energy, 1983. 10(4): p. 313-332.
63. Liu, C. and Rao, Z., *Challenges in various thermal energy storage technologies*. Science Bulletin, 2017. 62(4): p. 231-233.
64. Gil, A., Medrano, M., Martorell, I., Lázaro, A., Dolado, P., Zalba, B., and Cabeza, L. F., *State of the art on high temperature thermal energy storage for power generation. Part 1—Concepts, materials and modellization*. Renewable and Sustainable Energy Reviews, 2010. 14(1): p. 31-55.
65. Dennis, K., *Phase change materials & heat pump analysis for an electric vehicle*. Department of Mechanical Engineering, 1995, Lakehead University: Thunder Bay, Canada.

66. Zalba, B., Marín, J. M., Cabeza, L. F., and Mehling, H., *Review on thermal energy storage with phase change: materials, heat transfer analysis and applications*. Applied Thermal Engineering, 2003. 23(3): p. 251-283.
67. Farid, M. M., Khudhair, A. M., Razack, S. A. K., and Al-Hallaj, S., *A review on phase change energy storage: materials and applications*. Energy Conversion and Management, 2004. 45(9–10): p. 1597-1615.
68. Sharma, A., Tyagi, V. V., Chen, C. R., and Buddhi, D., *Review on thermal energy storage with phase change materials and applications*. Renewable and Sustainable Energy Reviews, 2009. 13(2): p. 318-345.
69. Kalnaes, S. E. and Jelle, B. P., *Phase change materials and products for building applications: A state-of-the-art review and future research opportunities*. Energy and Buildings, 2015. 94: p. 150-176.
70. Sharma, S. D. and Sagara, K., *Latent heat storage materials and systems: a review*. International Journal of Green Energy, 2005. 2(1): p. 1-56.
71. Jegadheeswaran, S. and Pohekar, S. D., *Performance enhancement in latent heat thermal storage system: a review*. Renewable and Sustainable Energy Reviews, 2009. 13(9): p. 2225-2244.
72. Iijima, S., *Helical microtubules of graphitic carbon*. Nature, 1991. 354(6348): p. 56-58.
73. Aqel, A., El-Nour, K. M. M. A., Ammar, R. A. A., and Al-Warthan, A., *Carbon nanotubes, science and technology part (I) structure, synthesis and characterisation*. Arabian Journal of Chemistry, 2012. 5(1): p. 1-23.
74. Xu, J. and Fisher, T. S., *Enhancement of thermal interface materials with carbon nanotube arrays*. International Journal of Heat and Mass Transfer, 2006. 49(9–10): p. 1658-1666.
75. *Multi walled carbon nanotubes products*. Cheap Tubes Inc, 2016 [cited 2016 December 26]; Available from: <https://www.cheaptubes.com/product-category/multi-walled-carbon-nanotubes/>.
76. Ma, P. C., Mo, S. Y., Tang, B. Z., and Kim, J. K., *Dispersion, interfacial interaction and re-agglomeration of functionalized carbon nanotubes in epoxy composites*. Carbon, 2010. 48(6): p. 1824-1834.
77. Wang, J. and Pui, D. Y. H., *Dispersion and filtration of carbon nanotubes (CNTs) and measurement of nanoparticle agglomerates in diesel exhaust*. Chemical Engineering Science, 2013. 85: p. 69-76.
78. Choudhary, V. and Gupta, A., *Polymer/Carbon Nanotube Nanocomposites*. Carbon Nanotubes - Polymer Nanocomposites. 2011, 2011: p. 65-90.
79. Green, M. J., Behabtu, N., Pasquali, M., and Adams, W. W., *Nanotubes as polymers*. Polymer, 2009. 50(21): p. 4979-4997.
80. Shofner, M. L., Rodríguez-Macías, F. J., Vaidyanathan, R., and Barrera, E. V., *Single wall nanotube and vapor grown carbon fiber reinforced polymers processed by extrusion freeform fabrication*. Composites Part A: Applied Science and Manufacturing, 2003. 34(12): p. 1207-1217.
81. Ghaffarizadeh, A., Ahmadi, K., and Flann, N. S., *Sorting unsigned permutations by reversals using multi-objective evolutionary algorithms with variable size individuals*. in *Evolutionary Computation (CEC), 2011 IEEE Congress on*. 2011: New Orleans, USA
82. Goldberg, D. E. and Holland, J. H., *Genetic algorithms and machine learning*. Machine learning, 1988. 3(2): p. 95-99.

83. *Genetic algorithm*. Wikipedia, 2016 [cited 2016 December 12]; Available from: https://en.wikipedia.org/wiki/Genetic_algorithm.
84. Schaffer, J. D., *Multiple objective optimization with vector evaluated genetic algorithms*. in *Proceeding of the First International Conference on Genetic Algorithms and Their Applications*, 1985: Hillsdale, USA.
85. Selman, J. R., Hallaj, S. A., Uchida, I., and Hirano, Y., *Cooperative research on safety fundamentals of lithium batteries*. Journal of Power Sources, 2001. 97-98: p. 726-732.
86. Saito, Y., Takano, K., and Negishi, A., *Thermal behaviours of lithium-ion cells during overcharge*. Journal of Power Sources, 2001. 97-98: p. 693-696.
87. Hallaj, S. A., Prakash, J., and Selman, J. R., *Characterization of commercial Li-ion batteries using electrochemical- calorimetric measurements*. Journal of Power Sources, 2000. 87: p. 186–194.
88. Eddahech, A., Briat, O., and Vinassa, J. M., *Thermal characterization of a high-power lithium-ion battery: Potentiometric and calorimetric measurement of entropy changes*. Energy, 2013. 61: p. 432-439.
89. Rao, L. and Newman, J., *Heat generation rate and general energy balance for insertion battery systems*. Journal of Electrochemical Society, 1997. 144(8): p. 2697-2704.
90. Bernardi, D., Pawlikowski, E., and Newman, J., *A general energy balance for battery systems*. Journal of Electrochemical Science and Technology, 1985. 132(1): p. 5-12.
91. Chen, Y. and Evans, J. W., *Thermal analysis of Lithium-ion batteries*. Journal of Electrochemical Science and Technology, 1996. 143(9): p. 2708-2712.
92. Hamut, H. S., Dincer, I., and Naterer, G. F., *Analysis and optimization of hybrid electric vehicle thermal management systems*. Journal of Power Sources, 2014. 247: p. 643-654.
93. Fathabadi, H., *High thermal performance lithium-ion battery pack including hybrid active–passive thermal management system for using in hybrid/electric vehicles*. Energy, 2014. 70: p. 529-538.
94. Keller, A. and Whitehead, G., *Thermal characteristics of electric vehicle batteries*. SAE International Journal of Passenger Cars, 1991. 10(6).
95. Kuper, C., Hoh, M., Houchin-Miller, G., and Fuhr, J., *Thermal management of hybrid vehicle battery systems*, in *EVS24*. 2009: Stavanger, Norway.
96. Pesaran, A. A. *Battery thermal management in EVs and HEVs: issues and problems*. in *Advanced Automotive Battery Conference*. 2001: Las Vegas, Nevada.
97. Liu, R., Chen, J., Xun, J., Jiao, K., and Du, Q., *Numerical investigation of thermal behaviors in lithium-ion battery stack discharge*. Applied Energy, 2014. 132: p. 288-297.
98. Zhang, X., Kong, X., Li, G., and Li, J., *Thermodynamic assessment of active cooling/heating methods for lithium-ion batteries of electric vehicles in extreme conditions*. Energy, 2014. 64: p. 1092-1101.
99. Saw, L. H., Tay, A. A. O., and Zhang, L. W., *Thermal management of lithium-ion battery pack with liquid cooling*. in *2015 31st Thermal Measurement, Modeling & Management Symposium (SEMI-THERM)*. 2015: San Jose, USA.
100. Duan, X. and Naterer, G. F., *Heat transfer in phase change materials for thermal management of electric vehicle battery modules*. International Journal of Heat and Mass Transfer, 2010. 53(23-24): p. 5176-5182.

101. Al-Hallaj, S. and Selman, J. R., *Thermal modeling of secondary lithium batteries for electric vehicle hybrid electric vehicle application*. Journal of Power Sources 2002. 110: p. 341-348.
102. Kizilel, R., Sabbah, R., Selman, J. R., and Al-Hallaj, S., *An alternative cooling system to enhance the safety of Li-ion battery packs*. Journal of Power Sources, 2009. 194(2): p. 1105-1112.
103. Kizilel, R., Lateef, A., Sabbah, R., Farid, M. M., Selman, J. R., and Al-Hallaj, S., *Passive control of temperature excursion and uniformity in high-energy Li-ion battery packs at high current and ambient temperature*. Journal of Power Sources, 2008. 183(1): p. 370-375.
104. Javani, N., Dincer, I., Naterer, G. F., and Rohrauer, G. L., *Modeling of passive thermal management for electric vehicle battery packs with PCM between cells*. Applied Thermal Engineering, 2014. 73(1): p. 305-314.
105. Martinelli, M., Bentivoglio, F., Caron Soupart, A., Couturier, R., Fourmigue, J. F., and Marty, P., *Experimental study of a phase change thermal energy storage with copper foam*. Applied Thermal Engineering, 2016. 101: p. 247-261.
106. Chen, P., Gao, X., Wang, Y., Xu, T., Fang, Y., and Zhang, Z., *Metal foam embedded in SEBS/paraffin/HDPE form-stable PCMs for thermal energy storage*. Solar Energy Materials and Solar Cells, 2016. 149: p. 60-65.
107. Xu, W., Yuan, X., and Li, Z., *Study on effective thermal conductivity of metal foam matrix composite phase change materials*. Journal of Functional Materials, , 2009. 40: p. 1329-1332.
108. Xiao, X., Zhang, P., and Li, M., *Preparation and thermal characterization of paraffin/metal foam composite phase change material*. Applied Energy, 2013. 112: p. 1357-1366.
109. Chen, J., Yang, D., Jiang, J., Ma, A., and Song, D., *Research progress of phase change materials (PCMs) embedded with metal foam (a Review)*. Procedia Materials Science, 2014. 4: p. 389-394.
110. Shaikh, S., Lafdi, K., and Hallinan, K., *Carbon nanoadditives to enhance latent energy storage of phase change materials*. Journal of Applied Physics, 2008. 103(9): p. 094302.
111. Babapoor, A., Azizi, M., and Karimi, G., *Thermal management of a Li-ion battery using carbon fiber-PCM composites*. Applied Thermal Engineering, 2015. 82: p. 281-290.
112. Bauer, C. A. and Wirtz, R. A., *Thermal characteristics of a compact passive thermal energy storage device*, in *ASME IMECE: Undergraduate Research and Design in Heat Transfer*. 2000: Florida.
113. Shiina, Y., *Reduction of temperature changes in heat transfer fluid by the use of latent heat storage technology*. Transactions of the Atomic Energy Society of Japan, 2006. 5: p. 190-199.
114. Kumaresan, V., Velraj, R., and Das, S. K., *The effect of carbon nanotubes in enhancing the thermal transport properties of PCM during solidification*. Heat and Mass Transfer, 2012. 48(8): p. 1345-1355.
115. Zhang, G. H. and Zhao, C. Y., *Thermal property investigation of aqueous suspensions of microencapsulated phase change material and carbon nanotubes as a novel heat transfer fluid*. Renewable Energy, 2013. 60: p. 433-438.

116. Choi, D. H., Lee, J., Hong, H., and Kang, Y. T., *Thermal conductivity and heat transfer performance enhancement of phase change materials (PCM) containing carbon additives for heat storage application*. International Journal of Refrigeration, 2014. 42: p. 112-120.
117. Wang, J., Xie, H., Xin, Z., Li, Y., and Chen, L., *Enhancing thermal conductivity of palmitic acid based phase change materials with carbon nanotubes as fillers*. Solar Energy, 2010. 84(2): p. 339-344.
118. Fan, L. W., Fang, X., Wang, X., Zeng, Y., Xiao, Y. Q., Yu, Z. T., Xu, X., Hu, Y. C., and Cen, K. F., *Effects of various carbon nanofillers on the thermal conductivity and energy storage properties of paraffin-based nanocomposite phase change materials*. Applied Energy, 2013. 110: p. 163-172.
119. Javani, N., Dincer, I., and Naterer, G. F., *New latent heat storage system with nanoparticles for thermal management of electric vehicles*. Journal of Power Sources, 2014. 268: p. 718-727.
120. Javani, N., Dincer, I., Naterer, G. F., and Yilbas, B. S., *Exergy analysis and optimization of a thermal management system with phase change material for hybrid electric vehicles*. Applied Thermal Engineering, 2014. 64(1-2): p. 471-482.
121. Hamut, H. S., Dincer, I., and Naterer, G. F., *Exergy analysis of a TMS (thermal management system) for range-extended EVs (electric vehicles)*. Energy, 2012. 46(1): p. 117-125.
122. Hamut, H. S., Dincer, I., and Naterer, G. F., *Exergy analysis and environmental impact assessment of using various refrigerants for hybrid electric vehicle thermal management systems*, in *Causes, Impacts and Solutions to Global Warming*. 2013, Springer New York. p. 879-908.
123. Sweeney, S., Berhanu, D., Misra, S. K., Thorley, A. J., Valsami-Jones, E., and Tetley, T. D., *Multi-walled carbon nanotube length as a critical determinant of bioreactivity with primary human pulmonary alveolar cells*. Carbon, 2014. 78: p. 26-37.
124. *Multi walled carbon nanotubes 50nm*. CheapTubes Inc, 2017 [cited 2017 May 12]; Available from: <https://www.cheaptubes.com/product/multi-walled-carbon-nanotubes-50nm/>.
125. Pals, C. R. and Newman, J., *Thermal modeling of the lithium/polymer battery*. Journal of the Electrochemical Society, 1995. 142(10): p. 3274-3281.
126. Chen, Y. and Evans, J. W., *Three-dimensional thermal modeling of lithium-polymer batteries under galvanostatic discharge and dynamic power profile*. Journal of the Electrochemical Society, 1994. 141(11): p. 2947-2952.
127. Wierschem, G., McKinney, B., and Nrotek, E., *Thermal management of lead-acid batteries for electric vehicles*. in *Research and development testing*. SAE Technical Paper, 1993: Detroit.
128. Jain, M., Gupta, S., Masand, D., and Agnihotri, G., *Analysis of a microgrid under transient conditions using voltage and frequency controller*. Advances in Power Electronics 2012. 2012: p. 18.
129. Forgez, C., Do, D. V., Friedrich, G., Morcrette, M., and Delacourt, C., *Thermal modeling of a cylindrical LiFePO₄/graphite lithium-ion battery*. Journal of Power Sources, 2010. 195: p. 2961-2968.

130. Samadani, E., Lo, J., Fowler, M., Fraser, R. A., and Gimenez, L., *Impact of temperature on the A123 Li-ion battery performance and hybrid electric vehicle range*. SAE Technical Paper, 2013.
131. Chapter: 18. Solver Theory, in *ANSYS FLUENT 12.0.1, User's Guide*. 2009, Ansys Inc.
132. Ramandi, M. Y., *Numerical modeling of transient transport phenomena in molten carbonate fuel cells*, in *Faculty of Engineering and Applied Science*. 2012, University of Ontario Institute of Technology: Oshawa, Canada.
133. *General scalar transport equation: discretization and solution*. ANSYS, 2013 [cited 2016 December 13]; Available from: https://www.sharcnet.ca/Software/Ansys/17.0/en-us/help/flu_th/flu_th_general_transport.html.
134. *ANSYS CFX-solver theory guide*. ANSYS, 2013 [cited 2016 December 12]; Available from: <http://148.204.81.206/Ansys/150/ANSYS%20CFX-Solver%20Theory%20Guide.pdf>.
135. 25.3.2 temporal discretization. Sharcnet, 2006 [cited 2016 December 9]; Available from: <https://www.sharcnet.ca/Software/Fluent6/html/ug/node993.htm>.
136. Chapter: 7. cell zone and boundary condition in *ANSYS FLUENT 12.0.1, User's Guide*. 2009, Ansys Inc.
137. Macke, C. J., *Experimental study of bubble plume with CFD benchmarking in Nuclear Engineering*. 2013, Purdue University: West Lafayette, USA.
138. Kuron, M., *3 criteria for assessing CFD convergence*. The Engineer, 2015 [cited 2017 May 12]; Available from: <http://www.engineering.com/DesignSoftware/DesignSoftwareArticles/ArticleID/9296/3-Criteria-for-Assessing-CFD-Convergence.aspx>.
139. 25.22.1 judging convergence (ANSYS Fluent). Sharcnet, 2006 [cited 2016 November 10]; Available from: <https://www.sharcnet.ca/Software/Fluent6/html/ug/node1067.htm>.
140. Dincer, I., Hamut, H. S., and Javani, N., *Thermal management of electric vehicle battery systems*. 2016: John Wiley & Sons.
141. Strauss, M. T. and Poher, R. L., *Nanotubes in liquids: effective thermal conductivity*. Journal of Applied Physics, 2006. 100(8): p. 084328.
142. Dincer, I. and Rosen, M. A., *Exergy: energy, environment and sustainable development*. 2012: Newnes.
143. Pesaran, A. A., *Battery thermal models for hybrid vehicle simulations*. Journal of Power Sources, 2002. 110(2): p. 377-382.
144. Rask, E., *Battery energy availability and consumption during vehicle charging across ambient temperatures and battery temperature*. Argonne National Laboratory, 2013: USA.
145. Notario, B., Pinto, J., Solorzano, E., de Saja, J. A., Dumon, M., and Rodríguez-Pérez, M. A., *Experimental validation of the Knudsen effect in nanocellular polymeric foams*. Polymer, 2015. 56: p. 57-67.
146. Al-Otaibi, D. A., Dincer, I., and Kalyon, M., *Thermoeconomic optimization of vapor-compression refrigeration systems*. International Communications in Heat and Mass Transfer, 2004. 31(1): p. 95-107.
147. *Electricity prices*. Ontario Energy Board, 2016 [cited 2017 December 27]; Available from: <http://www.ontarioenergyboard.ca/oeb/Consumers/Electricity/Electricity%20Prices>.
148. Al-Hallaj, S., *Safety and thermal management for li-ion batteries in transportation applications*. EV Li-ion Battery Forum 2012, 2012: Chicago, USA.